Science

13 March 2009 | $10

AAAS

CONTENTS

Volume 323 Issue 5920

EDITORIAL

NEWS OF THE WEEK

NEWS FOCUS

LETTERS

BOOKS *ET AL.*

POLICY FORUM

PERSPECTIVES

BREVIA

CONTENTS continued **>>**

page 1420

page 1432

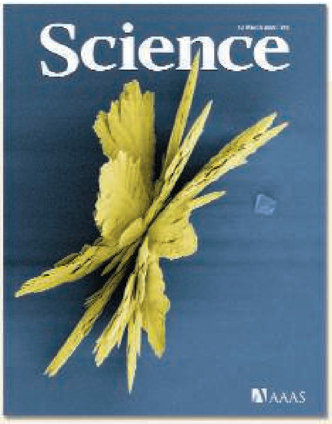

COVER

False-color scanning electron micrograph of oriented vaterite, a crystalline polymorph of calcium carbonate, formed through template-controlled nucleation. Formation starts with the aggregation of prenucleation clusters forming an amorphous phase from which the crystals develop at the template surface. This experimental process may be analogous to the natural formation of seashells and other marine skeletons. See page 1455.

Image: W. J. E. M. Habraken and C. J. van den Hoogen/ Eindhoven University of Technology

DEPARTMENTS

RESEARCH ARTICLES

1443 Wind-Driven Upwelling in the Southern Ocean and the Deglacial Rise in Atmospheric CO_2

R. F. Anderson et al.

Ventilation of carbon dioxide from the Southern Ocean preceded the last deglaciation.

>> Perspective p. 1434

1448 The Dynamic Control of Kiss-And-Run and Vesicular Reuse Probed with Single Nanoparticles

Q. Zhang et al.

A transient form of vesicle fusion that allows vesicle reuse is more prevalent early during synaptic response to a train of stimuli.

REPORTS

1453 Explosive Percolation in Random Networks

D. Achlioptas et al.

Simulations show that transitions in the connectivity within a random network can occur discontinuously.

>> Perspective p. 1438

1455 The Initial Stages of Template-Controlled $CaCO_3$ Formation Revealed by Cryo-TEM

E. M. Pouget et al.

Amorphous mineral particles attached to an ordered organic monolayer play a role in the crystallization of calcium carbonate.

1458 Self-Repairing Oxetane-Substituted Chitosan Polyurethane Networks

B. Ghosh and M. W. Urban

A polymer is modified to include a reactive group that can repair mechanical damage by exposure to ultraviolet light.

>> Science *Podcast*

1461 Nonporous Organic Solids Capable of Dynamically Resolving Mixtures of Diiodoperfluoroalkanes

P. Metrangolo et al.

An ionic crystal that traps iodine-capped fluorocarbons selectively and reversibly has potential for industrial separations.

1464 Time-Resolved Molecular Frame Dynamics of Fixed-in-Space CS_2 Molecules

C. Z. Bisgaard et al.

Transient alignment of CS_2 molecules by a short laser pulse allows resolution of otherwise obscured reaction dynamics.

1468 Clear Sky Visibility Has Decreased over Land Globally from 1973 to 2007

K. Wang et al.

The concentration of atmospheric aerosols has decreased over Europe but not over the tropics or the Southern Hemisphere.

1470 Recent Changes in Phytoplankton Communities Associated with Rapid Regional Climate Change Along the Western Antarctic Peninsula

M. Montes-Hugo et al.

Chlorophyll concentration has decreased by 12% over 30 years of ice retreat, with consequences for vertebrate populations.

1473 A Recessive Mutation in the APP Gene with Dominant-Negative Effect on Amyloidogenesis

G. Di Fede et al.

A mutation in the amyloid precursor protein gene causes Alzheimer's disease in homozygotic patients.

1477 Structure of the Anaphase-Promoting Complex/Cyclosome Interacting with a Mitotic Checkpoint Complex

F. Herzog et al.

Electron microscopy captures cell cycle checkpoint proteins in the act of inhibiting cell division in HeLa cells.

1481 A Functional Genomics Approach Reveals CHE as a Component of the *Arabidopsis* Circadian Clock

J. L. Pruneda-Paz et al.

A transcription factor (CHE) binds the promoter of the clock gene *CCA1*, adding to the molecular clock circuitry in plants.

>> Perspective p. 1440

1485 Paternal Control of Embryonic Patterning in *Arabidopsis thaliana*

M. Bayer et al.

Transcripts of a cytoplasmic gene from sperm are translated after fertilization and control asymmetric zygotic division.

>> Perspective p. 1439

1488 Preferential Generation of Follicular B Helper T Cells from $Foxp3^+$ T Cells in Gut Peyer's Patches

M. Tsuji et al.

Suppressor T cells selectively differentiate into helper T cells in the mouse gut and thereby promote immune homeostasis.

1492 Selective Erasure of a Fear Memory

J.-H. Han et al.

Fear memory in mice is erased by experimental killing of a subpopulation of lateral amygdala neurons.

>> Science *Podcast*

1496 Human Substantia Nigra Neurons Encode Unexpected Financial Rewards

K. A. Zaghloul et al.

Dopamine neurons in the human mid-brain are activated by unexpected rewards and differentiate positive and negative feedback.

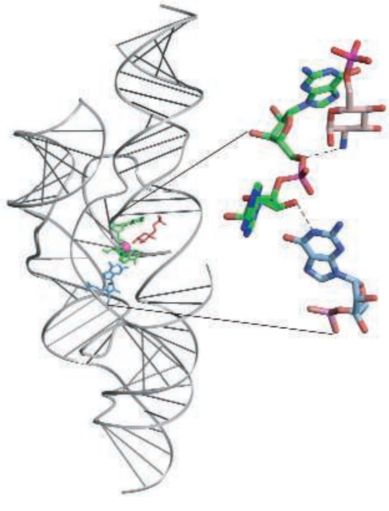

page 1436

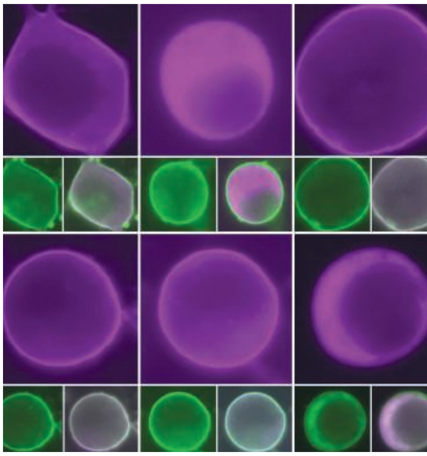

page 1500

1500 RSY-1 Is a Local Inhibitor of Presynaptic Assembly in *C. elegans*

M. R. Patel and K. Shen

The protein RSY-1 inhibits synapse formation by antagonizing assembly molecules during presynaptic development.

1503 The Role of Fingerprints in the Coding of Tactile Information Probed with a Biomimetic Sensor

J. Scheibert et al.

Fingertip ridges improve the tactile perception of fine features.

CONTENTS continued **>>**

Published by AAAS

SCIENCE**ONLINE**

SCIENCE**EXPRESS**

www.sciencexpress.org

Local DNA Topography Correlates with Functional Noncoding Regions of the Human Genome

S. C. J. Parker et al.

The molecular shape of DNA, as well as the nucleotide sequence itself, can have functional consequences and constrain evolution.

10.1126/science.1169050

Circadian Control of the NAD^+ Salvage Pathway by CLOCK-SIRT1

Y. Nakahata et al.

A transcriptional-enzymatic feedback loop controls interactions between metabolism and circadian rhythms in mouse cells.

10.1126/science.1170803

In Vivo Analysis of Dendritic Cell Development and Homeostasis

K. Liu et al.

The developmental pathway of lymphoid dendritic cells from myeloid progenitors is traced in mice.

10.1126/science.1170540

Solar Power Wires Based on Organic Photovoltaic Materials

M. R. Lee et al.

A transparent polymer coating allows optics to compensate for the shadowing effects of a metal wire electrode.

10.1126/science.1168539

TECHNICAL**COMMENTS**

Comment on "Detection, Stimulation, and Inhibition of Neuronal Signals with High-Density Nanowire Transistor Arrays"

P. Fromherz and M. Voelker

full text at www.sciencemag.org/cgi/content/full/323/5920/1429b

Response to Comment on "Detection, Stimulation, and Inhibition of Neuronal Signals with High-Density Nanowire Transistor Arrays"

B. P. Timko et al.

full text at www.sciencemag.org/cgi/content/full/323/5920/1429c

SCIENCE**NOW**

www.sciencenow.org

Highlights From Our Daily News Coverage

Arrest That Chimp!

Stone-throwing ape's actions are premeditated, researchers say.

A Curious Case of Genetic Resurrection

Series of unlikely events brings dead gene back to life.

Two Black Holes on a Collision Course

Astronomers find cosmic beasts in close orbit.

SCIENCE**SIGNALING**

www.sciencesignaling.org

The Signal Transduction Knowledge Environment

RESEARCH ARTICLE: *Rac1* Is a Critical Mediator of Endothelium-Derived Neurotrophic Activity

N. Sawada et al.

Rac1 drives transcriptional programs in endothelial cells that alter endothelial barrier property and expression of neurotrophic factors.

PERSPECTIVE: When the Endogenous Hallucinogenic Trace Amine N,N-Dimethyltryptamine Meets the Sigma-1 Receptor

T.-P. Su et al.

An endogenous hallucinogenic compound binds to a ligand-gated chaperone.

PERSPECTIVE: Reversible Phosphorylation of Histidine Residues in Proteins from Vertebrates

S. Klumpp and J. Krieglstein

The importance of kinases and phosphatases to signaling mechanisms is extended by their regulation of histidine residues.

NETWATCH: PubChem

Access a database of structural, chemical, and functional attributes of small bioactive molecules; in Bioinformatics Resources.

NETWATCH: Oncomine Research Platform

Compare data from various sources to identify commonalities in cancer gene expression profiles; in Bioinformatics Resources.

SCIENCE**CAREERS**

www.sciencecareers.org/career_magazine

Free Career Resources for Scientists

The One-Minute Talk

V. McGovern

You need to know how to respond quickly when asked "Tell me about yourself," whether in an elevator or anywhere else.

Opportunities: Kauffman's Twelve

P. Fiske

A new fellowship program will prepare 12 life scientists each year to commercialize their research findings.

Adding an Artistic Dimension to Science

E. Pain

Blending a passion for arts into a scientific career can greatly enrich both experiences.

SCIENCE**PODCAST**

www.sciencemag.org/multimedia/podcast

Free Weekly Show

Download the 13 March *Science* Podcast to hear about self-repairing materials, erasing a fear memory, nearing peak coal production, and more.

SCIENCE**NOW**
Thinking ahead.

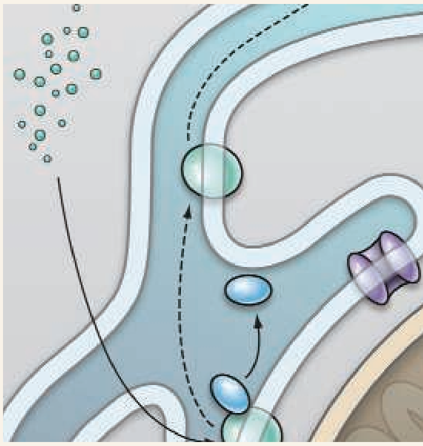

SCIENCE**SIGNALING**
Translocating the sigma-1 receptor.

ORIGINS**BLOG**

blogs.sciencemag.org/origins

A History of Beginnings

SCIENCE**INSIDER**

blogs.sciencemag.org/scienceinsider

Science Policy News and Analysis

SCIENCE (ISSN 0036-8075) is published weekly on Friday, except the last week in December, by the American Association for the Advancement of Science, 1200 New York Avenue, NW, Washington, DC 20005. Periodicals Mail postage (publication No. 484460) paid at Washington, DC, and additional mailing offices. Copyright © 2009 by the American Association for the Advancement of Science. The title SCIENCE is a registered trademark of the AAAS. Domestic individual membership and subscription (51 issues): $146 ($74 allocated to subscription). Domestic institutional subscription (51 issues): $835; Foreign postage extra: Mexico, Caribbean (surface mail) $55; other countries (air assist delivery) $85. First class, airmail, student, and emeritus rates on request. Canadian rates with GST available upon request, GST #1254 88122. Publications Mail Agreement Number 1069624. **Printed in the U.S.A.**

Change of address: Allow 4 weeks, giving old and new addresses and 8-digit account number. **Postmaster:** Send change of address to AAAS, P.O. Box 96178, Washington, DC 20090–6178. **Single-copy sales:** $10.00 current issue, $15.00 back issue prepaid includes surface postage; bulk rates on request. **Authorization to photocopy** material for internal or personal use under circumstances not falling within the fair use provisions of the Copyright Act is granted by AAAS to libraries and other users registered with the Copyright Clearance Center (CCC) Transactional Reporting Service, provided that $20.00 per article is paid directly to CCC, 222 Rosewood Drive, Danvers, MA 01923. The identification code for *Science* is 0036-8075. *Science* is indexed in the *Reader's Guide to Periodical Literature* and in several specialized indexes.

AAAS
ADVANCING SCIENCE, SERVING SOCIETY

CREDITS: (SCIENCE NOW) MATHIAS OSVATH/CURRENT BIOLOGY; (SCIENCE SIGNALING) CHRIS BICKEL

EDITED BY STELLA HURTLEY

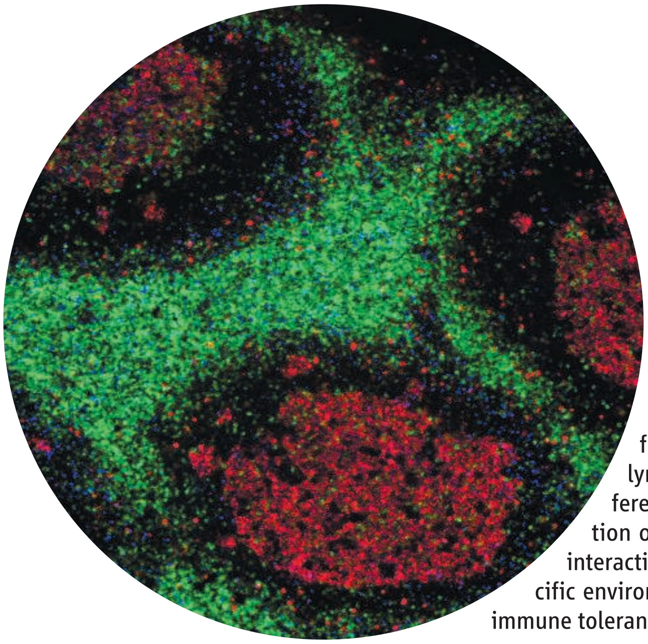

<< Immunological Balancing Act

Secretory immunoglobulin A (IgA) plays a crucial role in the gut by promoting immune tolerance to food and the microflora that colonize the gut. IgA is produced by B cells with the help of CD4$^+$ T follicular helper cells. How these helper CD4$^+$ T cells are generated in the gut is unclear. **Tsuji *et al.*** (p. 1488) found that suppressor Foxp3$^+$CD4$^+$ T cells can differentiate selectively into follicular B cell helper T cells (T$_{FH}$) in Peyer's patches, specialized lymphoid tissue in the gut, but not in other lymphoid tissue. Differentiation of suppressor T cells into T$_{FH}$ cells requires down-regulation of the suppressor T cell–specific transcription factor Foxp3 and interaction with B cells. Thus, flexibility of T cell populations and the specific environment of the gut help to maintain the critical balance between immune tolerance and activation.

Out of the Deep

The Southern Ocean may have provided a reservoir for atmospheric CO$_2$ during cold glacial periods, which could help to explain why the concentration of atmospheric CO$_2$ rose by roughly 50% during each of the last five deglaciations. **Anderson *et al.*** (p. 1443; see the Perspective by **Toggweiler**) find that burial rates of biogenic opal increased in the Southern Ocean during the last deglaciation, indicating more vigorous upwelling. More intense upwelling would have brought more CO$_2$, dissolved in deeper water, to the surface and vented to the atmosphere, potentially leading to the observed glacial-to-deglacial CO$_2$ rise.

Fusion Confusion

Vesicle fusion and neurotransmitter release are fundamental aspects of brain function. Efficient use of synaptic vesicles and the dynamics of neurotransmission depend critically on the mode of fusion. So-called kiss-and-run fusion and subsequent reuse of the same vesicle could in principle greatly expand information transfer at synapses. **Zhang *et al.*** (p. 1448, published online 12 February) used a quantum dot-based optical approach to investigate synaptic vesicle behavior that allowed kiss-and-run and classical full collapse fusion to be distinguished at the kind of synapses involved in learning and memory. The prevalence of kiss-and-run, relative to classical fusion, changed progressively over the course of a series of stimuli.

Crystallization Visualized

Crystal nucleation and growth from a melt or supersaturated solution is often kinetically driven by the presence of secondary materials or surfaces that alter the free energy of the system. **Pouget *et al.*** (p. 1455; see the cover) provide a description of calcium carbonate precipitation under Langmuir monolayers in which the monolayer controls the orientation of the precipitating crystals. Cryogenic transmission electron microscopy allowed the sequence of events to be traced starting from amorphous mineral particles, which attach to the ordered monolayer, until crystalline particles form on a structured template. Throughout the process amorphous calcium carbonate particles were observed, confirming their role in the crystallization process.

Self-Healing Polyurethanes

Self-healing materials may allow the fabrication of objects that can be repaired in situ. **Ghosh and Urban** (p. 1458) devised a self-repairing polyurethane in which the process that damages the material also initiates the first step in the healing process. Oxetane-substituted chitosan was incorporated into a polyurethane and, upon mechanical damage, the oxetane rings open up to form reactive end groups. With exposure to ultraviolet light, the chitosan chains are cut, and link to the oxetane reactive sites, thus leading to rapid healing and repair in a scratched polyurethane coating.

Squeezing in Fluorocarbons

Chemical separations using porous solids mostly rely on size selection: Compounds too large to squeeze through the pores are excluded. **Metrangolo *et al.*** (p. 1461) describe a class of ionic solids that can selectively capture certain fluorocarbons dynamically. The crystals comprise dicationic hydrocarbon chains capped at each end by positive ammonium groups, with negative iodide ions to balance the charge. Although structurally nonporous, the solids spontaneously stretch to accommodate iodine-capped fluorocarbon chains, which form robust intermolecular halogen bonds with iodides at each end. The encapsulation is highly selective for the fluorocarbon with a chain length scaled to the lattice dication. Moreover, the process is reversible, with the guests liberated on heating, offering potential for use in industrial fluorocarbon separations.

Mistier Blue Sky

Atmospheric aerosols have a large effect on how, and how much, the atmosphere is warmed by solar radiation, and uncertainties about their abundance has impeded a more nuanced understanding of the mechanisms of global warming. Recently, "global dimming" and "global brightening" have been observed when the amount of solar radiation incident on Earth's surface apparently decreased and increased. **Wang *et al.*** (p. 1468) analyzed records of aerosol optical depth gathered worldwide since 1973 and constructed a global map of trends in clear sky visibility. Skies have become less transparent over most, but not all, of the world, and the changes in aerosol optical depth correspond well to reports of dimming or brightening over the past 20 to 30 years.

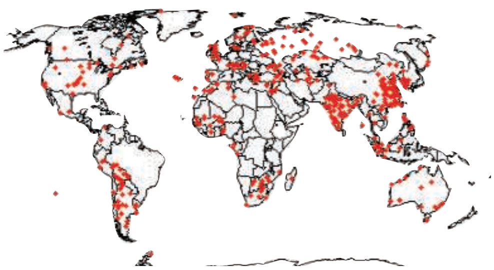

Continued on page 1403

CREDITS (TOP TO BOTTOM): SIDONIA FAGARASAN/RESEARCH CENTER FOR ALLERGY AND IMMUNOLOGY, RIKEN, YOKOHAMA, JAPAN; WANG *ET AL.*

Continued from page 1401

The CS_2 Point of View

Molecules in the liquid and gas phases tumble constantly, and techniques that probe reaction dynamics in these states often yield blurry information averaged over multiple orientations. **Bisgaard *et al.*** (p. 1464) used a short laser burst to push a sample of gaseous CS_2 molecules into temporary alignment and applied ultrafast spectroscopy to study photodissociation in the molecular reference frame, free of blurring. A complex progression of electronic motion was observed coupled to C-S bending and stretching vibrations preceding scission of a C-S bond.

Too Little of a Bad Thing

Mutations in the amyloid precursor protein (APP) are known to cause familial Alzheimer's disease. **Di Fede *et al.*** (p. 1473) now describe an APP mutation that is associated with disease only in the homozygous state. The A673V mutation affects APP processing, which leads to enhanced β-amyloid (Aβ) production, and also increases the Aβ's tendency to aggregate and form amyloid fibrils. However, co-incubation of mutated and wild-type Aβ peptides confers instability on Aβ aggregates and inhibits amyloidogenesis, consistent with the observation that heterozygous carriers do not develop the disease even at a very old age.

Check Out the Checkpoint

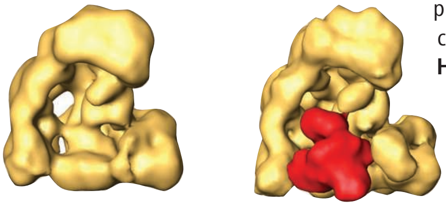

"Job one" for any living organism is to make cells that can reproduce and faithfully distribute chromosomes. Not only do eukaryotic cells manage to line up and segregate their chromosomes during cell division, but they have a fail-safe mechanism that prevents cell division from proceeding if all of the chromosomes are not lined up appropriately. **Herzog *et al.*** (p. 1477) provide a glimpse of the molecular machinery that makes this fail-safe mechanism work. At the heart of the mechanism is a ubiquitin ligase complex, the anaphase-promoting complex/cyclosome (APC/C), whose activity is modulated by an activator, Cdc20, or by an inhibitory complex called the mitotic checkpoint complex (MCC), which includes of Cdc20 together with other proteins. Proteins were purified from cells in which the mitotic checkpoint was active or inactive and the structure of APC/C complexes with or without its various partners bound was observed by single-particle electron microscopy. MCC inhibited APC/C by physically obstructing binding of APC/C's substrates for ubiquitinylation and by inducing changes in APC/C that lock it in a more compact conformation.

Selective Removal of Memories

How are memories encoded and stored in the brain, and which neurons are part of a specific memory? **Han *et al.*** (p. 1492) tried to establish a causal link between a defined population of neurons and the disruption of a specific fear memory. Neurons in the lateral amygdala overexpressing the transcription factor CREB are preferentially activated by fear memory testing, which suggests that this population of neurons is selectively recruited to the fear memory test. Selective killing of just these neurons after training impaired subsequent memory expression, whereas random destruction of a similar number of lateral amygdala neurons did not impact subsequent memory expression. This memory loss was robust, persistent, and not due to a disruption in reconsolidation or overall lateral amygdala function.

Windfall Wonder

Research on primates suggests that midbrain dopaminergic neurons encode unexpected reward signals that drive reinforcement learning. The reward-related properties of these neurons have not been measured directly in humans. Using microelectrode recordings during deep brain stimulation, **Zaghloul *et al.*** (p. 1496) investigated reinforcement learning mechanisms by analyzing neural activity in the substantia nigra of patients with Parkinson's disease while they engaged in a probability learning task. Neuronal responses were classified into four distinct categories based on an improved model for expectation: expected wins and losses, and unexpected wins and losses. Significant differences in spike activity were observed in response to unexpected wins and losses, while the difference in response to expected wins and losses was not significant. The human substantia nigra thus preferentially encodes unexpected reward and differentiates between unexpected positive and negative feedback.

CREDIT: HERZOG ET AL.

Published by AAAS

Christopher Reddy is director of the Coastal Ocean Institute, Woods Hole Oceanographic Institution, MA.

Scientist Citizens

PRESIDENT OBAMA'S INAUGURATION SPEECH DELIGHTED SCIENTISTS WHEN HE STATED, "WE WILL restore science to its rightful place." But he went on: "What is required of us now is a new era of responsibility.… This is the price and the promise of citizenship." For scientists, one often-overlooked responsibility is explaining their work to people. This is not an unreasonable price for receiving public funds to do research. And it promises to combat ignorance, guide sound policymaking, and garner more support for science, while simultaneously inspiring and recruiting new young scientists. Now more than ever, issues such as climate change, obesity, stem cell research, green technology, and evolution are migrating from scientific journals to the non-science community, from school halls to the halls of Congress. It's critical that scientists venture beyond their laboratories to put these issues into the correct contexts and help the public understand what is known, unknown, and under debate.

But the walls of the ivory tower remain formidable. Just last month, for example, an editorial in *Analytical Chemistry* commented that federal funding agency requirements for outreach detract from young scientists' ability to conduct research and think deeply. Lack of time is an obstacle for young scientists, but scientists are no more overtaxed than many professionals are. A more entrenched obstacle is that the academic tenure process claims to evaluate research, teaching, and service, but in practice, service is rarely expected or rewarded. In fact, reviewers are well versed in recognizing good research but have little ability or data to evaluate outreach.

Universities must begin to give more than lip service to the service component in tenure evaluations. Land-grant universities, for example, specifically make cooperative extension work part of some faculty members' jobs. At the least, universities and professional organizations should devise detailed guidelines for evaluating the amount, quality, and effectiveness of outreach, so that peers can recognize it when they see it. Universities should also integrate communications into young scientists' basic training. Like lawyers in courts, physicians in hospitals, or baseball players on the field, scientists speak an insular language that is unknowable and intimidating to the uninitiated. As the former Editor-in-Chief of this magazine, Donald Kennedy, wrote: "Science and technology are increasingly relevant to public policy, and unless those who speak for science can be understood, the policy decisions are likely to be wrong."

At Stockholm University, all new Ph.D. students in environmental and climate sciences are now offered training in speaking with the media. Stanford University's School of Earth Sciences has launched an innovative program to train graduate students in similar skills. The Woods Hole Oceanographic Institution offered a graduate student course co-taught by scientists and journalists called "How Not to Write for Peer-Reviewed Journals: Talking to Everybody Else." For more established scientists, professional programs exist: The Aldo Leopold Leadership Program, for example, has provided media training to a growing nucleus of more than 100 mid-career environmental scientists.

Such programs would provide incentive (or at least diminish the disincentive) for scientists to participate in outreach. Rather than viewing funding agency outreach requirements as annoying and vague, scientists can view them as opportunities to find ways to inspire young minds (and themselves), encourage underrepresented groups to enter science, establish collaborations between academia and industry, or otherwise enter the messy fray of democracy. The means by which the public and policymakers get scientific information have changed dramatically. The once linear transmission of research findings from the scientific community to the media, public, or policymakers has been transformed into a chaotic realm in which information (and disinformation) and opinions are voiced through traditional and electronic sources (real-time blogs, chat rooms, and wikis) and not necessarily by the scientific community. Thomas Jefferson wrote, "An enlightened citizenry is indispensable for the proper functioning of a republic." If we believe that science has a rightful role in our society, then it is the scientific community's responsibility to enlighten the public as to why and how. That doesn't mean scientists need to be celebrities, politicians, or lobbyists—just citizens.

– Christopher Reddy

10.1126/science.1173003

CREDITS: (TOP) TOM KLEINDINST/WOODS HOLE OCEANOGRAPHIC INSTITUTION; (RIGHT) ISTOCKPHOTO.COM

EDITORS' CHOICE

EDITED BY STELLA HURTLEY AND JAKE YESTON

ASTROPHYSICS

Explosions Near and Far

Our universe appears to be undergoing a period of accelerated expansion driven by dark energy. This phenomenon was brought to the fore in 1998, when distant type Ia supernovae—bright transient events that mark the explosion of an accreting white dwarf star—were observed to be dimmer than they would be in the absence of acceleration. The conclusion rests on the assumption, actively debated over the past decade, that the properties of type Ia supernovae are independent of their distance from the observation point; the dimming in that context may be attributed reliably to cosmic acceleration and not to systematic differences characterizing distant supernovae. Sullivan *et al.* contribute to this discussion by compiling spectra of type Ia supernovae spanning the past 9 gigayears. They constructed and compared the mean ultraviolet spectra, which are sensitive to the composition of the progenitor stars and the physics of the explosion, for supernovae at short, intermediate, and long distances. Although the strength of some spectral features varies with distance, the variation can be explained by a relative increase in explosions of younger stars in the distant, younger universe, a trend that has been seen in previous studies and for which it should be possible to correct. Thus, type Ia supernovae may be useful as tools to study the expansion history of the universe. — MJC

Astrophys. J. **693**, L76 (2009).

ECOLOGY

But the Butter's Melted

American lobsters (*Homarus americanus*) are iconic representatives of North America's northeastern Atlantic Ocean. The abundance of American lobster has experienced severe swings, but the cause of changes in their population is unknown. Recently the lobster fishery in southern New England has collapsed, while at the same time lobster populations in the Gulf of Maine have expanded massively. Wahle *et al.* use a time series analysis to create a larval settlement index that could predict the number of near-harvestable clawed lobsters. Their findings suggest that the way lobster populations vary significantly over time may be due to the combined effects of shell disease and a decline in the settlement of larvae. Because lobster larvae are typically transported over great distances before settlement, local outbreaks of shell disease cannot solely explain population demographic changes. Being better able to predict population density fluctuations and developing strategies to counteract predicted declines will be important in assessing the future viability of lobster fisheries. — LMZ

Mar. Ecol. Prog. Ser. **376**, 185 (2009).

BIOMEDICINE

Brittle Bones

Osteoarthritis occurs when the cartilage that covers the surface of bones at joints becomes degraded, resulting in pain and decreased mobility. The biomechanical properties of cartilage come from an extracellular matrix comprising proteoglycans embedded in a meshwork of collagen fibrils. Pathological changes in cartilage start at the molecular level and eventually lead to macroscopic structural and functional damage. Early detection of cartilage damage is important, both for diagnosis and to understand the mechanisms involved in disease progression with the goal of developing therapies. Indentation-type atomic force microscopy (IT-AFM) can measure the compressive stiffness of porcine articular cartilage at the micrometer and nanometer scales. Now Stolz *et al.* have used IT-AFM to monitor the development of an osteoarthritis-like condition in collagen-IX knockout mice. At the micrometer scale, no morphological changes were observed in articular cartilage of mutant as compared to control mice until 6 months of age. However, nanometer-scale IT-AFM showed disease-associated changes in fibril thickness and nanostiffness in mice as young as 1 month old. The biomechanical changes that occur during normal aging are distinct from pathological changes associated with disease progression. The success of IT-AFM in detecting these early changes suggests that it could serve as a useful diagnostic nanotool; the next step will be to develop such a minimally invasive surgical tool. — VV

Nat. Nanotechnol. 10.1038/nnano.2008.410 (2009).

APPLIED PHYSICS

Raising Online Speed Limits

The appetite for faster and faster Internet connections with greater and greater information-transfer capacity continues unabated. With the

CREDITS (TOP TO BOTTOM): MPIA/NASA/CALAR ALTO OBSERVATORY; ISTOCK PHOTO

likes of high-definition television, music and video streaming, and social networks all contributing to a 60% annual growth in Internet traffic, the increasing demand for information capacity is putting strain on present information-handling capabilities. In order to avoid a worldwide-wait scenario reminiscent of the dial-up era, optical engineers are developing information-processing technologies aimed at terabit-per-second capabilities, which will be able to pump data through optical fibers straight to the home. Galili *et al.* have developed an optical switch that heads toward this goal. The authors present a chalcogenide glass chip, exploiting the material's nonlinear property of four-wave mixing to produce an all-optical switch that can demodulate a 640-Gbit/s optical signal into a series of 10-Gbit/s tributaries. The demonstration of such high-speed and error-free signal processing indicates that Internet starvation might be staved off, at least for the time being. — ISO

Opt. Express **17**, 2182 (2009).

IMMUNOLOGY

Building a Brain Invasion

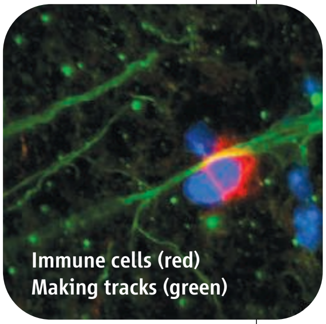

Immune cells (red)
Making tracks (green)

For good reason, our bodies tightly limit the access of immune cells to the brain, where they could do untold harm. However, during certain infections and autoimmune diseases, immune cells can gain access to the brain and cause tissue damage and destruction. In order to better understand how immune cells access the brain and move within it during an infection, Wilson *et al.* used multiphoton microscopy to visualize the behavior of $CD8^+$ T cells in cerebral cortex slices taken from mice with encephalitis that resulted from *Toxoplasma gondii* infection. Similar to T cell movements previously observed in lymph nodes, infiltrating $CD8^+$ T cells could be seen to use reticular fiber conduits to move within the brain. In contrast to the lymph node reticular networks that are present in the steady state, the conduits in the brain were observed only in infected mice, suggesting that in immune-privileged tissues such as the brain, scaffolds for lymphocyte motility are induced only under inflammatory conditions. — KLM

Immunity **30**, 300 (2009).

CREDIT: WILSON *ET AL.*, IMMUNITY **30**, 300 (2009)

CELL BIOLOGY

Reading the Signs

Posttranslational modifications are one of many ways to control the activity of proteins. Ubiquitin is a small molecule that is covalently attached to target proteins and regulates the function of many different biological processes. In yeast, up to 20% of proteins can be conjugated to ubiquitin, and all seven conserved lysine (K) residues in ubiquitin itself can be used to form both branched and linear polypeptide chains. These different combinations are thought to mark proteins for different cellular fates. The most abundant chain is linked through K48, which targets the associated proteins for degradation by the proteasome. K63-linked ubiquitin chains were previously thought to regulate proteasome-independent functions in vivo, such as DNA repair. Now, Saeki *et al.* have found that K63-linked ubiquitin can also target proteins to the proteasome. Using *Saccharomyces cerevisiae*, they studied the topology of the ubiquitin chains formed by the E3 ubiquitin ligase Rsp5, which is known to regulate both proteasome-dependent and -independent functions. In vitro, Rsp5 was found to generate only K63-linked ubiquitin chains, which were then unexpectedly recognized by the proteasome. Further in vivo studies showed K63-linked ubiquitin chains bound to the proteasome, suggesting that, like K48-linkages, K63-links may also have an extensive role in regulating protein degradation. — HP*

EMBO J. **28**, 359 (2009).

CHEMISTRY

Step by Step

In surface-catalyzed reactions, there are often myriad steps between the first contact of the reagents with the surface and the ultimate desorption of the final products. Characterization of these intermediate stages can help to unravel the reaction mechanism and thereby aid development of improved catalysts. Although scanning tunneling microscopy (STM) has been used to follow a number of reactions of adsorbed species on metal surfaces, there are few examples of such studies on metal oxides. Matthiesen *et al*. studied the oxidation by O_2 of adsorbed hydrogen atoms on a (110) surface of titanium dioxide using time-lapsed STM images and density functional theory calculations. The data provide evidence for several intermediate species—HO_2, H_2O_2, and H_3O_2—on the way to the formation of water. The coadsorption of water helps to promote hydrogen diffusion and thus allow these reactions to proceed at low temperatures (200 K). — PDS

ACS Nano **3**, 10.1021/nn8008245 (2009).

---

*Helen Pickersgill is a locum editor in *Science*'s editorial department.

Published by AAAS

www.sciencemag.org

Science

1200 New York Avenue, NW
Washington, DC 20005
Editorial: 202-326-6550, FAX 202-289-7562
News: 202-326-6581, FAX 202-371-9227
Bateman House, 82-88 Hills Road
Cambridge, UK CB2 1LQ
+44 (0) 1223 326500, FAX +44 (0) 1223 326501

Subscription Services For change of address, missing issues, new orders and renewals, and payment questions: 866-434-AAAS (2227) or 202-326-6417, FAX 202-842-1065. Mailing addresses: AAAS, P.O. Box 96178, Washington, DC 20090-6178 or AAAS Member Services, 1200 New York Avenue, NW, Washington, DC 20005

Institutional Site Licenses please call 202-326-6755 for any questions or information

Reprints: Author Inquiries 800-635-7181
Commercial Inquiries 803-359-4578

Permissions 202-326-7074, FAX 202-682-0816

Member Benefits AAAS/Barnes&Noble.com bookstore www.aaas.org/bn; AAAS Online Store www.apisource.com/aaas/ code MKB6; AAAS Travels: Betchart Expeditions 800-252-4910; Apple Store www.apple/eppstore/aaas; Bank of America MasterCard 1-800-833-6262 priority code FAA3YU; Cold Spring Harbor Laboratory Press Publications www.cshlpress.com/affiliates/aaas.htm; GEICO Auto Insurance www.geico.com/landingpage/go51.htm?logo=17624; Hertz 800-654-2200 CDP#343457; Office Depot https://bsd.officedepot.com/portalLogin.do; Seabury & Smith Life Insurance 800-424-9883; Subaru VIP Program 202-326-6417; VIP Moving Services www.vipmayflower.com/domestic/index.html; Other Benefits: AAAS Member Services 202-326-6417 or www.aaasmember.org.

science_editors@aaas.org	(for general editorial queries)
science_letters@aaas.org	(for queries about letters)
science_reviews@aaas.org	(for returning manuscript reviews)
science_bookrevs@aaas.org	(for book review queries)

Published by the American Association for the Advancement of Science (AAAS), *Science* serves its readers as a forum for the presentation and discussion of important issues related to the advancement of science, including the presentation of minority or conflicting points of view, rather than by publishing only material on which a consensus has been reached. Accordingly, all articles published in *Science*—including editorials, news and comment, and book reviews—are signed and reflect the individual views of the authors and not official points of view adopted by AAAS or the institutions with which the authors are affiliated.

AAAS was founded in 1848 and incorporated in 1874. Its mission is to advance science, engineering, and innovation throughout the world for the benefit of all people. The goals of the association are to: enhance communication among scientists, engineers, and the public; promote and defend the integrity of science and its use; strengthen support for the science and technology enterprise; provide a voice for science on societal issues; promote the responsible use of science in public policy; strengthen and diversify the science and technology workforce; foster education in science and technology for everyone; increase public engagement with science and technology; and advance international cooperation in science.

Information for Authors

See pages 807 and 808 of the 6 February 2009 issue or access www.sciencemag.org/about/authors

EDITOR-IN-CHIEF **Bruce Alberts**
EXECUTIVE EDITOR **Monica M. Bradford**
DEPUTY EDITORS **R. Brooks Hanson, Barbara R. Jasny, Katrina L. Kelner**
NEWS EDITOR **Colin Norman**

Editorial supervisory senior editor Phillip D. Szuromi; **senior editor/perspectives** Lisa D. Chong; **senior editors** Gilbert J. Chin, Pamela J. Hines, Paula A. Kiberstis (Boston), Marc S. Lavine (Toronto), Beverly A. Purnell, L. Bryan Ray, Guy Riddihough, H. Jesse Smith, Valda Vinson; **associate editors** Kristen L. Mueller, Jake S. Yeston, Laura M. Zahn; **online editor** Stewart Wills; **associate online editors** Robert Frederick, Tara S. Marathe; **web content developer** Martyn Green; **book review editor** Sherman J. Suter; **associate letters editor** Jennifer Sills; **editorial manager** Cara Tate; **senior copy editors** Jeffrey E. Cook, Cynthia Howe, Harry Jach, Barbara P. Ordway, Trista Wagoner; **copy editors** Chris Filiatreau, Lauren Kmec; **editorial coordinators** Carolyn Kyle, Beverly Shields; **publications assistants** Ramatoulaye Diop, Joi S. Granger, Jeffrey Hearn, Lisa Johnson, Scott Miller, Jerry Richardson, Jennifer A. Seibert, Brian White, Anita Wynn; **editorial assistants** Carlos L. Durham, Emily Guise, Patricia M. Moore; **executive assistant** Sylvia S. Kihara; **administrative support** Maryrose Madrid

News deputy news editors Robert Coontz, Eliot Marshall, Jeffrey Mervis, Leslie Roberts; **contributing editors** Elizabeth Culotta, Polly Shulman; **news writers** Yudhijit Bhattacharjee, Adrian Cho, Jennifer Couzin, David Grimm, Constance Holden, Jocelyn Kaiser, Richard A. Kerr, Eli Kintisch, Andrew Lawler (New England), Greg Miller, Elizabeth Pennisi, Robert F. Service (Pacific NW), Erik Stokstad; **intern** Jackie D. Grom; **contributing correspondents** Dan Charles, Jon Cohen (San Diego, CA), Daniel Ferber, Ann Gibbons, Robert Koenig, Mitch Leslie, Charles C. Mann, Virginia Morell, Evelyn Strauss, Gary Taubes; **copy editors** Linda B. Felaco, Melvin Gatling, Melissa Raimondi; **administrative support** Scherraine Mack, Fannie Groom; **bureaus** New England: 207-549-7755, San Diego, CA: 760-942-3252, FAX 760-942-4979, Pacific Northwest: 503-963-1940

Production director James Landry; **senior manager** Wendy K. Shank; **assistant manager** Rebecca Doshi; **senior specialists** Steve Forrester, Chris Redwood; **specialist** Anthony Rosen; **Preflight director** David M. Tompkins; **manager** Marcus Spiegler

Art director Yael Kats; **associate art director** Laura Creveling; **illustrators** Chris Bickel, Katharine Sutliff; **senior art associates** Holly Bishop, Preston Huey, Nayomi Kevitiyagala; **art associate** Jessica Newfield; **photo editor** Leslie Blizard

Science International

Europe (science@science-int.co.uk) **editorial: international managing editor** Andrew M. Sugden; **senior editor/perspectives** Julia Fahrenkamp-Uppenbrink; **senior editors** Caroline Ash, Stella M. Hurtley, Ian S. Osborne, Peter Stern; **associate editor** Maria Cruz; **editorial support** Deborah Dennison, Rachel Roberts, Alice Whaley; **administrative support** John Cannell, Janet Clements; **news: europe news editor** John Travis; **deputy news editor** Daniel Clery; **contributing correspondents** Michael Balter (Paris), John Bohannon (Vienna), Martin Enserink (Amsterdam and Paris), Gretchen Vogel (Berlin); **intern** Sara Coelho

Asia Japan Office: Asca Corporation, Eiko Ishioka, Fusako Tamura, 1-8-13, Hirano-cho, Chuo-ku, Osaka-shi, Osaka, 541-0046 Japan; +81 (0) 6 6202 6272, FAX +81 (0) 6 6202 6271; asca@os.gulf.or.jp; **asia news editor** Richard Stone (Beijing: rstone@aaas.org); **contributing correspondents** Dennis Normile (Japan: +81 (0) 3 3391 0630, FAX +81 (0) 3 5936 3531; dnormile@gol.com); Hao Xin (China: +86 (0) 10 6307 4439 or 6307 3676, FAX +86 (0) 10 6307 4358; cindyhao@gmail.com); Pallava Bagla (South Asia: +91 (0) 11 2271 2896; pbagla@vsnl.com)

EXECUTIVE PUBLISHER **Alan I. Leshner**
PUBLISHER **Beth Rosner**

Fulfillment Systems and Operations (membership@aaas.org); **director** Waylon Butler; **senior systems analyst** Jonny Blaker; **customer service supervisor** Pat Butler; **specialists** Latoya Casteel, LaVonda Crawford, Vicki Linton, April Marshall; **data entry supervisor** Cynthia Johnson; **specialists** Eintou Bowden, Tarrika Hill, William Jones

Business Operations and Administration director Deborah Rivera-Wienhold; **assistant director, business operations** Randy Yi; **manager, business analysis** Michael LoBue; **manager, business operations** Jessica Tierney; **financial analysts** Priti Pamnani, Celeste Troxler; **rights and permissions: administrator** Emilie David; **associate** Elizabeth Sandler; **marketing director** Ian King; **marketing manager** Allison Pritchard; **marketing associates** Aimee Aponte, Alison Chandler, Mary Ellen Crowley, Julianne Wielga, Wendy Wise; **marketing executive** Jennifer Reeves; **marketing/member services executive** Linda Rusk; **director, site licensing** Tom Ryan; **director, corporate relations** Eileen Bernadette Moran; **publisher relations, eResources specialist** Kiki Forsythe; **senior publisher relations specialist** Catherine Holland; **publisher relations, east coast** Phillip Smith; **publisher relations, west coast** Philip Tsolakidis; **fulfillment supervisor** Iquo Edim; **fulfillment coordinator** Laura Clemens; **electronic media: manager** Lizabeth Harman; **project manager** Trista Snyder; **assistant manager** Lisa Stanford; **senior production specialists** Christopher Coleman, Walter Jones; **production specialists** Nichele Johnston, Kimberly Oster

Advertising director, worldwide ad sales Bill Moran

Product (science_advertising@aaas.org); **midwest/west coast/w. canada** Rick Bongiovanni: 330-405-7080, FAX 330-405-7081; **east coast/e. canada** Laurie Faraday: 508-747-9395, FAX 617-507-8189; **uk/europe/asia** Roger Goncalves: TEL/FAX +41 43 243 1358; **japan** Mashy Yoshikawa: +81 (0) 3 3235 5961, FAX +81 (0) 3 3235 5852; **senior traffic associate** Deiandra Simms

Commercial Editor Sean Sanders: 202-326-6430

Project Director, Outreach Brianna Blaser

Classified (advertise@sciencecareers.org); **inside sales manager: midwest/canada** Daryl Anderson: 202-326-6543; **inside sales representative** Karen Foote: 202-326-6740; **key account manager** Joribah Able; **northeast** Alexis Fleming: 202-326-6578; **southeast** Tina Burks: 202-326-6577; **west** Nicholas Hintibidze: 202-326-6533; **sales coordinators** Rohan Edmonson, Shirley Young; **international: sales manager** Tracy Holmes: +44 (0) 1223 326525, FAX +44 (0) 1223 326532; **sales** Susanne Kharraz, Dan Pennington, Alex Palmer; **sales assistant** Louise Moore; **japan** Mashy Yoshikawa: +81 (0) 3 3235 5961, FAX +81 (0) 3 3235 5852; **advertising production operations manager** Deborah Tompkins; **senior production specialist/graphic designer** Amy Hardcastle; **senior production specialist** Robert Buck; **senior traffic associate** Christine Hall; **publications assistant** Mary Lagnaoui

AAAS Board of Directors retiring president, chair James J. McCarthy; **president** Peter C. Agre; **president-elect** Alice Huang; **treasurer** David E. Shaw; **chief executive officer** Alan I. Leshner; **board** Alice Gast, Linda P. B. Katehi, Nancy Knowlton, Cherry A. Murray, Julia M. Phillips, Thomas D. Pollard, David S. Sabatini, Thomas A. Woolsey

AAAS
ADVANCING SCIENCE, SERVING SOCIETY

RANDOMSAMPLES

EDITED BY CONSTANCE HOLDEN

Frozen in Time

Members of the Scott Antarctic expedition fuel up after nearly dying in a blizzard in 1911.

They are trendy tourist destinations today, but the polar regions once drew only the hardiest and most adventurous. Freeze Frame (www.freezeframe.ac.uk), a gallery launched last week by the Scott Polar Research Institute at the University of Cambridge in the United Kingdom, provides an inside glimpse of these explorers' grueling travels.

The site offers 20,000 digitized photos and images of more than 20 polar expeditions, most of them British, from the 1840s to the 1980s. There are lots of cold snaps from the journeys of the institute's namesake, the British naval officer Robert Falcon Scott, who lost the race to the South Pole in 1912 to Norway's Roald Amundsen and then died on the way back to his base camp. Other features include profiles of explorers such as Scott's sometime rival Ernest Shackleton, whose 1914–16 Antarctic expedition was marooned for more than a year but managed to reach safety.

Tuning the Brain

Evidence suggests that musical training, especially from an early age, fine-tunes a person's hearing not just for music but also for emotional aspects of speech. Now scientists at Northwestern University in Evanston, Illinois, say they've produced the first evidence of a biological basis for this phenomenon.

Neuroscientist Nina Kraus and colleagues tested 30 young adults in three categories: those with no musical training, those who started learning to play a musical instrument before age 7, and those who started later but had at least 10 years of training. The scientists hooked them up to electrodes that recorded the response of the auditory brainstem to a quarter-second of an emotion-laden sound: an infant's wail (see illustration). The subjects with the most musical experience responded the fastest to the sound, the scientists report this month in the *European Journal of Neuroscience*. Those who had practiced since early childhood had the strongest response to the parts of the cry for which timing, pitch, and timbre were most complex. The nonmusicians, in contrast, "didn't pick up on fine-grained information in the signal," says Kraus.

The experiment reveals "what [a person's] nervous system has become" as a result of musical training, says Kraus. The sounds to which musicians show enhanced perception, she says, are also those that are "poorly transcribed" in the brains of people with language-processing disorders, which means they might be helped by music. Composer Anthony Brandt of Rice University in Houston, Texas, says the study helps show that music is not just "auditory cheesecake," as once suggested by Steven Pinker, but that "its enjoyment is deeply rooted in our cognition."

Fish Gets Its 15 Minutes

A "bizarre" new species of frogfish, found in shallow waters near Indonesia, is striking for not only its swirling stripes but also its strange ways of propelling itself—sucking in and shooting out water, and pushing off the bottom with its fins. Reported in last month's issue of the journal *Copeia* by Theodore Pietsch and colleagues at the University of Washington, Seattle, the reaction "has been almost more than we can deal with," says Pietsch. Googling "psychedelica fish" yields 171,000 hits.

What Galileo Saw

Scientists and historians in Italy have constructed an exact replica of one of the telescopes used by Galileo Galilei 400 years ago. In Florence, researchers at the Institute and Museum of the History of Science and at the Arcetri Observatory have teamed up with optics specialists, nuclear physicists, and glassmakers to produce a 93-centimeter-long instrument with both a converging and a diverging lens that magnifies distant objects up to 20 times.

Telescope, with apparatus for digital conversion of images, points toward villa in Arcetri where Galileo spent his last 11 years.

Researchers have been repeating the observations of the moon, the satellites of Jupiter, the large stellar fields of Saturn, and the phases of Venus that Galileo described in 1610. Observatory Director Francesco Palla says the team hopes to distinguish between what Galileo, who eventually lost his sight, reported seeing and what he would actually have seen. Paolo Galluzzi, director of the Florence museum, is seeking permission to extract DNA from the remains, housed in the Basilica of the Holy Cross in Florence, to learn more about Galileo's eyesight.

CREDITS: SCOTT POLAR RESEARCH INSTITUTE; STRAIT ET AL., *EUROPEAN JOURNAL OF NEUROSCIENCE* **29** (2009); © DAVID HALL/SEAPHOTOS.COM; FEDELE DAMIANI, FIRENZE

Published by AAAS

NEWSMAKERS

EDITED BY YUDHIJIT BHATTACHARJEE

Sidelines

A ROOTING INTEREST. What did you do on Square Root Day? Ron Gordon, a California teacher who dreamed up the holiday—a date when both day and month are the square root of the year (03.03.09)—served root beer floats in square glasses to his students and tied square knots with them last week.

Gordon of Redwood City, who turns 8^2 in October, has been enamored with square root days since he recognized the oddity shortly before 9 September 1981. (The day comes but nine times a century.) This year, to popularize the concept, he offered $339 for efforts to attract more celebrants.

There are now a number of pages on Facebook dedicated to the holiday, including one with 760 members set up by Gordon's daughter. One popular activity is to cut radishes, carrots, and other "roots" into squares. Gordon's goal is "to give people a little math, a little smile, and a little fun in their day."

THEY SAID IT

"Last year, scientists captured the first pictures of what they believe to be faraway planets circling stars outside of our solar system. … These discoveries … leave us with the feeling that there is much more out there to be found. … From a law enforcement and intelligence perspective, [too,] there is always more to be found. The universe of crime and terrorism stretches out infinitely before us, and we, too, are working to find what we believe to be out there but cannot always see."

—Robert Mueller, director of the FBI, drawing a parallel between scientific inquiry and the grim business of tackling global terrorist threats, in a speech last month at the Council on Foreign Relations.

AWARDS

An astronomer who in 1999 made the first observations of an exoplanet eclipsing its parent star has been awarded the National Science Foundation's Alan T. Waterman Award. **David Charbonneau**, 34, was also head of the team that directly detected light from an exoplanet using the Spitzer Space Telescope in 2005. An associate professor at Harvard University, Charbonneau currently heads the MEarth project, a ground-based observation effort to detect planets orbiting low-mass stars cooler than the sun. The Waterman award, given to researchers under 35, provides a 3-year, $500,000 research grant.

Got a tip for this page? E-mail people@aaas.org

PIONEERS

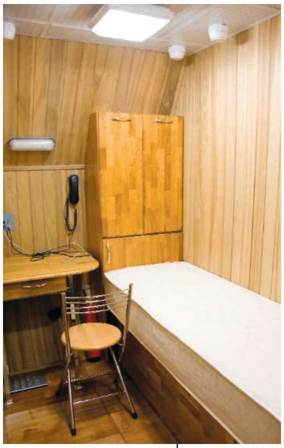

PRETEND JOURNEY. Two Europeans have been chosen to travel to Mars—sort of. Rather than go on a real mission, they will spend 105 days in a closed space capsule in Moscow. Oliver Knickel, an engineer in the German army, and Cyrille Fournier, a French airline pilot, will join four Russians for Mars500, a Mars mission simulation "launching" 31 March.

Competition for the berths was fierce, says Markus Bauer, a spokesperson for the European Space Agency (ESA), which is helping to fund the Russian-led project. A total of 5600 applicants from across Europe—most of them men—were screened using "the same process we use for selecting astronauts, including strict medical and psychological tests" as well as interviews to ensure willingness to be "taken out of normal life for so long," Bauer says.

The simulation will take place in a windowless, soundproof capsule, and the crew will communicate with mission control via radio with a built-in 20-minute delay to account for the distance to Earth. The goal is to identify problems that could crop up during a real mission to Mars. Knickel and Fournier—along with Oleg Artemyez, Sergei Ryazansky, Alexei Baranov, and Alexei Shpakov—will record daily data on their moods, hormone levels, and sleep quality and live on dehydrated food and vitamins, a menu served on the international space station. ESA officials hope the data will help them develop a crewed mission to Mars, which has been on the drawing board for years.

IN MEMORIAM

The U.S. Postal Service plans to release a 78-cent stamp on 14 May to honor **Mary Lasker**, the philanthropist who advocated for increased investments in medical research by starting the Lasker Foundation in 1942. The foundation has given out more than 300 awards to life science researchers since 1945; 78 of the awardees have gone on to win the Nobel Prize. Lasker died in 1994.

CREDITS (TOP TO BOTTOM): JIM STEVENS; ESA; SOURCE: THE LASKER FOUNDATION

Published by AAAS

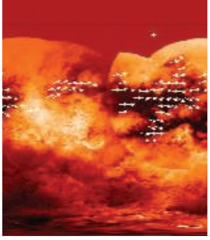

Crowd pleaser. Obama won a standing ovation for relaxing stem cell restrictions and promising to restore the integrity of science in decision-making.

BIOMEDICAL RESEARCH

A First Step in Relaxing Restrictions On Stem Cell Research

Scientists are breathing a huge sigh of relief now that President Barack Obama has put his signature on an executive order lifting the restrictions on stem cell research laid down by President George W. Bush on 9 August 2001.

In the same chandeliered White House room where 2 years ago Bush announced his veto of a bill passed by Congress to override his policy, Obama announced "we will lift the ban on federal funding for promising embryonic stem cell research [and] will vigorously support scientists who pursue this research."

The signing ended with a standing ovation from the crowd, which included politicians, lobbyists, ethicists, stem cell researchers, and a goodly contingent of Nobelists—including Harold Varmus, head of the President's Council of Advisors on Science and Technology. Even Kyoto University researcher Shinya Yamanaka—famous for developing induced pluripotent stem (iPS) cells—flew in for the event. Also in evidence was Robert Klein, maestro of the California Institute for Regenerative Medicine.

Obama also used the occasion to tackle the alleged politicization of the science behind subjects ranging from stem cells to global warming during Bush's reign. The president announced that he has sent a memorandum to the Office of Science and Technology Policy directing it to develop "a strategy for restoring scientific integrity to government decision-making" within the next 120 days. Kurt Gottfried, chair of the Union of Concerned Scientists, says the memo signals "a sea change from the last Administration."

The signing of the new executive order on human embryonic stem (hES) cells is "a great outcome," says University of Pennsylvania stem cell researcher John Gearhart. It "lifts a cloud in many areas. … It will allow more people to get involved [in hES cell research]—and it also sends a message internationally that [National Institutes of Health (NIH)-funded researchers] can collaborate with people." The development of iPS cells, ES-like pluripotent cells that can be grown without the destruction of embryos, has removed some of the intense pressure for scientists to have access to ES cells, and Gearhart himself is using iPS cells. Nonetheless, he says he still needs ES cells to study the mechanisms of embryogenesis and as a standard against which to compare iPS cells.

The executive order sweeps away a cumbersome level of bureaucracy that required researchers who receive both federal and private funds to keep separate accounting systems and use separate equipment depending on which cells they are working with. Harvard University researcher Kevin Eggan said earlier this year that the expected policy change "will have a huge immediate impact on my daily life." Roughly half his graduate students have NIH training grants, which has meant they could not participate in any non-NIH-approved work. The change, he said, "will mean I don't have to spend 7 or 8 hours a week dealing with Harvard administration making sure that the costing allocations for my lab are appropriately followed."

Some other scientists see the executive order's value as primarily symbolic. Because so many scientists are focusing on iPS cells, "I think it is going to have minimal effect in the short term" on research, says Martin Grumet, director of the Rutgers Stem Cell Research Center in Piscataway, New Jersey.

NIH has 120 days to finalize guidelines on research with the hundreds of hES cell lines that will soon be available to researchers. Such guidelines will likely draw heavily on existing ones on informed consent and other procedures that have been put out by the National Academy of Sciences and the International Society for Stem Cell Research. It's a "very exciting time at NIH right now," says Story Landis, head of the NIH Stem Cell Task Force.

NIH Acting Principal Deputy Director Lawrence Tabak said at a press conference that "our expectation is [that] some stimulus money will be available for use with the new guidelines." That's good news for researchers hoping for a piece of the package, which, among other things at NIH, allocates $200 million to a 2-year grants program that covers stem cells, regenerative medicine, and a dozen other fields.

Congress is already poised to pass legislation to codify the new order. The White House has been working with members of both the House and the Senate to ensure swift passage of the measure that was twice vetoed by Bush. Those bills (S. 487 and H.R. 873) ▸

CREDIT: LARRY DOWNING/REUTERS/LANDOV

specify that federally funded researchers can work only with ES cell lines derived from embryos created for fertility treatment that would otherwise be discarded.

Political battles are not yet over, however. Representative Chris Smith (R–NJ), co-chair of the House Pro-Life Caucus, held a press conference accusing the Administration of "incentivizing the creation and destruction of human embryos." Francis Collins, former head of NIH's National Human Genome Research Institute, told *Science* he is trying to help members of the religious community come to terms with the policy.

Federally funded scientists will still not be allowed to derive new lines of hES cells because of the 13-year-old Dickey-Wicker Amendment. Added annually to the health appropriations bill, the amendment prohibits federally funded researchers from harming human embryos. DeGette has indicated, however, that the time may be ripe to start asking legislators to reconsider their support for the measure. **–CONSTANCE HOLDEN**

RESEARCH FUNDING

England Spreads Its Funds Widely, Sparking Debate

Competitions always produce winners and losers, along with appeals to the referee about perceived unfairness, but last week's announcement of how £1.57 billion in annual research funding will be distributed to English universities drew complaints from some unlikely sources: top research institutions. Science heavyweights, including Imperial College London, Cambridge University, and Southampton University, received cuts or below-inflation increases in their annual funding, and they're not happy about it, warning of possible layoffs. Nottingham University; Queen Mary, University of London; and others that won substantial increases are not complaining. Indeed, a large number of England's "new universities," those created in the 1990s, are ecstatic, having earned money from this research pot for the first time. "This is a great encouragement," says Les Ebdon, vice-chancellor of the University of Bedfordshire.

Almost all of the U.K.'s universities are primarily state-funded, and to those conducting international-level research, the government allocates annual block grants to cover departmental overhead costs. But not every institution gets an equal share: The higher the quality of a university's research, the more it gets. Who gets what is decided by a competition held at irregular intervals called the Research Assessment Exercise (RAE), a huge peer-review process involving more than 1000 researchers serving on 15 subject panels and 67 subpanels. Two-thirds of the annual money is allocated according to the RAE results.

English officials used the last RAE, carried out in 2001, to concentrate funding in departments doing top-level international research, leaving many with no funding despite doing good work. (Scottish, Welsh, and Northern Irish education officials also use RAE data but independently devise their allocation strategies.) The RAE in 2008 saw a slight change of methodology: Instead of giving a single quality score to whole departments, it noted what percentage of each department was doing work in each of four grades, from nationally recognized to world leading (*Science*, 2 January, p. 24).

When the results were announced last December, the RAE revealed many "pockets of excellence" in institutions not normally lauded for their research, particularly those created after 1992 when a new law gave polytechnic colleges the right to become universities. In the allocations for England, revealed on 5 March, 25 institutions that previously received no RAE-allocated funding are now expecting a check in the mail, and others saw huge increases. The University of Lincoln, for example, sees its share of the research funding jump from £266,000 to £1.9 million. The new funding "will make it easier to hold on to world-class research teams," says Ebdon.

Changes in student demographics could have made the allocations even worse for England's traditional research universities. The number of university students in the United Kingdom has ballooned over the past decade, but most flocked to humanities and social science courses while the number enrolling in science has remained fairly steady. As a result, universities hired many more humanities and social science academics, who then won good ratings in the RAE. To prevent these newcomers draining money from science departments, the government decided that traditional science subjects would receive the same proportion of the whole pot as in previous years. "The ringfencing was absolutely crucial," says Hilary Leevers of the Campaign for Science and Engineering.

Nonetheless, there were some dramatic changes of fortune. Nottingham University will receive an extra £9.7 million in 2009–10, a 23.6% increase, while Imperial will get £5 million less, a 5.1% cut. The 16 English members of the Russell Group, which represents the United Kingdom's top research-intensive universities, together receive 3.3% more than last year. The whole fund being distributed was increased by 7.7%, however, indicating that England is spreading its research wealth more widely. That's a mistake, the traditional powerhouses warn. "Britain can't sustain 101 internationally competitive universities. If it's going to compete it's got to concentrate its resources," says epidemiologist Roy Anderson, rector of Imperial College. **–DANIEL CLERY**

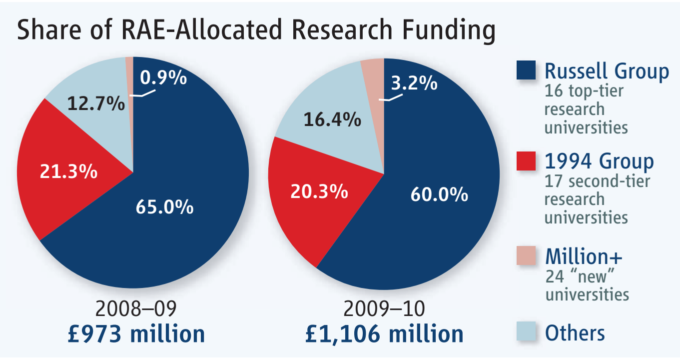

Shifting fortunes. New research quality data has led to shifts in research funding among English universities, with some earning such money for the first time.

SOURCE: *TIMES HIGHER EDUCATION* (5 MARCH 2009)

BIOMEDICAL RESEARCH

Humane Society Launches Offensive To Ban Invasive Chimp Research

The Humane Society of the United States (HSUS) last week stepped up its long-running campaign to end biomedical research with chimpanzees, orchestrating the broadcast of an "exclusive" story by ABC News that sharply criticized a leading primate research center, filing a 108-page complaint against the facility, accusing the U.S. National Institutes of Health (NIH) of violating its own moratorium on breeding chimpanzees, and working with Congress to draft and introduce new legislation that would ban "invasive" research on great apes. HSUS's efforts quickly grabbed the attention of researchers as well as government agencies that support or oversee the well-being of the 1200 "research" chimpanzees in the country.

On 4 March, HSUS revealed that for much of 2008, an unidentified employee at the New Iberia Research Center, part of the University of Louisiana (UL), Lafayette, worked undercover for HSUS and secretly videotaped the care and handling of some of the facility's 6000 monkeys and 350 chimpanzees. The video shows a chimpanzee falling from a perch and smacking the floor after being darted by a tranquilizer gun, an anesthetized monkey rolling off a table, a baby monkey writhing while receiving a feeding tube, and other strong images of caged primates. "A major issue for us is the psychological deprivation and torment that these animals are enduring," said HSUS President Wayne Pacelle at a press conference.

HSUS filed a complaint that day with the U.S. Department of Agriculture (USDA), alleging 338 "possible violations" of the Animal Welfare Act at New Iberia, one of four facilities in the United States that conducts biomedical research with chimpanzees. USDA Secretary Tom Vilsack immediately ordered a "thorough investigation." In January, USDA had received a separate complaint of alleged violations at New Iberia from Stop Animal Exploitation NOW. A USDA investigation revealed no violations, nor did a routine USDA inspection in September 2008.

HSUS also charged that the National Institute of Allergy and Infectious Diseases (NIAID) has violated NIH's own moratorium against breeding chimpanzees. The agency has had a $6.2 million contract with New Iberia to supply four to 12 infant chimpanzees each year between September 2002 and 2009 for research on several viral diseases.

On 5 March, Representative Edolphus Towns (D–NY) introduced the Great Ape Protection Act of 2009, which prohibits "invasive" research on great apes in the United States and federal support for such research anywhere. "Invasive" is defined as "any research that may cause death, bodily injury, pain, distress, fear, injury, or trauma." This would include drug testing, as well as anesthetizing or tranquilizing animals. The bill has 22 cosponsors and has been referred to the House Committee on Energy and Commerce. Kathleen Conlee, director of program management at HSUS, said her group helped draft the bill and that Towns "agreed to introduce the legislation on a timetable we asked for." Towns introduced a similar bill last year; it was referred to three committees but never moved forward.

Alleged violations. A Humane Society complaint to USDA charges that New Iberia does not handle its chimpanzees and monkeys with proper care.

UL Lafayette, NIH, and researchers who conduct invasive research on chimpanzees have challenged the HSUS media, regulatory, and legislative blitz on many fronts. UL Lafayette President E. Joseph Savoie said the images on the video "are based on interpretation and impression." At a press conference, employees at New Iberia contended that many of the most disturbing images were distorted. For example, they alleged that the person who shot the undercover video of the monkey falling from a table was a technician responsible for the care of anesthetized animals who possibly could have tended to the monkey. Savoie contended that HSUS's allegations against New Iberia were calculated to help pass the new legislation.

NIH told *Science* that its contract with New Iberia for the supply of infant chimpanzees does not violate its moratorium on breeding the animals. That moratorium applies only to chimpanzees owned or supported by NIH's National Center for Research Resources, which in 1995 abandoned a large chimpanzee-breeding program for fiscal reasons (*Science*, 26 January 2007, p. 450). "The moratorium was not intended for privately owned chimpanzees, or to apply to the other NIH Institutes," an NIH statement read, further noting that NIAID does not directly pay for breeding of the infant chimps, which are returned to New Iberia for long-term care. John McGowan, deputy director of science management at NIAID, says researchers there who study respiratory syncytial virus and different hepatitis viruses need infant chimps because they have not been exposed to these pathogens. He adds that they have also been used in biodefense studies related to smallpox and anthrax but that the animals were not harmed.

Several researchers who conduct studies on chimpanzees say the legislation is shortsighted. Geneticist John VandeBerg, the chief scientific officer at the Southwest Foundation for Biomedical Research in ▶

CREDIT: BRAD KEMP/*THE DAILY ADVERTISER*

San Antonio, Texas, says researchers there use chimpanzees primarily for testing drugs and vaccines against hepatitis B and C, diseases that he notes affect nearly 500 million humans.

Neuroscientist Todd Preuss of the Yerkes National Primate Research Center in Atlanta complains that the bill defines "invasive" too broadly. It would prohibit his and other groups from sedating chimpanzees to perform brain scans or drawing blood for behavioral experiments and endocrinology studies. He calls these interventions "minimally invasive."

Several scientific societies also oppose the ban. Alice Ra'anan, director of science policy at the American Physiological Society in Bethesda, Maryland, notes that existing government rules strictly regulate experiments on chimpanzees. "We can't afford to support an across-the-board ban," says Ra'anan. "There are diseases that can only be studied in chimpanzees."

Ajit Varki, a glycobiologist at the University of California, San Diego, who studies chimpanzees and disease but does not do invasive research himself, has long tried to find a middle ground between opponents and proponents of this controversial animal model. He says no research should be done on chimps that we would not do on humans. "On the other hand, I would no more think of banning all research on chimpanzees than of banning all research on humans," says Varki. "That would be a bad idea for the future of either species." **–JON COHEN**

SOLAR PHYSICS

Report Puts NASA's Solar Program Under a Cloud

A panel of space scientists has given NASA low grades on an ambitious 10-year plan to study the sun and its impact on Earth. A new report* from the National Academies' National Research Council (NRC) says rising project costs and an inadequate budget pose "a serious impediment" to the field of heliophysics. NASA officials disagree with the academies' harsh assessment of the agency's progress on a 10-year research plan adopted 5 years ago, citing a pipeline filled with major missions and increased funding for studying the results.

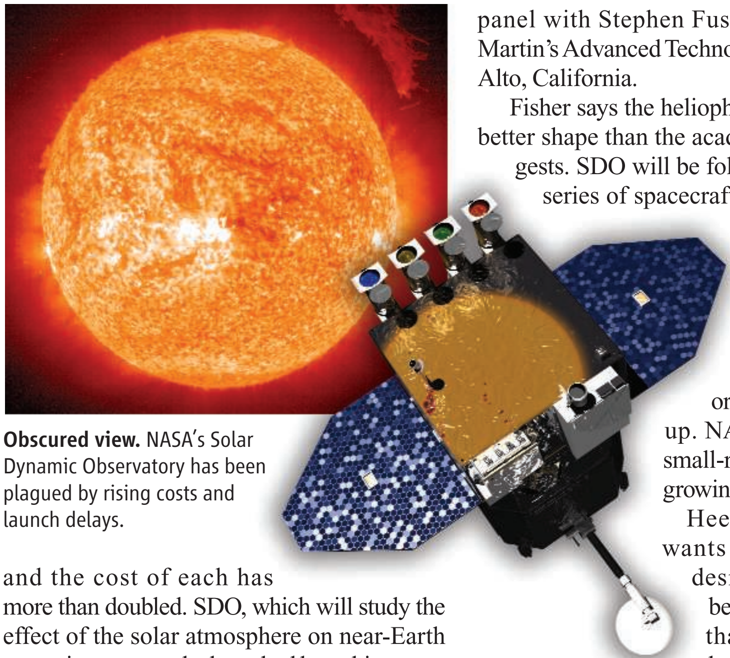

Obscured view. NASA's Solar Dynamic Observatory has been plagued by rising costs and launch delays.

The analysis, by a committee of the academies' Space Studies Board, is a midterm report card on the 2003 decadal plan that was requested by Congress. Although NASA receives average to good marks for its progress on many parts of the plan, it earns a D for making little progress on the Geospace Network, a program that would study the impact of solar variability on sensitive electronics used in satellites and ground-based power grids, and an F for failing to integrate its efforts with those of other disciplines and agencies, notably the Department of Energy.

Richard Fisher, who directs the heliophysics program at agency headquarters, acknowledges that the report may be "useful" but says he's disappointed that it included neither a clear scientific assessment of the current situation nor recommendations on what NASA might do better. "We would have welcomed such an assessment so as to better address … the allocation of scarce resources and flight-project decisions," he says.

The saga of two major projects featured in the 2003 decadal study—the Solar Dynamic Observatory (SDO) and the Magnetospheric Multiscale (MMS) mission—illustrates the problems facing NASA and the field. Both launches have been delayed by some 4 years, and the cost of each has more than doubled. SDO, which will study the effect of the solar atmosphere on near-Earth space, is now set to be launched later this year at a cost of nearly $900 million—far more than the original $400 million. The cost of MMS, which will use four separate spacecraft to study the structure of Earth's magnetosphere, has grown from $350 million to $1 billion with a scheduled launch in 2014. "The resources … have not been used effectively," says Daniel Baker, a space physicist at the University of Colorado, Boulder, who was on the original 2003 panel. "The result is disastrous."

The cost increases have deferred deployment of the Geospace Network until later in the next decade. And NASA's decision in 2004 and 2005 to trim smaller programs such as Explorer because of shrinking budgets has deprived solar scientists of expected opportunities to put their instruments into orbit. "There's just not enough money," says Roderick Heelis, a University of Texas, Dallas, physicist who co-chaired the 11-member NRC panel with Stephen Fuselier of Lockheed Martin's Advanced Technology Center in Palo Alto, California.

Fisher says the heliophysics program is in better shape than the academies' report suggests. SDO will be followed in 2012 by a series of spacecraft called the Radiation Belt Storm Probes, he notes, and NASA plans to launch the first satellite to orbit near the sun a year or so after MMS goes up. NASA's balloon and small-rocket programs are growing, he adds.

Heelis says the panel wants future missions designed to make the best use of the money that's available. But the forecast for funding solar exploration is cloudy at best. Under a long-term projection from the Bush Administration, the budget for heliophysics would drop from $831 million in 2007 to $598 million in 2010, before climbing to $747 million in 2013. The Obama Administration has not signaled what it plans to do.

Colorado's Baker is encouraged by the strong interest in climate change research shown by White House officials and their awareness of the importance of space weather, two areas that could bolster NASA's program. But solar scientists worry that their field may be eclipsed by overruns in the Mars Science Laboratory, the push to build a massive new spacecraft to orbit Jupiter, and the need to restart the flagging Earth science program. "There's a zero-sum game mentality, which makes it hard for our aspirations to be met," says Baker. **–ANDREW LAWLER**

**A Performance Assessment of NASA's Heliophysics Program* (www.nap.edu/catalog.php?record_id=12608).

CREDITS: SOHO-EIT CONSORTIUM/ESA/NASA; GSFC/NASA

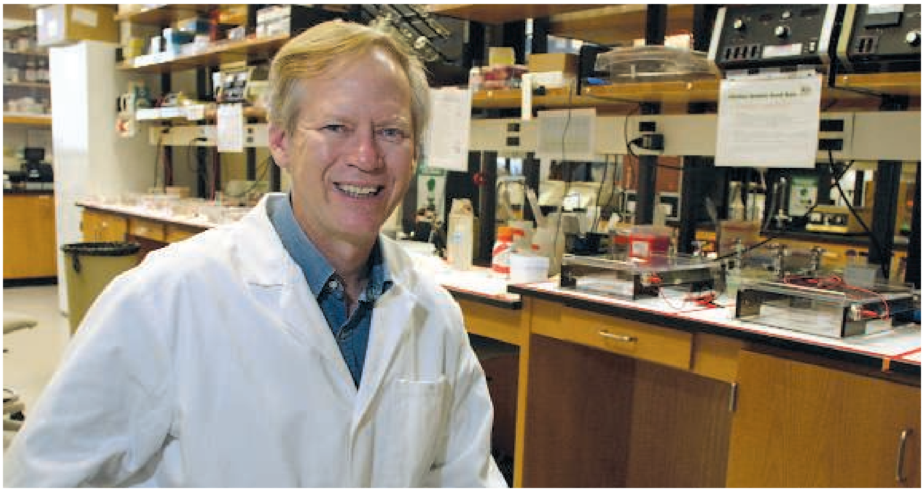

BIOSECURITY

Paul Keim on His Life With the FBI During the Anthrax Investigation

Hours after the first wave of the 2001 anthrax letters sickened a man in Florida—the first of five people to die in the attacks—geneticist Paul Keim got a phone call from the Federal Bureau of Investigation (FBI). Keim, of Northern Arizona University in Flagstaff, had 3 years earlier developed a genetic fingerprinting technique to distinguish between different types of *Bacillus anthracis*. The FBI wanted him to identify the anthrax strain the attacker had used. Keim and his lab continued to play a role in the investigation until last summer, when the FBI implicated U.S. Army researcher Bruce Ivins as the perpetrator of the attacks. In a recent interview with *Science*, Keim recounted some of the key moments from his involvement in the 7-year-long investigation. Some of his responses were edited for clarity. **–YUDHIJIT BHATTACHARJEE**

Q: When were you consulted about the case?
P.K.: Shortly after Florida's Robert Stevens [the first victim] became ill, officials contacted me to find out whether he could have contracted anthrax from drinking water out of a stream in North Carolina, where he had been traveling the week before, or from exotic Oriental food stores. But in the wake of September 11, we were all suspicious that it was a follow-on terrorist attack.

Q: How did your lab get involved?
P.K.: The FBI wanted us to analyze the anthrax in Stevens's cerebrospinal fluid. An FBI scientist, Doug Beecher, called me on the afternoon of October 4 to let me know that the culture was already in the air: It was arriving in a business jet from Atlanta, where an identical sample was being analyzed at the Centers for Disease Control.

My body went cold because I realized we only had a few hours to prepare for it. It was sundown when I drove to the commercial airport at Flagstaff. The airport officials let me drive out on the tarmac. I watched the jet land; an attractive blonde woman got off with a box containing the culture. It was a surreal experience. I felt like Humphrey Bogart in a scene from *Casablanca*. I put the box in my car and drove right back to the lab. The next morning, we called Atlanta to say that we'd determined the sample to be the Ames strain.

Q: What came next?
P.K.: Over the next few months, we analyzed anthrax from all the letters. After the FBI decided to pursue full genome sequencing of anthrax samples from labs all around the country and overseas to trace the source of the spores used in the attacks, we were contracted to prepare DNA from the samples. The DNA was shipped to The Institute for Genomic Research in Rockville, Maryland, for sequencing. Our lab also served as the repository for all of the samples.

Q: What was it like to be collaborating with an investigation?
P.K.: The conversion of an academic lab to a forensic lab was painful: We had to follow strict rules concerning the handling of evidence. Every little step in the process needed to have witnesses. But we took it very seriously; we were motivated by the fear of having a Johnnie Cochran cross-examining us in court.

We were sent some 1500 samples. … The work pressure was very high. … At one point, people in the lab were starting to revolt. After we developed some real-time PCR assays to identify the samples, we were able to cruise through.

Q: When did you learn that investigators were focusing on Bruce Ivins?
P.K.: On 14 May 2008, when FBI agents and Justice Department officials revealed his name in the course of questioning me about the timeline for how the technology for fingerprinting anthrax had improved since the mid-'90s.

Q: How did the interview unfold?
P.K.: It was in a room at the Courtyard Marriott near the Washington Dulles airport, where I was attending a meeting of the FBI's Scientific Working Group on Microbial [Genetics and] Forensics. There were five FBI agents and officials from the U.S. Attorney's office. … I remember making a nervous joke. I said I've greased up my wrists just so I can slip out of my handcuffs when you throw me in the back of the van. …

What they were trying to establish was how much Ivins would have known about the developments in fingerprinting [to distinguish between different strains]. They pulled out e-mails that Ivins and I had exchanged in 2001–2002 as part of ongoing discussions amongst anthrax researchers about the attacks. They wanted to know if I could tell, from those e-mails, if Ivins might have been attempting to cover his tracks.

Q: What did you conclude?
P.K.: I didn't see any smoking gun. I went back and looked at some other e-mails from him, and in one that he sent on 7 February 2002 to the group, he said, "The only place I know of that makes anthrax powder is the Dugway Proving Ground."

Q: Do you think Ivins was guilty?
P.K.: I don't know.

Q: Are all the samples still at your lab?
P.K.: No, the FBI took them in June 2008. The agency flew a propeller plane from the East Coast to Flagstaff to transport them to another destination.

Q: How can researchers learn more about the scientific work done on the case?
P.K.: Scientists are committed to publishing all of the research. The goal is to package all of the papers into one journal so that the community can evaluate the quality of the science all in one place.

CREDIT: NORTHERN ARIZONA UNIVERSITY

CHINA

Biologists Muscle Up With Major New Protein Facilities

BEIJING—When molecular biologist Xu Rui-Ming gave up a plum professorship at New York University to return to China last autumn, he knew the move would entail sacrifices: a pay cut, for starters, and the need to acclimate to Beijing, one of the fastest growing cities in the world. But the opportunity to help build a research empire was impossible to resist.

This month, Xu and colleagues here at the Institute of Biophysics (IBP) of the Chinese Academy of Sciences (CAS) will begin recruiting researchers for a National Laboratory of Protein Science (NLPS). In the spirit of Janelia Farm, the biomedical research haven in Virginia run by the Howard Hughes Medical Institute, the national lab will give a few dozen top-notch biologists generous contracts, access to top equipment, and protection from the vitality-sapping chase for research funding.

Last year, Premier Wen Jiabao called for the creation of several dozen national labs; NLPS is among the first in the biological sciences. "We are the guinea pigs," says Xu. They will get a leg up from an allied effort to lift biology boats countrywide. Science managers here and in Shanghai are divvying up $160 million for a National Core Facility for Protein Sciences that will be open to all Chinese researchers, including those at NLPS, and eventually to foreigners as well. "It's the first time in history that the government has funded a national facility in life sciences," says cell biologist He Fuchu, director of the Beijing Proteome Research Center.

Quickest off the blocks should be NLPS. It's the brainchild of former IBP Director Rao Zhihe, now rector of Nankai University in Tianjin, who floated the concept in 2003. CAS has spent $45 million over 5 years instrumenting IBP. Next, "we need high-caliber researchers," says Xu, a specialist on epigenetics who intends to recruit a significant number of the lab's initial 60 principal investigators from overseas.

To sweeten the appeal, the national lab will give researchers a salary and 5-year grants and let them loose in a setting akin to Cold Spring Harbor Laboratory, where Xu worked for 13 years. "This is an absolutely new concept in China," he says. Two-thirds of the initial recruits will be stationed at IBP and the rest spread around the country, like Howard Hughes investigators at their home institutions; the plan is to ramp up to 100 principal investigators, with a rising percentage located outside IBP. NLPS's budget is roughly $60 million a year.

CREDITS (TOP TO BOTTOM): QIANG WANG; R. STONE/*SCIENCE*

An even grander plan is the National Core Facility for Protein Sciences. After months of discussions, the research center is taking shape. Four organizations are orchestrating the Beijing part of the venture: the Academy of Military Medical Sciences, Tsinghua University, Peking University, and CAS. Last month, the partners agreed on the broad outlines of how they will spend $80 million from the agency that bankrolls major infrastructure projects—the National Development and Reform Commission (NDRC)—and a nearly equivalent sum on top of that from the Beijing municipal government, the Ministry of Education, and the Department of Logistics of the People's Liberation Army.

The Beijing facility, dubbed PHOENIX, will focus on proteomics, including high-throughput pipelines for protein expression profiling and protein-protein interactions; structure determination; proteome-wide functional analysis; large-scale protein and antibody production; and bioinformatics.

Beijing bio-glitterati. Xu Rui-Ming (*top*) will lead the National Laboratory of Protein Science, while He Fuchu is the top manager of PHOENIX, a planned proteomics facility.

User committees have begun drawing up wish lists of equipment. PHOENIX, says He, who will head it, will host more than 50 principal investigators. Outside researchers would be able to come for short periods to conduct experiments or tap into the complex remotely via high-speed data links. The core facility, backers say, will provide a platform for 'small science' projects conceived by individual investigators. Groundbreaking is expected to take place around the end of the year.

CAS's Shanghai Institutes of Biological Sciences (SIBS) will receive the other half of NDRC's largess to build a National Facility for Protein Science in Shanghai. Pending NDRC approval of an itemized budget, the facility will be located at a science and technology park that CAS and the Shanghai municipal government plan to build in Pudong district, just down the road from a third-generation synchrotron source set to come online this spring. The synchrotron will be a major resource of the Shanghai protein facility, which plans to construct five beamlines for solving protein structures, studying protein dynamics, and imaging molecules.

As with PHOENIX, the intent is not "big science," says SIBS vice president Wu Jiarui, chief scientist of the Shanghai component of the national core facility. "It may be considered a protein hospital," says Wu, in that biologists, like doctors examining patients, will use a variety of approaches—including electron microscopy and mass spectrometry—to probe protein structure, function, and interactions.

In China, biology has long been a poor cousin of the physical sciences, which until recently lured many of the country's finest minds and produced strategic advances such as a nuclear arsenal and human space flight. Now it is biology's turn to shine, says He. "We hope to make a great leap in understanding the functions of protein systems," he says.

–RICHARD STONE

With reporting by Hao Xin in Shanghai.

PLANETARY SCIENCE

In Dune Map, Titan's Winds Seem to Blow Backward

Christopher Columbus rode the trade winds from Europe to America. But on Saturn's moon Titan, a wind-driven westward voyage might not be possible. A new map of Titan's dunes reveals that near-surface winds at the equator blow the wrong way: from west to east. That's the opposite of the predictions made by models of Titan's atmosphere. Researchers say there's no clear path to reconciling those differences.

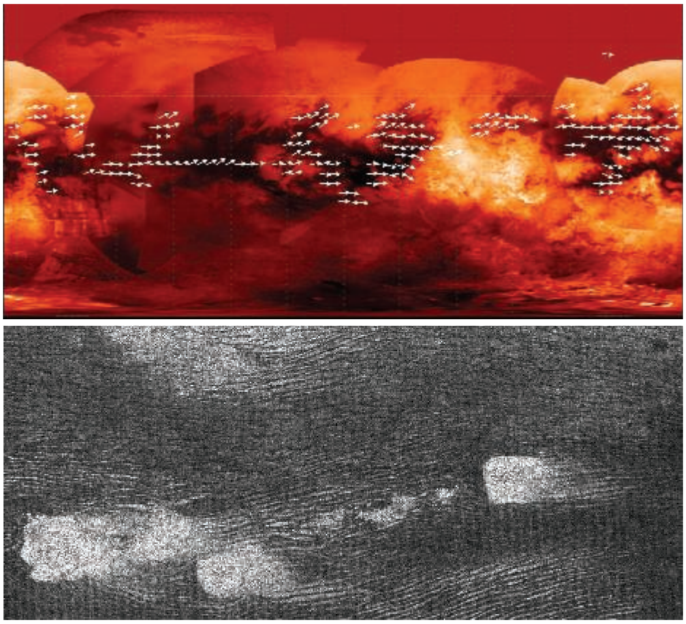

Dune world. Scientists used Cassini radar images (*bottom*) to map the direction of Titan's equatorial dunes (*top*). From that, they inferred the direction of the winds that formed the dunes. The result flew in the face of modeling predictions.

For the map, published in *Geophysical Research Letters* last month, planetary scientists Ralph Lorenz of Johns Hopkins University in Laurel, Maryland, and Jani Radebaugh of Brigham Young University in Provo, Utah, used images from the Synthetic Aperture Radar instrument on the Cassini spacecraft to map 16,000 individual dune segments, equivalent to 8% of Titan's surface. The dunes, all within 30° latitude of the equator, roughly align along an east-west axis. From the way the dunes divert around obstacles, the scientists inferred that the winds that formed them must have come from the west, Radebaugh says.

Titan global circulation modelers have found this conclusion difficult to swallow. They expected Titan's atmosphere to follow a pattern like that on other terrestrial bodies that rotate in the same direction, including Earth. On these bodies, the surface transfers its angular momentum to the near-surface atmosphere, pulling the atmosphere around after it. The equator is the part of the surface with the most angular momentum, because it's the farthest away from the rotation axis. Therefore, the atmosphere near the equator's surface should rotate no faster—and probably slower—than the surface itself, producing gentle westward winds such as Earth's trade winds. The near-surface winds would move eastward only if they could draw extra angular momentum from somewhere else—an unlikely scenario, says Jonathan Mitchell, a planetary scientist at the Institute for Advanced Study in Princeton, New Jersey.

Although unlikely, that's exactly what seems to be happening on Titan. "It almost seems to violate basic physical principles like conservation of angular momentum," Mitchell says.

Initially, the modelers questioned the results, says Claire Newman, a planetary scientist at the California Institute of Technology in Pasadena. "It's almost like you go, well, did they flip the images around the right way when they got them down from Cassini?" But now they concede that something must be missing from their models, which are adaptations of various general-circulation models of Earth or Mars. So far, the researchers have speculations but no answers.

For example, how the dunes form may be important, Newman says. The researchers have assumed that the dune formation requires average eastward winds. But average winds could be westward, as the models predict, if the rare eastward winds are somehow especially good at making the dunes—because they come at special times of the day or year, or at special speeds, such as storm speeds. Unfortunately, Newman says, nothing in her model stands out as special so far.

Alternatively, the dunes may not be what they seem, says Scot Rafkin, a planetary meteorologist at the Southwest Research Institute in Boulder, Colorado. The researchers used similar dunes on Earth to draw conclusions about how Titan's dunes formed. But there could be "some process operating on Titan that doesn't operate on Earth to produce dunes that look similar," he says. And although the dunes seem to be young, he says, they may be cemented in place, remnants of an atmospheric past.

The heights of Titan's topographic features are still not well mapped, so unknown hills and valleys could still be the culprits, says Sébastien Lebonnois, a planetary climatologist at the Laboratoire de Météorologie Dynamique (CNRS, University Paris 6) in Paris. Tetsuya Tokano, a planetary meteorologist at the University of Cologne in Germany, has added speculative topography to his model, to no avail. He now guesses that the dunes themselves could be diverting the winds, but the models don't have a fine enough resolution to study the dunes.

Mitchell plans to study the possible connection to Titan's atmospheric superrotation—fast-moving eastward winds high in the atmosphere over the equator. But how would that angular momentum move from high up to near the surface? "That's the missing piece," Mitchell says. "I'm trying to come up with ways" to make that happen in the model.

Lorenz, who is not an atmospheric modeler, draws a connection to another line of research, which indicates that the crust of Titan is separated from the core by a vast underground ocean. If that's the case, Titan's surface could spin at a variable rate over the course of Titan's year. Could that change the wind direction at the equator or create the dunes? "At this point, everything's on the table," Mitchell says.

The mystery may say less about Titan than about the state of Titan research: There's "too little data on one side and too primitive a state of modeling on the other side," says Anthony Del Genio, a planetary meteorologist at the NASA Goddard Institute for Space Studies in New York City and a member of the Cassini imaging team. With Jupiter's moon Europa recently chosen for NASA's next flagship mission to the outer solar system, it's not clear when a new mission will go to Titan. So progress depends on Titan modelers getting access to "sufficient computational resources," he says. "Then we'll have a better idea of whether this thing is really a mystery or whether it's something that is easily explainable."

–CHELSEA WALD

Chelsea Wald is a writer in New York City.

CREDITS (TOP TO BOTTOM): NASA/JPL/SPACE SCIENCE INSTITUTE; NASA/JPL

PALEOANTHROPOLOGY

Ice Age No Barrier to 'Peking Man'

Ever since a Canadian anatomist discovered the skullcap of "Peking Man" by candlelight in China's Zhoukoudian Cave in 1929, the cave has been known as the richest *Homo erectus* site in the world. Just 50 kilometers southwest of Beijing, the cave was the resting place for more than 40 individuals dragged there by predators. But with no volcanic sediments for traditional radiometric dating, researchers have not known precisely when early humans lived near the cave. Now, Chinese and American researchers have redated bones and tools from the site with a new radiometric method.

Cool-headed. *Homo erectus* may have been the first human species to survive a near-glacial winter.

They date the oldest human fossils to about 770,000 years ago, at least 200,000 years older than previously thought, in work published this week in *Nature*. The dates are not the oldest that have been claimed for Chinese *H. erectus*, but they suggest this species survived during a mild glacial period at Zhoukoudian. They provide the earliest evidence that *H. erectus* lived this far north (39.93° North latitude) during near-glacial conditions. "We always thought things were happening later in China," says Harvard University paleoanthropologist G. Philip Rightmire. "These findings bring *H. erectus* in China more closely in sync with Africa."

To get the new dates, geochronologist Darryl Granger of Purdue University in West Lafayette, Indiana, applied a method called cosmogenic burial dating, which is used to date the retreat of glaciers and has also been used in caves (*Science*, 25 April 2003, p. 562). When cosmic rays bombard rocks on Earth's surface, they produce unstable isotopes of beryllium and aluminum. The older the rock, the more isotopes it accumulates. When the rock is buried, the bombardment stops and the isotopes decay at a known rate; the ratio of the two isotopes thus works as a clock to reveal when the rock was buried (*Science*, 11 January 2002, p. 256).

Granger dated quartz from stone tools and the sedimentary layers where the oldest fossils were found and got a mean date of 770,000 years, with a fairly wide margin of error of 80,000 years. Some previous dates ranged from 200,000 to 500,000 years ago, although the new ages match less reliable uranium series and paleomagnetic dates, says lead author Guanjun Shen, a geochronologist at Nanjing Normal University in China.

If the new dates are right, then *H. erectus* was at Zhoukoudian during a relatively mild glacial period about 750,000 years ago that brought icy winds and snow to the region—similar, perhaps, to the cold, dry climate today in southern Siberia. Studies of animal fossils, isotopes, and dust in the cave also suggest that *H. erectus* was there when the climate fluctuated between cold, dry glacial periods and wet, warm interglacials for 400,000 years. Surviving the cold implies they used fire, which is not surprising for these big-brained hominids but has been very difficult to prove.

The new climate data and differences in anatomy suggest to some that *H. erectus* in the north was separate from *H. erectus* found on Java in Indonesia. As the species left its original home in Africa, there may have been "two migrations, one earlier to the south and one later to the north," says paleoanthropologist Russell Ciochon of the University of Iowa in Iowa City.

In any case, the new dates allow researchers to tie Zhoukoudian to other *H. erectus* sites in China, Africa, and Europe, providing "a more coherent picture," says paleoanthropologist Susan Antón of New York University in New York City. "This site was always an outlier [in time]."

–ANN GIBBONS

Ancestral tomb. New dates put *H. erectus* in this ancient cave earlier than expected.

PHOTO CREDITS (TOP TO BOTTOM): MEI HUIJI; DARRYL GRANGER

*Science*Insider

From the *Science* Policy Blog

The powerful chair of the House Judiciary Committee, **John Conyers** (D–MI), has explained why he believes the National Institutes of Health (NIH) should not require scientists it funds to make their research papers publicly available via the Internet. In an essay released last week, Conyers defended a bill he introduced that would reverse that **open-access** policy, which he sees as a threat to copyright law and, ultimately, peer review. Stanford University law professor Lawrence Lessig and open-access guru Michael Eisen of the University of California, Berkeley, had attacked Conyers as "shilling for special interests" in an essay.

Nobel Prize–winning physicist and Energy Secretary **Steven Chu** stayed in the headlines this week over ways to make coal power more climate friendly. He announced a new "true engineering collaboration" with science ministries from China, the United Kingdom, and other European allies to demonstrate **carbon capture** and storage technologies.

Patent reform came up in the form of a bipartisan bill introduced in both the House and the Senate. But judging from its reception, it's going to be another long fight to pass this always-contentious legislation. The initial response from the biomedical community was negative; a coalition of companies that favor strong patents blasted the bill as favoring "infringers over inventors." Others, who feel that the current system gives patent holders unfair rights, were more favorable toward it.

Harold Varmus, co-chair of the President's Council of Advisors on Science and Technology, pitched his new memoir on *The Daily Show* with host and comedian Jon Stewart. Although the former NIH director played it mostly straight, he did drop a nugget of news here and there, mentioning, for example, that he "was not" advising the president on his recent announcement to boost cancer research at NIH.

For the full postings and more, go to **blogs.sciencemag.org/scienceinsider**.

The planet's vast store of coal could fuel the world economy for centuries—and fiercely stoke global warming—but a few analysts are raising the prospect of an imminent shortfall

How Much Coal Remains?

To a geologist, gauging how much coal the world has left to burn is a fairly straightforward, if daunting, business. Millions upon millions of drill holes have revealed where the coal is. So geologists can just evaluate each seam's quality and the cost of extraction. Add up all the coal worth mining and you've got lots and lots—within the United States, a century or even two of U.S. consumption; globally, 150 years' worth for the world.

But there's another, emerging approach to assessing coal resources that yields more sobering results. Rather than go into the field, these analysts go to the record books to see how fast miners have been producing coal of late. By fitting curves to that production history, they come up with a number for the total amount of coal that will ever be mined and a date for the greatest production, the time of "peak coal," after which production inevitably declines.

Early results from this curve-fitting analysis of production history show much less coal being mined than geologists ever expected and a peak in coal production looming as early as a decade from now. Curve fitting "is a worthy competitor to a geological estimate" of remaining coal, says David Rutledge of the California Institute of Technology in Pasadena, a nongeologist who has produced such an estimate himself. Geologists beg to differ. "The whole notion of applying statistics to time series [of coal production] is fraught with danger," says energy resource geologist Peter McCabe of the Commonwealth Scientific and Industrial Research Organisation (CSIRO) in North Ryde, Australia. "I think what you see in Rutledge's presentation is a fundamental misunderstanding."

At stake are two central questions: How bad is greenhouse warming likely to get? And when must alternatives to coal come online? By Rutledge's calculations, burning all the coal, oil, and gas humans can get their hands on won't pump enough carbon dioxide into the atmosphere to drive global warming past 3°C, a far less intimidating ultimate warming than the 8°C or 10°C of some scenarios. But engineers developing energy alternatives would have only a few decades to get them in place.

Online
sciencemag.org
Podcast interview with author Richard A. Kerr.

Ringing the bell

The growing popularity of curve fitting to fossil fuel production got its start with geophysicist M. King Hubbert (1903–1989) and his bell-shaped curves. Hubbert—a prominent researcher at Shell Oil and then the U.S. Geological Survey—concluded that the rate at which oil was produced would follow the same bell-shaped curve over time as production from a single field does (see top figure, below).

Production in Hubbert's scheme gradually accelerates from the bell's left side as drillers tap the most accessible, most easily extracted oil pools at an ever-faster rate. But eventually, no matter how much they drill, it gets harder and harder to suck out the oil because the remaining pools are fewer, smaller, deeper, and more difficult to drain. The earlier acceleration now slows across the crown of the bell until production stops growing, peaking at the bell's top. It then declines until, at the right side, all the oil that will ever be produced has been produced.

In 1956, Hubbert published his curve-fitting prediction that U.S. oil production would peak in the early 1970s. He used the U.S. production history up to that point to set the shape of the curve and an estimate of the amount of oil that would ultimately be produced to set the area encompassed by a complete curve.

U.S. production in fact peaked in 1970, inspiring a generation of oil "peakists" to apply Hubbert's approach to world oil (*Science*, 21 August 1998, p. 1128). As of 1998, they broadly agreed that world oil would reach its peak by now or at least by the middle of the next decade. In fact, production outside oil-rich OPEC (Organization of the Petroleum Exporting Countries) has not risen since 2004, despite years of encouragement by high oil prices. And total world production has gone nowhere since 2005.

On to coal

In the last couple of years, forecasting coal production by Hubbert's approach has come into vogue, partly because geologists seemed to be having trouble assessing how much minable coal was left. For example, "40% of the world's coal disappeared in 3 years," recalls retired U.S. Geological Survey coal expert Harold Gluskoter. For the World Energy Council's triennial survey of coal resources in 1990, China cut its recoverable coal reserves—the amount

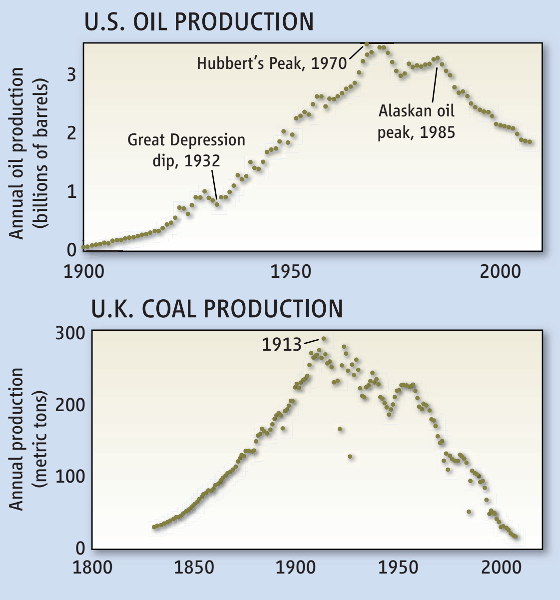

Up, down. Both U.S. oil production and U.K. coal production rose rapidly, peaked, and then declined.

CREDIT: RAIMOND SPEKKING/WIKIPEDIA; SOURCE: DAVID RUTLEDGE/CALTECH

of remaining coal geologists believe can be extracted with today's technology at today's prices—to one-sixth of what it had reported in 1987. The coal was mostly still there; the Chinese just decided they could extract only a smaller proportion of it.

Less dramatically, in 2007 a committee of the U.S. National Research Council that Gluskoter served on could not support the long-standing estimate of about 267 billion short tons of recoverable reserves in the United States. Divided by current U.S. production, the old estimate gave the oft-quoted figure of a 250-year supply for the United States. "We probably have 100 years. We don't know how much after that," says Gluskoter.

Reserve estimates around the world were also coming down, and dividing estimates of minable coal by current production says nothing about when coal might peak. To get at both forecasts, analysts tried a variation on curve fitting à la Hubbert. No results have been published in the peer-reviewed literature, but Rutledge's effort has probably gotten the widest exposure (rutledge.caltech.edu/).

Rutledge, an electrical engineer, adapted a technique used by geologist Kenneth Deffeyes, professor emeritus at Princeton University, to predict a world oil peak in 2005. (Deffeyes sees his prediction holding up nicely.) In the technique, an as-yet-to-peak production history (see bottom graph, left) is replotted in terms of cumulative production and annual production in such a way as to produce a straight line, at least if production approximates an ideal bell-shaped curve. The straight line intercepts the x-axis at the ultimate production—all the coal that will ever be produced—and the year in which half of the ultimate production will be achieved is the year of peak production.

Rutledge tested the method on regions long past their coal peaks. The coal production of the United Kingdom—once the world's premier energy supplier—peaked in 1913 and is now at about 6% of its peak. A straight line makes "a beautiful fit" to the replotted history, Rutledge told audience members at last December's meeting of the American Geophysical Union. The projected ultimate production in the United Kingdom is about 28 billion metric tons of coal, Rutledge said, which should be reached in 8 years. Geologic estimates made in the 19th century had reserves near 200 billion tons. In fact, the World Energy Council's geologically based reserve estimates—provided by the United Kingdom—stayed at 19th century levels until the 1970s, when they collapsed toward Rutledge's number.

> *"The whole notion of applying statistics to time series [of coal production] is fraught with danger."*
>
> **—PETER MCCABE, CSIRO**

Applied to 14 major coal-producing regions, Rutledge's method gives a world ultimate production of 660 billion metric tons. That's only one-quarter of geologic estimates of ultimate production, he says. And when combined with similar estimates of ultimate production of oil and gas, the total emissions of carbon as the greenhouse gas carbon dioxide till 2100 are smaller than any of the 40 emissions scenarios that climate scientists have been working with for the past 10 years.

As to when coal will peak, Rutledge declines to say, citing the way peak timing varied widely among regions already well past their peak. He will say, however, that in his projection the world will have produced a whopping 90% of its coal by 2069. Physicist Mikael Höök of Uppsala University in Sweden and his colleagues are willing to point to a peak. They have taken a similar approach to Rutledge's but with some reliance on estimated reserves. Still, they see world coal production topping out by 2020, entering a 30-year-long plateau, and then declining.

Outside influences

Geologists and resource economists aren't ready to give up on coal so soon. "The bell-shaped curve is nice to look at after the fact," says Gluskoter, but "I'm not sure how predictive it is." "You can put me in the skeptical camp" as well, says physicist and energy analyst Klaus Lackner of Columbia University. Rutledge "puts too much weight on a simple model," he says. "The world is not a two-parameter curve."

U.K. coal "did not decline because it reached some magic percentage of coal depletion," argues CSIRO's McCabe. "Gradually, [U.K.] demand disappeared. Coal was no longer used for power, steamships, railroads, domestic heating, or iron and steel production. When I was a kid in England many years ago, gas for the home was produced from coal. There are much cheaper alternatives in the U.K. for energy." Natural gas from the North Sea replaced coal gas in the home, he notes. Relatively inexpensive—and cleaner-burning—oil became available.

Does it matter why coal production behaves as it does? responds Rutledge. Whether it's a physical lack of resources or a demand shift to cheaper, more attractive sources, a limit is a limit. Gluskoter and many colleagues are betting on a demand shift. "I believe in technology," he says. But first, technology could actually stretch coal resources. "The resource is there," he notes, "it's perfectly minable. It's just not economical right now." Improved technology will let miners get at thinner, less accessible seams, he says; uneconomic coal might even be turned into gas right in the ground.

Despite any coal added by technology, "we'll stop using coal before we run out of it," says Gluskoter. Just as cleaner, cheaper fuels displaced British coal, less-polluting, less-expensive energy sources will replace coal worldwide, he argues. His bet is on solar energy. Plenty of usable coal will be left in the ground, he adds, but "we're not going to be burning coal in a couple hundred years."

–RICHARD A. KERR

NEUROSCIENCE

A Memorable Device

Wearable cameras offer help to people with memory problems and provide a tool for studying how the brain creates and retrieves personal histories

It was over drinks at a local pub in the spring of 2006 that cognitive psychologist Martin Conway of the University of Leeds in the United Kingdom first told his colleague Chris Moulin about using a wearable camera for memory research. But it took more than a few pints of beer to convince Moulin that SenseCam, a camera that periodically takes still photos while worn on the user's chest, might be a game-changer in the study of what psychologists call autobiographical memory. Although skeptical of the small device's usefulness, Moulin did finally agree to take one for a test drive.

Or rather, he took it on a test walk. Moulin regularly wore a SenseCam on a series of walks. When he reviewed the images 6 months later, to see how well his memories matched the camera's visual record, Moulin says he experienced an unexpected feeling of "mental time travel." One of the images triggered the memory of the song—Thom Yorke's "Black Swan"—that was playing on his iPod when the image was taken.

Conway says that many SenseCam users likewise report a sudden flood of memories of thoughts and sensations, what he calls "Proustian moments," when they review images taken by the device. SenseCam's images "correspond to the nature of human memory—they're fragmentary, they're formed outside your conscious control, they're visual in nature, they're from your perspective. All these features are very like what we call episodic memory," says Conway.

That's why he, Moulin, and dozens of other researchers have begun to test whether the images can help resolve how the brain handles personal memories. Cognitive experiments, however, represent just one line of inquiry supported by Microsoft Research, the scientific arm of the software giant and the inventor of SenseCam. Medical researchers are also evaluating whether the device can help people with memory problems due to illness or injuries.

In 2004, Narinder Kapur and Emma Berry, neuropsychologists at Addenbrooke's Hospital in Cambridge, U.K., were the first to use a SenseCam for memory rehabilitation work. They found that the device significantly helped Mrs. B, an elderly woman with memory problems due to brain damage from an infection. Mrs. B normally forgot events after 3 to 5 days, and even keeping a diary that she periodically reviewed helped her remember events for only about 2 weeks. But when she regularly reviewed SenseCam images of events, she could recall more details—and her memories persisted for months after she ceased reviewing the past images. Encouraged by that data, Kapur says he and Berry grew hopeful that "periodic, regular review of visual images of personal events … really does help long-term [memory] consolidation."

Shooting in the rain. The SenseCam (*left*) snaps dozens of wide-angle, low-resolution images from chest level on even a short walk.

They and others are getting a chance to test that hypothesis. After the pair reported the results from Mrs. B, Microsoft Research decided to provide more than $550,000 in funding to seven research groups, most of them focusing on people with memory problems, and to loan hundreds of cameras to other scientists. SenseCam has "very obvious applications in a whole range of clinical disorders," says one of the grant recipients, psychologist Philip Barnard of the University of Cambridge.

Personal black boxes

SenseCam grew out of a Microsoft Research project that aimed to create a "black box for the human body" which would record data that doctors might find useful if a person were in an accident, says Ken Wood of Microsoft Research Cambridge. In 1999, computer scientist Lyndsay Williams, then also at the same lab, suggested adding a camera to the device so it could double as a memory aid for mundane tasks such as finding lost keys.

In 2002, Kapur heard then-Microsoft CEO Bill Gates mention the project in a talk. Because his hospital is just a few miles from Microsoft Research Cambridge, it was easy enough for him and Berry to suggest using SenseCam prototypes for patients with memory problems due to Alzheimer's or brain injuries.

Clinicians who work with such people have typically focused on helping them with their prospective memory, i.e., remembering tasks to be completed in the future, such as keeping appointments. For this, the best aids are still simple tools such as checklists and alarm clocks. But for patients with difficulty recalling past events, clinicians have had little to offer beyond diary-keeping, a task many people, such as Mrs. B and her husband, complain is onerous.

In contrast, SenseCam records images passively, permitting a person to go about their day without interruption. The latest version is about the size and weight of a clunky mobile phone and appears to observe the world through two unmatched eyeballs. One is a passive infrared sensor, tuned to trigger the camera whenever another person passes by. The other is a wide-angle camera lens, set to capture most of the user's field of view. The device is also equipped with an ambient light sensor that triggers the camera when its user moves from one room to another, or goes in or out of doors. The camera can also be set to snap an image if the sensors haven't triggered a photo after an arbitrary number of seconds. A typical wearer might come home with 2000 to 3000 fragmentary, artless images at the end of a day.

It may be just those characteristics of the SenseCam images that make them so useful for memory rehabilitation and research, Kapur

CREDITS: MICROSOFT RESEARCH; KATALIN PAULY-TAKACS

says. Like Conway, he suspects that the reason the images stimulate memory retrieval and possibly consolidation is because they mimic "some of the representations that we have" of past events in our brains.

To move beyond the initial case study of Mrs. B, the Addenbrooke's team, under the direction of neuropsychologist Georgina Brown, has followed five additional people with memory problems over a nearly 3-year period, exploring the difference between the memory boost provided by visual and written diary-keeping. Establishing a baseline of how fast these people lose their memories, the team asked each about an event every other day for 2 weeks after the event, and then again after 1 month and after 3 months. Then they asked the patients to keep a diary of a separate event and review it every other day during an initial 2-week assessment, but not during subsequent months. Finally, patients reviewed their SenseCam's images for 2 weeks following a third event.

The preliminary results suggest that SenseCam use strengthened these patients' memories more than diary-keeping did. A full analysis of the data is in preparation, says Brown, whose team plans to submit it to the journal *Memory* for a special issue devoted to SenseCam research.

In a recent, separate study, Mrs. B has repeated a version of her trial, this time incorporating a brain scanner. Researchers compared the activity in her brain as she tried to remember events she had either reviewed in her written diary or with personal images from her SenseCam. Mrs. B recognized about 50% of images taken at an event she had studied using a diary, but 90% if she had studied images instead. And brain regions associated with autobiographical memory were more active when she recalled events she had studied using SenseCam images than when she recalled the diary-studied event, Berry and colleagues report online on 13 March in the *Journal of Neurology, Neurosurgery and Psychiatry.*

The Addenbrooke's work represents just a few patients with varying causes of memory loss, but Berry notes that worldwide there are about 30 ongoing SenseCam studies of memory patients. Adam Zeman of the University of Exeter in the United Kingdom leads one. "I think the main interest [in SenseCam] is that it gives you an opportunity to look at memory in what you might call a more ecological fashion than laboratory stimuli generally do," he says, and "it gives an opportunity to support and rehabilitate memory."

Memory walks

Normally, basic research precedes clinical studies, but the history of SenseCam has been the reverse. "The initial studies had a strong pragmatic aim," says Kapur, "but certainly once we started to collect data, [psychologists] began to look at these things from a theoretical slant." The question for cognitive scientists is whether SenseCam, or any similar wearable, point-of-view photographic device, can illuminate how healthy autobiographical memory works. Moulin, for example, has engaged volunteers to undertake memory walks in which they read a list of words while wearing the SenseCam. His student Katalin Pauly-Takacs has tested the participants' recall of the words on the day of their walks and then again 3 months later, with and without the help of SenseCam images. Their preliminary results suggest that volunteers remember more of the words from walks that they reviewed using SenseCam images.

Moulin's experiment is a nod to decades of autobiographical memory research, in which volunteers were tested on their ability to recall standard images or word lists they had previously seen. Some researchers suggest that the more personal nature of SenseCam images will be key to better studying autobiographical memory storage and retrieval. "Using SenseCam we can first, have more interesting stimuli and second, test [memory] processes that can generalize more easily to real life," explains Roberto Cabeza, a neuroscientist at Duke University in Durham, North Carolina, who is also working with the device.

Despite SenseCam's more personal touch, there are no guarantees it will break new ground in memory research. "Whether or not it will tell us different principles or something novel is unclear," says Larry Squire, a psychologist at the University of California, San Diego, who hasn't yet worked with the device.

William Brewer of the University of Illinois, Urbana-Champaign, notes that nobody really knows how best to evaluate SenseCam as a memory-consolidation aid or a retrieval cue. He and his graduate student Jason Finley have tested different aspects of memory using SenseCam images as cues, asking individuals how certain they are that they've seen an image before, or inquiring what they did after a certain image was taken. Such baseline studies, says Brewer, should help identify the most appropriate memory tests.

In addition to the seven Microsoft Research grants handed out in 2007, dozens of groups in cognitive psychology, clinical neuropsychology, education, and computer science are conducting research with borrowed SenseCams and independent funding. But there are no current plans to commercialize the hardware or the software from the SenseCam project—a fact that puzzles some fans of the device. In fact, to keep up with the growing demand for the devices, Microsoft would like to find another manufacturer willing to mass-produce the cameras, says Wood. Microsoft currently provides the cameras to only a limited number of patients under clinical supervision.

Even though he lobbies colleagues such as Moulin to try the device, Conway remains cautious about overselling SenseCam. There is still at least a decade's work ahead before "we can maximize its use for research and its use as an intervention scheme in helping failing memories," says the 56-year-old investigator. "By that time, I'll need to wear one permanently, myself."

–LUCAS LAURSEN

Lucas Laursen is a freelance writer based in Cambridge, U.K.

New source. Japan's Radioactive Isotope Beam Factory should crank out more unbound nuclei.

CREDIT: NISHINA CENTER FOR ACCELERATOR-BASED SCIENCE/RIKEN

NUCLEAR PHYSICS

Fathoming Matter's Heart Unbound

Going to extremes, physicists hunt for "unbound" nuclei that don't stick together at all

Ordinarily, the protons and neutrons in an atomic nucleus bind to one another with ferocious strength. The might of that binding explains why alchemists never found a way to change lead into gold: That would require prying apart the nucleus of one element to change it into another. Now, however, some physicists are eagerly creating odd nuclei that are so loosely built they are hardly nuclei at all. These rare beasts may provide a better understanding of the heart of matter.

In recent decades, experimenters have used particle accelerators to produce ever-more-unstable and fleeting radioactive nuclei. The new work pushes this exploration to its logical extreme with the creation of "unbound nuclei"—puffs of protons and neutrons so loosely jumbled together that there is literally nothing to keep them intact, not even momentarily. Some unbound nuclei could yield insights into stellar explosions that forge many of the heavy elements we see on Earth today. Others may stretch current theories of nuclear structure until they snap and thus yield new insights.

"In some sense, it's the most extreme test of our theories of nuclear structure," says Nigel Orr of the Laboratory for Corpuscular Physics (LPC) in Caen, France, one of three dozen physicists who gathered recently for a workshop on the subject.* Sydney Gales, director of the National Heavy Ion Accelerator (GANIL) in Caen, says: "We are discovering that there is a whole new kind of loosely formed matter. The physics is completely new."

So far, experimenters have snared a handful of the oddities. But interest in them is growing, as new accelerators now powering up or in planning should cough out many more.

Crossing the line

The study of unbound nuclei crosses a conceptual frontier. Researchers map nuclei on a chart resembling a crossword puzzle, with the number of protons increasing from bottom to top and the number of neutrons increasing from left to right (see diagram, p. 1425). The 255 stable nuclei form a diagonal "valley of stability," with their unstable radioactive brethren, less and more neutron-rich, to the left and right. In pursuing unbound nuclei, physicists strive to make nuclei ever richer in neutrons and, ultimately, to push across the "neutron drip line," beyond which binding is impossible. On the near side of this line, each nucleus can minimize its energy, at least temporarily, by forming a tight clump. On the far side, a nucleus can always reduce its energy by falling apart, so there is no energy barrier to hold the thing together.

Interest in unbound nuclei builds on the study of other strange-but-bound nuclei, says Angela Bonaccorso, a theorist with the Italian National Institute of Nuclear Physics in Pisa. In the 1980s, scientists discovered that the bound nucleus lithium-11, which has three protons and eight neutrons, possesses an unusual structure in which two of its neutrons form a diffuse "halo" roughly 10 times the radius of the nucleus's core. Oddly, one halo neutron can't stick without the other: Remove one to form lithium-10 (three protons and seven neutrons) and the other flies out, too. Lithium-10 is unbound.

This means that the drip line zigzags as unbound lithium-10 lies between bound lithium-9 and lithium-11. Similarly, unbound beryllium-13 lies between bound beryllium-12 and beryllium-14, and unbound helium-7 and helium-9 interleave with bound helium-6 and helium-8. These interlopers are barely unbound; if their lowest energy state were just slightly lower, they'd stick together.

Such unbound nuclei challenge established theories of nuclear structure. Protons and neutrons cling to one another through the strong force, and most theories assume that each particle whizzes about in a static force field determined by the average distribution of all the others. Such "mean field" models predict the existence of energy "shells"—like those for the electrons in an atom—into which the protons and neutrons stack.

In these barely unbound nuclei, the mean-field approach comes up short. That's because the precise energy of the entire system depends on the details of the continual jumbling of the protons and neutrons. In that case, the notion of a shell—which assumes that the energy can be calculated from an unchanging average distribution of the particles—is no longer strictly valid, says Horst Lenske, a theorist at the Justus Liebig University Giessen in Germany. In fact, Lenske says, whether a nucleus is bound may depend on the precise and exceedingly complicated dynamics of all the interacting protons and neutrons.

If theorists can account for these dynamics, then they might better understand all nuclei, Bonaccorso says. The basic shell model has been embellished in various ways to help account for dynamical effects and deal with specific nuclei. Insights from unbound nuclei might tie these ad hoc fixes together more coherently. "We are constructing theories that are far more general," Bonaccorso says.

Depends on how you look at it

Studying unbound nuclei is not easy, however. The experiments require intense beams of radioactive nuclei to make these rare beasts and sophisticated detection schemes to snare the fragments released as they fly apart in less than

---

*Unbound Nuclei Workshop, University of Pisa, Italy, 3–5 November 2008.

a trillionth of a nanosecond. An unbound nucleus also presents a challenge because its properties depend on how it is produced.

For example, physicists expect that lithium-10 consists of a lithium-9 core with a halo neutron whizzing around it, and they want to know the exact “state” of that far-flung neutron. To determine that, LPC’s Orr and his team fired beryllium-11 nuclei (with four protons and seven neutrons) through a carbon target in experiments at GANIL. A few of the collisions plucked one proton out of the beryllium nucleus to make a lithium-10 nucleus. That would instantly break into a lithium-9 nucleus and a neutron, and the experimenters would look for those pieces.

By measuring the energy with which the neutron and lithium-9 sped apart, researchers could probe their interactions; any pushing or shoving between them should create a peak in the energy spectrum. That spectrum would thus reveal the original state of the lithium-10 nucleus. Looking at the energy spectrum, Orr and his team found a broad peak that suggested the ejected neutron began in a state in which it had no angular momentum—a so-called s-state.

However, Haik Simon of the Helmholtz Center for Heavy Ion Research (GSI) in Darmstadt, Germany, and colleagues took a different approach to make lithium-10. They fired rare lithium-11 nuclei at a carbon target to try to knock one neutron out of the lithium nucleus. They then examined the resulting lithium-10 much as Orr did and observed an energy spectrum comprising three overlapping peaks. That suggests that the lithium-10 sometimes emerged in an s-state, sometimes in a p-state with one unit of angular momentum, and sometimes in a d-state with two units.

In spite of the incongruous results, there is an underlying consensus, Simon says. Both experiments show that, in spite of its infinitesimally brief existence, lithium-10 has a structure with well-defined energy states. They both also show that the lowest energy ground state is the s-state, as theory predicted. “Here we’re getting quite clear,” Simon says. “It has now been resolved.”

But not all unbound nuclei are so straightforward. Takashi Nakamura of the Tokyo Institute of Technology and colleagues see signs of a more complicated situation in unbound beryllium-13 (four protons and nine neutrons). In experiments at the Institute of Physical and Chemical Research’s (RIKEN’s) Nishina Center for Accelerator-Based Science in Wako, Japan, Nakamura and colleagues produced beryllium-13 by shooting beryllium-14 nuclei through a liquid hydrogen target to chip one neutron out of the incoming nucleus.

When the beryllium-13 fell apart, the researchers measured the energy spectrum of the rebounding pieces and observed a peak. But that peak seems to have the wrong energy and shape to be the expected s-state and may be a p-state, Nakamura says. That suggests that in beryllium-13, the quantum state of the beryllium-12 core is somehow altered, or “collapsed,” by the mere presence of the extra neutron, he says. Deciphering how the core is deformed is the sort of challenge theorists hope will lead to new insights.

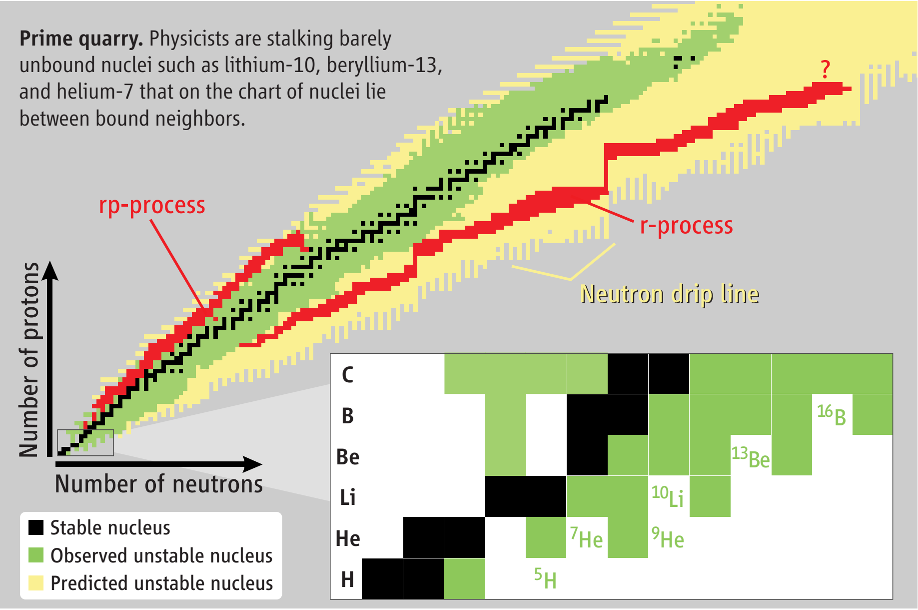

Prime quarry. Physicists are stalking barely unbound nuclei such as lithium-10, beryllium-13, and helium-7 that on the chart of nuclei lie between bound neighbors.

CREDIT: SOURCES: HENDRIK SCHATZ/NATIONAL SUPERCONDUCTING CYCLOTRON LABORATORY; INSET: NIGEL ORR/LABORATORY FOR CORPUSCULAR PHYSICS

Stellar explosions run backward

A nucleus can also become unbound if it absorbs too much energy, and such overamped nuclei may play starring roles in stellar explosions. In a blast called a nova or in a more-powerful one called an x-ray burst, heavier nuclei form when lighter ones rapidly absorb protons, in the so-called “rp-process.” For example, a magnesium-22 nucleus can absorb an energetic proton to make an aluminum-23 nucleus, which quickly spits out a photon to shed its excess energy.

Reproducing that interaction is difficult. However, RIKEN’s Tohru Motobayashi and colleagues have found an easier way to run it backward. They fire aluminum-23 nuclei through a lead target. As an aluminum nucleus passes through a lead nucleus’s electric field, it absorbs a “virtual” photon from the field. That unbinds the aluminum-23 and it splits into magnesium-22 and a proton.

The researchers measured the energy with which the magnesium-22 and proton flew away from each other. They found three overlapping peaks in the energy spectrum, the lowest at about 500 kiloelectron volts. Such details suggest that the forward process requires relatively high temperatures and densities and may play a bigger part in more-energetic explosions. “Our result implies that this process does not contribute so much to the nova but that it is important for the x-ray burst,” Motobayashi says.

The study of unbound nuclei is likely to grow, given the new facilities coming online or in planning, researchers say. Two years ago, the Nishina Center revved up the massive superconducting cyclotron that powers the lab’s Radioactive Isotope Beam Factory (*Science*, 15 December 2006, p. 1678). When fully functional, it will provide beams more than 1000 times as intense as those at older facilities. GSI is building a synchrotron-based facility that will power up in the middle of the next decade (*Science*, 2 November 2007, p. 738), and in December 2008, the U.S. Department of Energy chose Michigan State University in East Lansing to host its proposed linear-accelerator-based facility (*Science*, 19 December 2008, p. 1777).

With much more intense beams, researchers should be able to climb drip lines to make unbound elements up to aluminum or silicon, says Tokyo Tech’s Nakamura. Motobayashi says it should also be possible to study overenergized nuclei involved in an astrophysical progression called the r-process, in which lighter nuclei gobble up neutrons and which is thought to forge half the nuclei heavier than iron.

Exactly what unbound nuclei will reveal remains to be seen. Of course, the allure of the unknown is also leading nuclear physicists to test the bounds of their field. **–ADRIAN CHO**

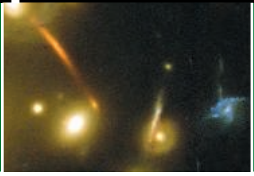

LETTERS

edited by Jennifer Sills

A National Initiative for Social Participation

THE TRANSFORMATIVE POWER OF THE INTERNET IS MORE THAN ACCESS TO INFORMATION; it is increasingly about contributing, collaborating, and participating. Metaphors based on information highways are giving way to community visions that capture the remarkable enthusiasm for user-generated content and social media. At the same time, President Obama is calling for civic service and personal responsibility to rebuild America. Combining these ideas could promote the shift from playful, discretionary Internet usage to larger, more serious projects aligned with national priorities such as health care, community safety, education, and innovation.

The good news is that there are many promising social action networks, but these nascent explorations could be greatly accelerated by an organized research program. This program would systematically study the emerging phenomena, determine the sources of success or failure, and disseminate best practices. The payoffs are large enough to warrant an intense national effort akin to NASA's space program or the National Institutes of Health.

Health discussion groups have long been one of the Internet's success stories. Now, clever entrepreneurs are exploring new social participation ideas with projects such as the www.PatientsLikeMe.com Web site, where users offer their medical experiences in the hope of learning about treatment outcomes from one another. At the same time, these users are building a remarkable resource for medical research and discovery. Physicians have already discussed 30,000 cases at www.sermo.com, where they can offer insights about innovative treatments as well as detect unusual disease patterns. Large corporations also recognize the opportunities and are inviting users to store their medical histories in the Microsoft Health Vault or at Google Health.

CREDIT: JUPITERIMAGES

Although social networking plays only a small role in national security, community safety could be enormously improved by expanding resident reporting systems, such as www.WatchJeffersonCounty.net, which collects reports of unusual behaviors. These reports provide important clues for civic officials to prevent crimes, control teenage gangs, or simply fix potholes. A huge success, now run by the U.S. Department of Justice, is the Amber Alert reporting system for abducted children. Beyond the 430 cases they claim to have helped solve, the awareness generated among 7 million participants may have prevented many more abductions. Web sites for reporting extreme weather effects, such as Storm Watchers typically run by local radio and television stations, are being joined by reporting schemes for earthquake damage, influenza outbreaks, food poisoning, and other community problems. The micro-blogging tool Twitter is now rapidly spreading, as users from Orange County firefighters to Mumbai police post their 140-character messages about where they are and what they are doing.

Reading Wikipedia articles is now a common tactic for learners of all ages, but the stronger boost to education comes when students start writing Wikipedia articles. They become engaged in the social process of commenting on each other's work, arguing over quality criteria, and discussing what needs to be added. E. O. Wilson's dream of the Encyclopedia of Life, with a Web page for each of Earth's 1.8 million species, is on its way to becoming a citizen science success story that raises environmental awareness. Even YouTube, whose success was spiked by playful videos, is becoming the go-to educational resource and the place for students to post their term projects. These and many other initiatives are based on the collect-relate-create-donate mantra that suggests education happens when students start by collecting information, then move on to working in teams to create ambitious projects for the benefit of someone outside their classroom.

Innovation itself is getting turbocharged by going social. Open-source software projects are now taken seriously by big companies who claim greater reliability for programs that have been tested and read by millions of eyes. Open innovation is gaining similar credibility as corporate research directors who post their problems on www.Innocentive.com get hundreds of serious solutions from diverse creative types. Bloggers are influencing every profession as these self-appointed information gatekeepers post hourly updates about what's new, thereby stimulating rapid progress on emerging problems and getting a jump on the news media.

The benefits of social media participation are well understood by Obama's staff—during the campaign, they engaged 4 million donors and volunteers. To replicate their success, a National Initiative for Social Participation could stimulate effective collaborations in many professions, restore community social capital, and coordinate national service projects. The challenge is to understand what motivates participants, such as altruism, reputation, or community service. Researchers would have to develop fresh strategies that increased the conversion rates from readers to contributors from the currently typical 100 to 1 to much higher rates. Getting contributors to collaborate for ambitious efforts and to become leaders or mentors are further challenges. Coping

Letters to the Editor

Letters (~300 words) discuss material published in *Science* in the previous 3 months or issues of general interest. They can be submitted through the Web (www.submit2science.org) or by regular mail (1200 New York Ave., NW, Washington, DC 20005, USA). Letters are not acknowledged upon receipt, nor are authors generally consulted before publication. Whether published in full or in part, letters are subject to editing for clarity and space.

Westerlies go south

1434

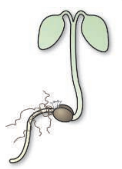

Plant sperm signals

1439

with legitimate dangers such as privacy violations, misguided rumors, malicious vandalism, and infrastructure destruction or overload all demand careful planning and testing of potential solutions.

The huge research effort required for a National Initiative for Social Participation would tap the skills of computer scientists to build scalable and reliable systems, interface designers to accommodate diverse user needs, and social scientists to study successes and failures. The risks are substantial, but the payoffs could be enormous. **BEN SHNEIDERMAN**

Department of Computer Science, University of Maryland, College Park, MD 20742, USA. E-mail: ben@cs.umd.edu

Note

1. To participate in this initiative, join the Facebook group named iparticipate.

Indian Neutrino Detector: The Elephant in the Room

THE VERY SERIOUS ENVIRONMENTAL IMPLICAtions of establishing the India-based Neutrino Observatory (INO) in Singara within the Nilgiri Biosphere Reserve and in the buffer zone of the Mudumalai Tiger Reserve ("Indian neutrino detector hits snag on environmental concerns," P. Bagla, News of the Week, 9 January, p. 197) must be recognized if India is to save its most viable Asian elephant population from extinction. This population has declined so precipitously over the past three decades due to poaching and habitat loss that it is on the verge of collapse (*1*). Fully mature Tuskers (bulls) have become very rare in this range. The study of the smallest particles on Earth, neutrinos, should not justify driving the last viable Asian elephant herd and tiger population in India into extinction. **MICHAEL W. FOX**

Global Communications for Conservation Inc., New York, NY 10155, USA. E-mail: ipan@erols.com

Reference

1. R. Bandara, *South Asia Econ. J.* **5**, 283 (2004).

Indian Neutrino Detector: Environmental Costs

I WOULD LIKE TO SPELL OUT THE ENVIRONMENtal costs of building the India-based Neutrino Observatory (INO) discussed in the News of the Week story "Indian neutrino detector hits snag on environmental concerns" (P. Bagla, 9 January, p. 197). The first foreseeable impact would be a sizable increase in the human population, furthering habitat destruction. Transporting the estimated 630,000 tons of debris and 147,000 tons of construction material would require about 156,000 truck trips through a vital protected area. INO would require 320,000 liters of water per day, further draining a drought-prone region. The Environmental Impact Assessment (*1*) upon which this project was approved was not based on scientific data and is widely acknowledged as being seriously flawed (*2*).

The international scientific community should be aware that the INO project is not site specific—in theory, a neutrino observatory can be located in any underground site with sufficient rock cover. There was no attempt to find suitable sites in less critical areas. The INO team limited its search to only two sites: Rammam in Darjeeling and Singara in the Nilgiri Biosphere Reserve. Because Rammam is in an area of higher seismic activity, the team selected Singara.

PRIYA DAVIDAR

Department of Ecology and Environmental Sciences, Pondicherry University, Puducherry 605 014, India. E-mail: pdavidar@gmail.com

References

1. P. A. Azeez, S. Bhupathy, P. Balasubramanian, R. Chandra, P. P. Nikhilraj, "India-based Neutrino Observatory—Rapid EIA" (SACON report, 2007).
2. A. Desai, P. Davidar, J.-P. Puyravaud, G. Srinivasan, N. Mohanraj, T. Thekaekara, "Environmental concerns around the proposed site for the India-based Neutrino Observatory" (NBR Alliance report, 2008); www.nbralliance.org/downloads/environmental-concerns-around-ino-site.pdf.

Response

THE PROPOSED INDIA-BASED NEUTRINO Observatory (INO) (*1*) would be located in Singara, which is 7 to 15 km from the boundary of the Mudumalai Wildlife Sanctuary in the Nilgiri Biosphere Reserve. The INO collaboration is fully committed to protecting the environment and wildlife and will take all possible steps to minimize the impact during the construction of the underground laboratory. During the operation phase, it is expected to have no impact at all.

Regarding population growth, the laboratory will be located deep underground and accessed by a tunnel 2 km in length. Researchers will be located at the main INO research and development center in the city of Mysore, about 100 km away. Except during the construction phase, the number of scientists and engineers manning the laboratory will be kept at a bare minimum (at most 30 people). The present population of Masinagudi village area, in which the project will be housed, is 12,535. INO will not significantly increase this population.

The initial site survey was conducted over a period of 5 years with the assistance of geologists and engineers. The two sites mentioned by Davidar were selected for more serious study. The Singara site was chosen over Rammam on the basis of a geotechnical analysis that considered physics requirements, safety, and long-term stability of the laboratory. About 13 km of tunnels have been constructed over the past decade in the vicinity of the proposed INO site to locate a large underground hydroelectric power station whose access portal is within a few hundred meters of the proposed INO tunnel portal. Due to the proximity of this hydroelectric power station, we do not have to build any new roads, thereby causing minimum damage to the environment.

Regarding transport of material, about 608,000 tons of debris (mainly granite) will be excavated. However, this debris will be stored onsite for a long time. About 35,000 tons of construction material and 51,000 tons of detector material (86,000 tons in all) will be brought into the site over a period of 7 years. The heavy-vehicle traffic required to do so will be no more than six round trips per day over a period of 7 years, which is negligible compared with the existing traffic. The major concern with the transportation of this material is that the access road to the INO site cuts through an elephant corridor. To address this, we plan to restrict the traffic to six round trips a day during daylight hours.

The water requirement is 342,000 liters of water per day, which is 0.2% of the availability at the Singara diversion weir (68,086 million liters of water available per annum). The INO project has been engaged in talks with the local people to clarify these issues, and the local village administration has passed a resolution welcoming the INO project.

The INO project is a pure science laboratory and not an industry. We believe that it is possible to build and run the underground laboratory to explore the working of nature without damaging it. INO is both an opportunity and a challenge to be a model project that combines pure science research with sensitivity to its local ecology and environment.

NABA K. MONDAL

Tata Institute of Fundamental Research, Homi Bhabha Road, Mumbai 400005, India. E-mail: nkm@tifr.res.in

Reference

1. India-based Neutrino Observatory (www.imsc.res.in/~ino).

CORRECTIONS AND CLARIFICATIONS

Reviews: "The psychology of transcending the present" by N. Liberman and Y. Trope (21 November 2008, p. 1201). On page 1203, the legend to Fig. 3 should read as follows: "Items from the Street Gestalt Completion Test (courtesy of Teachers College, Columbia University)." The text referring to the figure should be changed to "the Gestalt Completion Test (Fig. 3), see also (*11*)."

Reviews: "Oxytocin, vasopressin, and the neurogenetics of sociality" by Z. R. Donaldson and L. J. Young (7 November 2008, p. 900). The peptide sequence annepressin should have been referred to as annetocin to be consistent with previous literature.

TECHNICAL COMMENT ABSTRACTS

COMMENT ON "Detection, Stimulation, and Inhibition of Neuronal Signals with High-Density Nanowire Transistor Arrays"

Peter Fromherz and Moritz Voelker

Patolsky *et al.* (Reports, 25 August 2006, p. 1100) used silicon nanowires to record action potentials in rat neuronal axons and found increases in conductance of about 85 nanosiemens. We point out that the data correspond to voltage changes of about –85 millivolts on the nanowire and that conceivable mechanisms of axon-nanowire interaction lead to signals that are opposite in sign or smaller by orders of magnitude.

Full text at www.sciencemag.org/cgi/content/full/323/5920/1429b

RESPONSE TO COMMENT ON "Detection, Stimulation, and Inhibition of Neuronal Signals with High-Density Nanowire Transistor Arrays"

Brian P. Timko, Fernando Patolsky, Charles M. Lieber

Fromherz and Voelker make incorrect assumptions about our experiments that raise serious questions about the validity of their claims. We show that our calibrated signals are consistent with previously published data and a general model with biophysically relevant parameters. Additionally, the wide variation in previously published signal amplitudes suggests caution in applying and drawing conclusions from the models of Fromherz and Voelker.

Full text at www.sciencemag.org/cgi/content/full/323/5920/1429c

Comment on "Detection, Stimulation, and Inhibition of Neuronal Signals with High-Density Nanowire Transistor Arrays"

Peter Fromherz* and Moritz Voelker

Patolsky *et al*. (Reports, 25 August 2006, p. 1100) used silicon nanowires to record action potentials in rat neuronal axons and found increases in conductance of about 85 nanosiemens. We point out that the data correspond to voltage changes of about –85 millivolts on the nanowire and that conceivable mechanisms of axon-nanowire interaction lead to signals that are opposite in sign or smaller by orders of magnitude.

Patolsky *et al*. described how they stimulated, recorded, and modified action potentials (AP) in dendrites and axons of rat neurons using p-type silicon nanowires (NW) (*1*, *2*). As discussed below, we have concerns about the sign and amplitude of the recordings they reported.

The recordings were presented as changes of NW conductance, with an average increase of 85 nS [figure S3 in (*1*)]. The authors emphasized the proportionality of changes in NW conductance and intracellular (IC) potential "because the relative potential at the outer membrane becomes more negative and then more positive (opposite to the measured IC potential)." They pointed out that the typical active junction area for devices is "three orders of magnitude smaller than microfabricated electrodes and planar FETs [field-effect transistors]." No value was presented for the extracellular potential, and no explanation was given for why a small size is advantageous. Here, we describe a voltage calibration of the data and then try to explain the data by various mechanisms.

NWs work similar to electrolyte-oxide-semiconductor (EOS) FETs (*1*, *3*). A voltage change ΔV_{NW} along their length L = 2.6 to 3 μm induces a conductance change $\Delta G_{NW}/\Delta V_{NW} = -\mu_p\ C_{NW}/L$ that is –3.7 to –4.3 nS/mV for $C_{NW} = 2.8{\cdot}10^{-10}\ \mathrm{F/m}$ and $\mu_p = 400\ \mathrm{cm^2/Vs}$. That value can be verified from the experimental pH effect $\Delta G_{NW}/\Delta pH \approx 100 \pm 20\ \mathrm{nS/pH}$ (*2*). Assuming a Nernstian sensitivity –59 mV/pH of the surface potential, we obtain –1.7 nS/mV. With a sub-Nernstian sensitivity of –30 mV/pH, common for silicon dioxide (*4*), we get –3.3 nS/mV.

An axon with a diameter d_{axon} = 0.6 to 1 μm affects only a fraction of the NW (*1*). The local voltage change ΔV_J yields a conductance change $\Delta G_{NW}/\Delta V_J = (d_{axon}/L){\cdot}\Delta G_{NW}/\Delta V_{NW}$ that is around –1 nS/mV. Thus, recordings of +85 nS correspond to voltage changes of about –85 mV. This value is rather large compared with recordings using micropipettes (*5*), microfabricated metal electrodes (*6*), or planar transistors (*7*). For example, beneath the soma of individual rat neurons (E19), EOSFETs recorded about ±300 μV after 1 to 2 weeks in serum-free medium on oxidized silicon with polylysine, culture conditions similar to those in (*1*).

To explain their data, Patolsky *et al*. (*1*) used a circuit with a seal resistance between NW and axon, a membrane capacitance, and a leakage conductance [figure S10 in (*1*)]. They estimated an increase in NW conductance of 13 to 47 nS (μS is obviously a typing error) but did not explain how they arrived at that value. If membrane leakage dominates, the inward current in the resting state would be lowered during the AP. There would be a positive ΔV_J proportional to the AP (*8*). The NW conductance would decrease, opposite to the data. For a dominating capacitive current, ΔV_J would be the first derivative of the AP (*8*), apparently incompatible with the data. If the seal resistance were extremely high, because the NW touches the lipid bilayer of the axon, the change of the IC voltage ΔV_M = +100 mV would act by a field effect across a bilayer/oxide stack with a positive voltage change $\Delta V_J = \Delta V_M c_M/(c_M + c_{OX})$ on the NW due to the serial capacitances of membrane and oxide (*9*). The NW conductance would decrease, opposite to the data in (*1*).

A negative ΔV_J could be induced by a sodium inward current that flows along the seal resistance. We estimated its amplitude, even though the signal would not mirror the IC signal (*10*). Let us assume that the NW forms a linear junction on the axon with a width d_J = 20 nm, given by the diameter of the NW, and a sheet resistance r_J. The balance of current (*8*) is described by $-r_J^{-1} d^2 \Delta V_J/dx^2 = g_{JM}^{Na}(V_M - V_0^{Na} - \Delta V_J)$ with a conductance g_{JM}^{Na} and a reversal voltage V_0^{Na}. For boundary conditions $\Delta V_J = 0$ at the edges, ΔV_J is expressed by hyperbolic functions. With $\tilde{d}_J = d_J\sqrt{g_{JM}^{Na} r_J/4}$, the average is $\langle \Delta V_J \rangle = (V_M - V_0^{Na})(1 - \tilde{d}_J^{-1} \tanh \tilde{d}_J)$ and $\langle \Delta V_J \rangle \approx (V_M - V_0^{Na}) g_{JM}^{Na} r_J d_J^2/12$ for small signals. During an AP, the Na conductance may rise to $g_{JM}^{Na} = 50\ \mathrm{mS/cm^2}$ at a driving force $V_M - V_0^{Na} \approx -50\ \mathrm{mV}$. When we use r_J = 10 MΩ/square for rat neurons on oxidized silicon with polylysine (*11*), we obtain $\langle \Delta V_J \rangle \approx -8\ \mathrm{nV}$. Alternatively, we assume that a linear junction is formed between axon and substrate of a width d_J = 0.6 μm, given by the diameter of the junction, and the NW as an embedded probe. We get $\langle \Delta V_J \rangle \approx -7\ \mu\mathrm{V}$. In both configurations, the estimated signals are far smaller that the –85 mV reported in (*1*). Tens of millivolts could only be obtained with sheet resistances of 50,000 GΩ and 30 GΩ, respectively. In such junctions, ion currents would be suppressed and a signal generation by Na current would cease.

Two further remarks on the Na current mechanism may be helpful. First, for comparison, we consider a circular junction as it was used to describe the coupling of transistors to axon stumps of leech neurons and somata of rat neurons (*7*, *10*). The average signal is $\langle \Delta V_J \rangle \approx (V_M - V_0^{Na}) g_{JM}^{Na} r_J d_J^2/32$ (*12*). For a typical diameter d_J = 17 μm (*7*, *10*) and other parameters as above, we obtain $\langle \Delta V_J \rangle \approx 2.3\ \mathrm{mV}$ in good agreement with observed recordings in the millivolt range (*7*, *10*). Unlike the soma/transistor junction, the NW/axon and axon/substrate junctions are much smaller. Consequently, as the signals scale with the squared diameter of the junction, the expected signals in NW/axon or axon/substrate junctions are smaller by orders of magnitude. Second, the estimated amplitude of –7 μV for axon/substrate junctions is an upper limit for a rather high Na conductance as it may occur in mature rat neurons (3 to 4 weeks in culture). Younger neurons (1 to 2 weeks old) exhibit a lower expression of Na channels. Accordingly, the observed amplitudes were about –300 μV in soma/transistor junctions, compared with –3 mV for mature neurons (*7*). Considering the short culture time (4 to 8 days) in (*1*), the expected amplitudes are lower than –7 μV, and the discrepancy to the reported –85 mV becomes even larger.

As further alternatives, we consider two electrostatic models: (i) When ion channels open, gating charges are displaced across the membrane. A NW within the Debye length of the electrolyte may be affected by a field effect. The gating kinetics during an AP are well known (*13*). A change of NW conductance that matches the AP is impossible. (ii) An increase of NW conductance can be caused by a drop of the negative surface potential on silicon dioxide (*4*), as it may be induced by a dissociation of protons (*4*) or other cations. A change of –85 mV implies an increase by three pH units at a sensitivity of –30 mV/pH. Generally, proton channels open for outward current, thus lowering the extracellular pH (*14*). Further, gating of proton channels and proton binding to silicon dioxide (*15*) are slow, such that ion binding would not follow an AP.

As the mechanisms discussed so far fail to explain the data in (*1*), one might resort to an unknown "nanoscale" process involving NW/axon interactions on a molecular level. As the electrical

---

Department of Membrane and Neurophysics, Max Planck Institute for Biochemistry, D82152 Martinsried/Munich, Germany.

*To whom correspondence should be addressed. E-mail: fromherz@biochem.mpg.de

effects of neurons (ion current, gating charges) rely on single protein molecules, their inherent stochastic dynamics would inevitably translate to a stochastic modulation of NW conductance, in contrast to the reported smooth modulation. To explain the data, a "nanoscale" mechanism would have to mediate the deterministic AP to a deterministic change of NW conductance without introducing stochastic effects. It cannot rely on a small number of molecules. Effects of macroscopic parameters, however, have been shown above to be incompatible with the data.

In conclusion, on the basis of common neurophysiology, surface science, and semiconductor physics, we are not able to find a physical rationale for the sign and amplitude of the NW recordings described by Patolsky *et al*. (*1*).

References

1. F. Patolsky *et al*., *Science* **313**, 1100 (2006).
2. Corrections and Clarifications, Reports, F. Patolsky *et al*., *Science* **317**, 320a (2007).
3. Y. Cui, Q. Wei, H. Park, C. M. Lieber, *Science* **293**, 1289 (2001).
4. M. Borkovec, B. Jönsson, G. J. M. Koper, in *Surface and Colloid Science, Vol. 16,* E. Matijevic, Ed. (Kluwer Academic, New York, 2001).
5. E. Claverol-Tinture, J. Pine, *J. Neurosci. Methods* **117**, 13 (2002).
6. Y. Nam, J. C. Chang, B. C. Wheeler, G. J. Brewer, *IEEE Trans. Biomed. Eng.* **51**, 158 (2004).
7. M. Voelker, P. Fromherz, *Small* **1**, 206 (2005).
8. R. Weis, P. Fromherz, *Phys. Rev. E Stat. Phys. Plasmas Fluids Relat. Interdiscip. Topics* **55**, 877 (1997).
9. R. F. Pierret, *Semiconductor Device Fundamentals* (Addison-Wesley, Reading, MA, 1996).
10. R. Schätzthauer, P. Fromherz, *Eur. J. Neurosci.* **10**, 1956 (1998).
11. D. Braun, P. Fromherz, *Biophys. J.* **87**, 1351 (2004).
12. M. Schmidtner, P. Fromherz, *Biophys. J.* **90**, 183 (2006).
13. B. Hille, *Ion Channels of Excitable Membranes* (Sinauer, Sunderland, MA, ed. 3, 2001).
14. T. E. Decoursey, *Physiol. Rev.* **83**, 475 (2003).
15. P. Woias, L. Meixner, D. Amandi, M. Schönberger, *Sensors Actuators B* **24**, 211 (1995).

18 January 2008; accepted 17 February 2009
10.1126/science.1155416

Response to Comment on "Detection, Stimulation, and Inhibition of Neuronal Signals with High-Density Nanowire Transistor Arrays"

Brian P. Timko,[1] Fernando Patolsky,[2] Charles M. Lieber[1,3]*

Fromherz and Voelker make incorrect assumptions about our experiments that raise serious questions about the validity of their claims. We show that our calibrated signals are consistent with previously published data and a general model with biophysically relevant parameters. Additionally, the wide variation in previously published signal amplitudes suggests caution in applying and drawing conclusions from the models of Fromherz and Voelker.

Patolsky *et al.* (*1*) used arrays of silicon nanowire field-effect transistors to record neuronal signals along the individual axons and dendrites of cortical rat neurons. In their comment (*2*), Fromherz and Voelker claim that a physical rationale cannot be found for our recordings. However, there are three substantial deficiencies in their assumptions and analysis that raise doubts about the validity of their claims. First, Fromherz and Voelker make incorrect conclusions about the properties of our nanowire field-effect transistor (NWFET) devices and report signals that lead to greater than one order of magnitude error in the estimated voltage signals in our experiments. Second, they carry out analyses with models that either have no physical relevance to our experiments or use rigid parameters that cannot explain their own related published work. Third, the authors may not recognize the complexity of the interfaces between cells and conventional planar as well as newer nanoelectronic devices, which correspondingly leads to uncertainties in parameters used to describe such interfaces. Below, we address these three issues and show that (i) the average signal changes reported in our work yield calibrated voltages within the range of values reported for related studies using planar transistors by Fromherz and co-workers (*3*–*5*) and others (*6*), and that (ii) a general model applicable to our experiments and reported ranges of biophysical parameters yields signals consistent with our published results.

Central to the critique of Fromherz and Voelker (*2*) is their claim that our recorded signals correspond to a change of about –85 mV at the NW surface. This claim arises from their assumption that the NWFETs have a calibration factor of 1 nS/mV and that the typical recorded signal is 85 nS; unfortunately, neither of these assumed values is correct. First, the transconductance value used by Fromherz and Voelker to convert our measured signals to an estimated voltage is based on some of the earliest devices published by our group in 2001 (*7*) and estimated values for oxide capacitance (C_{ox}) and hole-carrier mobility (μ). Given the substantial improvements in NWFET performance since this initial work (*8*–*10*), the Fromherz and Voelker assumption is not representative of devices produced after 2001. Below, we show that their assumption is conservatively an order of magnitude too small. Second, the results shown in figure 1 to 4 of (*1*) yield an average ± 1 standard deviation (SD) of 66 ± 21 nS for the signal change recorded by the NWFETs. Thus, the recorded signal value used by Fromherz and Voelker barely lies within +1 SD of those shown and is not statistically representative.

The device sensitivity can be assessed experimentally without assumptions. Data for two NWFETs representative of those used in (*1*) yield device sensitivities, $\Delta G/\Delta V_g$, of 7 and 15 nS/mV (fig. S1). This measured range of sensitivity values is substantially above the estimate of Fromherz and Voelker. The low value they estimated can be attributed in large part to the small value of C_{ox} used, which contrasts both calculated and experimental results (*11*, *12*). A calculated value of $C_{ox} = 2.3 \times 10^{-9}$ F/m, which is in good agreement with measured values (*11*, *12*), yields a maximum sensitivity of 30 nS/mV for a device with the same geometry and carrier mobility as in (*1*) [see Supporting Online Material (SOM)]. Experimentally measured sensitivities of 20 to 30 nS/mV, which are substantially larger than the 10 nS/mV used in our analysis, have also been reported in recent studies (*10*).

Based on these results, we used a conservative calibration factor for the cell/substrate interface ($\Delta G/\Delta V_J$) of –10 nS/mV and the average NWFET/neuron conductance change of 66 nS from (*1*) to obtain a voltage ΔV_J = –6.6 mV, not –85 mV as claimed by Fromherz and Voelker (*2*). We note that this calibration is a reasonable approximation, but assuming the higher device sensitivity as reported recently for NWs prepared in a similar manner (*10*) would imply even smaller ΔV_J values of between –3.3 and –2.2 mV. Our calculated voltage, which is independent of the size of the device used for recording, is similar to values from at least three independent studies published by Fromherz and co-workers where ΔV_J values up to 8 mV were reported (*3*–*5*), and substantially smaller than the 30 mV value shown by Cohen *et al.* with mechanical pressure (*6*). For completeness, we tabulated the $>10^3$ range of voltage values reported by Fromherz and others for FET recording from neurons (table S1) and return to the important implications of this large range below. Therefore, the signals reported in (*1*) are consistent with values published in the literature, in contrast to the claims of Fromherz and Voelker.

Fromherz and Voelker (*2*) use models as a major basis for their claims, but their analysis has two important shortcomings. First, their models based on ultra-small junctions, pH changes, and capacitance are physically untenable and/or not applicable to our measurements. For example, the models and parameters used to criticize our work would show that many of the signals published by Fromherz and co-workers likewise lack a physical rationale (see SOM for detailed discussion about the validity of models). Second, for the current flow model relevant to our experiments, Fromherz and Voelker make questionable choices for parameters to give a maximum value of –7 μV. The value they chose for Na^+-channel conductance per unit area was for the soma and not the axon, the latter of which is known to have a much larger value (*13*, *14*). Their selected value for r_J, which has not been measured in the specific case of axons, lies at the low end of a range that spans 10^4 (*15*, *16*). In addition, another group not cited in (*2*) was unable to fit their opposite sign signals (*17*) and, thus, had to derive an entirely different model from Fromherz and Voelker to explain their data. Last, Fromherz and co-workers have measured both +4 and –4 mV signals simultaneously from two devices under the same cell. To qualitatively rationalize these signals, they invoke an inhomogeneous ion-channel distribution model (*3*). The models applied to our work, however, assume uniform average parameters, which cannot explain their results.

We find that the general current-flow model described by Fromherz and Voelker and the reported ranges of biophysical parameters yield signals consistent with our experiments. Specifically, the approximate potential change at the NWFET can be calculated from $\langle \Delta V_J \rangle = (V_M - V_0^{Na})(1 - \tilde{w}_J^{-1} \tanh \tilde{w}_J)$, where $\tilde{w}_J = w_J\sqrt{r_J g_{JM}^{Na}/4}$. Using $w_J = 1$ μm, the estimated axon width crossing a NWFET, a reasonable

---

[1] Department of Chemistry and Chemical Biology, Harvard University, Cambridge, MA 02138, USA. [2] School of Chemistry, Tel Aviv University, Tel Aviv 69978, Israel. [3] School of Engineering and Applied Sciences, Harvard University, Cambridge, MA 02138, USA.

*To whom correspondence should be addressed. E-mail: cml@cmliris.harvard.edu

value for the Na^+-channel conductance of g_{JM}^{Na} = 200 mS/cm^2 (*13*, *14*), a mid-range sheet resistance of r_J = 300 MΩ/square (*15*, *16*), and $(V_M - V_0^{Na})$ = –50 mV yields $\langle \Delta V_J \rangle$ = –2.4 mV. This value is within a factor of 2 to 3 of our experimental value, –6.6 mV, and values reported by Fromherz and co-workers (*3*–*5*). Therefore, estimates using parameters within published biophysical ranges yield modeled signals consistent with those reported in (*1*).

It is important to emphasize that the interfaces between cells and devices have significant variability, which necessarily leads to considerable uncertainty in parameters used to describe these interfaces and correspondingly suggests caution in using and drawing conclusions from the models proposed by Fromherz and Voelker. A review of published data (table S1 and SOM text) shows that measurements from the same types of neurons and devices have yielded variations in signal amplitude of 400 and sometimes more. In certain cases, the values have been modeled, but not a priori predicted, by adjusting parameters, although other work published by Fromherz and co-workers and other groups could not be explained by their standard variation of parameters (*5*). This variability should not be surprising given that a living cell is a dynamic entity that will respond to the local environment of a device surface to yield, for example, inhomogeneous distributions of ion channels (*3*). In (*5*), Fromherz and Voelker invoke an argument of enhanced ion channels to qualitatively explain their larger signals, yet parameters such as those chosen to criticize our work cannot explain their own recordings. In our own experiments, the NWFET device protrudes above the plane of the substrate surface (fig. S2), and the nonuniform NW-neuron interactions could lead to larger signals due to recruitment and enrichment of ion channels (*18*) or enhanced local pressures at the NW-neuron interface (*6*). Notably, recent studies of cultured rat neurons on carbon nanotubes show that these nanoscale wires generate tighter junctions than expected for typical planar substrates (*19*). Therefore, we can conclude that (i) in general, cell-device interfacial properties are highly variable, (ii) interfacial parameters could be enhanced by stronger interactions with nanostructured surfaces, such as NWFETs, and (iii) together these points challenge the rigid choice of parameters used by Fromherz and Voelker to justify their claims.

We have shown that the average signal changes reported in our work yield calibrated voltages within the range of values reported by several groups and thus conclude that our results are both physically reasonable and consistent with expectations from the existing literature. We have also shown that a current-flow model and reported ranges of biophysical parameters yield signals consistent with our experimental results. However, we emphasize that parameters used to describe the interfaces between cells and conventional planar or our nanoscale devices have substantial uncertainty, and thus we suggest caution in using and drawing conclusions from the models proposed by Fromherz and Voelker.

References and Notes

1. F. Patolsky *et al.*, *Science* **313**, 1100 (2006).
2. P. Fromherz, M. Voelker, *Science* **323**, 1429 (2009); www.sciencemag.org/cgi/content/full/323/5920/1429b.
3. A. Lambacher *et al.*, *Appl. Phys. A.* **79**, 1607 (2004).
4. M. Merz, P. Fromherz, *Adv. Funct. Mater.* **15**, 739 (2005).
5. M. Voelker, P. Fromherz, *Small* **1**, 206 (2005).
6. A. Cohen, J. Shappir, S. Yitzchaik, M. E. Spira, *Biosens. Bioelectron.* **23**, 811 (2008).
7. Y. Cui, Q. Wei, H. Park, C. M. Lieber, *Science* **293**, 1289 (2001).
8. F. Patolsky *et al.*, *Proc. Natl. Acad. Sci. U.S.A.* **101**, 14017 (2004).
9. G. Zheng, F. Patolsky, Y. Cui, W. U. Wang, C. M. Lieber, *Nat. Biotechnol.* **23**, 1294 (2005).
10. B. P. Timko *et al.*, *Nano Lett.* **9**, 914 (2009).
11. D. J. Griffiths, *Introduction to Electrodynamics* (Prentice Hall, Englewood Cliffs, NJ, 1999).
12. R. Tu, L. Zhang, Y. Nishi, H. Dai, *Nano Lett.* **7**, 1561 (2007).
13. L. G. Nowak, J. Bullier, *J. Exp. Brain Res.* **118**, 477 (1998).
14. M. H. P. Kole *et al.*, *Nat. Neurosci.* **11**, 178 (2008).
15. V. Kiessling, B. Müller, P. Fromherz, *Langmuir* **16**, 3517 (2000).
16. D. Braun, P. Fromherz, *Biophys. J.* **87**, 1351 (2004).
17. A. Cohen, J. Shappir, S. Yitzchaik, M. E. Spira, *Biosens. Bioelectron.* **22**, 656 (2006).
18. V. Lovat *et al.*, *Nano Lett.* **5**, 1107 (2005).
19. G. Cellot *et al.*, *Nat. Nanotechnol.* **4**, 126 (2009).
20. Harvard University has applied for a patent based on the work described in (*1*).

Supporting Online Material

www.sciencemag.org/cgi/content/full/323/5920/1429c/DC1
SOM Text
Figs. S1 and S2
Table S1
References

25 February 2008; accepted 2 March 2009
10.1126/science.1155917

PHYSICS

Giant Ring on the Prairie

Robert W. Seidel

Fermilab
Physics, the Frontier, and Megascience

by Lillian Hoddeson, Adrienne W. Kolb, and Catherine Westfall

University of Chicago Press, Chicago, 2008.
513 pp. $45, £31.
ISBN 9780226346236.

Few readers of *Science* will be unaware of the Fermi National Laboratory and its programs. Like Ernest Lawrence's Radiation Laboratory, Brookhaven National Laboratory, and CERN, it is a pioneering institution in high-energy physics. Until the Large Hadron Collider at CERN goes into operation, it will continue to lead the field in terms of the energy of its accelerator, the Tevatron. Unlike those institutions, however, Fermilab has, until now, lacked a history worthy of its accomplishments and historical significance.

Therefore, it is delightful to have in hand and to read the work of historians Lillian Hoddeson, Adrienne Kolb, and Catherine Westfall. *Fermilab* weaves their accounts into a coherent narrative in limpid prose that should be accessible to anyone with an interest in the history of late-20th-century science. Although the laboratory engaged in a number of highly technical projects, the authors lead the reader through those faithfully without sacrificing the essence of the laboratory's ambitions and accomplishments. Their artful depiction of the origins and growth of the laboratory under its first two directors, Robert R. Wilson and Leon M. Lederman, makes clear the challenges Fermilab faced in achieving leadership in high-energy physics despite difficult political and scientific fortunes.

The site in 1977. Main ring.

The origins of Fermilab, explored extensively by Catherine Westfall in her Ph.D. dissertation, form the focus of the book's first chapters. One of the casualties of Cold War competition in high-energy physics was the Midwest Universities Research Association's plan for an advanced accelerator, which fell victim to the Joint Committee on Atomic Energy's desire to exceed the energy of a 10-GeV Soviet accelerator by instead constructing a 12-GeV proton synchrotron at Argonne National Laboratory. After the high-energy physics community, acting through the Atomic Energy Commission (AEC), supported the Lawrence Radiation Laboratory's design of a 200-GeV machine and Stanford's 2-mile electron linear accelerator (SLAC) in the early 1960s and Brookhaven won support to study a follow-on 1000-GeV machine, the flyover states sought redress from Washington for their grievances. The democratic inclinations of the Great Society and the complaints of physicists excluded from beam time on the Berkeley and Brookhaven accelerators forced the AEC into a overt site selection competition under the aegis of the National Academy of Sciences, which resulted in the selection of a Weston, Illinois, site. Berkeley's designers were insulted by the choice and injured by the attacks on their design by Wilson, who excoriated the extravagance and irrelevance of the accelerator and claimed he could build it more economically and expeditiously. Once inseminated with this idea, the AEC abandoned its efforts to move California physicists to the prairies of Illinois and embraced Wilson as the pioneer of the venture.

As promised, but not without difficulty, Wilson assembled the accelerator on time and under budget—although, as the authors explain, his "cut and try" approach led to some fairly spectacular mistakes in the construction. Wilson's frugality, appropriate to the Lawrence's Depression-era laboratory in Berkeley where he had begun his career, frustrated the potential users of what had been billed a "truly national laboratory," especially when they were required to supply their own experimental equipment to the leaky temporary buildings that Wilson allowed to take up positions around the ring. His own contributions to the design of the laboratory were artistic and ecological, from the high-rise headquarters to the buffalo that occupied the restored prairie in the main ring. This recreation of the frontier, the authors emphasize, symbolized the ideology and rhetoric Wilson employed in his vision for the laboratory. Wilson achieved twice the design energy despite the political exigencies of the 1970s—Vietnam, energy crises, the demise of the AEC, and the growth of the Department of Energy (DOE) bureaucracy—although his distaste for computers and other frills and extras that preoccupied high-energy physics laboratories elsewhere certainly played a role in the disappointment some felt with the results.

When the DOE failed to support his initiatives to retrieve the situation by building another accelerating structure with superconducting magnets to again double the energy of his machine, he resigned—and the Laboratory's contract manager surprised him by accepting his resignation. He was succeeded by Lederman, an able scientific citizen whose string of experiments set the pattern for user homesteading of experimental areas around the ring. He led Fermilab out of the wilderness into the promised land of bigger computers, bigger detectors, colliding-beam accelerators, and sounder management. The new ring of superconducting magnets (built below the original main ring) gave way to a 1000-GeV machine, the Tevatron, which required the kinds of massive detectors and data-analysis networks already under development at CERN, SLAC, and other high-energy laboratories.

Lederman, however, overreached in seeking first to assemble an international consortium to build a very big accelerator, which became the Superconducting Super Collider (SSC) once the Reagan administration deemed it an appropriate effort for the community they hoped would produce the Strategic Defense Initiative. Lederman won the Nobel Prize and departed for the University of Chicago before the SSC was sited in Texas. He left John Peoples to redeem Fermilab and bury the SSC by reinvigorating research in Illinois and shutting down the Waxahachie ring after Congress terminated the project in 1993.

By careful selection of their detailed case studies (e.g., the main ring and Lederman's string), the authors provide sufficient detail to understand both the value and the achievements these represent. They illuminate the laboratory and political contexts that contributed to failures and successes on the high-energy frontier. Fermilab's story is well told and attractively framed in the book, a fitting capstone for the edifice of historical scholarship

---

The reviewer is at the History of Science, Technology and Medicine Program and the Department of Chemical Engineering and Materials Science, 151 Amundson Hall, University of Minnesota, Minneapolis, MN 55455, USA. E-mail: rws@umn.edu

CREDIT: COURTESY FNAL VISUAL MEDIA SERVICES

that the authors have erected over 30 years. Megascience requires "megahistory," and Hoddeson knows how to pioneer in that field.

10.1126/science.1170899

ASTRONOMY

Through a Glass of Darkness

Pedro Ferreira

Einstein's Telescope
The Hunt for Dark Matter and Dark Energy in the Universe

by Evalyn Gates

Norton, New York, 2009.
328 pp. $25.95, C$28.50.
ISBN 9780393062380.

"Astronomers don't know math," a colleague of mine once said. He is a bit of a troublemaker, and what he said was bizarre, unfair, and quite clearly incorrect. But I understood what he was getting at: when astronomers unleashed the power of mathematics—and by that I mean the wonderful, exciting, cutting-edge mathematics of geometry and statistics that has emerged over the past century—there would be many wonderful things to discover out in the cosmos. My belligerent colleague felt that astronomers simply didn't do enough of it.

Evalyn Gates's *Einstein's Telescope* is a testament to what can be done when beautiful mathematics is applied to astronomy. Einstein's general theory of relativity gave us a revolutionary new way of understanding the force of gravity, which effectively governs the behavior of the universe on large scales. Einstein argued that space-time took on a life of its own and in doing so would affect the way things moved. In particular, he showed that the paths of light rays would be deformed by the presence of massive objects like planets, stars, galaxies, and clusters of galaxies. And by looking at the how light rays are deformed, we might be able to learn about not only the light sources but also the objects that have warped the space through which the rays propagate, i.e., the lenses. In my mind, this is one of the most wonderful applications of elegant mathematics and has led to truly groundbreaking observations. Astronomers do know math.

The bulk of *Einstein's Telescope* focuses on the history and important advances in the field of gravitational lensing, and Gates tells the story well. A particle astrophysicist at the University of Chicago's Kavli Institute for Cosmological Physics, she has worked on a number of aspects of dark matter and its astrophysical consequences. She has also been an active promoter of outreach, as a former vice president for science and education at Adler Planetarium in Chicago. Gates is therefore well equipped to come up with clear, well-thought-out explanations of the various areas in which lensing is used. So, for example, she expertly walks us through the minutiae of detecting what are known as massive compact halo objects (MACHOs—a contrived acronym, I know) and the quest for extrasolar planets. She describes the progress in weighing clusters of galaxies through their effect on the light emitted from the tapestry of distant background galaxies, an approach that has provided a genuinely new view on how mass is distributed in the universe. One of my favorite parts is her description of gravitational lensing by stellar black holes. Although some pundits predicted that the required alignment of Earth-hole-star would be too rare to be observable, two separate teams were able to detect such an event in the bulge of our galaxy. That lens remains, according to Gates, "the only lone stellar-mass black hole ever discovered." All in all, this is a story of teasing out improbable, almost indiscernible signals to great effect.

The author chose a considered, meticulous style for most of the book. She digs into the details of how things work and doesn't dwell on personal anecdotes about the various protagonists. This approach makes for drier reading than many other books in the field, although Gates does sprinkle the text with "compelling," "unprecedented," and "beautiful," adjectives that are de rigeur in cosmology. And I fully support her approach because she makes the science (and the math that underpins it) tell the story, and the story is indeed compelling. In her preface, Gates suggests that readers look at the set of color illustrations at the book's center before they start reading and then look at those figures again after having finished. This is a helpful recommendation because, read carefully, her explanations of gravitational lensing and dark matter should really enhance the experience and appreciation of the color images.

Unfortunately, toward its end the book loses focus and depth. Gates's explanations of dark matter and dark energy echo what has been written in countless other popular science books and articles. She has, sadly, neglected the effects that gravitational lensing might have on the relic radiation left over from the Big Bang, a truly new frontier in the field. Her claim that "we live in a flat … Universe" would have been acceptable four or five years ago, but it isn't in 2009, when we know that more detailed studies of dark energy have severely hampered our ability to make precise quantitative statements about the geometry of the universe. And the brief section on modified gravity is in places incorrect. Gates claims that, without dark matter, the gravitational field should trace the light, but there are a number of counterexamples where this has been shown not to be true. Her statement plays a crucial role in her interpretation of recent results, and this is one of the situations in which she should have looked at the math in more detail and not only at the pictures.

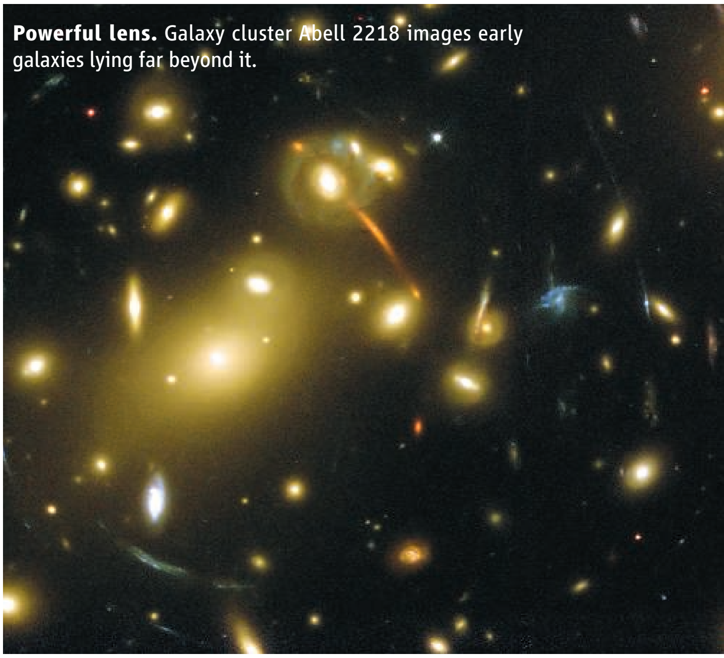

Powerful lens. Galaxy cluster Abell 2218 images early galaxies lying far beyond it.

CREDIT: NASA, ESA, RICHARD ELLIS/CALTECH AND JEAN-PAUL KNEIB/OBSERVATOIRE MIDI-PYRENEES, FRANCE

Overall, *Einstein's Telescope* is worth reading for its level of detail and the way it brings together the disparate applications of gravitational lensing. Gates uses one of Einstein's great ideas to weave together mathematics, astrophysics, and cosmology into a coherent and, dare I say, it, compelling narrative that maps out the frontiers of contemporary research.

10.1126/science.1171766

The reviewer is at Astrophysics, Department of Physics, Denys Wilkinson Building, University of Oxford, Keble Road, Oxford OX1 3RH, UK. E-mail: p.ferreira1@physics.ox.ac.uk

RESOURCE POLICY

Wood Energy in America

Sustainable wood energy offers recurring economic, social, and environmental benefits.

Daniel deB. Richter Jr.,[1]* Dylan H. Jenkins,[2] John T. Karakash,[3] Josiah Knight,[4]
Lew R. McCreery,[5] Kasimir P. Nemestothy[6]

Consumers increasingly want energy that is renewable, clean, and affordable from solar, wind, hydroelectric, geothermal, and biomass sources (*1*). One of the simplest and oldest of renewables is direct combustion of wood (*2*, *3*). Wood supplied more energy than fossil fuels in the United States until the 1880s, when coal superseded wood. This transition occurred earlier in Europe, but today, thanks to regrowth of forests and improved technologies, advanced wood combustion (AWC) is being deployed throughout Europe, supplying heat, cooling, and power and reducing greenhouse-gas emissions (*4*). We argue that the European experience can guide successful implementation of community-based AWC in many regions of the United States.

Long important in Scandinavia, over the last two decades, AWC has grown in its contribution to energy use of France, Germany, and central and eastern Europe. More than 1000 AWC facilities have been constructed in Austria (*5*), nearly all local community–based; more than 100 combine heat and electric power. Most serve towns, portions of cities, industrial complexes, and public institutions, and nearly all are 0.1 to 10 MW (thermal). The facilities emit remarkably low quantities of air pollutants, including greenhouse gases, and have thermal efficiencies across the system approaching 90% (*6*). A high-efficiency wood-burning plant was recently opened in Simmering-Vienna with total thermal capacity of 65 MW, delivering electricity to the grid and heat to the city's district energy system (*7*).

Whether a plant of this size can be sustainably fueled is an open question. However, Europe's thousands of new community-scale AWC facilities clearly demonstrate that, with public backing, AWC can be rapidly implemented, can reduce oil imports and greenhouse gas emissions, and can increase energy security with wood drawn from local woodsheds. AWC can also help communities transition to other renewable energies.

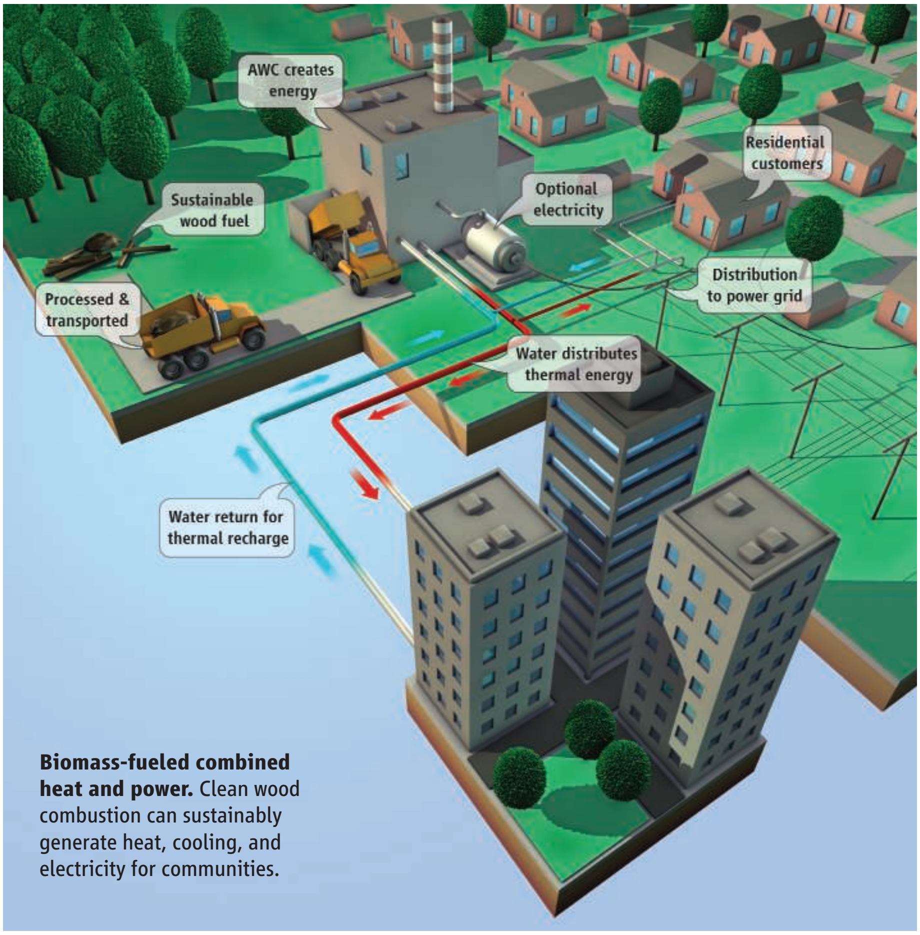

Biomass-fueled combined heat and power. Clean wood combustion can sustainably generate heat, cooling, and electricity for communities.

CREDIT: C. BICKEL/*SCIENCE*

Rakos (*8*) argues that the major barriers to AWC implementation are social, and not economic or technical, and that communities with successful AWC systems adopt systematic approaches to wood-energy policy and practice (*2*, *5*–*8*). To gain public support, decision-makers must increase community appreciation for AWC system reliability, air pollution control, and sustainable forest management, as well as for how wood-energy dollars add jobs and profits to local businesses. Community leadership and public education are critical.

Considerations in Adopting Wood Energy

American forests were recently estimated to be able to sustainably produce 368 million dry tons of wood for energy generation per year (*9*, *10*). This yield is likely an underestimate, as it does not account for wood used for pulp and paper or low-value solid products, or wood from fast-growing trees on nonagricultural lands (*11*). Wood energy can add financial value to the forest and can support restoration and improvement in the form of timber-stand thinnings. The sustainability of local woodsheds will need careful monitoring to assure that forest-energy outputs enhance rather than deplete ecosystems (*12*, *13*). Forest bioenergy planning can include detailed inventories and management plans; education for foresters, loggers, and the public; forest-management certification; and thoughtful consideration within U.S. renewable fuel and energy standards.

Carbon policies need to distinguish renewable sources of energy (such as wood) that recirculate CO_2 already in the biosphere's carbon cycle from fossil fuels that add more CO_2 to that in active circulation.

European technical advances in wood-

---

[1]University Program in Ecology, Southern Center for Sustainable Forests, Nicholas School of the Environment, Duke University, Durham, NC 27708, USA. [2]The Nature Conservancy, Pennsylvania Forest Conservation Program, Williamsport, PA 17701, USA. [3]Resource Professionals Group, Durham, NC 27707, USA. [4]Pratt School of Engineering, Duke University, Durham, NC 27708, USA. [5]State and Private Forestry, USDA Forest Service, Morgantown, WV 26505, USA. [6]Austrian Chamber of Agriculture, Department of Forestry and Energy, A-1014 Vienna, Austria.

*Author for correspondence. E-mail: drichter@duke.edu

Published by AAAS

energy development include automated control over combustion and air pollution. For example, Austria's 1000 AWC facilities emit minimal amounts of sulfur oxides, mercury and other metals, particulates, and carbon monoxide (*5–7*, *14*). Minimal pollutant emissions result from high-quality combustion control (*15*, *16*) and from wood's low pollutant content compared with that of fossil fuels. Critical activities to facilitate adoption of reliable wood-based technologies include training of plumbers, steamfitters, and electricians (*8*) and adaptation of international standards for equipment specifications, operation, pollution-control, and safety.

Wood-energy economics are generally more favorable in North America than in Europe (*14*), and it is ironic that AWC was initiated in Europe (*17*, *18*). If American communities have sustainable wood supplies and AWC gains public support, acute financial pressure will spur wood-energy development because fossil fuel costs currently exceed those of wood by four times per unit of energy produced (*17*, *19*, *20*).

Thermally efficient conversion of wood fuel for heating and cooling of buildings or combined heat and power is a most important factor in sustainable siting and operation of AWC systems. Wood is too valuable to use inefficiently.

AWC Initiatives

To rekindle wood energy in America, we propose three energy initiatives that can have wide-ranging, positive effects in many kinds of communities over the coming few years. First, in localities with sustainable wood supplies, make AWC an energy system of choice for new construction and renovation. This initiative seems well targeted to the Northeast U.S.A., given the region's abundant forest land and dependence on heating oil (*21*), but AWC has great potential in the Southeast and West. Relatively rapid transitions to AWC heating and cooling are technically and economically achievable in schools, municipal offices, hospitals, prisons, and industrial facilities. A number of states promote renewable AWC in "Fuels for Schools" programs. In Vermont, for example, 20% of public school students now attend wood-heated schools (*22*).

Second, make better use of wood collected by municipalities from diseased and storm-damaged trees and from construction sites. The volume of safely combustible urban wood in the United States is nearly 30 million tons per year (*9*, *10*). Often, local communities dispose of this wood at some expense and miss energy benefits that could come from its clean combustion. Examples of successful operations include one in Minnesota where a refurbished coal-plant has been generating heat, cooling, and power by cleanly burning about 250,000 tons per year of urban wood waste and organic materials in downtown St. Paul (*23*).

Third, expand district-energy systems (in which heat is supplied from a central source to several sites) tied to AWC. District-energy AWC is used throughout Europe. It can be observed in downtown St. Paul, Minnesota; in hospitals and public buildings in Akron, Ohio; and on campuses such as Colgate University and the universities of Idaho and South Carolina. District energy is attractive for high-density communities and eco-friendly urban and suburban housing.

Wood Energy in Perspective

We use two wood-resource calculations to demonstrate the potential value of community-based AWC in America. The first considers a hypothetical program in a medium-sized U.S. state that develops community-based AWC on a scale similar to that in Austria (*24*). Consider if North Carolina were to install one community-scale AWC project per year (at 75 hp, 0.75 MW thermal) in each of 100 counties over a 5-year construction period. Although incremental investment might be \$100 million in each of the five construction years, fuel savings could grow to at least \$100 to \$180 million per year (*24*), and emissions of fossil CO$_2$ could decrease by 0.75 to 1.0 million ton per year (*24*). The fuel wood required by such a program would amount to about 20% of a recent estimate of the state's energy-wood supply (*25*).

The second calculation considers wood energy in relation to total U.S. energy consumption (*26*), currently about 100 quads [100×10^{15} British thermal units (BTUs) or 25.2×10^{15} kcal] per year. Today, wood supplies the nation with about 2 quads per year (*26*), and the national sustainable energy-wood supply (*9*, *10*) potentially contains about 5 quads per year (*24*). Although these rates may seem small, they are enormous quantities of energy, comparable to power production from hydroelectric sources (~3 quads per year) or the content of energy in the nation's Strategic Petroleum Reserve (~4 quads) (*27*). Considering the controversial plans to expand the nation's nuclear capacity, currently at 10 quads per year (*26*), how can we not ask about the future potential of wood energy, especially if the nation were to target its development not only in forests and woodlands, but on low-productivity agricultural lands and in cities?

References and Notes

1. Renewable Energy Policy Network for the 21st Century (REN21), *Renewables 2007 Global Status Report* (Worldwatch Institute, Washington, DC, 2008).
2. J. Perlin, *A Forest Journey: The Role of Wood in the Development of Civilization* (Norton, New York, 1989).
3. R. A. Ristinen, J. J. Kraushaar, *Energy and the Environment* (Wiley, New York, 2005).
4. AWC is defined as an automated, high-efficiency wood-fired energy system with strict air pollution controls.
5. R. Hackstock, *Renewable Energy—The Way Forward for the Next Century* (Austrian Energy Agency, Vienna, 2008); www.energyagency.at/(en)/projekte/res_overview.htm.
6. B. Voglauer, J. Rathbauer, *Austrian Biomass Boiler Manufacturers Survey* (Austrian Bioenergy Center, BLT-Wieselburg, Austria, 2004).
7. R. Madlener, M. Bachhiesl, *Energy Policy* **35**, 1075 (2007).
8. C. Rakos, in *Bioenergy—Realizing the Potential* (Elsevier, Amsterdam, 2005), pp. 47–57.
9. R. D. Perlack *et al.*, *Biomass as a Feedstock for a Bioenergy and Bioproducts Industry* [U.S. Department of Agriculture/Department of Energy (DOE), ORNL TM-2005/66, Oak Ridge, TN, 2005].
10. This estimate of the sustainable energy-wood supply does not include wood from forests protected for social, environmental, or economic reasons.
11. G. A. Keoleian, T. A. Volk, *Crit. Rev. Plant Sci.* **24**, 385 (2005).
12. D. A. Perry, R. Oren, S. C. Hart, *Forest Ecosystems* (Johns Hopkins Univ. Press, Baltimore, MD, 2008).
13. National Commission on Science for Sustainable Forestry, *Conserving Biodiversity Through Sustainable Forestry* (National Council on Science and the Environment, Washington, DC, 2007).
14. D. Hagauer, B. Lang, K. P. Nemestothy, *Instruction Manual for the Calculation of Wood Fuel Parameters* (Austrian Energy Agency, Vienna, 2008); www.klimaaktiv.at/article/archive/12740/.
15. M. Wörgetter *et al.*, *Bioenergy in Austria: Potential, Strategies, Success Stories* (BLT Wieselburg, Wieselburg, Austria, 2002); www.blt.bmlf.gv.at/vero/veroeff/0783_Bioenergy_in_Austria_e.pdf.
16. N. Kippel, T. Nussbaumer, *Einfluss der Betriebsweise auf die Partikelemissionen von Holzöfen* (Bundesamt fuer Energie, Bern, Switzerland, 2007); www.verenum.ch/Publikationen/SBOfenmessun.pdf.
17. Timber Mart-South (University of Georgia, Athens, 2008); www.tmart-south.com/tmart/.
18. H. Serup, *Wood for Energy Production* (Center for Biomass Technology, Danish Energy Agency, Copenhagen, Denmark, 2002).
19. Energy Information Administration (EIA), *Heating Oil and Propane Update* (DOE, Washington, DC, 2008).
20. EIA, *Natural Gas Prices* (DOE, Washington, DC, 2008).
21. Energy Efficiency and Renewable Energy Office, *Buildings Energy Data Book* (DOE, Washington, DC, 2007).
22. Vermont Fuels for Schools, Montpelier, VT, 2008; www.biomasscenter.org/services/programs/vermont-fuels-for-schools-vffs.html.
23. S. R. Schill, *Biomass* **2008**, no. 1428 (February 2008); www.biomassmagazine.com/article.jsp?article_id=1428&q=schill.
24. Supplemental calculations are available as supporting material on *Science* Online.
25. LaCapra Associates Team, *Analysis of a Renewable Portfolio Standard for North Carolina* (LaCapra Associates, Boston, MA, 2006); www.lacapra.com/downloads/NC_RPS_Report.pdf.
26. EIA, *Annual Energy Review 2007* (DOE, Washington, DC, 2008).
27. About 706 million barrels of crude oil are being stored in the United States' Strategic Petroleum Reserve (SPR), according to (*28*).
28. D. G. Victor, S. Eskreis-Winkler, *Foreign Aff.* **87**, 70 (2008).

Supplementary Online Material
www.sciencemag.org/cgi/content/full/323/5920/1432/DC1

10.1126/science.1166214

CLIMATE CHANGE

Shifting Westerlies

What caused atmospheric westerly winds to shift after the last glacial period?

J. R. Toggweiler

The westerlies are the prevailing winds in the middle latitudes of Earth's atmosphere, blowing from west to east between the high-pressure areas of the subtropics and the low-pressure areas over the poles. They have strengthened and shifted poleward over the past 50 years, possibly in response to warming from rising concentrations of atmospheric carbon dioxide (CO_2) (*1–4*). Something similar appears to have happened 17,000 years ago at the end of the last ice age: Earth warmed, atmospheric CO_2 increased, and the Southern Hemisphere westerlies seem to have shifted toward Antarctica (*5*, *6*). Data reported by Anderson *et al.* on page 1443 of this issue (*7*) suggest that the shift 17,000 years ago occurred before the warming and that it caused the CO_2 increase.

The CO_2 that appeared in the atmosphere 17,000 years ago came from the oceans rather than from anthropogenic emissions. It was vented from the deep ocean up to the atmosphere in the vicinity of Antarctica. The southern westerlies are important in this context because they can alter the oceanic circulation in a way that vents CO_2 from the ocean interior up to the atmosphere. The prevailing view has been that the westerlies shifted 17,000 years ago as part of a feedback: A small CO_2 increase or small warming initiated a shift of the westerlies toward Antarctica; the shifted westerlies then caused more CO_2 to be vented up to the atmosphere, which led to more warming, a greater poleward shift of the westerlies, more CO_2, and still more warming (*5*). But Anderson *et al.* show that the westerlies did not shift in response to an initial CO_2 increase; rather, they shifted early in the climate transition and were probably the main cause of the initial CO_2 increase.

The strongest southern westerlies are found several hundred kilometers to the north of a broad oceanic channel that circles the globe around Antarctica. The stress from the westerlies on the ocean drives the Antarctic Circumpolar Current (ACC) through the channel. This stress also draws mid-depth water from north of the ACC to the surface around Antarctica. Over the past 50 years, the westerlies have shifted southward so that they are better aligned with the ACC and draw more mid-depth water to the surface than they did before (*8*, *9*). At the peak of the last ice age, the opposite situation prevailed: The westerlies were so far north of today's position that they were no longer aligned with the ACC and could not draw much mid-depth water to the surface.

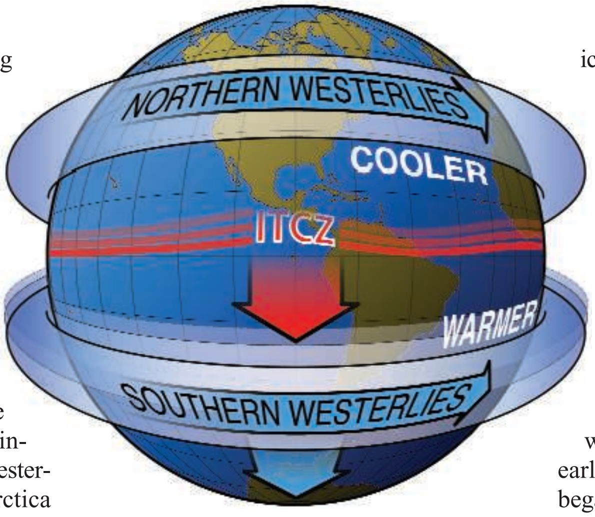

Southward movement. At the end of the last ice age, the ITCZ and the Southern Hemisphere westerlies winds moved southward in response to a flatter temperature contrast between the hemispheres (*5*, *6*, *11*). According to Anderson *et al.*, the northern westerlies may have also shifted to the south; this shift is not depicted in the figure.

CREDIT: J. TOGGWEILER/CARNEGIE MELLON UNIVERSITY

The mid-depth water upwelled by the westerlies is rich in CO_2 and in silica, a nutrient that fuels biological production in the surface waters around Antarctica. Siliceous remains of the organisms settle to the sea floor and accumulate in the sediments. Anderson *et al.* show that the accumulation of siliceous sediment increased dramatically during the transition out of the last ice age. They attribute this increase to a poleward shift of the westerlies that drew more CO_2- and silica-rich water up to the surface.

A detailed analysis of the ice-core records from Antarctica shows that atmospheric CO_2 concentrations rose in two steps along with the air temperatures over Antarctica (*10*). The silica accumulation in Anderson *et al.*'s best resolved record also shows two pulses that correspond in time to the two steps (*7*). To create such a pulse in silica accumulation, larger quantities of silica-rich deep water must be drawn to the surface. As mentioned above, silica-rich deep water tends to be high in CO_2. It is also warmer than the near-freezing surface waters around Antarctica.

A shift of the westerlies that draws more warm, silica-rich deep water to the surface is thus a simple way to explain the CO_2 steps, the silica pulses, and the fact that Antarctica warmed along with higher CO_2 during the two steps. Anderson *et al.*'s two silica pulses occur right along with the two CO_2 steps, which implies that the westerlies shifted early as the level of CO_2 in the atmosphere began to rise. Had the westerlies shifted in response to higher CO_2, one would expect to see more upwelling and more silica accumulation after the second CO_2 step when the level of CO_2 is highest, but instead the silica accumulation drops back down.

What made the westerlies shift when they did? The answer seems obvious empirically but may be difficult to understand theoretically. The Northern Hemisphere is systematically warmer than the Southern Hemisphere, especially near the Atlantic Ocean, where the overturning circulation transports heat across the equator from south to north. As a result, Earth's thermal equator—the Intertropical Convergence Zone (ITCZ)—is north of the equator. The easterly trade winds that flank the ITCZ to the north and south are also skewed toward the Northern Hemisphere.

Anderson *et al.*'s two pulses of sediment accumulation took place along with Heinrich Event 1 and the Younger Dryas—events in which icebergs and melting glaciers flooded the North Atlantic with fresh water, thereby weakening the overturning. The weakened overturning cooled the Northern Hemisphere and warmed the Southern Hemisphere, thus reducing the temperature asymmetry. Sediment records from the southern Caribbean Sea show that the trade winds shifted to the south during the two pulses (*11*, *12*). Thus, the ITCZ shifted closer to the equator and the southern westerlies apparently shifted toward Antarctica along with the southward movement of the trade winds (see the figure).

The sediment accumulation rate during Anderson *et al.*'s two pulses was five times as high as it was at the Last Glacial Maximum (just before the two pulses), and twice as high

---

Geophysical Fluid Dynamics Laboratory/National Oceanic and Atmospheric Administration, Princeton University, Princeton, NJ 08540, USA. E-mail: robbie.toggweiler@noaa.gov

Published by AAAS

as it is today. This points to massive changes in the wind-driven upwelling around Antarctica during the transition out of the last ice age and suggests that the westerlies were closer to (or stronger next to) Antarctica during the transition than they are now.

Climate scientists have attributed changes in the westerlies over the past 50 years to the warming from higher CO_2. The changes predicted by climate models in response to higher CO_2 are fairly small, however, and tend to be symmetric with respect to the equator. The observed changes have been quite asymmetric, with much larger changes in the Southern Hemisphere than in the north (*3*). The results of Anderson *et al.* (*7*) suggest that in the past, the westerlies shifted asymmetrically toward the south in response to a flatter temperature contrast between the hemispheres. The magnitude of the shift seems to have been very large. If there was a response to higher CO_2 back then, it paled in comparison. Changes in the north-south temperature contrast today are not going to be as large as they were at the end of the last ice age, but even small changes could be an additional source of modern climate variability.

References

1. J. W. Hurrell, H. van Loon, *Tellus Ser. A* **46**, 325 (1994).
2. G. J. McCabe *et al.*, *J. Climate* **14**, 2763 (2001).
3. N. P. Gillett *et al.*, *Nature* **422**, 292 (2003).
4. D. T. Shindell, G. A. Schmidt, *Geophys. Res. Lett.* **31**, L18209 (2004).
5. J. R. Toggweiler, J. L. Russell, S. R. Carson, *Paleoceanography* **21**, PA 2005 (2006).
6. F. Lamy *et al.*, *Earth Planet. Sci. Lett.* **259**, 400 (2007).
7. R. F. Anderson *et al.*, *Science* **323**, 1443 (2009).
6. O. A. Saenko *et al.*, *Climate Dyn.* **25**, 415 (2005).
9. J. L. Russell *et al.*, *J. Climate* **19**, 6382 (2006).
10. E. Monnin *et al.*, *Science* **291**, 112 (2001).
11. G. H. Haug *et al.*, *Science* **293**, 1304 (2001).
12. D. W. Lea, D. K. Pak, L. C. Peterson, K. A. Hughen, *Science* **301**, 1361 (2003).

10.1126/science.1169823

CHEMISTRY

Inducing Chirality with Circularly Polarized Light

An unexpected difference in electron transfer rates for right- and left-handed versions of a molecule is caused by quantum interference.

Robert J. Cave

We have an intuitive understanding of how the shape and symmetry of objects affects their use from our hands. Each hand is chiral: Its mirror image (the right versus the left hand) is different from it. When we extend right hands, they can clasp because the thumbs point in opposite directions. A baseball bat fits equally well into either hand and does not work better for a right-handed hitter than a lefty. Similarly, we do not expect to see processes in molecules to be faster in the right-handed or left-handed versions, but a recent study of electron transfer induced by circularly polarized light rotating in a fixed direction reported unexpected differences in yields—on the order of several tenths of a percent—for molecules that differ only in their handedness (*1*). In a recent paper, Skourtis *et al.* (*2*) explain how these differences may arise through quantum interference when there are inequivalent pathways for electron transfer.

Electron transfer can occur within a molecule when light excites an electron at a donor site that then tunnels through the barrier set up by the bonds in the molecule to an acceptor site. The yield of electron transfer will depend on the width and height of the barrier, which is determined by the distance between the sites and the type of bonds in the intervening medium, called the bridge (*3*). A simple "tight-binding" model captures this distance dependence (*4*), and to a first approximation, the rate will be faster the more the donor and acceptor states delocalize onto the bridge lowering the effective mass of the electron and leading to more efficient tunneling.

This delocalization is enhanced when bonding is strong between the donor, acceptor, and bridge, and the energies of the three sets of sites are close to one another. A model of a donor-bridge-acceptor system is shown in the figure, panel A, in which initially there is only a single bond between the donor and the bridge (the solid line). In this tight-binding model, reversing the helicity of the bridge while preserving the bonding strength and relative energetics would yield equivalent electron transfer rates through the two possible bridge helicities.

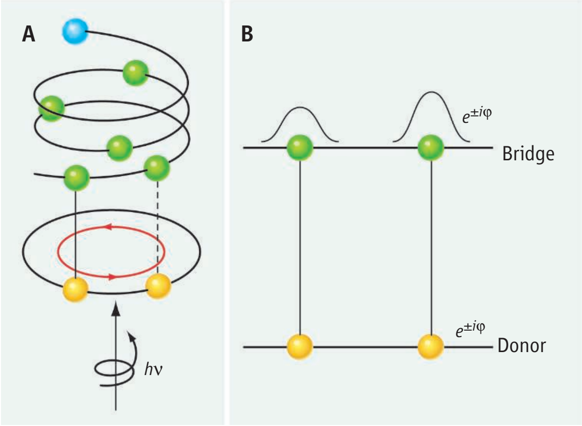

Inequivalent paths. (**A**) A simple model for electron transfer mediated by a chiral structure, with a cyclic donor (atomic sites shown in yellow) attached via a single bond (solid line) or two bonds (solid and dashed lines) to a helical bridge (shown in green) terminated at its opposite end by an electron acceptor (shown in blue). Circularly polarized light (bottom, energy *hv*) excites a ring current in a particular direction. (**B**) The circularly polarized light imparts a relative complex phase to the delocalization originating from the two ring sites. Different acceptor amplitudes (and thus different rates) arise from the two relative phases.

How then can a preference for one bridge configuration be induced? In the Skourtis *et al.* model, circularly polarized light, which carries angular momentum, can excite ring currents that circulate in a particular direction in donors possessing degenerate electronic states—states of the same energy and similar shapes (*5*). For the simple model of atoms on a ring, excitation with circularly polarized light yields equal electron density at each ring site, but the amplitudes at the various sites differ in their complex phase (*6*).

Reversing the polarization of the light reverses the direction of the ring current. The electron density remains unchanged, but the opposite handedness of the light produces different relative phases between sites. However, excitation of either current direction would still yield no preference for transfer through the helical bridge because the electron density at the site connecting the donor to the bridge is unchanged.

Department of Chemistry, Harvey Mudd College, Claremont, CA 91711, USA. E-mail: Robert_Cave@HMC.edu

Published by AAAS

The key to inducing asymmetry in the transfer rates for the two types of excitation is modification of the system to include two or more points of contact (or bonds) between the donor and bridge (see the figure, panel A, now including both bonds between the donor and the bridge**)**. The yield of electron transfer between the donor and acceptor now depends on the interference between tunneling paths stemming from these two points. Switching the direction of the light polarization changes the relative phases between these paths, leading to different final acceptor amplitudes (see the figure, panel B). Skourtis *et al.* show that the asymmetry of transfer efficiencies for the two types of excitation polarization can lead to observable changes in yield and that an equivalent effect can be obtained for a given light polarization if the bridge configuration is reversed.

This model is idealized in a number of respects, so Skourtis *et al.* have tested the sensitivity of the predictions to several system and environmental factors. The observation of the asymmetry requires that the relative phase between donor sites is preserved. Skourtis *et al.* still observed asymmetry when dephasing (the loss of phase coherence caused by interactions with the environment) was introduced and state-lifetimes were lengthened, within reasonable limits.

These results support recent experimental studies of Waldeck, Naaman, and co-workers (*1*, *7*). When circularly polarized light was used to excite porphyrins (*7*), which have a pair of near-degenerate electronic states, electron transfer yields differed through chiral monolayers when excited with left- and right-hand circularly polarized light. The yield difference was reversed by changing the configuration of the helix through which tunneling occurred. Similar results have been observed in related experiments for spin-polarized electron scattering from oriented thin films of chiral molecules (*7*)

This differential response to excitation by circularly polarized light could be used to detect local chiral environments or to control current flow in well-defined chiral systems. Skourtis *et al.* suggest using circularly polarized light to excite target molecules intercalated in DNA and then follow electron transfer as a function of distance along the helix. Electron transfer along DNA fragments has been well studied (*8*) and would allow investigation of several of the model's features, including its sensitivity to relative energies, lifetime, and distance.

Perhaps the most interesting point these results illustrate is that chiral asymmetries can arise through the manipulation of relative quantum phases in molecular systems and do not necessarily depend on inherent asymmetries, such as those seen in the weak force (*9*). The latter may indeed manifest themselves, but in the present case a simpler and controllable phenomenon is more likely at play.

References

1. J. J. Wei *et al.*, *J. Phys. Chem. B* **110**, 1301 (2006).
2. S. S. Skourtis, D. N. Beratan, R. Naaman, A. Nitzan, D. H. Waldeck, *Phys. Rev. Lett.* **101**, 238103 (2008).
3. M. D. Newton, *Chem. Rev.* **91**, 767 (1991).
4. C. Kittel, *Introduction to Solid State Physics* (Wiley, New York, 1956), p. 586.
5. I. Barth, J. Manz, Y. Shigeta, K. Yagi, *J. Am. Chem. Soc.* **128**, 7043 (2006).
6. L. Salem, *The Molecular Orbital Theory of Conjugated Systems* (Benjamin, London, 1974), pp. 110–117.
7. K. Ray, S. P. Ananthavel, D. H. Waldeck, R. Naaman, *Science* **283**, 814 (1999).
8. D. N. Beratan, S. Priyadarshy, S. M. Risser, *Chem. Biol.* **4**, 3 (1997).
9. M. Quack, *Angew. Chem., Int. Ed.* **41**, 4618 (2002).

10.1126/science.1169338

BIOCHEMISTRY

The Evolution of Ribozyme Chemistry

Insights into the mechanisms by which ribonucleic acid enzymes catalyze reactions may help us to understand how life progressed from an early RNA world.

Timothy J. Wilson and David M. J. Lilley

Ribozymes are RNA molecules that catalyze reactions on themselves or other molecules; they are enzymes that happen to be made of RNA, not amino acids (*1*). They may have played a key role in the formation of life on our planet, because they do not require the complex translation apparatus needed to form protein enzymes. Although the list of natural ribozymes is short, several ribozymes perform essential reactions. For example, the ribosome translates the genetic code into proteins, and ribonuclease P (RNase P) processes transfer RNA into its mature form in all kingdoms of life. Perhaps these are living molecular fossils from an "RNA world" that is postulated to have existed billions of years ago when life first began. So, just how do ribozymes work, and do their mechanisms provide clues to their evolutionary origins?

Ribozymes can achieve impressive rate accelerations—for example, by a factor of ~10^{11} for group I self-splicing introns, which would not disgrace a protein enzyme—even though RNA is limited to four rather similar nucleobases and a hydroxyl group, whereas proteins have side chains that exhibit a wide range of aqueous chemistry. A glimpse into the chemistry of an RNA world has been offered by the evolution of ribozymes in the laboratory that carry out reactions necessary for an RNA-based metabolism. Such ribozymes are selected from a pool of random RNA sequences. A recently generated ribozyme catalyzes the replication of RNA from an RNA template (*2*); this would be essential in an RNA world.

Complete or partial crystal structures now exist for most known ribozymes, but finding out how catalysis occurs requires analysis of the transition state of a reaction, which is not accessible by purely structural methods. Such analysis has shown that evolution has equipped different classes of ribozyme with different catalytic strategies, based on either metal ions or the transfer of protons.

The polypeptide backbone of proteins is electrically neutral, whereas nucleic acids are polyelectrolytes with charged phosphate groups at physiological pH. Metal ions are therefore required to fold RNA, and in principle, bound metal ions can be recruited to a catalytic role. The observation that many protein enzymes involved in phosphoryl transfer use divalent metal ions for catalysis led Steitz and Steitz to propose a two-metal ion mechanism, in which the nucleophile is activated and the leaving group stabilized (*3*). They suggested that this mechanism might also apply to self-splicing intron ribozymes (a group of ribozymes, found in noncoding sequences—or introns—within mRNA, that catalyze precise intron excision). Both this class of ribozyme and RNase P do indeed appear to act as metalloenzymes. Two metal ions have been

---

Cancer Research UK Nucleic Acid Structure Research Group, MSI/WTB Complex, University of Dundee, Dow Street, Dundee DD1 5EH, UK. E-mail: d.m.j.lilley@dundee.ac.uk

found at the active site of the *Azoarcus* group I intron ribozyme (*4*) and in the presumed active site of a group II intron ribozyme (*5*).

However, to prove that metal ions participate in the catalytic chemistry, it is necessary to perform functional analysis. Herschlag, Piccirilli, and their co-workers have developed atomic mutagenesis methods in which the reduced activities of specific sulfur or nitrogen substitutions are restored by addition of soft metal ions that have a higher affinity for these atoms (*6*). These experiments rigorously define the roles of the ions and their ligands (*7*) in the transition state of the reaction. Detailed analysis of the first catalytic step of a group I intron ribozyme has shown the importance of metal ions for binding the two reactants in an appropriate orientation for reaction, activating the nucleophile to initiate the reaction, and stabilizing the developing negative charge in the transition state. A similar mechanism may occur in the group II intron ribozymes.

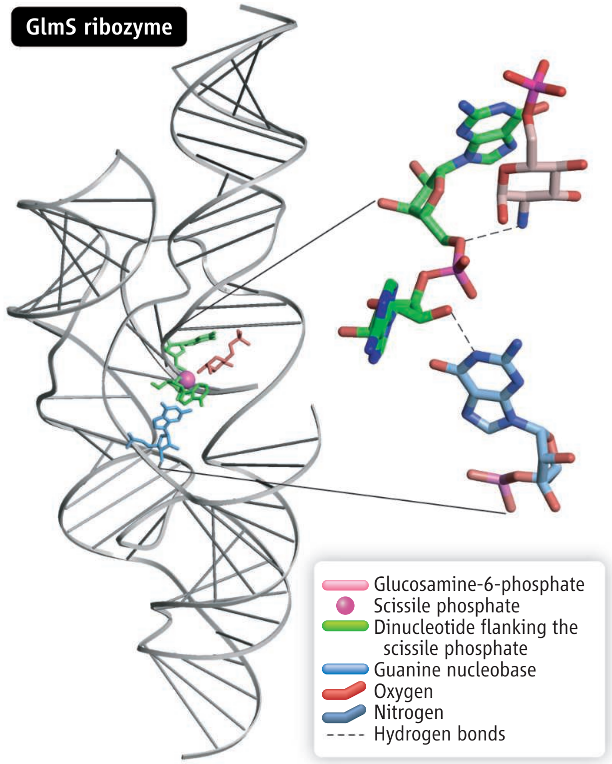

A ribozyme that has recruited a small-molecule cofactor. A pocket at the center of the GlmS ribozyme specifically binds a molecule of glucosamine-6-phosphate close to the scissile phosphate (*11*); the glucosamine-6-phosphate plays a key role in GlmS acid-base catalysis. Similar recruitment of amino acids as cofactors might have been the first step from an RNA world to the present protein-based life.

A decade ago, small nucleolytic ribozymes (used to process replication intermediates or to control gene expression) were widely assumed also to act as metalloenzymes. Instead, they use general acid-base catalysis carried out mostly by nucleobases. These ribozymes perform site-specific cleavage of the phosphodiester backbone of RNA by attack of the 2′-hydroxyl group, and in some cases the reverse ligation reaction that joins them back together (*8*, *9*). The same reaction is catalyzed by the protein enzyme ribonuclease A (RNase A), with two histidine residues used as general acid and base. Under physiological conditions, RNase A is a much better catalyst than the ribozymes, because its histidines are more often in the correct protonation state for reaction (illustrating the greater chemical diversity of proteins), but the intrinsic rates are similar for the RNA- and protein-catalyzed reactions.

Does this mean that metal ions have no direct role in catalysis by the nucleolytic ribozymes? Not necessarily. The HDV ribozyme uses a cytosine nucleobase and a metal ion–bound hydroxide as acid and base, respectively (*10*, *11*). Moreover, in the structure of the hammerhead ribozyme (*12*), a guanine nucleobase is well placed to act as the general base for the cleavage reaction, but the only contender for the general acid is the 2′-hydroxyl of another nucleotide, which is generally unsuited for this role. Recent molecular dynamics simulations suggest that a metal ion might stabilize the transition state and increase the acidity of the 2′-hydroxyl (*13*). Although this is far from proven, we should not be too ready to rule out any role for metal ions in the catalytic mechanisms of nucleolytic ribozymes.

The nucleolytic ribozyme GlmS provides another exception to the exclusive use of nucleobases in general acid-base catalysis. Here, the general acid is a small molecule, glucosamine-6-phosphate, that binds selectively to the RNA structure (see the figure) (*14*). This observation has profound implications for the origins of life: The recruitment of amino acids or peptides by ribozymes in an RNA world might have been the first step toward the present protein-based life.

The spliceosome (a large ribonucleoprotein complex that catalyzes the removal of introns from RNA) may have traveled farther down this evolutionary path. It was thought probably to be a ribozyme because the chemistry of the splicing is identical to that catalyzed by the group II intron, and certain domains of spliceosomal RNA have sequences similar to those of the catalytic domains of the intron. However, structural and genetic data suggest that the RNase H–like domain that forms part of the spliceosomal protein Prp8 serves to position the RNA for reaction (*15*, *16*); in a plausible model, the splice site is adjacent to the putative active site of the RNase H–like domain. This site lacks two of the four cation-binding residues observed in RNase H (*17*), and no metal ion binding has been detected (*15*). It thus seems unlikely that Prp8 carries out the chemistry unaided, which raises the intriguing possibility that the spliceosome is a hybrid in which both protein and RNA domains contribute to catalysis.

A ribozyme that appears to use proton transfer in a rather different way from the nucleolytic ribozymes is the ribosome, which is the cell's protein synthesis assembly line. The ribosome accelerates amino acid condensation by a factor of 10^7. It contrasts with the preceding reactions in that the nucleophile is an amine and the target an sp^2-hybridized carbonyl. There are no data to support metal ion or nucleobase participation in the reaction. However, a critical role seems to be played by the 2′-hydroxyl of the 3′-terminal nucleotide of the transfer RNA that carries the growing polypeptide (*18*). In a proposed mechanism, protons flip between the attacking nucleophile, the key 2′-hydroxyl, and the leaving group in a concerted manner (*19*). It has also been proposed that that the α-amine remains uncharged in the ribosome's transition state (*20*). However, interpretation of the present data is not yet fully nailed down, and we have not read the final word on the ribosome mechanism yet.

Evolution has found a variety of ways to exploit the limited chemical resources of RNA to achieve some impressive feats of catalysis. We are beginning to understand these mechanisms, but much remains unknown. For example, why is a particular mechanism used by a given class of ribozyme? The study of ribozyme mechanisms elucidates the evolution of catalytic chemistry during the formation of life, but the most intriguing question remains: Why are some reactions still catalyzed by RNA while most ribozymes have been superseded by proteins?

References

1. D. M. J. Lilley, F. Eckstein, Eds., *Ribozymes and RNA Catalysis* (Royal Society of Chemistry, Cambridge, 2008).
2. T. A. Lincoln, G. F. Joyce, *Science* **323**, 1229 (2009); published online 8 January 2009 (10.1126/science.1167856).
3. T. A. Steitz, J. A. Steitz, *Proc. Natl. Acad. Sci. U.S.A.* **90**, 6498 (1993).
4. P. L. Adams, *et al.*, *Nature* **430**, 45 (2004).
5. N. Toor *et al.*, *Science* **320**, 77 (2008).
6. S. O. Shan *et al.*, *Proc. Natl. Acad. Sci. U.S.A.* **96**, 12299 (1999).
7. M. Forconi *et al.*, *Biochemistry* **47**, 6883 (2008).
8. P. B. Rupert *et al.*, *Science* **298**, 1421 (2002); published online 10 October 2002 (10.1126/science.1076093).
9. T. J. Wilson, A. C. McLeod, D. M. J. Lilley, *EMBO J.* **26**, 2489 (2007).
10. S. Nakano, D. M. Chadalavada, P. C. Bevilacqua, *Science* **287**, 1493 (2000).
11. S. R. Das, J. A. Piccirilli, *Nat. Chem. Biol.* **1**, 45 (2005).
12. M. Martick, W. G. Scott, *Cell* **126**, 309 (2006).
13. T. S. Lee *et al.*, *J. Am. Chem. Soc.* **130**, 3053 (2008).
14. D. J. Klein, M. D. Been, A. R. Ferré-D'Amaré, *J. Am. Chem. Soc.* **129**, 14858 (2007).
15. V. Pena *et al.*, *EMBO J.* **27**, 2929 (2008).
16. D. B. Ritchie *et al.*, *Nat. Struct. Mol. Biol.* **15**, 1199 (2008).
17. M. Nowotny *et al.*, *Cell* **121**, 1005 (2005).
18. J. S. Weinger *et al.*, *Nat. Struct. Mol. Biol.* **11**, 1101 (2004).
19. T. M. Schmeing *et al.*, *Mol. Cell* **20**, 437 (2005).
20. D. A. Kingery *et al.*, *Chem. Biol.* **15**, 493 (2008).

10.1126/science.1169231

MATHEMATICS

Emergence of Connectivity in Networks

Can the evolution of real-world networks be accurately modeled?

Tom Bohman

A network consists of a collection of nodes and a collection of connections that join pairs of nodes. In the language of mathematics, such an object is called a graph.

Real-world objects such as the Internet (*1*), social networks (*2*), disease modeling (*3*), and bibliometric data harvesting are increasingly being modeled using graphs. When these objects do not have useful computer-based realizations, randomly generated graphs play a central role in their modeling (*4*). All of the models that have been rigorously analyzed thus far follow a common pattern in the emergence of the connectivity structure. On page 1453 of this issue, Achlioptas *et al.* (*5*) describe a simple, randomized network formation process that does not follow this pattern—it exhibits an extremely abrupt phase transition in its connectivity structure. Termed "explosive percolation" the transition is considerably more severe than the analogous phase transitions in related models, and may have important implications for network evolution in general.

The study of randomly generated discrete mathematical objects—such as graphs or codes—is a component of probabilistic combinatorics. Randomly constructed discrete objects can have characteristics that are difficult to achieve by explicit construction (a rule that dictates the full structure), and the best known results on many central problems in combinatorics are achieved using random constructions (*6*). Many useful algorithms make use of random choices (*7*)—these are known as randomized algorithms (*8*, *9*).

A common feature of randomly generated discrete objects is the sudden emergence of structural properties. A small change in the number of random choices made transforms the distribution from one in which a certain property is very uncommon to one in which the property is extremely likely. These sudden changes are known as phase transitions, and they are related to the phase transitions in physics and materials science (*6*, *10*).

One of the simplest, and best understood, randomized network formation processes is the Erdös-Rényi random graph. Starting off with a collection of n nodes, where n is extremely large, connections between pairs of nodes are chosen at random one at a time and added to the graph. This evolving graph goes through a number of structural transitions as it proceeds from the empty graph, which has no connections between pairs of nodes, to the complete graph in which all pairs of nodes are connected.

One such structural transition in the graph's evolution is in the size of the largest component. A component is a collection of nodes, any two of which are connected by some path in the network (see the figure). Suppose we have added m random connections. If m is slightly less than $n/2$, then it is likely that the network has many components that are all very small. On the other hand, if m is slightly larger than $n/2$, then there is a unique component that encompasses many of the nodes, whereas all the other components are still small. This single large component—called the giant component—slowly grows to cover the entire set of nodes as more connections are added (*11*–*13*).

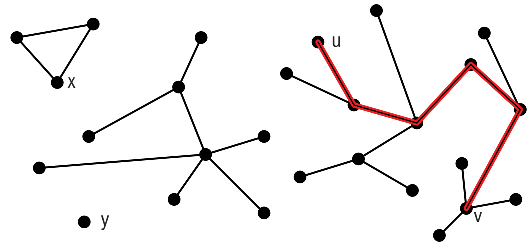

Components in a network. The network depicted here has four components. Nodes u and v are in the same component because there is a path along connections in the network that joins these two vertices (this path is marked in red). Nodes u and x, on the other hand, are in different components because there is no way to travel from u to x using the connections that are present in the network. Single nodes such as y are themselves components if they are not involved in any network connections.

The evolution of the component structure has been studied in a wide array of more intricate random graph models. These include models in which the graph is chosen as a random subgraph of some underlying graph (*14*) and inhomogeneous models in which the probabilities of connection between pairs of nodes vary (*15*). In any such model, there is not only the natural question as to if and when the giant component appears but also the question of how the giant component grows after it appears. The emergence of the giant component in all of the models mirrors the phase transition in the Erdös-Rényi random graph in several important ways: For example, the number of nodes in the giant component grows smoothly as random connections are added. In contrast, the model known as the product rule, studied by Achlioptas *et al.*, exhibits wildly different behavior. The giant component emerges very suddenly, covering more than half of the nodes essentially immediately.

If randomly generated graphs serve as useful models for real-world phenomena then this kind of percolation could have implications for those phenomena. For example, the

Department of Mathematical Sciences, Carnegie Mellon University, Pittsburgh, PA 15213, USA. E-mail: tbohman@math.cmu.edu

mathematical mechanism whereby the giant component emerges in an evolving network is related to the mechanism whereby a spreading disease in such a network becomes an epidemic (*3*). Perhaps there are nonclassical, but still natural, models for the spread of a disease in a network for which epidemics emerge in unexpected ways.

It is important to note that the results presented by Achlioptas *et al.* are given by computer simulation rather than formal mathematical proof. So it may be the case (although it seems unlikely) that for larger values of *n*, some other kind of behavior becomes apparent. Indeed, whether or not this happens is a very intriguing mathematical issue. This question will certainly draw considerable attention in the near future, and its solution (like the solution of any mathematical problem that appears to be beyond the reach of the current state of the art in mathematical technique) may lead to deeper insights into the evolution of randomized network formation models in general.

References and Notes

1. A. Barabási, R. Albert, *Science* **286**, 509 (1999).
2. D. Watts, S. Strogatz, *Nature* **393**, 409 (1998).
3. R. Durrett, *Random Graph Dynamics* (Cambridge Univ. Press, Cambridge, 2007).
4. M. Keeling, K. Eames, *J. R. S. Interface* **2**, 295 (2005).
5. D. Achlioptas *et al.*, *Science* **323**, 1453 (2009).
6. N. Alon, J. Spencer, *The Probabilistic Method* (Wiley, New York, 2008).
7. M. Dyer *et al.*, *Assoc. Comput. Mach.* **38**, 1 (1991).
8. M. Mitzenmacher, E. Upfal, *Probability and Computing: Randomized Algorithms and Probabilistic Analysis* (Cambridge Univ. Press, Cambridge, 2005).
9. R. Motwani, P. Raghavan, *Randomized Algorithms* (Cambridge Univ. Press, Cambridge, 1995).
10. M. Mézard *et al.*, *Science* **297**, 812 (2002).
11. P. Erdös, A. Rényi, *Publ. Math. Inst. Hung. Acad. Sci.* **5**, 17 (1960).
12. B. Bollobás, *Random Graphs* (Cambridge Univ. Press, Cambridge, 2001).
13. S. Janson *et al.*, *Random Graphs* (Wiley, New York, 2000).
14. C. Borgs, J. Chayes, R. van der Hofstad, G. Slade, J. Spencer, *Random Struct. Algorithms* **27**, 137 (2005).
15. B. Bollobás, S. Janson, O. Riordan, *Random Struct. Algorithms* **31**, 3 (2007).
16. I acknowledge National Science Foundation grant DMS-0701183.

10.1126/science.1171297

PLANT SCIENCE

Paternal Patterning Cue

A signaling factor in sperm couples fertilization to the first plant patterning event.

Ueli Grossniklaus

More than 2000 years ago, Aristotle reflected on the contributions of mother and father to their offspring and proposed that the mother provided "matter" while the father provided "form" (*1*). The former is best illustrated by the development of enucleated sea urchin eggs into normal pluteus larvae without any contribution from the zygotic genome (*2*). In plants, it was long thought that any parental effects on embryogenesis were nonexistent. Over the past decade, however, several mutations that exert maternal effects on embryogenesis have been described in the model plant *Arabidopsis thaliana* (*3*). On page 1485 of this issue, Bayer *et al.* (*4*) describe the first paternal effect on plant embryogenesis, demonstrating that a temporal cue provided by the sperm cell triggers the events leading to the first asymmetric division of the plant embryo.

Unlike in animals, where the products of meiosis (cell division that forms gametes) differentiate directly into haploid egg and sperm (harboring one set of chromosomes), plant spores divide to form multicellular gametophytes. The male gametophyte (pollen) harbors two sperm cells, which are delivered to the female gametophyte (embryo sac) that is embedded in the ovule, the precursor of the seed. In flowering plants (such as *Arabidopsis*), one sperm fuses with the egg cell to form the zygote, whereas the second fuses with the central cell and develops into the endosperm, a nutritive tissue supporting the growth of the embryo. After fertilization, the zygote elongates and divides asymmetrically to form a small apical cell, the precursor of the embryo proper, and a large basal cell, which develops into a filamentous structure called the suspensor (see the figure). *Arabidopsis* zygotes that inherit a paternal mutant *short suspensor* (*ssp*) allele fail to elongate and show defects in suspensor development. In extreme cases, the suspensor is completely lacking, implicating *SSP* in promoting suspensor fate (*4*).

Bayer *et al.* show that in *Arabidopsis*, the *SSP* gene encodes an interleukin-1 receptor–associated kinase/Pelle-like kinase. This enzyme activates a signaling pathway in the zygote that involves the MAP kinase kinase kinase YODA (YDA) and the MAP kinases MPK3 and MPK6. This cascade of activated kinases (the *YDA* pathway) promotes elongation of the zygote and suspensor development (*5*, *6*). The SSP protein contains an amino-terminal motif for myristoylation/palmitoylation (diacylation), a central kinase domain, and a carboxyl-terminal tetratricopeptide repeat.

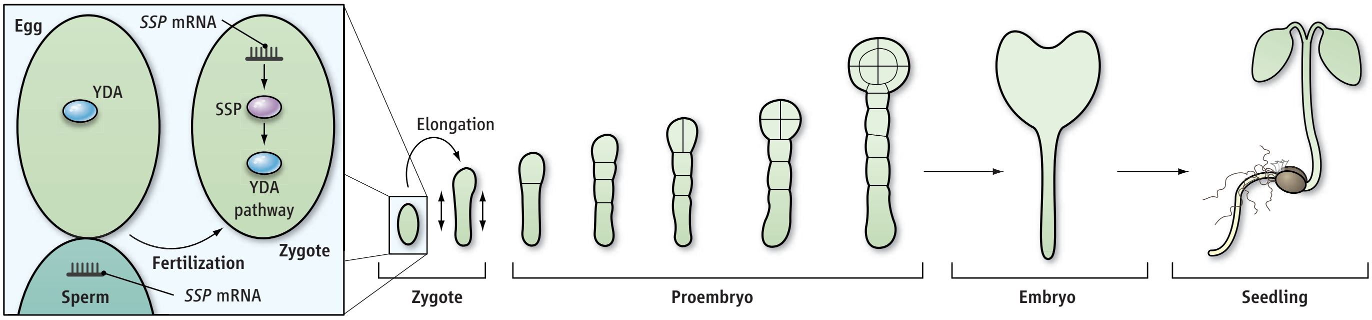

Developmental direction. Early development of the *Arabidopsis* embryo includes zygote elongation, asymmetric cell division, and the differentiation of distinct fates. Factors that trigger zygote elongation and the first asymmetric cell division after fertilization are shown.

CREDIT: C. BICKEL/SCIENCE

Institute of Plant Biology and Zürich-Basel Plant Science Center, University of Zürich, Zollikerstrasse 107, 8008 Zürich, Switzerland. E-mail: grossnik@botinst.uzh.ch

Although membrane association through the diacyl modification and the repeats are essential for SSP function, the kinase domain is dispensable. These findings strongly suggest that SSP acts at the plasma membrane, possibly by recruiting a *YDA* pathway activator.

Interestingly, the *ssp* mutation affects early embryogenesis only if it is paternally inherited. Though parent-of-origin effects were already known to mule breeders in Asia Minor more than 3000 years ago (*7*), genetic parent-of origin effects were only recognized in the 1950s. In plants, which can be regenerated from single cells in culture through somatic embryogenesis, parental effects influencing embryogenesis were not thought to play a crucial role. In general, parent-of-origin effects can be mediated through nonnuclear, cytoplasmic contributions by the gametes or through the nonequivalent contribution of maternal and paternal alleles. The former is well illustrated by maternal effects in the fruit fly *Drosophila melanogaster*, where body axis determination depends on maternally stored cytoplasmic products (*8*). The latter, referred to as genomic imprinting, has only been described in mammals and seed plants. In *Arabidopsis*, both types of parent-of-origin effects likely exist. The first maternal effect gene identified in *Arabidopsis* turned out to be regulated by genomic imprinting (*9*). Furthermore, about half of the female gametophytic mutants isolated to date show defects in early seed development (*3*), and most of the paternally inherited genome is silent or active only at a low level during the first few embryonic divisions in maize and *Arabidopsis* (*10*, *11*). Both findings suggest that there may be extensive maternal control over early embryogenesis that is mediated, in part, by cytoplasmically stored products (*12*).

The mechanism by which *SSP* exerts its paternal effect may provide a means to subvert this maternal predominance. Bayer *et al.* show that mRNAs encoding *SSP* are only present in mature sperm cells, where they are apparently not translated into protein. By contrast, SSP protein is transiently detectable in the zygote and endosperm, suggesting that it is produced from paternally provided transcripts upon fusion of the egg and central cell with the sperm cells. Given the complex complement of transcripts present in plant sperm cells (*13*, *14*), more paternal effect genes may be discovered. Whether this mechanism evolved as a consequence of a parental conflict, as has been proposed for the evolution of genomic imprinting (*9*), remains to be determined.

The known mutations in *Arabidopsis* that disrupt imprinted loci show normal early embryonic development, but affect cell proliferation of embryo and endosperm at later stages and eventually lead to seed abortion. By contrast, *spp* mutants are viable and have no effect on endosperm development, but affect the very first, asymmetric division of the zygote. Thus, *SSP* transcripts delivered to the zygote by the sperm provide a molecular cue that links fertilization to the first zygotic division, which establishes apical-basal polarity of the embryo. This mechanism ensures that the activation of the *YDA* signaling pathway can only occur after fertilization and, thus, provides a temporal cue to initiate embryogenesis. Such a temporal cue would be of particular importance if most factors required for early development are already stored in the egg (*12*). This leaves the question, however, as to how embryonic activation is (de)regulated in apomictic plants, in which an egg develops into an embryo in the absence of fertilization (*15*). Is the *YDA* signaling pathway activated independently of *SSP*, or is *SSP* expressed from the maternal allele in the egg of apomictic plants? Future investigations will reveal how prominent paternal cues are to stimulate embryonic development, which predominantly depends on maternally provided factors, at least in animals and likely also in plants. In other words, how instructive is the Aristotelean paternal "form" to the maternal "matter"?

References

1. M. Cobb, *Nat. Rev. Genet.* **7**, 953 (2006).
2. E. B. Harvey, *Biol. Bull.* **71**, 101 (1936).
3. V. Brukhin *et al.*, *Curr. Sci.* **89**, 1844 (2005).
4. M. Bayer *et al.*, *Science* **323**, 1485 (2009).
5. W. Lukowitz *et al.*, *Cell* **116**, 109 (2004).
6. H. Wang, N. Ngwenyama, Y. Liu, J. C. Walker, S. Zhang, *Plant Cell* **19**, 63 (2007).
7. T. H. Savory, *Sci. Am.* **223**, 102 (1970).
8. C. Nüsslein-Vollhard, *Dev. Suppl.* **1**, 1 (1991).
9. U. Grossniklaus, in *Annual Plant Reviews: Plant Epigenetics*, P. Meyer, Ed. (Blackwell, Sheffield, UK, 2005), pp. 174–200.
10. D. Grimanelli *et al.*, *Plant Cell* **17**, 1061 (2005).
11. J.-P. Vielle-Calzada *et al.*, *Nature* **404**, 91 (2000).
12. C. Baroux *et al.*, *Cold Spring Harb. Symp. Quant. Biol.* 10.1101/sqb.2008.73.053 (2009).
13. F. Borges *et al.*, *Plant Physiol.* **148**, 1168 (2008).
14. M. L. Engel *et al.*, *Plant J.* **34**, 697 (2005).
15. R. A. Bicknell, A. M. Koltunow, *Plant Cell* **16** (suppl.) S228 (2004).

10.1126/science.1171412

CIRCADIAN RHYTHMS

Linking the Loops

C. Robertson McClung

A new module in the plant circadian clock provides a long-missing link in the oscillator.

The evolution of life on a rotating planet has placed a premium on the temporal coordination of biological function with dramatic daily changes in environment. Thus, organisms from cyanobacteria to humans have evolved circadian clocks, endogenous oscillators with periods approximating the solar day, which provide temporal organization of many biological processes. The circadian clocks of different taxonomic groups comprise unrelated proteins, suggesting multiple evolutionary origins. Despite this phylogenetic diversity, there is a common logic to the molecular circuitry of these clocks—they are composed of feedback loops with positive and negative components (*1*). On page 1481 of this issue, Pruneda-Paz *et al.* (*2*) solve a major puzzle in our understanding of the plant clock and provide mechanistic insight into the positive arm of a core oscillatory loop first described nearly a decade ago (*3*).

Circadian clocks are composed of multiple interlocked feedback loops (*1*). Such complexity may increase clock stability and enhance the flexibility of response to multiple exogenous and endogenous time cues, thus integrating environmental signals with metabolic and physiologic information (*4*). The resonance of the internal periodicity imposed by the endogenous circadian clock with the environmental period imposed by Earth's rotation is important for fitness. For example, net photosynthesis falls dramatically when internal and external periods diverge (*5*). Recently, it was shown that altered clock function contributes to the increased growth, called "hybrid vigor," observed in hybrids and allopolyploids (*6*).

The clock of the plant *Arabidopsis thaliana* includes at least three interlocked loops (*7*–*9*). The initial identification of a putative core clock feedback loop in plants came with the establishment of reciprocal regulation between two Myb transcription factors—CIRCADIAN CLOCK ASSOCIATED 1 (CCA1) and LATE ELONGATED HYPOCOTYL (LHY)—and a pseudo-response regulator (PRR) called TIMING OF CAB EXPRESSION 1 (TOC1) (*3*). CCA1 and LHY also participate in a second

---

Department of Biological Sciences, Dartmouth College, Hanover, NH 03755, USA. E-mail: c.robertson.mcclung@dartmouth.edu

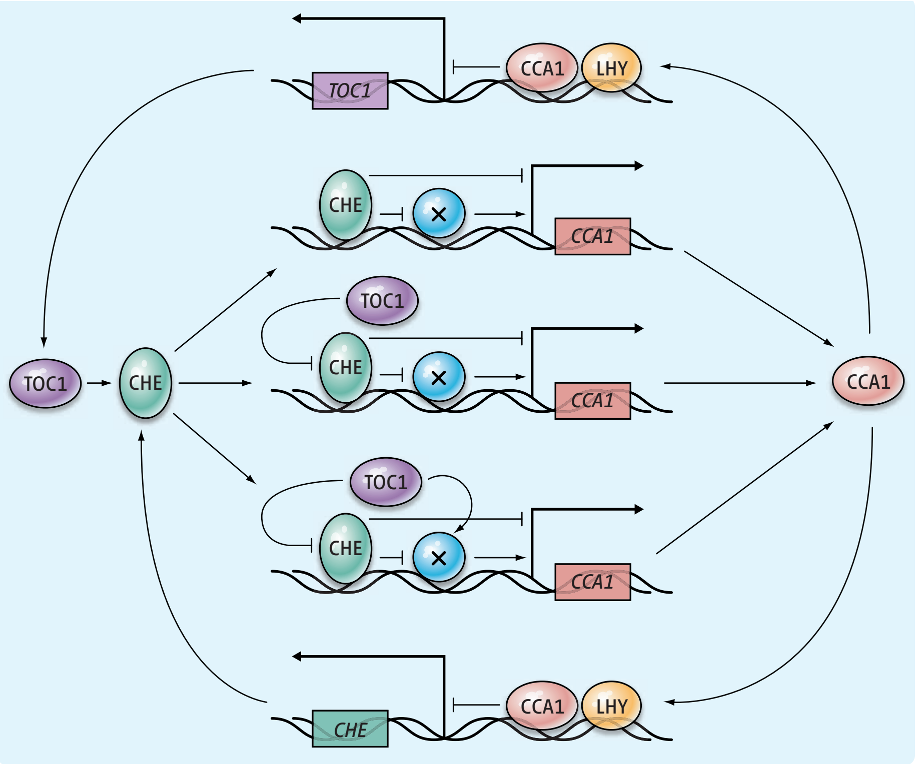

Plant clock architecture. The transcription factors CHE and CCA1 regulate each other through promoter binding. CHE may directly or indirectly (through some transcription factor X) repress *CCA1* expression. CCA1 (and LHY) negatively regulates *TOC1* expression through promoter binding. TOC1 binds to the *CCA1* promoter, and interacts with CHE, positively regulating *CCA1* expression. TOC1 may interact with both CHE and other transcription factors (X) at the *CCA1* promter to relieve repression of *CCA1* expression.

loop as positive regulators of a pair of TOC1 paralogs, PRR7 and PRR9. The latter pair feed back as negative regulators of CCA1 and LHY (*7*, *9*). TOC1 participates in a third loop as a negative regulator of component Y, which includes GIGANTEA, itself a positive regulator of TOC1 (*7*).

What of mechanism? In the core loop, CCA1 and LHY bind to the promoter region of the *TOC1* gene to repress its transcription, thus forming the negative arm of a feedback loop (*3*). Loss-of-function and overexpression experiments established TOC1 as a positive regulator of *CCA1* and *LHY* expression. Absent mechanistic insight, it was unclear whether the regulation of *CCA1* and *LHY* by TOC1 was direct or indirect. TOC1 lacks known DNA binding motifs, so if this regulation were direct, the underlying mechanism likely would involve partners that recruit TOC1 to the *CCA1* and *LHY* promoters. For some years, one of the major challenges of plant clock biology has been to establish the molecular link between TOC1 and the expression of *CCA1* and *LHY* (*10*). Pruneda-Paz *et al*. provide that link.

In plants, functional redundancy among transcription factors often limits the ability to identify key regulators through "forward genetics" (genetic screens for new genes). Accordingly, Pruneda-Paz *et al.* screened a library of clock-regulated *Arabidopsis* transcription factors for the ability to bind to the *CCA1* promoter and identified a transcription factor of the TCP class named CCA1 Hiking Expedition (CHE). CHE binds to a canonical TCP binding site in the *CCA1* promoter in vitro and in vivo. Curiously, CHE does not bind to the *LHY* promoter, distinguishing *CCA1* and *LHY* expression and leaving unresolved the puzzle of *LHY* regulation.

CHE overexpression decreases *CCA1* transcription, and *che* loss-of-function mutants show increased *CCA1* transcription, indicating that CHE, like LHY, is a repressor of CCA1. Circadian oscillation of *CCA1* expression is required for proper clock period. However, loss of CHE function does not alter the period length of the clock, consistent with redundancy of CHE with LHY and possibly other transcription factors for the negative regulation of *CCA1*. A *che lhy* double mutant shows greater period shortening than does the *lhy* mutant, further demonstrating the redundancy of CHE and LHY in *CCA1* repression.

The negative regulation of CHE on *CCA1* is reciprocated: CCA1 (and also LHY) binds to the *CHE* promoter both in vitro and in vivo to repress *CHE*. This identifies a new CHE-CCA1 loop in the *Arabidopsis* clock in which both components negatively regulate each other. Direct positive regulators of *CCA1* are not yet known. Genetic data identify LUX ARRHYTHMO (LUX) (*11*) and EARLY FLOWERING 4 (ELF4) (*12*, *13*) as positive regulators of CCA1 expression, but this could be via indirect means. Thus, it is certain that our understanding of this new loop will grow in complexity.

How does CHE close the loop between TOC1 and CCA1? Pruneda-Paz *et al*. show that CHE and TOC1 interact physically in a two-hybrid assay. Chromatin immunoprecipitation shows that both CHE and TOC1 are bound to the *CCA1* promoter at or near to the TCP binding site, which offers a mechanism by which TOC1 might affect *CCA1* expression. Perhaps CHE bound to the TCP site in the *CCA1* promoter recruits TOC1, which antagonizes the repressive effect of CHE on *CCA1* expression. However, things are unlikely to be this simple. Although CHE and TOC1 are in physical contact at the *CCA1* promoter, it is not known whether CHE is necessary to recruit TOC1 to the *CCA1* promoter; other transcription factors might in fact recruit TOC1. In addition, CHE antagonizes TOC1 function. TOC1 overexpression lengthens the circadian period (*14*), and this period lengthening is blocked by CHE overexpression. One possibility is that excess CHE sequesters TOC1, interfering with an interaction with other transcription factors bound to the *CCA1* promoter that is necessary for positive regulation of *CCA1* expression by TOC1.

The identification of CHE represents an important advance, but our understanding of *CCA1* regulation remains incomplete. Similarly, the picture of the regulation of the other genes constituting the clock remains fragmentary. Full understanding of the plant circadian clock mechanism needs more time.

References and Notes

1. H. Wijnen, M. W. Young, *Annu. Rev. Genet.* **40**, 409 (2006).
2. J. L. Pruneda-Paz *et al.*, *Science* **323**, 1481 (2009).
3. D. Alabadí *et al.*, *Science* **293**, 880 (2001).
4. D. A. Rand *et al.*, *J. Theor. Biol.* **238**, 616 (2006).
5. A. N. Dodd *et al.*, *Science* **309**, 630 (2005).
6. Z. Ni *et al.*, *Nature* **457**, 327 (2009).
7. J. C. W. Locke *et al.*, *Mol. Syst. Biol.* **2**, 59 (2006).
8. C. R. McClung, *Plant Cell* **18**, 792 (2006).
9. M. N. Zeilinger *et al.*, *Mol. Syst. Biol.* **2**, 58 (2006).
10. C. R. McClung, *Curr. Opin. Plant Biol.* **11**, 5213 (2008).
11. S. P. Hazen *et al.*, *Proc. Natl. Acad. Sci. U.S.A.* **102**, 10387 (2005).
12. E. A. Kikis *et al.*, *Plant J.* **44**, 300 (2005).
13. H. G. McWatters *et al.*, *Plant Physiol.* **144**, 391 (2007).
14. P. Más *et al.*, *Plant Cell* **15**, 223 (2003).

15. Supported by NSF grant IOB-0517111.

10.1126/science.1171418

CREDIT: C. BICKEL/SCIENCE

Time-Variable Deformation in the New Madrid Seismic Zone

Eric Calais[1] and Seth Stein[2]

At plate boundary faults, a balance is achieved over <1000 years between the rates at which strain accumulates and is released in large earthquakes. Whether this steady-state model, which forms the basis for seismic hazard estimation, applies to continental plate interiors, where large earthquakes are infrequent, is unresolved. The New Madrid Seismic Zone (NMSZ, Fig. 1A) in North America is a focus for this issue. Large-magnitude ($M > 7$) earthquakes in 1811 and 1812 make hazard estimation a priority. Recent geodetic results have shown motions between 0 to 1.4 mm year^{-1}, allowing opposite interpretations (*1*) (Fig. 1B). The upper bound is consistent with steady-state behavior, in which strain accumulates at a rate consistent with a repeat time for magnitude ~ 7 earthquakes of about 600 to 1500 years, as seen in the earthquake record. However, the lower bound cannot be reconciled with this record, implying that the recent cluster of large-magnitude events does not reflect long-term fault behavior and may be ending.

New analysis including 3 additional years of Global Positioning System (GPS) data and three additional sites (*2*) shows root mean square (RMS) velocities relative to the rigid interior of North America of less than 0.2 mm year^{-1} (Fig. 1C). These residual velocities are below their uncertainties at 95% confidence (Fig. 1A). A simulation shows that even these residuals can be explained as nontectonic artifacts (*2*), so the observations do not require motions different from zero during this time. Our results correspond to strain rates lower than 1.3×10^{-9} year^{-1}, less than predicted by a model in which large earthquakes occur because the NMSZ continues to be loaded as a deeper weak zone relaxes (*3*).

At steady state, a rate of 0.2 mm year^{-1} implies a minimum repeat time of 10,000 years for low $M = 7$ earthquakes with ~2 m of coseismic slip and one longer than 100,000 years for $M = 8$ events (Fig. 1D). In contrast, the geologic data show a series of large earthquakes between 300 ± 200 Common Era and present and an additional cluster between 2200 and 1600 Before the Common Era (*4*). This implies an average repeat time of at most 900 years over that interval, much shorter than the geodetic data imply. Strain in the NMSZ over the past several years has therefore accumulated too slowly to account for seismicity over the past ~5000 years, hence excluding steady-state fault behavior.

Elsewhere throughout the plate interior, GPS data also show average deformation less than 0.7 mm year^{-1} (*5*), and paleoseismic records show earthquake migration and temporal earthquake clustering (*6*).

These data imply that fault loading, strength, or both vary with time in the North American continental interior. Time variations in stress could be due to local loading and unloading from ice sheets or sediments or after earthquakes on other faults. Alternatively, midcontinent faults may be loaded at a constant rate too small to be detected geodetically yet but sufficient to accumulate strain released in clustered events. In this hypothesis, clustering and migration could reflect time variations in fault strength (*7*).

Earthquake hazard estimates assuming that recent seismicity reflects long-term steady-state behavior may thus be inadequate for plate interiors and may overestimate the hazard near recent earthquakes and underestimate it elsewhere.

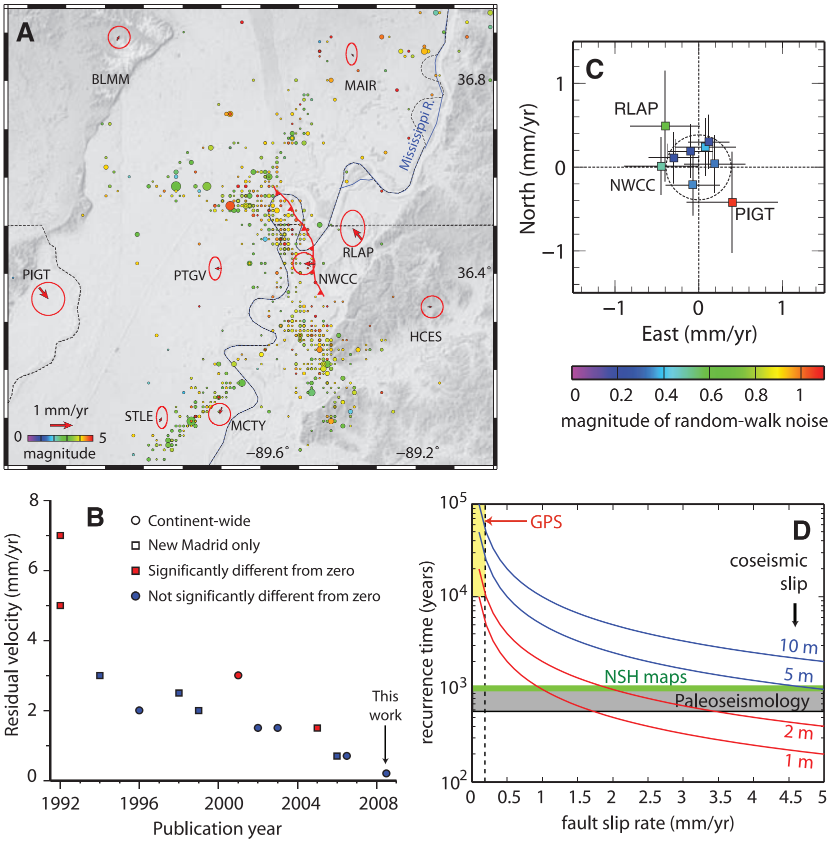

Fig. 1. (**A**) GPS site velocities in the NMSZ relative to North America and uncertainties (95% confidence). Circles show earthquake epicenters since 1974. Red line shows the Reelfoot fault. BLMM, HCES, MAIR, MCTY, NWCC, PIGT, PTGV, RLAP, and STLE indicate the names of the continuous GPS stations used in this work (*2*). (**B**) Maximum permissible deformation rates in the NMSZ as a function of publication year. References are listed in (*2*). Circles show continent-wide studies; squares show NMSZ studies. Red are publications claiming rates significantly different from zero; blue are upper bounds for publications claiming rates not significantly different from zero. The decrease in rates as a function of time reflects more-precise site velocity estimates because of both more precise site positions and the longer time span of observations. (**C**) Scatter plot of residual velocities. Sites are color-coded by the level of noise in their position time series. Bars show 95% error in velocities. Dashed circle shows 1-σ RMS of the data set. Note that sites with the largest noise have the largest residuals. (**D**) Earthquake recurrence interval as a function of slip rate across the fault in a steady-state model, with two end-member values of coseismic slip for magnitude 7 (red curves) and magnitude 8 (blue curves) earthquakes. The GPS and paleoseismology domains do not overlap. NSH indicates National Seismic Hazard maps.

References and Notes

1. E. Calais *et al.*, *Nature* **438**, 10.1038/nature04428 (2005).
2. Materials and methods are available as supporting material on *Science* Online.
3. S. J. Kenner, P. Segall, *Science* **289**, 2329 (2000).
4. J. Holbrook *et al.*, *Tectonophysics* **420**, 431 (2006).
5. E. Calais *et al.*, *J. Geophys. Res.* **111**, 10.1029/2005JB004253 (2006).
6. A. Crone *et al.*, *Bull. Seismol. Soc. Am.* **93**, 1913 (2003).
7. Q. Li *et al.*, *Bull. Seismol. Soc. Am.* **99**, 52 (2009).

Supporting Online Material

www.sciencemag.org/cgi/content/full/323/5920/1442/DC1
Materials and Methods
Fig. S1
References and Notes

5 November 2008; accepted 9 February 2009
10.1126/science.1168122

---

[1] Department of Earth and Atmospheric Sciences, Purdue University, West Lafayette, IN 47906, USA. [2] Department of Earth and Planetary Sciences, Northwestern University, Evanston, IL 60208, USA.

Wind-Driven Upwelling in the Southern Ocean and the Deglacial Rise in Atmospheric CO_2

R. F. Anderson,[1,2]* S. Ali,[1,2] L. I. Bradtmiller,[1,2]† S. H. H. Nielsen,[3] M. Q. Fleisher,[1]
B. E. Anderson,[1] L. H. Burckle[1]

Wind-driven upwelling in the ocean around Antarctica helps regulate the exchange of carbon dioxide (CO_2) between the deep sea and the atmosphere, as well as the supply of dissolved silicon to the euphotic zone of the Southern Ocean. Diatom productivity south of the Antarctic Polar Front and the subsequent burial of biogenic opal in underlying sediments are limited by this silicon supply. We show that opal burial rates, and thus upwelling, were enhanced during the termination of the last ice age in each sector of the Southern Ocean. In the record with the greatest temporal resolution, we find evidence for two intervals of enhanced upwelling concurrent with the two intervals of rising atmospheric CO_2 during deglaciation. These results directly link increased ventilation of deep water to the deglacial rise in atmospheric CO_2.

Scientists have long sought to unravel the combination of physical and biogeochemical processes responsible for the tight coupling between atmospheric CO_2 concentrations and Earth's climate that has persisted for at least the last 600,000 years (*1*), with the expectation that knowledge of the processes linking CO_2 and climate in the past will improve projections of future climate change under rising anthropogenic CO_2 levels. It is believed that no single mechanism can account for the full amplitude of past CO_2 variability (*2*, *3*). Although multiple processes operating synergistically may be involved (*4*, *5*), there is general agreement that lower CO_2 levels during glacial periods require increased (relative to interglacials) isolation of deep-water masses from the atmosphere—for example, by increased stratification in the ocean (*2*, *4*–*8*).

Previous studies [e.g., (*2*, *9*)] have inferred a vital role for the Southern Ocean in regulating glacial-interglacial variability of atmospheric CO_2 because deep-water masses outcrop in the Southern Ocean and exchange gases with the atmosphere. Indirect evidence favoring Southern Ocean control includes the tight coupling between CO_2 and Antarctic temperatures (*1*, *10*–*12*); the phase relationship between CO_2 and other environmental parameters during deglaciation (*5*, *13*, *14*); the widespread distribution of ^{13}C-depleted carbon, most likely of deep-sea origin, that invaded the upper ocean and atmosphere during deglaciation (*4*, *15*, *16*); and the precipitous drop during deglaciation in ^{14}C activity of dissolved inorganic carbon (DIC) in North Pacific intermediate waters, requiring injection of carbon from a reservoir long isolated from the atmosphere, such as the deep sea (*17*). However, until now there has been no direct evidence for a change in Southern Ocean circulation that could have altered substantially the partitioning of CO_2 between the atmosphere and the deep sea.

Biogenic opal as an upwelling proxy. Burial of biogenic opal, the microscopic tests of marine diatoms, provides a link to past changes in upwelling and ventilation of deep-water masses in the Southern Ocean. Diatoms live in the euphotic zone where they use dissolved silicic acid (H_4SiO_4) to form opal tests. The zone of maximum production of biogenic silica (opal) occurs just south of the Antarctic Polar Front (APF) (*18*, *19*), corresponding to the region of maximum supply of dissolved nutrients (including Si) to surface waters by upwelling of nutrient-rich deep-water masses (Fig. 1) (*20*).

Within the zone of maximum opal production, diatom growth throughout spring and summer typically depletes surface waters of dissolved Si supplied during the previous winter (*20*, *21*). Consequently, although the physiological status and growth rate of individual diatom cells may be limited by iron (*22*), the total amount of biogenic opal produced each year within this region is ultimately limited by the supply of dissolved Si (*18*–*20*). Therefore, past changes in the production and burial of opal within this region are tied directly, although not necessarily linearly, to the rate of upwelling.

Deglacial changes in upwelling. Three sediment cores (TN057-13PC, NBP9802-6PC, and E27-23PC; Fig. 2) with relatively high accumulation rates [10 to 20 cm/kyr (10^3 years)] were

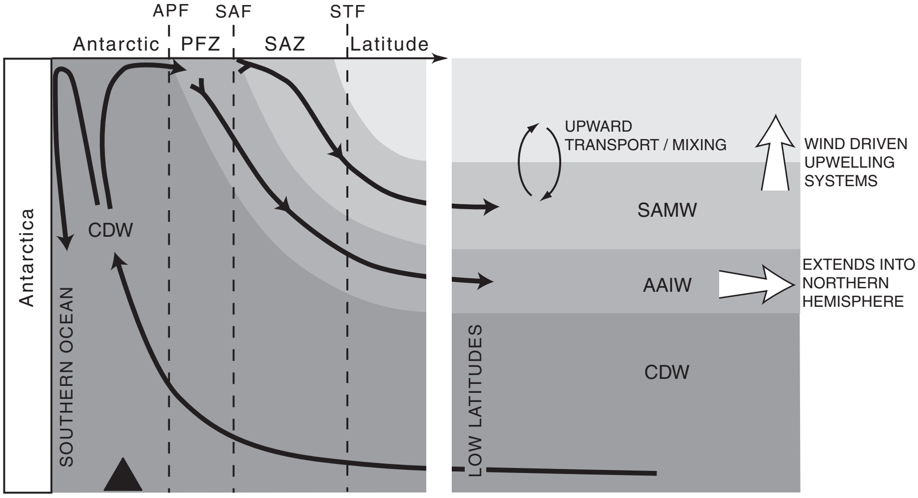

Fig. 1. Water masses entering and leaving the Southern Ocean. Wind-driven upwelling brings Circumpolar Deep Water (CDW) to the surface within the zone south of the Antarctic Polar Front (APF). A portion of the upwelled water moves southward and loses buoyancy, eventually forming Antarctic Bottom Water along the coast of Antarctica. The remainder of the upwelled water moves northward at the surface under the forcing by the prevailing westerlies. Part of the Antarctic surface water mixes with subtropical surface water to form Subantarctic Mode Water (SAMW), a water mass that feeds the thermocline of the Southern Hemisphere (SH) oceans. The densest form of surface water becomes Antarctic Intermediate Water (AAIW), which may be traced northward beyond the equator. Nutrients carried by SAMW are mixed into the surface layer throughout the SH oceans, but especially in upwelling regions such as the eastern equatorial Pacific Ocean (*21*). The Polar Front Zone (PFZ) and Subantarctic Zone (SAZ) are the regions between the APF and Subantarctic Front (SAF), and between the SAF and Subtropical Front (STF), respectively. Approximate location of cores used in this study from sites just south of the APF is shown by a triangle at the bottom. This figure is modified from figure 4 in (*21*).

---

[1] Lamont-Doherty Earth Observatory of Columbia University, Post Office Box 1000, Palisades, NY 10964, USA. [2] Department of Earth and Environmental Sciences, Columbia University, New York, NY 10027, USA. [3] Antarctic Marine Geological Research Facility, Florida State University, Tallahassee, FL 32306, USA.

*To whom correspondence should be addressed. E-mail: boba@ldeo.columbia.edu

†Present address: Department of Marine Chemistry and Geochemistry, Woods Hole Oceanographic Institution, Woods Hole, MA 02543, USA.

selected to provide high-resolution records of opal accumulation during the most recent deglaciation. A fourth core, TN057-14PC, was studied to produce an opal flux record for the last glacial period. The age model for E27-23PC was based initially on biostratigraphy and then was refined with ^{14}C dates of mixed planktonic foraminifera (tables S1 and S2 and fig. S1). We developed an age model for TN057-14PC using biostratigraphy (tables S3 and S4 and fig. S3) that compares well with a published age model (*23*) based on ^{14}C and ^{18}O (fig. S4). We used published age models for the other cores (*24*, *25*). Opal concentrations were measured spectrophotometrically after alkaline dissolution (*26*). Sediment burial rates, corrected for sediment focusing, were evaluated with the ^{230}Th-normalization method (*27*). Uranium and Th isotopes, together with ^{231}Pa, were measured by inductively coupled plasma mass spectrometry (*28*). A summer (February) sea surface temperature (SST) record for TN057-13PC, constructed by applying the modern analog technique (*29*, *30*) to diatom species assemblages measured at ~50-year resolution, is taken from Nielsen (*31*).

Each of the three deglacial records (Fig. 3) exhibits a rapid increase in opal flux coinciding with the onset of deglaciation at about 17,000 years ago (ka), followed by a deglacial maximum and declining fluxes into the Holocene (after ~10 ka). Most of the opal produced by diatoms in the Southern Ocean is regenerated, either in the water column or during early sediment diagenesis (*18*, *19*), complicating the interpretation of opal fluxes. Therefore, an independent proxy is required to discriminate between changes in opal production (Si supply) versus changes in opal preservation as the ultimate cause of the deglacial maximum in opal burial.

To discriminate between production and preservation of opal, we measured the ^{231}Pa/^{230}Th ratio of the sediments. Like ^{230}Th, ^{231}Pa is produced uniformly throughout the ocean by radioactive decay of dissolved uranium, and both isotopes are removed from seawater by scavenging onto sinking particles (*32*). However, ^{231}Pa has a strong affinity for sorption to biogenic opal, and ^{231}Pa/^{230}Th ratios of particulate material throughout the open ocean are tightly correlated with the opal content of particles (*33*). Although ^{231}Pa/^{230}Th ratios of sinking particles and sediments are influenced by particle flux as well as by the opal content of particles, the strong correlation between ^{231}Pa/^{230}Th ratio and opal flux (*25*, *34*, *35*) in many sediment records supports the view that opal flux is the primary variable determining sedimentary ^{231}Pa/^{230}Th ratios. Furthermore, particulate ^{231}Pa/^{230}Th ratios are not altered by loss of biogenic phases during early diagenesis of sediments (*36*), allowing the downcore record of ^{231}Pa/^{230}Th ratios to be interpreted in terms of past changes in opal flux. Based on the positive correlation between ^{231}Pa/^{230}Th and opal flux in each of our records (Fig. 3), we conclude that the deglacial maximum in opal flux reflects past changes in opal production and Si supply rather than variable opal preservation.

Reconstructed opal fluxes indicate maximum rates during deglaciation in each sector of the Southern Ocean (Fig. 3). Shifting circulation patterns and biogeographic provinces to the north or south will not lead to greater biogenic silica production than that occurring today because the core sites are all from the region of maximum dissolved Si supply and opal production in the modern ocean (see above). Therefore, we conclude that the supply of dissolved Si to surface waters south of the APF, which is intimately linked to upwelling of deep-water masses, was at its maximum during deglaciation.

Impact on low-latitude surface waters. Enhanced upwelling in the Southern Ocean during deglaciation would have introduced a chemical signature during the formation of Antarctic Intermediate Water (AAIW) and Subantarctic Mode Water (SAMW), water masses that entrain upwelled deep water during their formation (Fig. 1). Mode waters carry a chemical signature from upwelled deep water (e.g., nutrient concentrations, δ^{13}C of DIC) throughout the thermocline of the Southern Hemisphere. This chemical signature is transmitted to surface waters via upward mixing, and it is particularly strong in upwelling regions (*21*). Spero and Lea (*16*) invoked this mechanism to explain the deglacial minimum in δ^{13}C of planktonic foraminifera that is observed at many sites throughout the Southern Hemisphere, as well as in a record of the δ^{13}C of atmospheric CO$_2$ derived from the Taylor Dome ice core (*15*). However, others have been reluctant to use the δ^{13}C of planktonic foramininfera as a proxy for entrainment of upwelled deep water because vital effects can overprint the δ^{13}C signature from DIC that is incorporated into the shells of foraminifera (*4*). Therefore, we sought evidence for deep-water injection into the thermocline that would be independent of these effects.

If the deglacial minimum in δ^{13}C of planktonic foraminifera were truly a chemical signature of increased upwelling of deep water in the Southern Ocean, then one would expect a contemporary maximum in the supply of dissolved Si and, therefore, in the growth of diatoms in low-latitude regions where water masses originating in the Southern Ocean are known to upwell. This is expected because deep waters are enriched in dissolved Si just as they are in ^{13}C-depleted DIC. To test this prediction, we have determined the accumulation rate of opal at a site in the eastern equatorial Pacific Ocean (EEP), where SAMW upwells today (*37*) and near the site studied by Spero and Lea (*16*). There, we find a clear correlation between the deglacial minimum in δ^{13}C of *Neogloboquadrina dutertrei* and a corresponding maximum in the

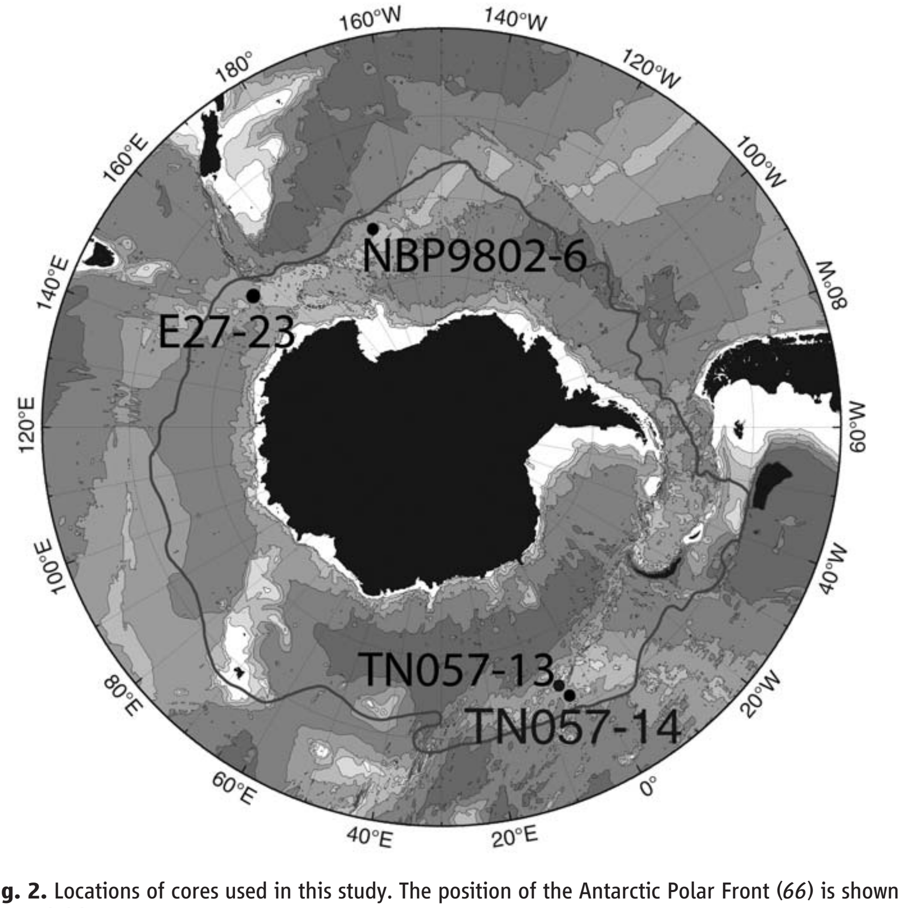

Fig. 2. Locations of cores used in this study. The position of the Antarctic Polar Front (*66*) is shown as a solid line.

accumulation rate of opal (Fig. 4). *N. dutertrei* is the preferred species to use in such a comparison because it inhabits the deep mixed layer and upper thermocline, thereby providing the purest record of changes in the chemical composition of waters derived from the Southern Ocean (*16*).

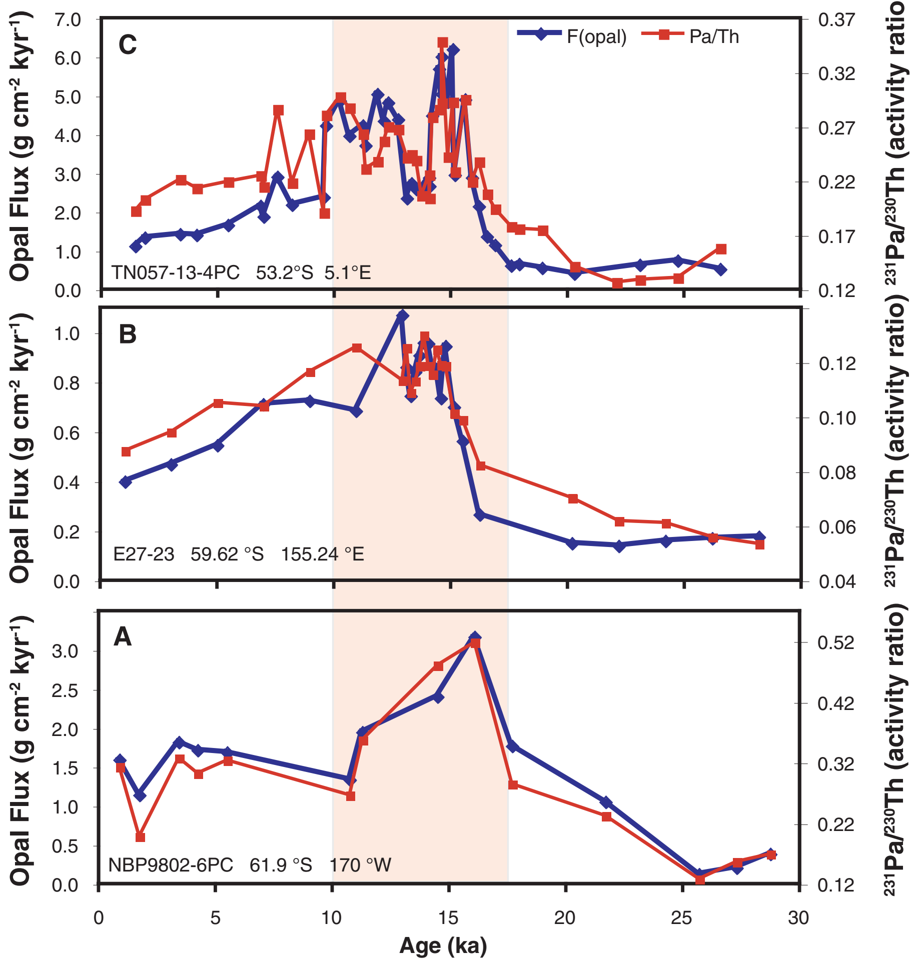

Fig. 3. Opal fluxes, a proxy for upwelling south of the Antarctic Polar Front, from three sites in the Southern Ocean. Increased upwelling during the deglacial period, roughly 17,000 to 10,000 years ago (highlighted in shaded box), is evident in opal fluxes at sites in the Pacific (**A**), Indian (**B**), and Atlantic (**C**) sectors of the Southern Ocean. Initial unsupported $^{231}Pa/^{230}Th$ ratios mirror the pattern of opal flux in each core, supporting the view that the opal flux reflects changes in upwelling and opal production rather than changes in opal preservation (see text). Results plotted in (A) are from (*25*).

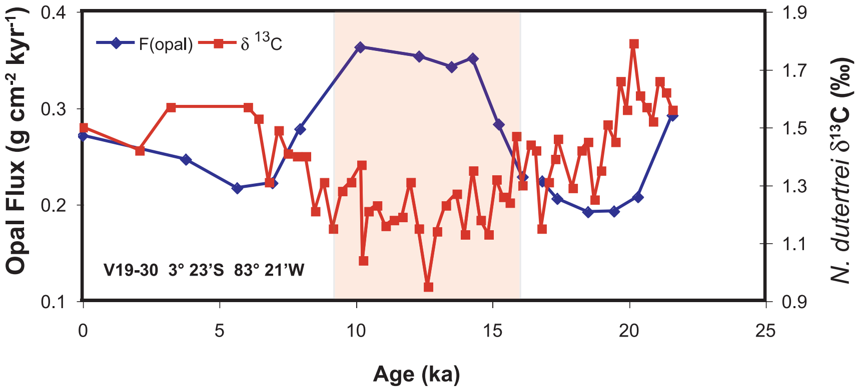

Fig. 4. Two proxy records exhibiting a chemical signature of Southern Ocean water reaching the surface of the eastern equatorial Pacific Ocean. The deglacial minimum in $\delta^{13}C$ of *N. dutertrei* and the corresponding maximum in opal flux (shaded interval) are both consistent with increased supply of nutrient-rich deep water upwelled in the Southern Ocean during this period (*16*). Original $\delta^{13}C$ data from (*67*); opal data from (*34*).

Sediment records from other sites in the EEP have also been shown recently to contain a deglacial maximum in opal accumulation (*34*, *38*), indicating that the feature illustrated in Fig. 4 is widespread. Subsequent work has found the deglacial maximum in opal flux to have occurred throughout the equatorial Atlantic Ocean, as well (*35*). Although other factors (e.g., changes in local upwelling) could have influenced these opal burial records, they are independent of the vital effects thought to overprint the $\delta^{13}C$ of planktonic foraminifera. Consequently, we interpret the widespread deglacial minimum in $\delta^{13}C$ of planktonic foraminifera (*16*), concurrent with the deglacial maximum in opal burial in equatorial upwelling regions, to reflect a period of enhanced entrainment of nutrient-rich deep water during the formation of SAMWs that eventually surface in tropical upwelling regimes.

Link to atmospheric CO_2. Increased upwelling in the Southern Ocean, inferred from the opal flux records, coincided with the deglacial warming in Antarctica, as well as with the rise in atmospheric CO_2 (Fig. 5, A, C, and D). In TN057-13, the sediment record with the highest temporal resolution, the opal flux declined during the Antarctic Cold Reversal (ACR; ~14.5 to ~12.5 ka), corresponding to a plateau in CO_2 concentration. Although precise age control is lacking for portions of the TN057-13 record, the timing of the ACR is constrained reliably by a radiocarbon date just before its onset (Fig. 5) and by the SST record from this core. Within the resolution of the sample intervals, the decrease in upwelling coincided with the reduction in SST corresponding to the ACR (Fig. 5, B and C). Furthermore, the ACR is also manifest in TN057-13 sediments as a local maximum in the $\delta^{18}O$ of planktonic foraminifera and by a maximum in the abundance of ice-rafted debris (*24*), both expected consequences of cooling during the ACR. Increased upwelling resumed following the ACR, coinciding with the second phase of Antarctic warming and rising CO_2 (Fig. 5). The overall timing and character of events recorded in the upwelling proxy record from TN057-13, including the mid-deglacial interruption of upwelling, lead us to conclude that enhanced upwelling of the Southern Ocean was a primary contributor to the deglacial rise in atmospheric CO_2.

During deglaciation, the $\Delta^{14}C$ of atmospheric CO_2 dropped by 15 to 20% (Fig. 5E), a much greater change than can be attributed to a contemporary decrease in ^{14}C production, thereby requiring dilution of atmospheric CO_2 with carbon from an older (lower $\Delta^{14}C$) reservoir (*39*, *40*). Ventilation of the deep ocean around Antarctica, as proposed here, would have supplied the necessary ^{14}C-depleted carbon by exposing the atmosphere to DIC that had been isolated in the deep sea for centuries, if not millennia. Like the rise in atmospheric CO_2, the deglacial drop in $\Delta^{14}C$ exhibited a pause coinciding approximately with the reduced upwelling in the Southern Ocean (Fig. 5). Marchitto *et al.*

(*17*) linked the atmospheric Δ^{14}C record to upwelling in the Southern Ocean when interpreting the ^{14}C ages of benthic foraminifera in a core from intermediate depth off the west coast of Mexico. Their results show an injection of ^{14}C-depleted DIC into intermediate waters during deglaciation, occurring in two pulses that coincided with the intervals of rising atmospheric CO_2. Marchitto *et al*. inferred that the injection of ^{14}C-depleted DIC was a consequence of increased overturning in the Southern Ocean, with the signal being transmitted via AAIW (Fig. 1). Opal fluxes reported here support the interpretation of Marchitto *et al*., showing periods of increased upwelling coincident with rising atmospheric CO_2 and declining Δ^{14}C of CO_2 (Fig. 5).

The deep North Atlantic Ocean. Deglacial changes in the ventilation of the Southern Ocean were associated with deep-water signals at locations as distant as the high-latitude North Atlantic Ocean. For example, coincident with the increased upwelling in the Southern Ocean, deep waters at ~40°N in the Atlantic Ocean are inferred to have borne an Antarctic Δ^{14}C signature (*41*), at a time when sedimentary ^{231}Pa/^{230}Th ratios are also interpreted to indicate a shutdown of North Atlantic Deep Water formation (*42*). Furthermore, upper deep waters at ~60°N had a strong Antarctic δ^{13}C signature (*43*) during deglaciation, with a pattern of temporal variability resembling that of the upwelling record from the Southern Ocean (fig. S2).

Northern Hemisphere trigger and atmospheric teleconnection. Two general conditions are believed to have contributed to increased overturning of the Southern Ocean during deglaciation. Watson and Garabato (*6*) invoked increased heat fluxes into the ocean as a consequence of rising air temperatures. They reasoned that the downward mixing of this surface buoyancy flux would favor increased upwelling. Toggweiler (*7*) called upon a poleward shift in the mean position of the Southern Hemisphere (SH) Westerlies, with a corresponding increase in northward Ekman transport of surface waters. We propose a combination of these conditions linked to initial forcing within the North Atlantic followed by transmission of the signal to the Southern Ocean via a reorganization of atmospheric circulation.

The onset of rapid warming in Antarctica and the deglacial rise in atmospheric CO_2 concentration coincided with the interval of intense cold in the North Atlantic region surrounding Heinrich Event 1 (HE1) (*8*, *17*, *44*). A north-south linkage is further supported by the coincident interruption of Antarctic warming and CO_2 rise during the Bølling-Allerød period of warmth in the north, and the resumption of Antarctic warming and CO_2 rise during the Younger Dryas (YD), another period of intense cold in the Northern Hemisphere (NH). Recent studies have presented evidence for a global reorganization of atmospheric circulation during NH cold events such as HE1 and the YD. Paleo proxy evidence for a southward shift in the Intertropical Convergence Zone (ITCZ) during HE1 and/or the YD is found in records from Africa (*45*, *46*), Asia (*47*), and South America (*48*–*50*). Modeling studies suggest that a southward shift in the ITCZ is a robust feature of atmospheric reorganization, regardless of whether cold NH conditions are induced by imposing sea ice (*51*) or fresh water (*52*, *53*) on the North Atlantic Ocean.

Less attention has been paid to the westerlies, but lake sediments in Germany record a substantial reorganization of NH westerlies during the YD (*54*), while rising levels of paleo Lake Lahontan in the western United States during HE1 and the YD are consistent with a southward shift of the NH westerlies during those intervals (*55*). A rapid warming of SSTs off the coast of Chile at the onset of HE1, and again during the YD, has been attributed to a southward shift of the SH westerlies (*44*). In support of these findings, five coupled General Circulation Models exhibit a southward displacement of the SH westerlies and an intensification of wind stress at the latitude of the Drake Passage when cold NH conditions are induced by imposing fresh water on the North Atlantic Ocean (*56*).

An increase in wind stress at the latitude of the Drake Passage is thought to be a key factor regulating upwelling in the Southern Ocean (*7*). However, enhanced wind stress alone may have been insufficient to increase upwelling. A corresponding increase in baroclinicity of the Antarctic Circumpolar Current would have established a southward eddy transport that largely offset the increase in northward Ekman transport caused by the winds (*57*). Therefore, it may be necessary to invoke increased buoyancy forcing, possibly caused by the southward shift of the SH westerlies, via a combination of increased sea-ice divergence, increased precipitation, and direct warming (*6*), to complement the increased wind stress (*7*) and fully account for the deglacial increase in upwelling evident in our records (Figs. 3 and 5).

Corresponding events during the last glacial period. Atmospheric CO_2 concentrations rose by 10 to 20 parts per million (ppm) during periods of intense NH cooling throughout the last glacial period (*12*). Rising CO_2 coincided both with Heinrich Events (between 30 and 60 ka) and with cold intervals before interstadials 19, 20, and 21 (60 to 90 ka). These NH cold intervals corresponded to the warming phase of Antarctic warm events A1 to A7 (*58*).

Evidence from low latitudes for changes in hydrological conditions at times of NH cooling—for example, in Chinese cave deposits (*47*) and in the Cariaco Basin (*48*)—suggests that a global reorganization of atmospheric circulation similar to that proposed for the last deglaciation may have occurred at those times. If true, then shifts in the SH wind system may have been responsible for rising atmospheric $CO_{2,}$ and one would expect to find evidence for contemporary increases of upwelling in the Southern Ocean.

To test this possible link between NH cooling and upwelling in the Southern Ocean, we measured the opal accumulation rate in core TN057-14PC, which was recovered from a site ~1° north of the location of TN057-13PC (Fig.

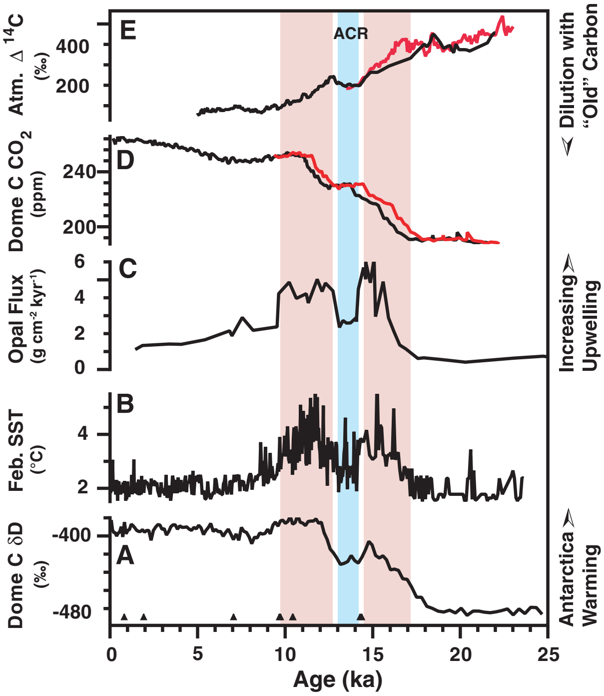

Fig. 5. Deglacial records illustrating the coupling between warming in Antarctica, upwelling in the Southern Ocean, and rising atmospheric CO_2. (**A**) Deuterium proxy for air temperature over Antarctica from the EPICA Dome C ice core on the EDC1 time scale (*68*). (**B**) February SST estimated by applying the modern analog technique (*29*, *30*) to diatom species assemblages extracted from TN057-13PC (*31*). (**C**) Opal flux from TN057-13PC (Fig. 3) as a proxy for upwelling in the Southern Ocean. Opal flux and February SST are plotted on the published age model for TN057-13PC (*24*), based partly on ^{14}C ages from depths in the core indicated by triangles at the bottom of the graph. (**D**) Atmospheric CO_2 concentrations reconstructed from analysis of the European Project for Ice Coring in Antarctica (EPICA) Dome C (EDC) ice core samples. The black curve is on the EDC1 age model (*11*, *69*). The red curve is the same data placed on the age model of the Greenland Ice Sheet Project 2 (GISP2) ice core (*17*). (**E**) Radiocarbon content of atmospheric CO_2. The black curve is the INTCAL reconstruction (*70*). The red curve is the Cariaco Basin record placed on the Hulu Cave age scale (*40*). Periods of warming in Antarctica are highlighted in red, while the Antarctic Cold Reversal (ACR) is highlighted in blue. The age model for TN057-13 is not constrained well enough during the onset of deglaciation to establish a lead or lag relationship between the onset of increased upwelling and the initial increase in atmospheric CO_2.

2). Because of changes in the dynamics of the Antarctic Circumpolar Current, conditions that led to the preferential deposition of sediment (sediment focusing) at the site of TN057-13PC during deglaciation were located farther north during the last glacial period. Consequently, it is necessary to combine records from multiple sites when constructing a high-resolution record of opal flux throughout the last glacial cycle. During the interval between 30 and 60 ka, when we have the best constraints on the age model of TN057-14PC (see Supporting Online Material), the opal flux record provides evidence for increased upwelling associated with each period of elevated CO_2 (Fig. 6). Uncertainties in the age model for TN057-14PC do not allow for meaningful assessments of apparent lead-lag relationships between upwelling and CO_2. Rather, the principal conclusion to be drawn from these results is that each interval of elevated CO_2 was accompanied by a period of increased upwelling.

Before 60 ka, constraints for the age model of TN057-14PC are less robust. Nevertheless, the opal flux record indicates increased upwelling associated with Antarctic warm events A5 and A6, and possibly with A7 (Fig. 6). We interpret the general correspondence of elevated CO_2 and increased upwelling with periods of intense NH cooling to indicate a common mechanism operating throughout the last glacial period, as well as during deglaciation. In each case, intense NH cooling induced a reorganization of global atmospheric circulation, leading to a southward shift in the SH westerlies, increased upwelling in the Southern Ocean, and rising atmospheric CO_2 levels. Complementary evidence for a northward shift in the SH westerlies and reduced ventilation of deep water in the Southern Ocean at the onset of glaciation supports this interpretation of a governing role for SH winds (*59*).

Implications for the future. A southward displacement and intensification of the SH westerlies has been observed in recent decades (*60–62*). The implications for ocean-atmosphere exchange of CO_2, and for future ocean uptake of anthropogenic CO_2, have been the subject of discussion and debate (*63–65*). Our evidence for the response of the Southern Ocean to past shifts in the winds may help guide the further development of models used to predict future CO_2 fluxes in this critical region for the exchange of CO_2 between the atmosphere and the deep sea.

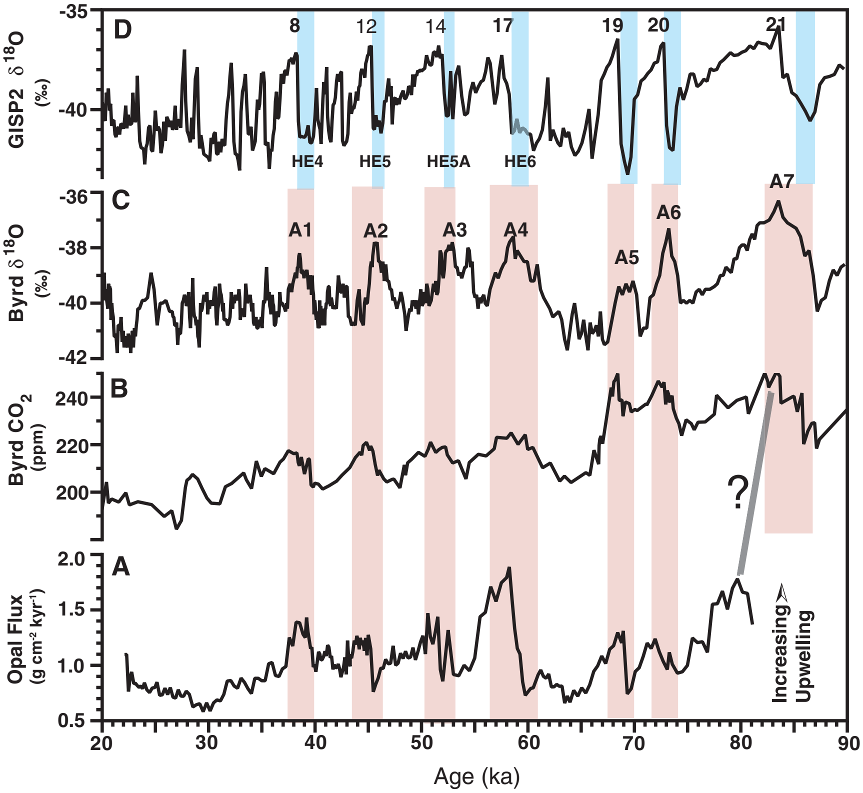

Fig. 6. Records from the last glacial period illustrate the coupling between warming in Antarctica, upwelling in the Southern Ocean, and rising atmospheric CO_2. (**A**) Opal flux proxy for upwelling in core TN057-14PC (51°59.059'S, 4°30.976'E, 3648 m; Fig. 2) on the GISP2 time scale (figs. S3 and S4). (**B**) Atmospheric CO_2 from the Byrd ice core on the GISP2 time scale (*12*). (**C**) $\delta^{18}O$ of ice in the Byrd ice core on the GISP2 time scale (*58*). (**D**) $\delta^{18}O$ of ice in the GISP2 ice core as reproduced in (*58*). Selected interstadials are labeled in (D). Antarctic warm events (*58*) are labeled in (C). Blue vertical bars indicate Heinrich Events (*71*) and cold intervals before interstadials 19 to 21. Red vertical bars indicate periods of relative warmth in Antarctica that include increased upwelling and elevated CO_2. The gray tie-line indicates a possible correlation between upwelling and CO_2 at the bottom of the TN057-14PC record, corresponding to A7, where the age model has an uncertainty of ~5 ka (fig. S4).

References and Notes

1. U. Siegenthaler *et al.*, *Science* **310**, 1313 (2005).
2. D. M. Sigman, E. A. Boyle, *Nature* **407**, 859 (2000).
3. D. Archer, A. Winguth, D. Lea, N. Mahowald, *Rev. Geophys.* **38**, 159 (2000).
4. P. Köhler, H. Fischer, G. Munhoven, R. E. Zeebe, *Global Biogeochem. Cycles* **19**, GB4020 10.1029/2004GB002345 (2005).
5. S. Peacock, E. Lane, J. M. Restrepo, *Global Biogeochem. Cycles* **20**, GB2010 10.1029/2005GB002448 (2006).
6. A. J. Watson, A. C. N. Garabato, *Tellus B Chem. Phys. Meterol.* **58**, 73 (2006).
7. J. R. Toggweiler, J. L. Russell, S. R. Carson, *Paleoceanography* **21**, 10.1029/2005PA001154 (2006).
8. D. M. Sigman, A. M. de Boer, G. H. Haug, in *Ocean Circulation: Mechanisms and Impacts*, A. Schmittner, J. C. H. Chiang, S. R. Hemming, Eds. (American Geophysical Union, Washington, DC, 2007), pp. 335–349.
9. R. François *et al.*, *Nature* **389**, 929 (1997).
10. J. R. Petit *et al.*, *Nature* **399**, 429 (1999).
11. E. Monnin *et al.*, *Science* **291**, 112 (2001).
12. J. Ahn, E. J. Brook, *Science* **322**, 83 (2008).
13. W. S. Broecker, G. M. Henderson, *Paleoceanography* **13**, 352 (1998).
14. N. Caillon *et al.*, *Science* **299**, 1728 (2003).
15. H. J. Smith, H. Fischer, M. Wahlen, D. Mastroianni, B. Deck, *Nature* **400**, 248 (1999).
16. H. J. Spero, D. W. Lea, *Science* **296**, 522 (2002).
17. T. M. Marchitto, S. J. Lehman, J. D. Ortiz, J. Fluckiger, A. van Geen, *Science* **316**, 1456 (2007).
18. P. Pondaven *et al.*, *Nature* **405**, 168 (2000).
19. D. M. Nelson *et al.*, *Deep Sea Res. Part II Top. Stud. Oceanogr.* **49**, 1645 (2002).
20. T. Trull, S. R. Rintoul, M. Hadfield, E. R. Abraham, *Deep Sea Res. Part II Top. Stud. Oceanogr.* **48**, 2439 (2001).
21. J. L. Sarmiento, N. Gruber, M. A. Brzezinski, J. P. Dunne, *Nature* **427**, 56 (2004).
22. P. W. Boyd *et al.*, *Nature* **407**, 695 (2000).
23. S. H. H. Nielsen, D. A. Hodell, G. Kamenov, T. Guilderson, M. R. Perfit, *Geochem. Geophys. Geosyst.* **8**, Q12005 (2007).
24. A. Shemesh *et al.*, *Paleoceanography* **17**, 1056 10.1029/2000PA000599 (2002).
25. Z. Chase, R. F. Anderson, M. Q. Fleisher, P. Kubik, *Deep Sea Res. Part II Top. Stud. Oceanogr.* **50**, 799 (2003).
26. R. A. Mortlock, P. N. Froelich, *Deep Sea Res. Part I Oceanogr. Res. Pap.* **36**, 1415 (1989).
27. R. Francois, M. Frank, M. M. Rutgers van der Loeff, M. P. Bacon, *Paleoceanography* **19**, PA1018 10.1029/2003PA000939 (2004).
28. M. Q. Fleisher, R. F. Anderson, *Deep Sea Res. Part II Top. Stud. Oceanogr.* **50**, 693 (2003).
29. X. Crosta, J. J. Pichon, L. H. Burckle, *Paleoceanography* **13**, 284 (1998).
30. X. Crosta, A. Sturm, L. Armand, J. J. Pichon, *Mar. Micropaleontol.* **50**, 209 (2004).
31. S. H. H. Nielsen, thesis, University of Tromsø (2004).
32. R. F. Anderson, M. P. Bacon, P. G. Brewer, *Earth Planet. Sci. Lett.* **62**, 7 (1983).
33. Z. Chase, R. F. Anderson, M. Q. Fleisher, P. Kubik, *Earth Planet. Sci. Lett.* **204**, 215 (2002).
34. L. I. Bradtmiller, R. F. Anderson, M. Q. Fleisher, L. H. Burckle, *Paleoceanography* **21**, PA4201 10.1029/2006PA001282 (2006).
35. L. I. Bradtmiller, R. F. Anderson, M. Q. Fleisher, L. H. Burckle, *Paleoceanography* **22**, PA4216 10.1029/2007PA001443 (2007).
36. Z. Chase, R. F. Anderson, M. Q. Fleisher, P. Kubik, *Deep Sea Res. Part II Top. Stud. Oceanogr.* **50**, 739 (2003).
37. J. R. Toggweiler, K. Dixon, W. S. Broecker, *J. Geophys. Res. Oceans* **96**, 20467 (1991).
38. S. S. Kienast, M. Kienast, S. Jaccard, S. E. Calvert, R. Francois, *Geophys. Res. Lett.* **33**, L15607 10.1029/2006GL026651 (2006).
39. K. Hughen *et al.*, *Science* **303**, 202 (2004).
40. K. Hughen, J. Southon, S. Lehman, C. Bertrand, J. Turnbull, *Quat. Sci. Rev.* **25**, 3216 (2006).
41. L. F. Robinson *et al.*, *Science* **310**, 1469 (2005).
42. J. F. McManus, R. Francois, J. M. Gherardi, L. D. Keigwin, S. Brown-Leger, *Nature* **428**, 834 (2004).

43. R. E. M. Rickaby, H. Elderfield, *Geochem. Geophys. Geosyst.* **6**, Q05001 10.1029/2004GC000858 (2005).
44. F. Lamy *et al.*, *Earth Planet. Sci. Lett.* **259**, 400 (2007).
45. J. E. Tierney, J. M. Russell, *Geophys. Res. Lett.* **34**, L15709 10.1029/2007GL029508 (2007).
46. E. T. Brown, T. C. Johnson, C. A. Scholz, A. S. Cohen, J. W. King, *Geophys. Res. Lett.* **34**, L20702 10.1029/2007GL031240 (2007).
47. Y. J. Wang *et al.*, *Science* **294**, 2345 (2001).
48. L. C. Peterson, G. H. Haug, K. A. Hughen, U. Rohl, *Science* **290**, 1947 (2000).
49. X. Wang *et al.*, *Nature* **432**, 740 (2004).
50. C. Placzek, J. Quade, P. J. Patchett, *Geol. Soc. Am. Bull.* **118**, 515 (2006).
51. J. C. H. Chiang, C. M. Bitz, *Clim. Dyn.* **25**, 477 (2005).
52. K. Dahl, A. Broccoli, R. Stouffer, *Clim. Dyn.* **24**, 325 (2005).
53. R. Zhang, T. L. Delworth, *J. Clim.* **18**, 1853 (2005).
54. A. Brauer, G. H. Haug, P. Dulski, D. M. Sigman, J. F. W. Negendank, *Nat. Geosci.* **1**, 520 (2008).
55. L. Benson, M. Kashgarian, M. Rubin, *Palaeogeogr. Palaeoclimatol. Palaeoecol.* **117**, 1 (1995).
56. A. Timmermann *et al.*, *J. Clim.* **20**, 4899 (2007).
57. R. Hallberg, A. Gnanadesikan, *J. Phys. Oceanogr.* **36**, 2232 (2006).
58. T. Blunier, E. J. Brook, *Science* **291**, 109 (2001).
59. A. Govin *et al.*, *Paleoceanography* **24**, PA1202 10.1029/2008PA001603 (2009).
60. D. W. J. Thompson, S. Solomon, *Science* **296**, 895 (2002).
61. G. J. Marshall, *J. Clim.* **16**, 4134 (2003).
62. G. Chen, I. M. Held, *Geophys. Res. Lett.* **34**, L21805 10.1029/2007GL031200 (2007).
63. C. Le Quéré *et al.*, *Science* **316**, 1735 (2007).
64. K. Zickfeld, J. C. Fyfe, M. Eby, A. J. Weaver, *Science* **319**, 570b (2008).
65. R. M. Law, R. J. Matear, R. J. Francey, *Science* **319**, 570a (2008).
66. A. H. Orsi, T. Whitworth, N. Worth, *Deep-Sea Res.* **42**, 641 (1995).
67. N. J. Shackleton, M. A. Hall, J. Line, C. Shuxi, *Nature* **306**, 319 (1983).
68. EPICA Community Members, *Nature* **429**, 623 (2004).
69. E. Monnin *et al.*, *Earth Planet. Sci. Lett.* **224**, 45 (2004).
70. P. J. Reimer *et al.*, *Radiocarbon* **46**, 1029 (2004).
71. H. Rashid, R. Hesse, D. J. W. Piper, *Earth Planet. Sci. Lett.* **205**, 281 (2003).

72. Work described in this paper was funded by a grants/cooperative agreement from the National Oceanic and Atmospheric Administration, by the National Science Foundation, and by the Norwegian Research Council and the Norwegian Polar Institute as part of VISTA project 6535. The views expressed herein are those of the authors and do not necessarily reflect the views of NOAA or any of its sub-agencies. Comments on earlier drafts of the manuscript by J. R. Toggweiler, L. K. Armand, and M.-E. Carr led to substantial improvements. W. S. Broecker brought to our attention the importance of paleo lake level records. Discussions with P. de Menocal, J. McManus, and D. Martinson helped clarify our thinking about processes discussed in this paper. Comments from two anonymous reviewers improved the manuscript. Samples from TN057 cores were provided by the repository at Lamont-Doherty Earth Observatory; samples from E27-23 were provided by the Antarctic Marine Geology Research Facility at Florida State University.

Supporting Online Material

www.sciencemag.org/cgi/content/full/323/5920/1443/DC1
SOM Text
Figs. S1 to S4
Tables S1 to S4
References

20 October 2008; accepted 9 February 2009
10.1126/science.1167441

The Dynamic Control of Kiss-And-Run and Vesicular Reuse Probed with Single Nanoparticles

Qi Zhang, Yulong Li, Richard W. Tsien*

Vesicular secretion of neurotransmitter is essential for neuronal communication. Kiss-and-run is a mode of membrane fusion and retrieval without the full collapse of the vesicle into the plasma membrane and de novo regeneration. The importance of kiss-and-run during efficient neurotransmission has remained in doubt. We developed an approach for loading individual synaptic vesicles with single quantum dots. Their size and pH-dependent photoluminescence change allowed us to distinguish kiss-and-run from full-collapse fusion and to track single vesicles through multiple rounds of kiss-and-run and reuse, without perturbing vesicle cycling. Kiss-and-run dominated at the beginning of stimulus trains, reflecting the preference of vesicles with high release probability. Its incidence was increased by rapid firing, a response appropriate to shape the kinetics of neurotransmission during a wide range of firing patterns.

As a keystone of neuronal communication, the exocytosis and endocytosis of synaptic vesicles may take different forms (*1*). In full-collapse fusion (FCF), vesicles flatten completely into the plasma membrane, lose their identity, and must be replaced eventually by newly generated vesicles (*2*). In contrast, transient fusion and retrieval, often called "kiss-and-run" (K&R), would preserve a limited supply of releasable vesicles for reuse (*3*). Although nonclassical modes akin to K&R have been demonstrated in nonneuronal cells (*4*–*8*) and in a specialized calyceal synapse (*9*), it remains uncertain whether K&R is appreciable in small nerve terminals typical of the mammalian brain, which rely on only a few dozen releasable vesicles (*8*, *10*). Vesicle recycling in these terminals has been studied by optical reporters such as styryl dyes or synaptopHluorin (synaptophysin fused with pH-sensitive green fluorescent protein) (*11*–*15*). However, the limited signal-to-noise (S/N) ratio of such probes has left uncertainty about the functional impact of K&R.

Quantum dots have been widely used for applications requiring high S/N ratios (*16*–*18*). Those with peak emission at 605 nm and a diameter of ~15 nm (Qdots hereafter; fig. S1A) provided suitable artificial cargo: small enough to fit into the vesicular lumen (~24 nm), yet large enough to be rejected by putative K&R fusion pores (1 to 5 nm) (*9*, *19*). Furthermore, the pH dependence of Qdot emission (*17*) would allow reporting of exocytotic events, similar to pHluorin-based indicators (*20*, *21*).

Imaging single Qdot-loaded vesicles. Sparse Qdot loading was accomplished by mildly stimulating neurons. Functional synapses in the Qdot images were identified by subsequent FM4-64 staining (Fig. 1A). At many FM4-64–positive synapses, the Qdot signal was close to background ($P > 0.10$, *t* test), indicating no Qdot uptake (Fig. 1A). The remaining synapses (~42%) showed higher intensities distributed in two evenly spaced peaks (Fig. 1A). The interpeak spacing matched the unitary Qdot signal determined by blinking, a spontaneous intermittency of photoluminescence (*22*) ($P > 0.25$, *t* test). This calibration (*23*, *24*) confirmed that peak 1 corresponded to uptake of a single Qdot per synapse.

Qdot photoluminescence was pH-dependent: It increased by ~15% when pH was raised from 5.48 (intravesicular) to 7.34 (extracellular) (Fig. 1B). Indeed, photoluminescence of single Qdots in pH 7.34 agarose gel [72.1 ± 2.1 arbitrary units (a.u.), $n = 371$] exceeded that in nerve terminals by ~15% ($P < 0.01$, *t* test), a difference reversibly nullified by perfusion with pH 5.48 solution (fig. S2C). These data suggested that synapse-loaded Qdots were harbored at pH ~5.5, presumably within synaptic vesicles, as seen directly in electron microscopy images (*25*).

The pH dependence predicted distinct patterns of Qdot photoluminescence upon K&R and FCF (Fig. 1B): K&R would allow protons but not the Qdot to escape, causing transient deacidification and Qdot brightening. FCF would appear as similar Qdot brightening followed by loss of signal as the Qdot departs.

Qdots unambiguously identify FCF and K&R. Qdot-loaded boutons did exhibit different patterns of photoluminescence upon stimulation (0.1 Hz, 2 min; Fig. 1C): (i) baseline noise, (ii) a transient positive deflection (uptick), (iii) an uptick followed immediately by a negative step (downstep), and (iv) patterns ii and iii in sequence. The uptick level showed as a distinct peak ~15% above baseline, distinct from baseline noise (Fig. 1D). Amplitudes of the upticks with or without downsteps were the same (~9.9 a.u., fig. S3A). Invariably, downsteps followed an uptick, were irreversible (236/236 events, fig. S3B), and were identical in amplitude to that of single Qdots ($P > 0.25$, *t* test), consistent with the disappearance of Qdots after FCF. With or without downsteps, the great majority of upticks were stimulus-locked

---

Department of Molecular and Cellular Physiology, Stanford University, Stanford, CA 94305, USA.

*To whom correspondence should be addressed. E-mail: rwtsien@stanford.edu

(Fig. 1C, Fig. 2, and Fig. 3B), with latency briefer than the image acquisition interval (fig. S3, C and D). Some traces (8.6%) included events that were not clearly stimulus-locked (fig. S3C), presumably reflecting spontaneous exocytosis.

The upticks were probed by blocking vesicular H^+ transport with bafilomycin A1 (Baf). Without Baf, all nonblank records could be classified as K&R alone, FCF alone, or K&R + FCF in succession (Fig. 1C and Fig. 2). With acute exposure to Baf, which spares the pre-exocytotic pH gradient but prevents postexocytotic reacidification (*25*), isolated upticks were replaced by persistent increases (upsteps) of the same amplitude (10.47 ± 1.14 a.u., *n* = 49). This was expected if Qdots remained in post-K&R vesicles that failed to reacidify. After an upstep, subsequent uptick-downsteps were replaced by simple downsteps, 73.6 ± 3.4 a.u. (*n* = 157), 115% of the basal Qdot signal. After 1 hour of Baf incubation, which abolishes both the existing pH gradient and vesicular reacidification (*26*), prestimulation photoluminescence rose to ~115% of control, and no further increase was ever observed upon stimulation; all downsteps proceeded without a prior uptick. The amplitudes of upticks, upsteps, and downsteps showed expected interrelationships (fig. S4). Note that upsteps were never observed in the absence of Baf, contrary to expectations if Qdots externalized by FCF had clung on long enough to be recaptured by conventional endocytosis [time constant, τ, estimated at 14, 17, and 48 s, respectively, in (*13*, *14*, *27*)]. Instead, the upticks can be attributed to vesicular retention of the Qdot and reacidification upon closure of a fusion pore.

This interpretation was tested further by increasing external pH buffering with 50 mM Tris

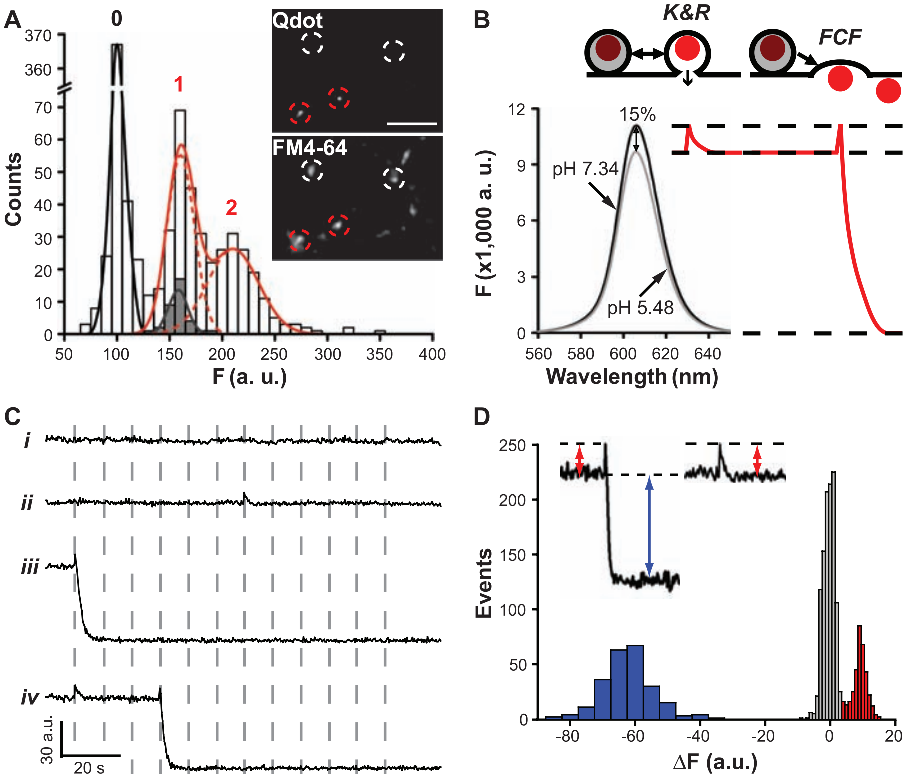

Fig. 1. Single Qdots loaded into synaptic boutons exhibit distinct patterns of photoluminescence change. (**A**) Neurons stimulated (10 Hz, 1 s) with 400 nM Qdots present, then thoroughly washed. The distribution of photoluminescent intensity was measured at FM4-64–defined regions of interest. Best fit was obtained with three evenly spaced Gaussians (black line and red dashed lines labeled 0, 1, and 2; red line indicates the summation of Gaussians 1 and 2), 63.9 a.u. apart. Spacing agrees with amplitude of blinking events (gray bars with the black line indicating a Gaussian fitting; mean 61.3 ± 4.5 a.u.) ($P > 0.25$, *t* test). Inset: Circles mark functional boutons identified by FM4-64 staining, with (red) or without (white) single Qdot loading. Scale bar, 3 μm. (**B**) pH-dependent Qdot photoluminescence. Cartoons show hypothetical Qdot signals arising from pH dependence. (**C**) Photoluminescence traces recorded during 0.1-Hz field stimulation for 2 min (dashed lines). (**D**) Upon stimulation, changes in Qdot signal (ΔF) could be classified as noise (gray bars, centered at 0 a.u.) or a clear positive deflection (red bars, centered at ~9 a.u., >2.5 SD of noise), ~15% of size of subsequent negative deflections (blue bars, centered at ~ –63 a.u.). Insets indicate measurements leading to the corresponding histograms.

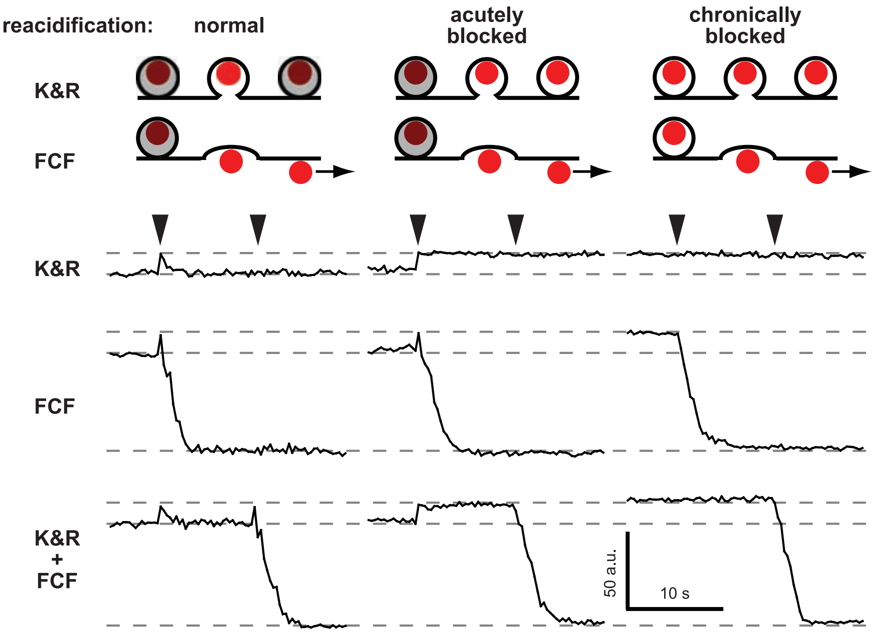

Fig. 2. Upward transients in Qdot signal report pH changes within the vesicle lumen. Cartoons show hypothesized effect of acute or chronic block of vesicular H^+–adenosine triphosphatase with bafilomycin A1 (Baf). Without Baf (normal), Qdot photoluminescence is diminished (maroon) by acidic luminal pH (gray). Deacidification upon vesicle fusion removes this quenching and Qdot brightens (red). Acute application of Baf (acutely blocked) prevents reacidification after vesicle retrieval; chronic Baf (chronically blocked) removes all pH gradients. Experimental traces illustrate typical photoluminescence patterns under three conditions. Patterns are classified as K&R, FCF, or K&R + FCF (labeled rows) according to analysis of collected data (fig. S4).

instead of 10 mM HEPES (pH$_o$ always 7.3). If Tris entered the vesicle and remained sequestered along with the Qdot, luminal reacidification should be slowed (*12*). Indeed, the uptick decay was longer ($P < 0.01$, *t* test; fig. S5A). In contrast, the time course of uptick-downsteps remained unchanged with Tris (fig. S5B), as expected for externalized Qdots.

Tracking the motion of single Qdots during and after fusion (movie S1) buttressed our interpretation of the two kinds of Qdot signals (supporting online text). Downsteps were always associated with the Qdot moving out of synapses (fig. S6); the diffusion coefficient, $D = 1.7 \pm 0.1$ μm^2/s, resembled that of Qdots tethered to membrane proteins (*28*). In contrast, in instances of uptick alone, Qdots remained close to their position at the moment of fusion (displacement 50 ± 6 nm, $n = 43$), consistent with the idea of K&R as "retrieval on the spot" (*29*). Was the Qdot-reported K&R inadvertently promoted by Qdot adherence? Previous findings with FM4-64 coloaded with Qdots argued against this idea (*25*). For further verification, we monitored vesicle cycling with the use of pHluorin-tagged vesicular glutamate transporter 1 (*30*) but found no difference in vesicle dynamics before, during, or after maximal loading with Qdots (fig. S7).

Timing and prevalence of K&R and FCF. The all-or-none nature of Qdot uptake allowed us to track a single vesicle in the total recycling pool (TRP) until its final FCF. Labeling of individual vesicles in the TRP was obtained with strong stimulation (10 Hz, 2 min) at low Qdot concentration (4 nM). Among 793 vesicles in single Qdot–loaded boutons, 302 exhibited fusion and are represented as raster lines (Fig. 3A); the others showed no fusion with field stimulation but only with later high K$^+$ challenges. Of the 302 vesicles, 292 fused upon field stimulation; of these, 13 showed one K&R, 58 showed one K&R followed by FCF, 1 showed two K&R events, and 220 showed FCF only. Thus, K&R occurred in ~25% of all vesicles and accounted for 21% of all fusion events over the field stimulation.

Intriguingly, the prevalence of K&R and FCF was dependent on stimulus number. K&R events were predominant initially (63.4 ± 9.9% at first stimulus) but became less prevalent as stimulation continued (Fig. 3C), falling to <10% later in the train (Fig. 3E). Because Qdots can report FCF after K&R but not vice versa, we examined first-fusion events specifically, and found the same trend.

K&R is favored by RRP vesicles. What is the basis of the decaying K&R ratio? One possibility is that vesicles with higher release probability per vesicle ($P_{r/v}$), namely readily releasable pool (RRP) vesicles, prefer K&R (*31*, *32*). Alternatively, the shift in fusion modes might arise from a cumulative effect of electrical activity, independent of $P_{r/v}$. To test these ideas, we prefaced field stimulation with a hypertonic challenge to selectively mobilize RRP vesicles without electrical activity or Ca^{2+} elevation (*33*). Rapid application of Tyrode's solution + 500 mM sucrose for 10 s caused vesicular turnover, reflected by upticks and uptick-downsteps whose peak-aligned averages were virtually identical to the corresponding responses to electrical stimulation. The two types of events were similarly timed [$P > 0.1$, Kolmogorov-Smirnov (K-S) test] and clustered between 1 and 7 s after the hypertonic challenge started. The hypertonic challenge elicited more K&R than FCF (Fig. 3E), yielding a K&R ratio (0.63 ± 0.05) similar to that found with the first field stimulus. During the subsequent electrical stimulation, the numbers of K&R and FCF events held steady, then fell in parallel as Qdot-labeled vesicles were depleted (Fig. 3E). Consequently, the K&R ratio stayed at ~15% during the whole stimulus train (Fig. 3F). Thus, RRP-resident vesicles displayed a strong propensity for K&R, but once-fused RRP vesicles and vesicles freshly recruited from the reserve pool were less favorably disposed to K&R, thus accounting for the observed drop in the K&R ratio.

K&R increases upon rapid stimulation. Hippocampal neurons often fire in bursts with intraburst frequencies far greater than 0.1 Hz. A key question is whether the balance between modes of fusion tilts when neurotransmission intensifies. Accordingly, after single Qdots had been loaded into the TRP, we applied 10-Hz field stimulation for 2 min. The fusion rate clearly increased (Fig. 4A). Qdot-loaded vesicles were sorted according to their behavior during the stimulation (Fig. 4B). Again, the prevalence of K&R started high but fell with continual stimulation (Fig. 4C). The initial contribution of K&R was significantly greater at 10 Hz (~88%) than at 0.1 Hz (~62%; $P < 0.05$, *t* test); likewise for the later steady level of K&R prevalence (~30% versus 10%; $P < 0.05$, *t* test). Among Qdot-labeled vesicles responding to electrical stimulation, 68% supported one or more K&R events, considerably more than with 0.1-Hz stimulation, and this effect likely extended beyond the RRP (<30% of vesicles) (*11*, *32*, *33*). At 10 Hz, individual vesicles supported as many as three rounds of K&R before a final FCF (Fig. 4A). Various combinations of fusion and retrieval events were observed (Fig. 4B).

To clarify the increase in reuse, we sorted Qdot-loaded vesicles according to overall performance and plotted the respective latencies to first fusion. Of the vesicles undergoing FCF alone, ~84% fused

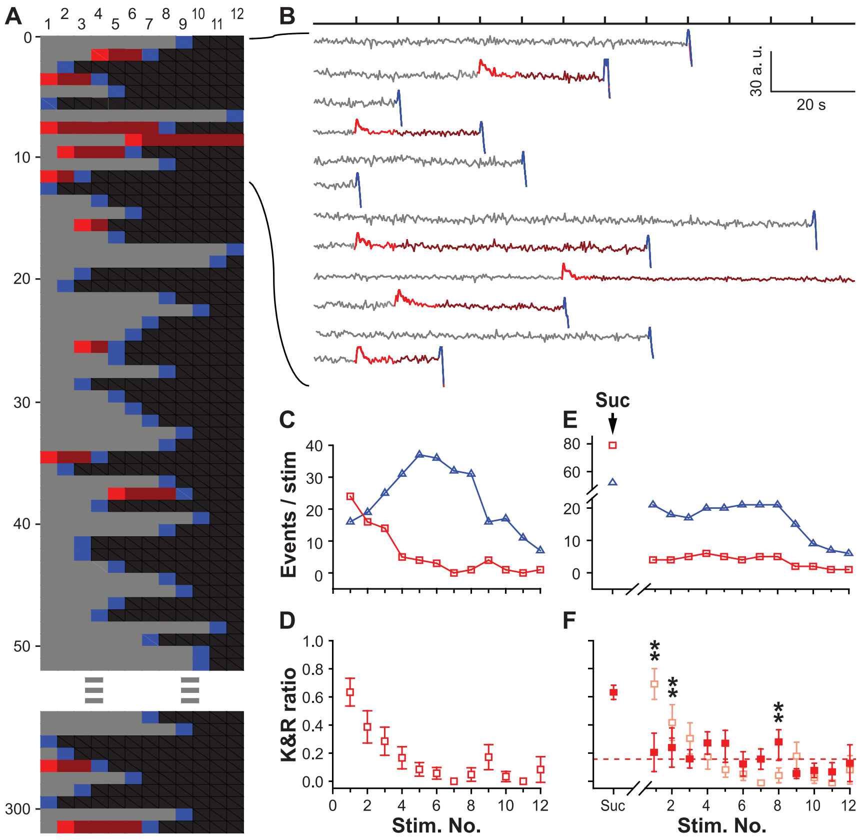

Fig. 3. Prevalence of K&R changes over the course of stimulation as RRP vesicles are depleted. (**A**) Raster representation of traces ($n = 302$) from single Qdot-loaded vesicles that responded to 0.1-Hz field stimulation for 2 min. For each stimulus and subsequent interval, Qdot signals registered as nonresponse (gray), K&R (red), nonresponse after K&R (maroon), FCF (blue), or Qdot no longer present in region of interest (black). Pooled traces from $N = 8$ cover slips, three separate cultures. (**B**) Traces corresponding to the first 12 rasters in (A). Photoluminescence changes are color-coded for each stimulus and ensuing interval as in (A). (**C**) Numbers of K&R (red squares) and FCF events (blue triangles), plotted for every stimulus. (**D**) K&R ratio for every stimulus ($N = 8$). Vertical bars are ±SEM. (**E**) Numbers of K&R (red squares) and FCF events (blue triangles), plotted for prestimulation hypertonic challenge (suc) and for each field stimulus. (**F**) Corresponding K&R ratio (solid red squares), compared with control [faded red squares, copied from (D)] (**$P < 0.01$, χ^2 test).

with a delay of >30 s, late enough to ensure that they originated from the reserve pool rather than the RRP (*11*, *32*). In contrast, all vesicles generating three K&R events first fused within <30 s. Overall, the earlier the first fusion of a vesicle (higher $P_{r/v}$), the more K&R it supported (Fig. 4D). This was not simply due to a longer time span from stimulation onset to final FCF, because this span was independent of the number of K&R events (fig. S8). Instead, residence in the RRP (and high $P_{r/v}$) favors K&R, in agreement with findings with hypertonic challenges (Fig. 3, E and F).

How soon after K&R can a vesicle be reused under rapid stimulation? We focused on cases wherein two consecutive K&R events were followed by FCF, to obtain a balanced comparison between K-K intervals (i.e., elapsed time between two consecutive K&R events) and K-F intervals (i.e., elapsed time between K&R and ensuing FCF). K-K intervals (Fig. 4E) were briefer (shortest, 2.67 s; median, 5.67 s; average, 10.26 ± 2.04 s) and faster than the classic exocytosis-endocytosis cycle in hippocampal terminals (*8*). In contrast, the K-F interval (Fig. 4E) was longer than the K-K interval by a factor of ~3 (median, 22.3 s; average, 26.8 ± 3.6 s). However, the K-F interval was faster than the latency to FCF only by a factor of 3 (~60 s); vesicles undergoing reuse by FCF after K&R still enjoyed a big kinetic advantage over unused vesicles destined for FCF.

Rapid reacidification and activity-dependent fusion pore open time. For functional advantage, speedy reuse of vesicles must be complemented by prompt fusion pore closure and fast reacidification, so as to allow vesicular refilling with neurotransmitter (*34*) and avoid "shooting blanks." Using 30-Hz imaging, we found that once the Qdot signal increased upon stimulation (single pulse; intertrial interval ~20 s), it remained at the highest level for a variable time before returning to baseline (Fig. 5A, inset). Such a plateau was expected while the fusion pore remained open. Indeed, experimental traces were better fitted with a plateau preceding a single-exponential decay than with an exponential alone (Fig. 5A). The median plateau duration was 0.367 s (average 0.527 ± 0.085 s, $n = 43$) and the median time constant of decay was 0.69 s (average 0.95 ± 0.18 s, $n = 43$). To verify the separation of plateau and decay phases, we again applied 50 mM Tris (Fig. 5, B and C). The Qdot signal showed the same amplitude and plateau duration as with HEPES (Fig. 5F; both $P > 0.5$, K-S test) while the decay was slowed (Fig. 5F; $P < 0.01$, K-S test), as also seen with low-frequency imaging (fig. S5A). The buffer insensitivity of the plateau amplitude and duration confirmed that the plateau represented the period preceding vesicle reacidification.

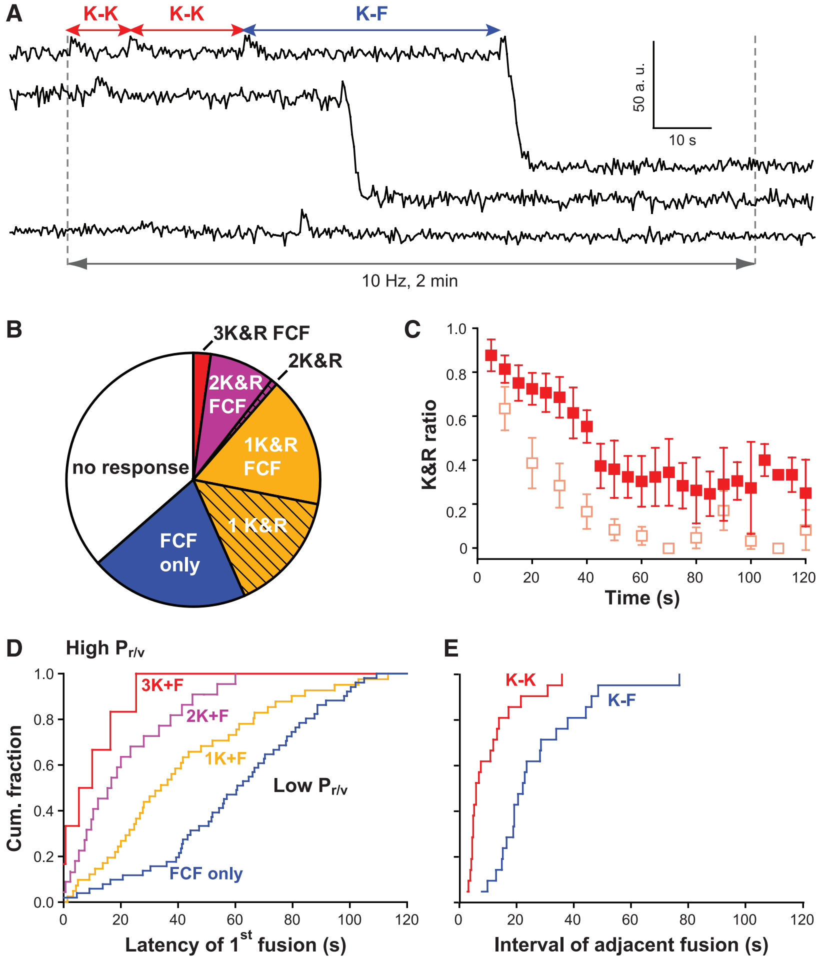

Fig. 4. Up-modulation of K&R prevalence with intense stimulation. (**A**) Sample traces from Qdot-loaded vesicles. (**B**) Categorization of vesicles with different fusion behaviors. (**C**) The K&R ratio during 10-Hz stimulation for 2 min (analyzed with 5-s time bins to improve S/N) was significantly higher than that during 0.1-Hz stimulation (faded symbols, data from Fig. 3D). (**D**) Latency of first fusion in the different categories [same color coding as (B)]. Each plot normalized by the number of vesicles in that category. The higher its $P_{r/v}$, the more K&R events a vesicle could support ($P_{r/v}$ = 0.051, 0.023, 0.010, and 0.001, respectively, for 3K + F, 2K + F, K + F, and FCF only). (**E**) The interval between two consecutive K&R events (K-K, red) was significantly shorter than that between K&R and a subsequent FCF of the same vesicle (K-F, blue) ($P < 0.01$, K-S test).

Because H^+ transport is the likely rate-limiting step for transmitter refilling (*1*, *34*), full reestablishment of ΔpH suggests that transmitter refilling was also nearly complete. Our direct measurements yield a vesicle reacidification rate faster than most previous estimates (*13*, *14*), with one exception (*12*). To probe whether the fusion pore open time and the vesicle reacidification rate are subject to change, we applied 10-Hz stimulation for 5 s. The plateau duration became longer (Fig. 5, D and E), increasing from ~0.5 s to 1.05 ± 0.18 s ($n = 46$), but both plateau amplitude and recovery time constant of decay, τ_{decay}, remained unaltered (Fig. 5F). Thus, reacidification proceeded rapidly at 10 Hz ($\tau_{decay} = 0.99 \pm 0.12$ s, $n = 46$), just as it did at low frequency. The frequency-dependent lengthening of plateau duration developed gradually during the 10-s stimulation train ($P < 0.01$, Pearson correlation test), indicating again that fusion pore gating was under physiological control.

Discussion. Using Qdots, we developed a method to distinguish multiple fusion modes with sharply different optical signals and single-event resolution, which enabled us to clarify the uncertainty about K&R at small nerve terminals of the central nervous system (*11*–*14*, *26*, *35*). As indivisible nanoparticles, Qdots could label individual vesicles in either the RRP or the reserve pool, which allowed us to monitor them without loss of signal continuity or amplitude through multiple rounds of reuse. In future studies, Qdots of different sizes and colors could be used to manipulate the vesicular volume available for neurotransmitter or to track different vesicles. Furthermore, Qdots might be engineered to give a larger pH-dependent signal and to permanently attach to the presynaptic membrane, enabling long-term tracking of presynaptic activity in situ.

Using Qdots, we could characterize the rapid reuse of vesicles. K&R gradually gave way to FCF as the dominant fusion mode during a stimulus train, contrary to the simple assumption of a fixed ratio (*26*). Consequently, K&R and FCF can each be predominant under different conditions. K&R appears most prominent under high-activity demand. FCF outweighs K&R under steady-state stimulation at low rates—that is, under conditions typical of studies in which K&R has been difficult to detect (*13*, *14*, *35*).

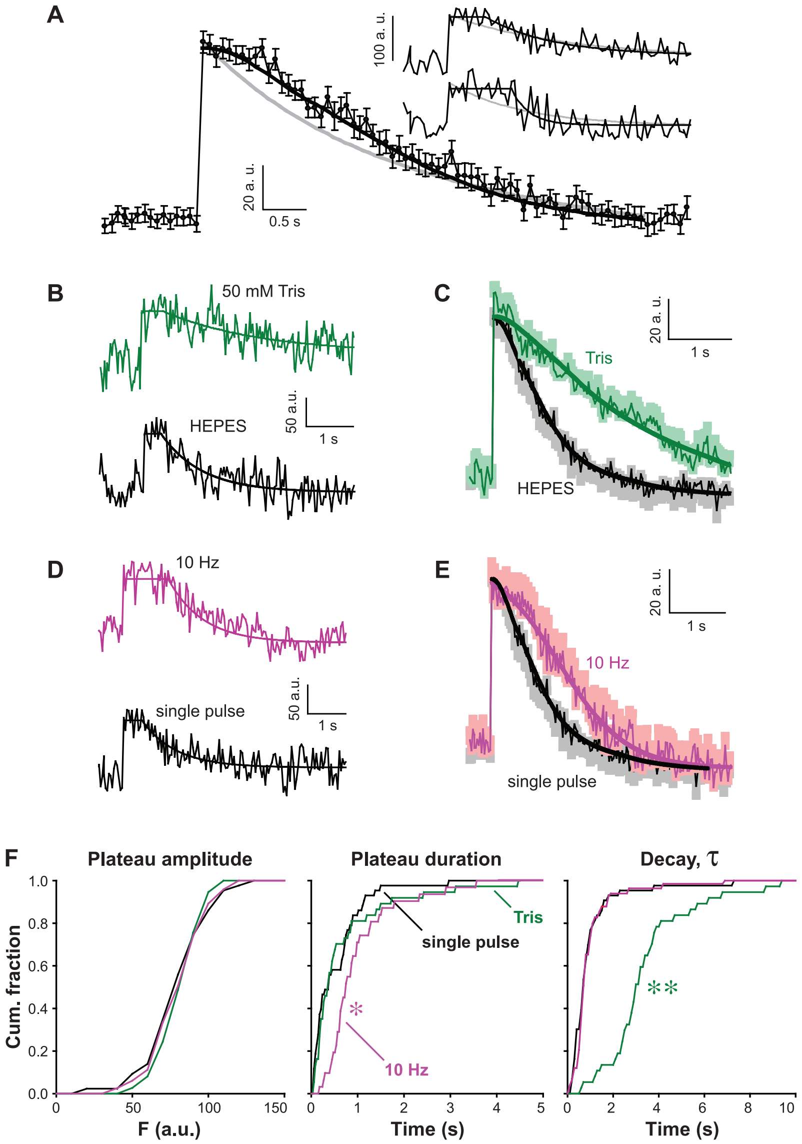

Fig. 5. High-speed imaging of Qdots reveals adjustable fusion pore open time but constant vesicle reacidification rate with different levels of activity. (**A**) Comparison of pooled data exemplified by insets (black symbols with error bars indicating SEM, $n = 43$) and averages of the two kinds of fits (gray and black). Insets: Samples taken in normal Tyrode's solution with single shocks; interstimulus interval, >20 s. Two types of fits were overlaid: a single-exponential decay (gray) and a plateau followed by an exponential (black), the latter fitting significantly better even after statistical penalization for the extra parameter (Akaike information criterion score, –60.5; $P < 0.001$). (**B**) Samples in 50 mM Tris (green) and in 10 mM HEPES (black). (**C**) Corresponding pooled data in Tris ($n = 37$) and in HEPES [same as (A)]. (**D**) Samples (normal Tyrode's solution) with 10-Hz (pink) and single-pulse stimulation (black). Smooth lines are corresponding fits as above. (**E**) Pooled data taken with 10-Hz ($n = 46$) and single-pulse stimulation [same as (A)]. (**F**) Cumulative distributions of fit parameters. Plateau amplitude: distributions were not different (all $P > 0.1$, K-S test); plateau duration: only distribution for 10-Hz stimulation was longer (*$P < 0.01$, K-S test); τ_{decay}: only distribution for 50 mM Tris was slower (**$P < 0.001$, K-S test).

The duration of fusion pore opening (0.5 to 1 s) was in good agreement with the capacitance measurements in the calyx of Held (*9*) and chromaffin cells (*36*). A subsecond opening would easily allow complete emptying of small neurotransmitters. Further study is needed to determine whether flickering or gradual widening of the fusion pore (*37*, *38*) allows gradual release of neurotransmitter and postsynaptic receptor desensitization at excitatory synapses.

K&R confers multiple functional advantages. Some RRP vesicles could fuse up to four times, allowing more efficient recycling, particularly with the intermittent patterns of burst firing found for hippocampal neurons in vivo. The rate of vesicle reuse we recorded was much faster than could be previously estimated (*11*)—a kinetic advantage if reuse of the same vesicle is an alternative to readying a fresh vesicle at the same release site. Nonetheless, the shortest interval between successive fusion events still left enough time for nearly complete reacidification (and, by inference, replenishment with neurotransmitter), consistent with preservation of quantal size even at high firing rates (*39*). On the other hand, persistent occupancy of release sites by a K&R vesicle awaiting reuse might also contribute to "release site inactivation" and falling $P_{r/v}$ during sustained firing.

With regard to synaptic variability, the repeated reuse of a small population of vesicles in successive bursts (*11*) would reduce variations in neurotransmitter content arising from differences in vesicle volume or in luminal transmitter concentration (*34*). Reuse of the same release site would also lower "release location–dependent variability" (*40*). In both ways, reuse would improve the fidelity of information transfer during neurotransmission.

References and Notes

1. T. C. Südhof, *Annu. Rev. Neurosci.* **27**, 509 (2004).
2. J. E. Heuser, T. S. Reese, *J. Cell Biol.* **57**, 315 (1973).
3. R. Fesce, F. Grohovaz, F. Valtorta, J. Meldolesi, *Trends Cell Biol.* **4**, 1 (1994).
4. G. Alvarez de Toledo, R. Fernandez-Chacon, J. M. Fernandez, *Nature* **363**, 554 (1993).
5. C. R. Artalejo, J. R. Henley, M. A. McNiven, H. C. Palfrey, *Proc. Natl. Acad. Sci. U.S.A.* **92**, 8328 (1995).
6. J. W. Taraska, D. Perrais, M. Ohara-Imaizumi, S. Nagamatsu, W. Almers, *Proc. Natl. Acad. Sci. U.S.A.* **100**, 2070 (2003).
7. T. Fulop, S. Radabaugh, C. Smith, *J. Neurosci.* **25**, 7324 (2005).
8. S. M. Smith, R. Renden, H. von Gersdorff, *Trends Neurosci.* **31**, 559 (2008).
9. L. He, X. S. Wu, R. Mohan, L. G. Wu, *Nature* **444**, 102 (2006).
10. S. An, D. Zenisek, *Curr. Opin. Neurobiol.* **14**, 522 (2004).
11. A. M. Aravanis, J. L. Pyle, R. W. Tsien, *Nature* **423**, 643 (2003).
12. S. P. Gandhi, C. F. Stevens, *Nature* **423**, 607 (2003).
13. B. Granseth, B. Odermatt, S. J. Royle, L. Lagnado, *Neuron* **51**, 773 (2006).
14. J. Balaji, T. A. Ryan, *Proc. Natl. Acad. Sci. U.S.A.* **104**, 20576 (2007).
15. X. Chen, S. Barg, W. Almers, *J. Neurosci.* **28**, 1894 (2008).
16. A. P. Alivisatos, W. Gu, C. Larabell, *Annu. Rev. Biomed. Eng.* **7**, 55 (2005).
17. X. Gao, W. C. Chan, S. Nie, *J. Biomed. Opt.* **7**, 532 (2002).
18. M. Heine *et al.*, *Science* **320**, 201 (2008).
19. M. B. Jackson, E. R. Chapman, *Annu. Rev. Biophys. Biomol. Struct.* **35**, 135 (2006).
20. G. Miesenböck, D. A. De Angelis, J. E. Rothman, *Nature* **394**, 192 (1998).
21. S. Sankaranarayanan, T. A. Ryan, *Nat. Cell Biol.* **2**, 197 (2000).
22. M. Nirmal *et al.*, *Nature* **383**, 802 (1996).
23. M. Howarth, K. Takao, Y. Hayashi, A. Y. Ting, *Proc. Natl. Acad. Sci. U.S.A.* **102**, 7583 (2005).
24. B. Cui *et al.*, *Proc. Natl. Acad. Sci. U.S.A.* **104**, 13666 (2007).
25. Q. Zhang, Y. Q. Cao, R. W. Tsien, *Proc. Natl. Acad. Sci. U.S.A.* **104**, 17843 (2007).
26. N. C. Harata, S. Choi, J. L. Pyle, A. M. Aravanis, R. W. Tsien, *Neuron* **49**, 243 (2006).
27. V. J. Mueller, M. Wienisch, R. B. Nehring, J. Klingauf, *J. Neurosci.* **24**, 2004 (2004).
28. M. Dahan *et al.*, *Science* **302**, 442 (2003).
29. F. Valtorta, J. Meldolesi, R. Fesce, *Trends Cell Biol.* **11**, 324 (2001).
30. S. M. Voglmaier *et al.*, *Neuron* **51**, 71 (2006).
31. C. F. Stevens, J. H. Williams, *Proc. Natl. Acad. Sci. U.S.A.* **97**, 12828 (2000).
32. J. L. Pyle, E. T. Kavalali, E. S. Piedras-Renteria, R. W. Tsien, *Neuron* **28**, 221 (2000).
33. C. Rosenmund, C. F. Stevens, *Neuron* **16**, 1197 (1996).
34. R. H. Edwards, *Neuron* **55**, 835 (2007).
35. T. Fernandez-Alfonso, T. A. Ryan, *Neuron* **41**, 943 (2004).
36. S. A. Chan, C. Smith, *J. Physiol.* **537**, 871 (2001).
37. R. G. Staal, E. V. Mosharov, D. Sulzer, *Nat. Neurosci.* **7**, 341 (2004).

38. S. Choi, J. Klingauf, R. W. Tsien, *Philos. Trans. R. Soc. London Ser. B* **358**, 695 (2003).
39. Q. Zhou, C. C. Petersen, R. A. Nicoll, *J. Physiol.* **525**, 195 (2000).
40. K. M. Franks, C. F. Stevens, T. J. Sejnowski, *J. Neurosci.* **23**, 3186 (2003).
41. We thank N. C. Harata for help with high-frequency imaging and data analysis, R. J. Reimer and members of the Tsien lab for comments, J. W. Mulholland and J. J. Perrino for help with imaging, and X. Gao and M. Bruchez for consultation on quantum dots. Supported by grants from the Grass Foundation (Q.Z.), the National Institute of Mental Health, and the Burnett Family Fund (R.W.T.).

Supporting Online Material
www.sciencemag.org/cgi/content/full/1167373/DC1
Materials and Methods
Figs. S1 to S9
Movie S1
References

20 October 2008; accepted 27 January 2009
Published online 12 February 2009;
10.1126/science.1167373
Include this information when citing this paper.

Explosive Percolation in Random Networks

Dimitris Achlioptas,[1] Raissa M. D'Souza,[2,3]* Joel Spencer[4]

Networks in which the formation of connections is governed by a random process often undergo a percolation transition, wherein around a critical point, the addition of a small number of connections causes a sizable fraction of the network to suddenly become linked together. Typically such transitions are continuous, so that the percentage of the network linked together tends to zero right above the transition point. Whether percolation transitions could be discontinuous has been an open question. Here, we show that incorporating a limited amount of choice in the classic Erdös-Rényi network formation model causes its percolation transition to become discontinuous.

A large system is said to undergo a phase transition when one or more of its properties change abruptly after a slight change in a controlling variable. Besides water turning into ice or steam, other prototypical phase transitions are the spontaneous emergence of magnetization and superconductivity in metals, the epidemic spread of disease, and the dramatic change in connectivity of networks and lattices known as percolation. Perhaps the most fundamental characteristic of a phase transition is its order, i.e., whether the macroscopic quantity it affects changes continuously or discontinuously at the transition. Continuous (smooth) transitions are called second-order and include many magnetization phenomena, whereas discontinuous (abrupt) transitions are called first-order, a familiar example being the discontinuous drop in entropy when liquid water turns into solid ice at 0°C.

We consider percolation phase transitions in models of random network formation. In the classic Erdös-Rényi (ER) model (*1*), we start with n isolated vertices (points) and add edges (connections) one by one, each edge formed by picking two vertices uniformly at random and connecting them (Fig. 1A). At any given moment, the (connected) component of a vertex v is the set of vertices that can be reached from v by traversing edges. Components merge under ER as if attracted by gravitation. This is because every time an edge is added, the probability two given components will be merged is proportional to the number of possible edges between them which, in turn, is equal to the product of their respective sizes (number of vertices).

One of the most studied phenomena in probability theory is the percolation transition of ER random networks, also known as the emergence of a giant component. When rn edges have been added, if $r < \frac{1}{2}$, the largest component remains miniscule, its number of vertices C scaling as $\log n$; in contrast, if $r > \frac{1}{2}$, there is a component of size linear in n. Specifically, $C \approx (4r - 2)n$ for r slightly greater than $\frac{1}{2}$ and, thus, the fraction of vertices in the largest component undergoes a continuous phase transition at $r = \frac{1}{2}$ (Fig. 1C). Such continuity has been considered a basic characteristic of percolation transitions, occurring in models ranging from classic percolation in the two-dimensional grid to random graph models of social networks (*2*).

Here, we show that percolation transitions in random networks can be discontinuous. We demonstrate this result for models similar to ER, thus also establishing that altering a network-formation process slightly can affect it dramatically, changing the order of its percolation transition. Concretely, we consider models that, like ER, start with n isolated vertices and add edges one by one. The difference, as illustrated in Fig. 1B, is that to add a single edge we now first pick two random edges $\{e_1,e_2\}$, rather than one, each edge picked exactly as in ER and independently of the other. Of these, with no knowledge of future edge-pairs, we are to select one and insert it in the graph and discard the other. Clearly, if we always resort to randomness for selecting among the two edges, we recover the ER model. Whether nonrandom selection rules can delay (or accelerate) percolation in such models, which have become known as Achlioptas processes, has received much attention in recent years (*3*–*6*).

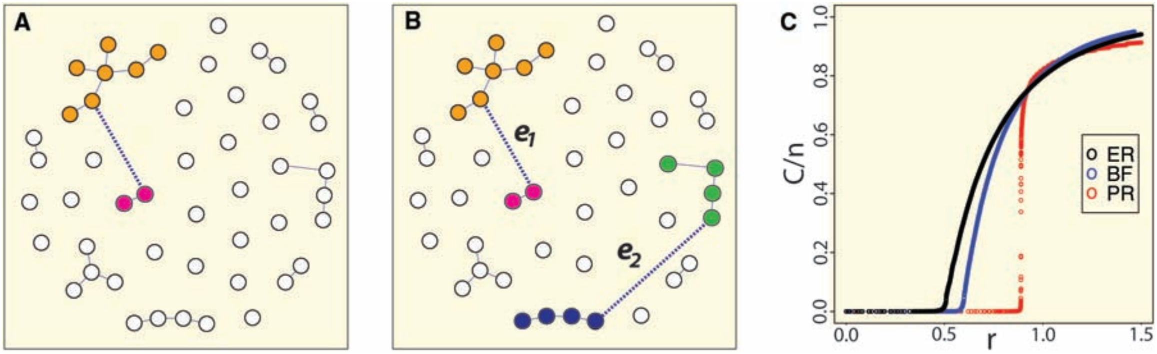

Fig. 1. Network evolution. (**A**) Under the Erdös-Rényi (ER) model, in each step two vertices are chosen at random and connected by an edge (shown as the dashed line). In this example, two components of size 7 and 2 get merged. (**B**) In models with choice, two random edges $\{e_1,e_2\}$ are picked in each step yet only one is added to the network based on some selection rule, whereas the other is discarded. Under the product rule (PR), the edge selected is the one minimizing the product of the sizes of the components it merges. In this example, e_1 (with product $2 \times 7 = 14$) would be chosen and e_2 discarded (because $4 \times 4 = 16$). In contrast, the rule selecting the edge minimizing the sum of the component sizes instead of the product would select e_2 rather than e_1. (**C**) Typical evolution of C/n for ER, BF (a bounded size rule with $K = 1$), and PR, shown for $n = 512{,}000$.

---

[1] Department of Computer Science, University of California at Santa Cruz, Santa Cruz, CA 95064, USA. [2] Department of Mechanical and Aeronautical Engineering, University of California at Davis, Davis, CA 95616, USA. [3] Santa Fe Institute, 1399 Hyde Park Road, Santa Fe, NM 87501, USA. [4] Courant Institute of Mathematical Sciences, New York University, New York, NY 10012, USA.

*To whom correspondence should be addressed. E-mail: raissa@cse.ucdavis.edu

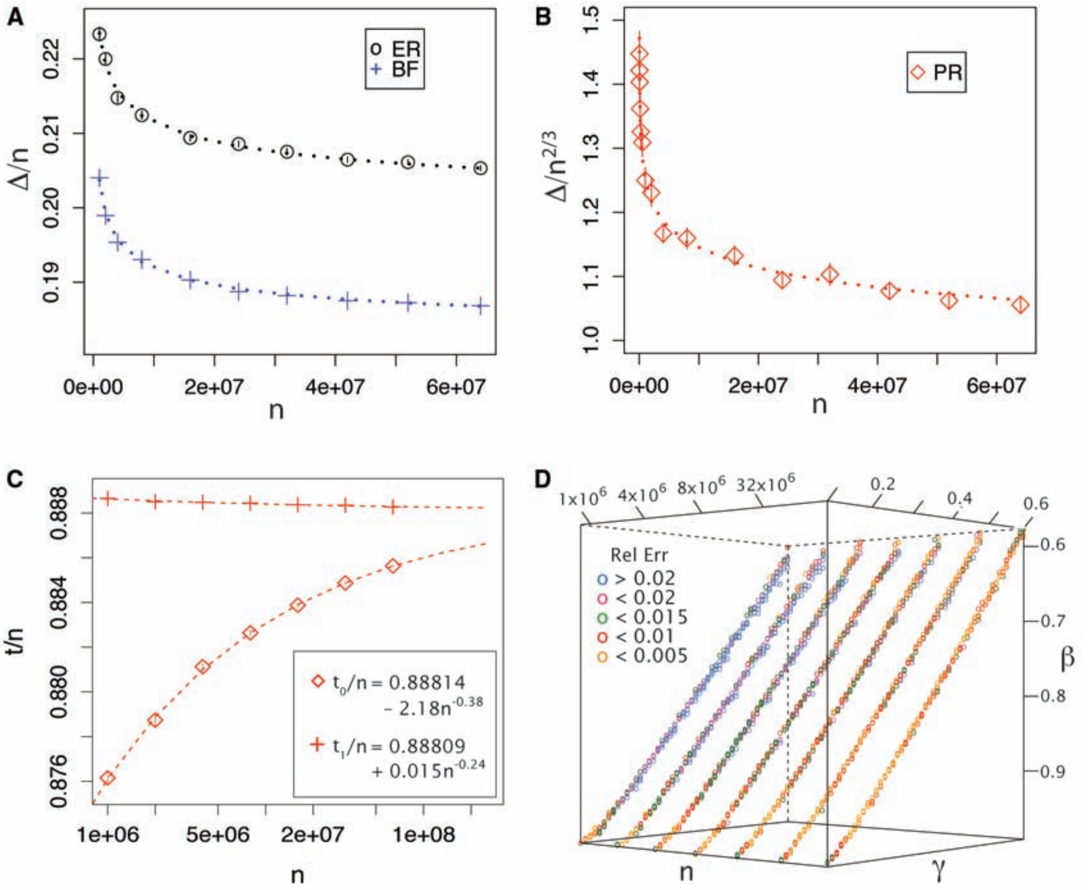

Fig. 2. (**A**) The ratio Δ/*n* for ER and BF for increasing system sizes. (**B**) The ratio $\Delta/n^{2/3}$ for PR for increasing system sizes. (**C**) Convergence to $r_c = 0.888\ldots$ from above and below (the two curves fitted independently). (**D**) A linear scaling relation is obeyed in the range $\gamma \in [0.2,0.6]$, shown here for $A = 0.5$. Color shows convergence with increasing system size *n* to the relation $\gamma + 1.2\beta = 1.3$. Our numerical experiments establish this scaling relation for $A \in [0.1,0.6]$ and we expect that in larger system sizes this range of *A* would broaden, particularly the lower end.

A selection rule is classified as "bounded-size" if its decision depends only on the sizes of the components containing the four end points of $\{e_1,e_2\}$ and, moreover, it treats all sizes greater than some (rule-specific) constant *K* identically. For example, a bounded-size rule with $K = 1$ due to Bohman and Frieze (BF) (*3*), the first selection rule to be analyzed, proceeds as follows: If e_1 connects two components of size 1, it is selected; otherwise, e_2 is selected. So, in Fig. 1B, e_2 would be selected. Bounded-size rules, in general, are amenable to rigorous mathematical analysis, and in (*3*, *4*) it was proven that such rules are capable both of delaying and of accelerating percolation. In contrast, unbounded-size rules seem beyond the reach of current mathematical techniques. A crucial point is that the percolation transition is strongly conjectured to be continuous for all bounded-size rules (*4*). This conjecture is supported both by numerical evidence and mathematical considerations, though a fully rigorous argument has remained elusive.

Here, we provide conclusive numerical evidence that, in contrast, unbounded-size rules can give rise to discontinuous percolation transitions. For concreteness, we present evidence for the so-called product-rule (PR): Always retain the edge that minimizes the product of the sizes of the components it joins, breaking ties arbitrarily (Fig. 1B). Thus, the PR selection criterion attempts to reduce the aforementioned gravitational attraction between components. We note that other unbounded-size rules also yield first-order transitions. For example, results similar to those for PR hold when "product" is replaced by "sum." It is also worth noting that the criterion employed by PR can also be used to accelerate percolation by always selecting the edge that maximizes rather than minimizes the product of the size of the components it merges (and similarly for sum). Nevertheless, in that case, the percolation transition remains continuous, reflecting the completely different evolution of the component-size distribution in the maximizing versus the minimizing case.

Let *C* denote the size of the largest component, t_0 denote the last step for which $C < n^{1/2}$, and t_1 the first step for which $C > 0.5n$. In continuous transitions, the interval $\Delta = t_1 - t_0$ is always extensive, i.e., linear in *n*. For example, $\Delta > 0.193n$ in ER. In contrast, as we show in Fig. 2B, Δ is not extensive for the product rule; indeed, $\Delta < 2n^{2/3}$ and it appears that $\Delta/n^{2/3} \rightarrow 1$. As a result, the fraction of vertices in the largest component jumps from being a vanishing fraction of all vertices to a majority of them "instantaneously." Although t_0/n and t_1/n converge to $r_c = 0.888\ldots$ (Fig. 2C), the variance in the value of t_0 and t_1 is enough to prevent the direct observation of a first-order transition. That is, measuring the size of the largest component as a function of the number of steps and averaging it over different realizations smears out the transition point, motivating our introduction of Δ and its measurement along different realizations. Specifically, each data point in Fig. 2, A to C, represents an average over an ensemble of 50 independent identically distributed realizations, and the dashed lines are the statistical best fits to the data (for details, see the supporting online material). Our computer implementation makes use of efficient procedures (*7*) for tracking how components merge as edges are added.

Our choice of $n^{1/2}$ and $0.5n$ above for defining Δ was simply illustrative. To demonstrate the discontinuity of PR's percolation transition, it suffices to find constants $A > 0$ and $\beta,\gamma < 1$ such that the number of steps between $C < n^{\gamma}$ and $C > An$ is smaller than n^{β}. Indeed, we have discovered a general scaling law associated with PR's percolation. For a range of values for *A*, we find that the same simple linear scaling relation governs the boundary of valid parameter choices, namely $\gamma + \lambda\beta = \mu$, where to the best of our numerical estimates, $\lambda \approx 1.2$ and $\mu \approx 1.3$. Convergence to this behavior for $A = 0.5$ is shown in Fig. 2D. Here, each data point depicts an individual realization, and color is used to show the relative error between the empirical value and that predicted by the scaling relation (see supporting online material for details).

We have demonstrated that small changes in edge formation have the ability to fundamentally alter the nature of percolation transitions. Our findings call for the comprehensive study of this phenomenon, and of its potential use in bringing phase transitions under control.

References and Notes

1. P. Erdős, A. Rényi, *Publ. Math. Inst. Hungar. Acad. Sci.* **5**, 17 (1960).
2. M. E. J. Newman, D. J. Watts, S. H. Strogatz, *Proc. Natl. Acad. Sci. U.S.A.* **99**, 2566 (2002).
3. T. Bohman, A. Frieze, *Random Structures Algorithms* **19**, 75 (2001).

4. J. Spencer, N. Wormald, *Combinatorica* **27**, 587 (2007).
5. A. Beveridge, T. Bohman, A. Frieze, O. Pikhurko, *Proc. Am. Math. Soc.* **135**, 3061 (2007).
6. M. Krivelevich, E. Lubetzky, B. Sudakov, "Hamiltonicity thresholds in Achlioptas processes"; available at http://arxiv.org/abs/0804.4707 (2008).
7. M. E. J. Newman, R. M. Ziff, *Phys. Rev. E Stat. Nonlin. Soft Matter Phys.* **64**, 016706 (2001).

8. We thank Microsoft Research, where our collaboration initiated, for its support. D.A. is supported in part by NSF CAREER award CCF-0546900, an Alfred P. Sloan Fellowship, and IDEAS grant 210743 from the European Research Council.

Supporting Online Material
www.sciencemag.org/cgi/content/full/323/5920/1453/DC1
SOM Text

28 October 2008; accepted 16 January 2009
10.1126/science.1167782

The Initial Stages of Template-Controlled $CaCO_3$ Formation Revealed by Cryo-TEM

Emilie M. Pouget,[1,2] Paul H. H. Bomans,[1,2] Jeroen A. C. M. Goos,[1] Peter M. Frederik,[2,3] Gijsbertus de With,[1,2] Nico A. J. M. Sommerdijk[1,2]*

Biogenic calcium carbonate forms the inorganic component of seashells, otoliths, and many marine skeletons, and its formation is directed by an ordered template of macromolecules. Classical nucleation theory considers crystal formation to occur from a critical nucleus formed by the assembly of ions from solution. Using cryotransmission electron microscopy, we found that template-directed calcium carbonate formation starts with the formation of prenucleation clusters. Their aggregation leads to the nucleation of amorphous nanoparticles in solution. These nanoparticles assemble at the template and, after reaching a critical size, develop dynamic crystalline domains, one of which is selectively stabilized by the template. Our findings have implications for template-directed mineral formation in biological as well as in synthetic systems.

In nature, hybrid materials consisting of a combination of soft organic and hard inorganic components are used for a variety of purposes, including mechanical support, navigation, and protection against predation (*1*, *2*). These biominerals, such as bones, teeth, and shells, often combine fascinating shapes with remarkable mechanical (*3*) and optical (*4*) properties, which generally are related to a high level of control over structure, size, morphology, orientation, and assembly of the constituents.

Calcium carbonate is the most abundant crystalline biomineral. In nature, its formation generally takes place in specialized, self-assembled compartments, such as vesicles or layered macromolecular structures, where domains of acidic proteins induce oriented nucleation (*5*, *6*). Avoiding the complexity and dynamics of the biological mineralization systems, template-directed $CaCO_3$ mineralization has been studied in vitro through the use of two-dimensional (2D) molecular assemblies as model systems (*7*).

According to classical nucleation theory, the crystallization of inorganic minerals starts from their constituting ions, which, on the basis of their ionic complementarity, form small clusters in a stochastic process of dynamic growth and disintegration (*8*). These clusters become stable when a critical size is reached at which the increasing surface energy related to the growing surface area is balanced by the reduction of bulk energy related to the formation of a crystal lattice. The resulting primary nanoparticles form the critical crystal nuclei that are the basis of further growth through the associated reduction of the Gibbs free energy of the system.

In contrast to what is described by classical nucleation theory, calcium carbonate crystal formation has been shown to occur from a transient amorphous precursor phase, both in biological (*9*, *10*) and in biomimetic systems (*11*, *12*). Moreover, it was recently shown that $CaCO_3$ nucleation (*13*) is preceded by the formation of nanometer-sized prenucleation clusters, which also is not foreseen by classical nucleation theory. Although a recent model described how a template can direct orientated nucleation from an amorphous calcium carbonate (ACC) precursor phase (*14*), the role of prenucleation clusters in template-directed mineralization is still unknown.

Previously, with the use of a vitrification robot and attached glovebox, we were able to load a self-organized monolayer with adhered mineralization solution onto a holey carbon cryotransmission electron microscopy (cryo-TEM) grid with minimal disturbance of the system while maintaining 100% humidity and constant temperature (fig. S1) (*11*, *15*). Plunge-freeze vitrification of the sample at various time points allowed trapping of the different stages of the mineralization reaction and monitoring of the development of the mineral phase in its native hydrated state by cryo-TEM. Using 2D imaging and diffraction, we showed the formation of a transient ACC phase and demonstrated its transformation into oriented vaterite before the formation of the final product, oriented calcite. However, this study did not show which steps in the mineralization process depended critically on the presence of the monolayer, nor did it discover the prenucleation clusters.

The present work used a stearic acid monolayer as a template deposited on a supersaturated 9 mM $Ca(HCO_3)_2$ solution (*16*). We studied the system through a combination of cryoelectron tomography (cryo-ET) (*17*) and low-dose selected-area electron diffraction (SAED), obtaining morphological and structural information with 3D spatial resolution. This allowed us to image, locate, and identify $CaCO_3$ nanoparticles in solution and to establish whether they were actually in contact with the template. Also, by using high-resolution cryo-TEM, we could visualize prenucleation clusters and collect evidence for their role in the nucleation of the amorphous nanoparticles. Tomography revealed that these particles nucleated in solution but later assembled at the template surface, where crystallinity developed; low-dose SAED showed selective stabilization of single crystallographic orientation through the interaction of the mineral with the monolayer.

High-resolution cryo-TEM studies of fresh 9 mM $Ca(HCO_3)_2$ solutions showed prenucleation clusters with dimensions of 0.6 to 1.1 nm (Fig. 1, A and B). At the same time, a small population of larger clusters (<4 nm) was detected (Fig. 1C, inset), indicating the onset of the aggregation process leading to nucleation. After reaction times of 2 to 6 min, small nanoparticles with a size distribution centered around 30 nm were observed (Fig. 2A).

Samples were taken from the crystallization solution at different time points (figs. S2 and S3) (*15*) and analyzed with analytical ultracentrifugation, which detects species in solution according to the difference in their sedimentation coefficient *s* (*18*). Large and dense particles sediment faster than smaller or less dense particles, thereby yielding a higher value of *s*. These experiments confirmed the presence of nanoclusters ($s = 1.5 \times 10^{-13}$ to 3×10^{-13} s) coexisting with ions ($s \leq 0.6 \times 10^{-13}$ s), followed by the aggregation of the clusters ($s \geq 4.5 \times 10^{-13}$ s) before the nucleation event.

Gebauer *et al.* (*13*) provided convincing evidence that the existence of prenucleation clusters is due to thermodynamic equilibrium among solvent, individual hydrated ions, and hydrated clusters, as represented by

$$z\{\mathrm{Ca}^{2+}\}_{\mathrm{aq}} + z\{\mathrm{CO_3}^{2-}\}_{\mathrm{aq}} \leftrightarrow \{\mathrm{CaCO_3}\}_{z,\mathrm{aq}} \quad (1)$$

in which the clusters are considered as a solute entity and *z* is the number of $CaCO_3$ units in a cluster. In the absence of data on prenucleation cluster concentrations, and a value for *z*, quantitative assessment is currently not possible. They speculated that the release of water molecules from the hydration shell of ions provides a substantial entropy gain favoring prenucleation cluster formation.

Low-dose SAED showed that the 30-nm nanoparticles were amorphous, and cryo-ET dem-

---

[1] Laboratory of Materials and Interface Chemistry, Eindhoven University of Technology, P.O. Box 513, 5600 MB Eindhoven, Netherlands. [2] SoftMatter CryoTEM Unit, Eindhoven University of Technology, P.O. Box 513, 5600 MB Eindhoven, Netherlands. [3] EM Unit, Department of Pathology, University of Maastricht, Universiteitssingel 50, 6229 ER Maastricht, Netherlands.

*To whom correspondence should be addressed. E-mail: n.sommerdijk@tue.nl

onstrated that they were present throughout the whole solution (Fig. 2, A, D, and E) (*15*), implying that their formation is independent of the presence of the organic template. The SAED patterns obtained from the ACC particles and the fresh $Ca(HCO_3)_2$ solutions were indistinguishable and were clearly different from vitrified films of pure water and aqueous 10 mM $CaCl_2$ solutions (Fig. 1D). The similarities and differences among the different samples are not only immediately clear from the position of the second diffraction ring [at 4.61 ± 0.05 Å for ACC and 9 mM $Ca(HCO_3)_2$; at 4.82 ± 0.05 Å and 4.90 ± 0.05 Å for water and 10 mM $CaCl_2$, respectively], but are also statistically significant in the maximum of the first diffraction ring (tables S1 and S2) (*15*). These results suggest that the prenucleation clusters present in freshly prepared $Ca(HCO_3)_2$ solutions consist of ACC.

In contrast to the observations of Gebauer *et al.* (*13*), our experiments showed that the prenucleation clusters persisted after nucleation. We speculate that the formation of the ~30-nm nanoparticles is due to aggregation of the prenucleation clusters via Brownian motion. Considering that the prenucleation clusters already have the structure of the ACC particles found after nucleation, the aggregation of clusters mainly leads to a gain in surface enthalpy. We consider this to be the main driving force for stabilization of the ACC nanoparticles. However, it is noteworthy that experiments (*19*) and simulations (*20*) have indicated that $CaCO_3$ domains with sizes of ≤ 2 nm may already possess short-range local order.

After longer reaction times (10 to 20 min), larger particles with sizes ranging from 70 to 250 nm were observed (Fig. 2, B, D, and F) in coexistence with a persistent population of the ~30-nm nanoparticles. Tomograms showed that the larger particles were found exclusively at the interface with the monolayer and that all exhibited a smooth face interacting with the template. Low-dose SAED revealed that some of these were still amorphous (Fig. 2D, particle 2), whereas others produced complex spot patterns (Fig. 2D, particles 3 to 5) that could be assigned to vaterite displaying multiple crystallographic orientations (fig. S4) (*15*). The template-associated amorphous particles were larger than those found in solution and had a size range of 70 to 120 nm, which implies that these are temporarily stabilized by the monolayer. The particles in which crystallinity had developed were found in all sizes (70 to 250 nm), which suggests that in the present system the size of ~120 nm is a critical upper limit for the stability of the amorphous phase. Conversely, the observations that most ACC particles have a size of <70 nm, whereas polycrystalline $CaCO_3$ has a minimal particle diameter of ~70 nm, imply that this size is critical for the development of crystalline domains inside an amorphous matrix.

The size of the particles further increased, and an increasing fraction of these particles showed a dominating or even a single diffraction pattern (particle diameters of >300 nm) (Fig. 2, F and G, and fig. S4) (*15*). In accordance with literature (*16*, *21*, *22*), SAED identified this plane as (00.1) vaterite (Fig. 2, C and D); in the absence of a monolayer, a mixture of randomly oriented calcite and vaterite was obtained (fig. S6) (*15*). Tomograms showed that after a reaction period of 30 to 60 min, the nanoparticles were still present throughout the solution, and in many cases they were found to decorate the surface of the 300- to 500-nm vaterite crystals (Fig. 2G).

In accordance with electron microscopy observations (*9*, *14*) and simulations (*23*), the present results imply a locally confined transformation of the amorphous to the crystalline state. Also, structural and spectroscopic techniques have demonstrated the development of short-range order in transient ACC, indicating a gradual development of crystallinity within the material (*24*, *25*). None-

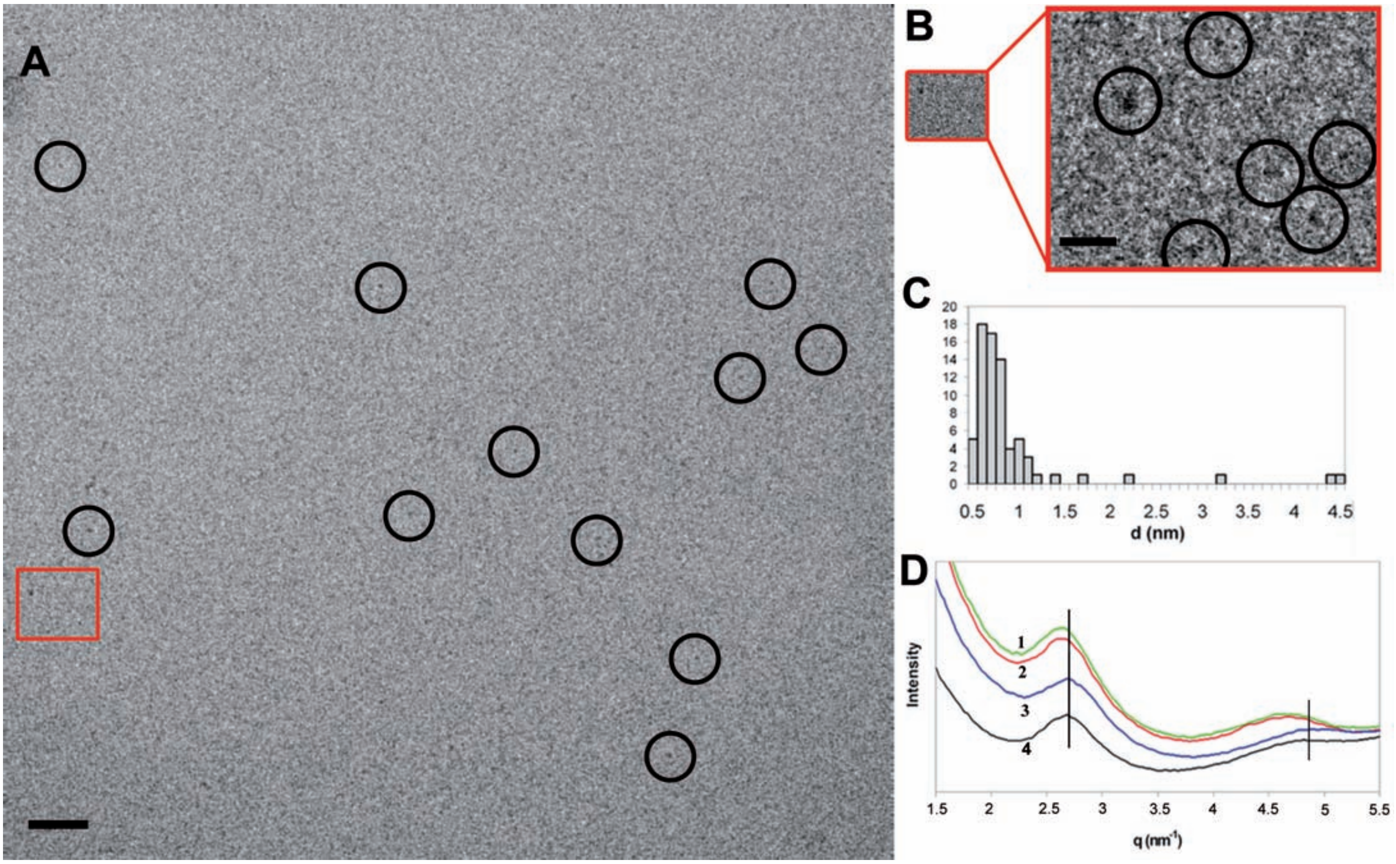

Fig. 1. (**A**) High-resolution cryo-TEM image of a fresh 9 mM $Ca(HCO_3)_2$ solution after image processing (*15*) in which prenucleation clusters are observed. An arbitrary number of clusters are highlighted by black circles. Scale bar, 20 nm. (**B**) Nonfiltered images representing the zone delimited by the red square in (A). In the high-magnification image, all particles present are highlighted by black circles. Particle sizes below the detection limit of 0.45 nm (3 times the pixel size) are considered noise. Scale bar, 5 nm. (**C**) Particle diameter (*d*) distribution of the prenucleation clusters observed in the cryo-TEM images. (**D**) Radial integration of the diffraction patterns of vitrified aqueous solutions of (1) ACC (green), (2) 9 mM $Ca(HCO_3)_2$ (red), (3) water (blue), and (4) 10 mM $CaCl_2$ (black). Vertical (black) lines are drawn to indicate the shifts of the diffraction rings of the different samples with respect to that of a vitrified film of pure water.

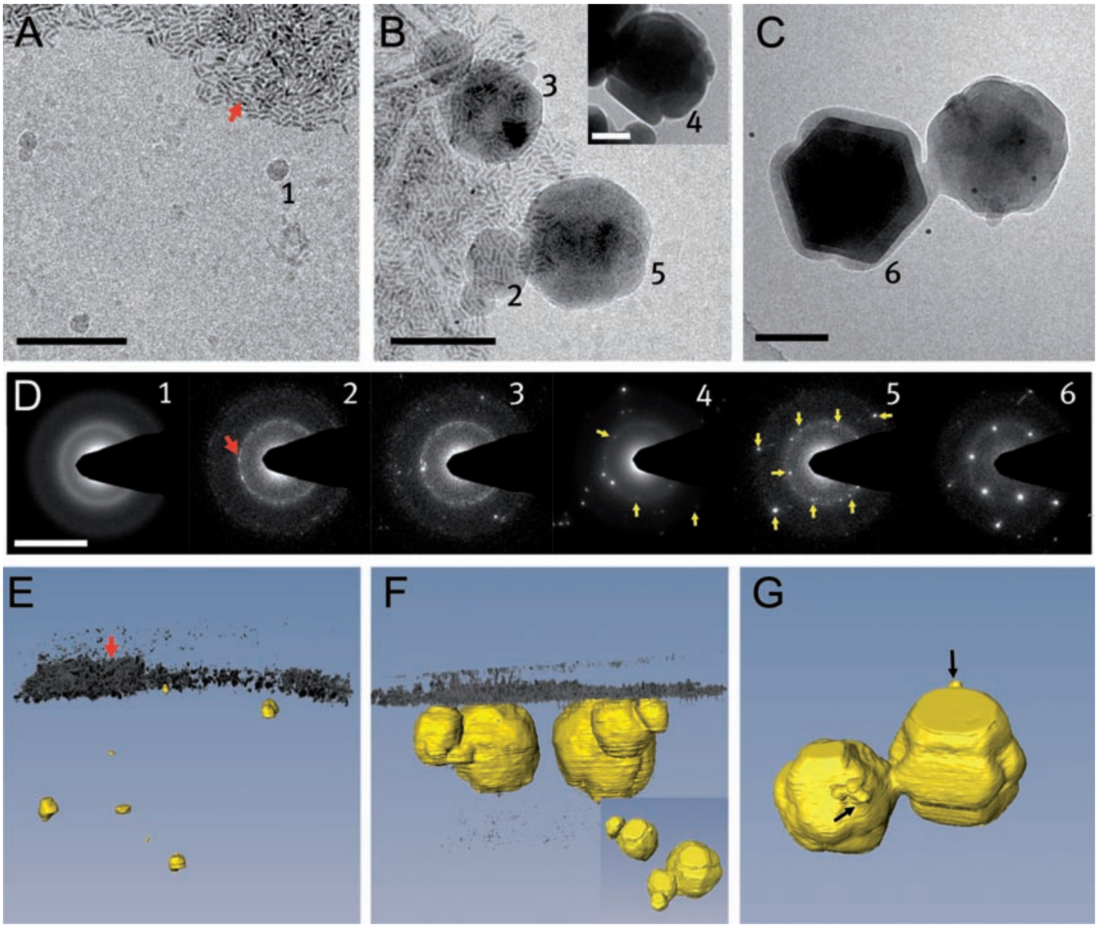

Fig. 2. (**A** to **C**) Cryo-TEM images of the early, intermediate, and mature stages, after reaction times of 6 min, 11 min, and 45 min, respectively. Inset in (B) is a micrograph taken from a different area. Scale bars, 200 nm. (**D**) Diffraction patterns of the particles marked in (A) to (C), showing the development of crystallinity during the mineralization. Scale bar, 5 nm^{-1}. Particles 1 and 2 are amorphous; particles 3 to 5 are polycrystalline. The marked spots can be indexed (yellow arrows) as vaterite oriented (00.1). The *d*-spacings of the other spots fit with the vaterite distances. Particle 6 is vaterite (00.1). See details of the diffraction pattern indexation in (*15*). (**E** to **G**) Computer-aided visualization of the tomograms recorded from the areas shown in (A) to (C) (*15*). The red arrows in (E) show the nanorods marking the monolayer (fig. S5) (*15*). The black arrows in (G) show the 30-nm ACC decorating the more mature crystals. Inset in (F) shows the particle surfaces that interact with the monolayer.

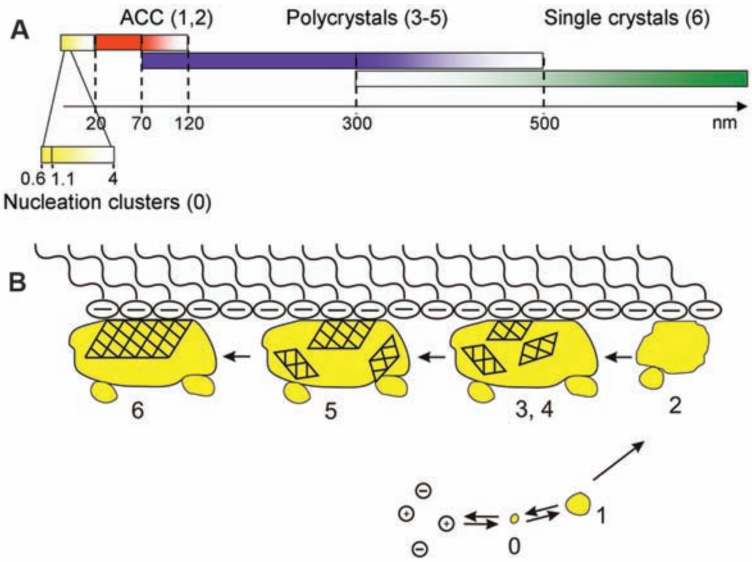

Fig. 3. The different stages of template-controlled calcium carbonate formation. (**A**) The distribution of particle diameters at different stages of crystal development. (**B**) Schematic pathway of the mineralization of an organic matrix. Step 0: formation of prenucleation clusters. Step 1: Aggregation of the clusters to form 30-nm ACC nanoparticles. Step 2: Clustering and growth of the ACC particles at the surface of the organic matrix. Step 3: Start of the crystallization; formation of poorly crystalline particles. Step 4: Formation of nanocrystalline domains inside the amorphous particle. Step 5: Prevalent growth of the crystalline domain stabilized by the template. Step 6: Formation and growth of oriented single crystals. Numbers in parentheses in (A) and step numbers in (B) relate to the particle numbers in Fig. 2.

theless, for several other calcium carbonate–based systems, crystallization proceeds through a dissolution-reprecipitation mechanism (*12*, *26*). Moreover, we cannot exclude the possibility that the presence of water mediates this phase transformation through the solubilization of ACC on a nanoscopic scale (*19*).

The narrow size distribution of the initial ACC particles suggests an optimal stability at a diameter of ~30 nm, similar to previous reports for mineral nanoparticles in studies of calcium carbonate from nacre (*6*) and calcium phosphate from enamel (*27*). The presence of these nanoparticles in all stages of the mineral formation process (fig. S8) (*15*) supports proposals that these nanoparticles form the feedstock on which the larger particles and crystals grow (*11*, *28*). Although the observation that nanoparticles adhere to the surface of the vaterite crystals (Fig. 2G) suggests that growth proceeds through the direct addition of such particles, no crystals with roughened surfaces have been observed. Therefore, also considering the high solubility of ACC in water (1.7 mM) (*29*), one may expect that the nanoparticles exist in equilibrium with the material in solution, and we propose that the growth of the larger particles occurs through a dissolution-reprecipitation mechanism at the expense of the nanoparticles (*30*).

We propose that the template-directed crystallization of $CaCO_3$ proceeds through several distinct steps (Fig. 3) (*15*). The starting point is the formation of prenucleation clusters with dimensions of 0.6 to 1.1 nm (step 0). In analogy to the chemistry of calcium phosphate (*31*), we consider them to be the smallest stable agglomerates of $CaCO_3$ present from the beginning of the reaction. Aggregation of these clusters in solution leads to the nucleation of ACC nanoparticles with a size distribution centered around 30 nm (step 1). Association of these particles with the template surface initiates the growth of ACC (step 2), using the nanoparticles in their neighborhood as feedstock. Next, randomly oriented nanocrystalline domains are formed inside the otherwise amorphous particles (steps 3 and 4). On the basis of the model of Zhang *et al.* (*23*), we expect these domains to be unstable and in equilibrium with the amorphous phase. In the last steps, the orientation that is stabilized through the interaction with the monolayer becomes dominant (step 5) and develops into a single crystal (step 6). This single crystal probably grows by the further addition and incorporation of ions and clusters from solution.

The initial experiments of Mann and co-workers showed that the present system could produce calcite ($1\bar{1}.0$) or vaterite (00.1) depending on the precise conditions (*16*, *32*). Later, it was demonstrated that rapid CO_2 evaporation favors the kinetic product, vaterite (*21*, *22*), whereas lower evaporation rates lead to the calcitic form (*21*). These results are confirmed by our finding of (00.1) oriented vaterite in the present work (i.e., in a fast-outgassing thin film) and the formation of ($1\bar{1}.0$) oriented calcite in crystallization dishes (fig. S7) (*15*) from which CO_2 outgassing is slower. Moreover, the observation of randomly oriented vaterite crystals also puts in perspective the synchrotron x-ray scattering experiments that showed the formation of randomly oriented crystals from the same system (*22*).

The nanoscopic prenucleation clusters that we visualized are the smallest stable form of $CaCO_3$ and are likely the building blocks of the amorphous precursor particles observed in biomineralization; such particles are also observed in many synthetic systems and are not restricted to calcium carbonate (*13*, *31*). As a consequence of their aggregation, ACC nucleates in solution and subsequently assembles at the template. There, it is present as a temporarily stabilized but transient phase that mediates the transfer of information from the template to the mineral phase. This occurs through the selective stabilization of only one of the orientations present, leading to the development of a single crystal.

References and Notes

1. H. A. Lowenstam, S. Weiner, *On Biomineralization* (Oxford Univ. Press, New York, 1989).
2. M. E. Davis, *Science* **305**, 480 (2004).
3. B. L. Smith *et al.*, *Nature* **399**, 761 (1999).
4. J. Aizenberg *et al.*, *Science* **309**, 275 (2005).
5. J. R. Young, J. M. Didimus, P. R. Bown, B. Prins, S. Mann, *Nature* **356**, 516 (1992).
6. L. Addadi, D. Joester, F. Nudelman, S. Weiner, *Chem. Eur. J.* **12**, 980 (2006).
7. N. A. J. M. Sommerdijk, G. de With, *Chem. Rev.* **108**, 4499 (2008).
8. M. Volmer, *Kinetik der Phasenbildung* (Steinkopff, Dresden, 1939).
9. Y. Politi, T. Arad, E. Klein, S. Weiner, L. Addadi, *Science* **306**, 1161 (2004).
10. E. Beniash, J. Aizenberg, L. Addadi, S. Weiner, *Proc. R. Soc. London Ser. B* **264**, 461 (1997).
11. B. P. Pichon, P. H. H. Bomans, P. M. Frederik, N. A. J. M. Sommerdijk, *J. Am. Chem. Soc.* **130**, 4034 (2008).
12. J. R. I. Lee *et al.*, *J. Am. Chem. Soc.* **129**, 10370 (2007).
13. D. Gebauer, A. Völkel, H. Cölfen, *Science* **322**, 1819 (2008).
14. C. L. Freeman, J. H. Harding, D. M. Duffy, *Langmuir* **24**, 9607 (2008).
15. See supporting material on *Science* Online.
16. S. Mann, B. R. Heywood, S. Rajam, J. D. Birchall, *Nature* **334**, 692 (1988).
17. S. Nickell, C. Kofler, A. P. Leis, W. Baumeister, *Nat. Rev. Mol. Cell Biol.* **7**, 225 (2006).
18. The sedimentation coefficient s is defined as the velocity v_t of the particle per unit gravitational acceleration (centrifugal acceleration: $\omega^2 r$, where ω is angular velocity and r is the radial distance to the rotation axis).
19. F. M. Michel *et al.*, *Chem. Mater.* **20**, 4720 (2008).
20. D. Quigley, P. M. Rodger, *J. Chem. Phys.* **128**, 221101 (2008).
21. E. Loste, E. Diaz-Marti, A. Zarbakhsh, F. C. Meldrum, *Langmuir* **19**, 2830 (2003).
22. E. DiMasi, M. J. Olszta, V. M. Patel, L. B. Gower, *CrystEngComm* **5**, 346 (2003).
23. T. H. Zhang, X. Y. Liu, *J. Am. Chem. Soc.* **129**, 13520 (2007).
24. Y. Politi *et al.*, *Adv. Funct. Mater.* **16**, 1289 (2006).
25. R. S. K. Lam, J. M. Charnock, A. Lennie, F. C. Meldrum, *CrystEngComm* **9**, 1226 (2007).
26. J. Aizenberg, D. A. Muller, J. L. Grazul, D. R. Hamann, *Science* **299**, 1205 (2003).
27. R. Tang *et al.*, *Angew. Chem. Int. Ed.* **43**, 2697 (2004).
28. G. Luquet, F. Marin, *C. R. Palevol* **3**, 515 (2004).
29. L. Brecevic, A. E. Nielsen, *J. Cryst. Growth* **98**, 504 (1989).
30. J. J. J. M. Donners, B. R. Heywood, E. W. Meijer, R. J. M. Nolte, N. A. J. M. Sommerdijk, *Chem. Eur. J.* **8**, 2561 (2002).
31. A. S. Posner, F. Betts, *Acc. Chem. Res.* **8**, 273 (1975).
32. S. Rajam *et al.*, *J. Chem. Soc. Faraday Trans.* **87**, 727 (1991).

33. Supported by the European Community (project code NMP4-CT-2006-033277) and the Netherlands Organization for Scientific Research (NWO). We thank A. Völkel and H. Cölfen for performing and evaluating the ultracentrifugation measurements; D. Gebauer and A. Verch for time-dependent solution composition determination of the mineralization solutions; F. L. Boogaard, E. J. Creusen, J. J. van Roosmalen, and P. Moeskops for their contribution to the 3D reconstructions of the tomograms; and P. T. K. Chin for providing the CdSe nanorods.

Supporting Online Material

www.sciencemag.org/cgi/content/full/323/5920/1455/DC1
Materials and Methods
SOM Text
Table S1
Figs. S1 to S7

5 December 2008; accepted 30 January 2009
10.1126/science.1169434

Self-Repairing Oxetane-Substituted Chitosan Polyurethane Networks

Biswajit Ghosh and Marek W. Urban*

Polyurethanes have many properties that qualify them as high-performance polymeric materials, but they still suffer from mechanical damage. We report the development of polyurethane networks that exhibit self-repairing characteristics upon exposure to ultraviolet light. The network consists of an oxetane-substituted chitosan precursor incorporated into a two-component polyurethane. Upon mechanical damage of the network, four-member oxetane rings open to create two reactive ends. When exposed to ultraviolet light, chitosan chain scission occurs, which forms crosslinks with the reactive oxetane ends, thus repairing the network. These materials are capable of repairing themselves in less than an hour and can be used in many coatings applications, ranging from transportation to packaging or fashion and biomedical industries.

When a hard or sharp object hits a vehicle, it is likely that it will leave a scratch, and for this reason the automotive industry looks for coatings with high scratch resistance. Because of their hardness and elasticity, polyurethanes exhibit good scratch resistance but can still suffer from mechanical damage. An ideal automotive coating would mend itself while a vehicle is driven. To heal mechanical damage in plants, suberin, tannins, phenols, or nitric oxide are activated to prevent further lesions (*1*–*3*), whereas in a human skin, the outer flow of blood cells is arrested by the crosslink network of fibrin, giving rise to wound-healing (*4*, *5*). Concentration gradients or stratification in living organisms inspired the development of spatially heterogeneous remendable polymers (*6*, *7*), composites containing micro-encapsulated spheres (*8*–*11*), encapsulated fibers (*12*–*14*), reversible cross-linking (*15*, *16*), and microvascular networks (*17*). One example is epoxy matrices containing a glass hollow fiber filled with a monomer and an initiator with the "bleeding" ability to heal polymer networks during crack formation (*12*). A similar phenomenon was used in another approach, in which a micro-encapsulated dicyclopentadiene monomer was introduced in a catalyst-embedded polymer matrix, which healed the crack near the ring opening of the monomer (*8*–*11*). Reversibility of Diels-Alder reactions resulted in another approach to thermally repair damaged areas, and approach using malemide-furan adducts (*15*, *16*). Mimicking of microvascular structures (*17*), water-responsive expandable gels (*7*), and formation of supramolecular assemblies (*18*) are other avenues of remendability.

This study departs from previous approaches and reports the development of heterogeneous

---

School of Polymers and High Performance Materials, Shelby F. Thames Polymer Science Research Center, The University of Southern Mississippi, Hattiesburg, MS 39406, USA.

*To whom correspondence should be addressed. E-mail: marek.urban@usm.edu

polyurethane (PUR) networks based on oxetane-substituted derivative of chitosan (OXE-CHI), which upon reaction with hexamethylene diisocyante (HDI) and polyethylene glycol (PEG) (*19*) form heterogeneous OXE-CHI-PUR networks. The choice of these components was driven by their ability to serve specific functions; PUR networks provide desirable heterogeneity through polyurethane and polyurea components, and OXE-CHI provides the cleavage of a constrained four-membered ring (OXE) and ultraviolet (UV) sensitivity through CHI, the latter being a product of deacetylation of chitin, which is the structural element of exoskeletons of crustaceans (e.g., crabs and shrimp) occurring in abundance in nature. Figure 1 illustrates a two-step reaction sequence leading to the OXE-CHI-PUR formation (*20*). The first step in this investigation was the synthesis of OXE-CHI, in which the primary alcohol of CHI was reacted with chloromethyl of OXE (*21*). An OXE ring was reacted to the C_6 position of the chitosan molecule, which is confirmed by infrared (IR), Raman, and ^{13}C-NMR (nuclear magnetic resonance) spectroscopy (*20*) (figs. S1, S2, and S3, respectively). The second step illustrates the reactions leading to the incorporation of OXE-CHI into trifunctional HDI in the presence of PEG (1:1.4 and 1:1.33 molar ratios), confirmed by IR and ^{13}C-NMR spectroscopy (*20*) (figs. S4 and S5, respectively).

Networks were allowed to crosslink under ambient conditions to form solid films and then were mechanically damaged by creating a scratch. Figure 2A1 illustrates a mechanical damage of OXE-CHI-PUR films. When the damaged area is exposed to a 120 W fluorescent UV lamp at 302 nm wavelength of light for 15 (Fig. 2A2) and 30 (Fig. 2A3) min, the damaged area vanishes. The upper portion of Fig. 2 illustrates IR images of the damaged area, whereas the lower part illustrates optical images. Also, IR images of the damaged area exhibit chemical changes resulting from the repair and are shown in figs. S8 and S9. A series of controlled experiments were conducted on specimens prepared by varying molar ratios of OXE-CHI with respect to the PUR content (table S1). Optical images shown in Fig. 3, A to D, illustrate the results of the experiments conducted under the same UV exposure conditions (0, 15, and 30 min) conducted on the specimens listed in table S1.

These experiments illustrate that the presence of OXE-CHI precursor is the key factor responsible for remendability of the network (Figs. 2 and 3). Neither PUR nor CHI-PUR alone (table S1, specimens A and B) is able to repair the mechanical damage, whereas the presence of covalently bonded OXE-CHI (table S1, specimens C and D) entities facilitates the self-healing process.

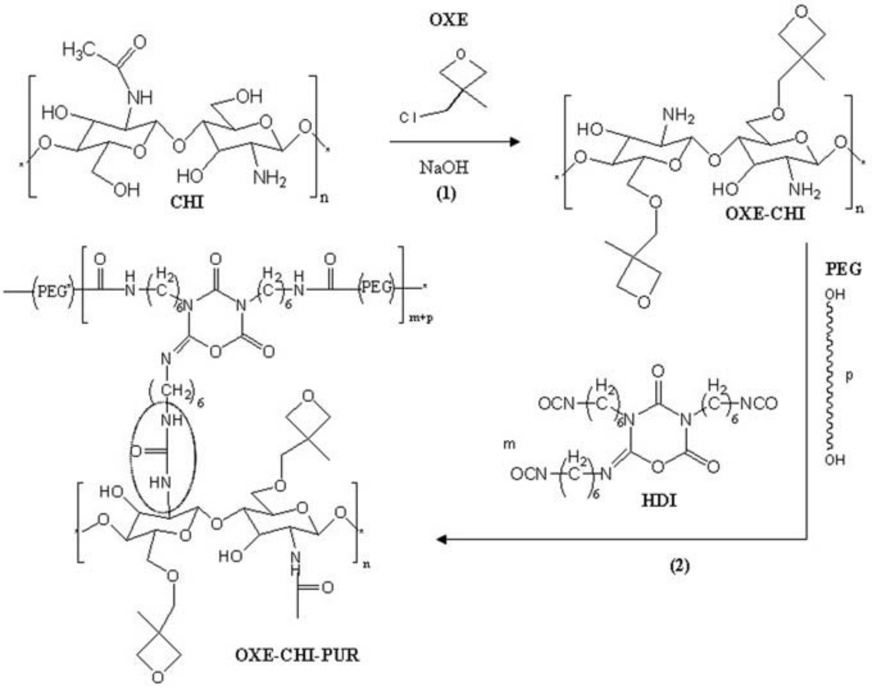

Fig. 1. Synthetic steps involved in the formation of OXE-CHI. 1, Reactions of OXE with CHI, leading to the formation of OXE-CHI precursor; 2, Reactions of OXE-CHI with HDI and PEG, leading to formations of remendable OXE-CHI-PUR network.

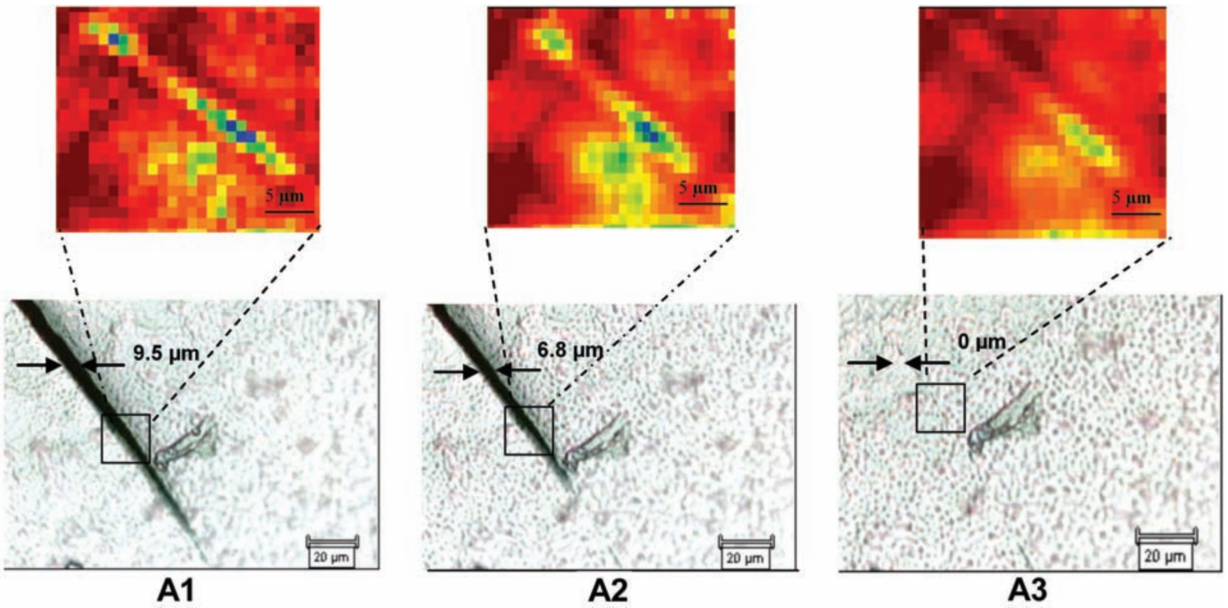

Fig. 2. IR (**upper**) and optical (**lower**) images of OXE-CHI-PUR networks recorded as a UV exposure time. A1, 0 min; A2, 15 min; A3, 30 min. (SOM provides details regarding spectroscopic changes detected by IR imaging.)

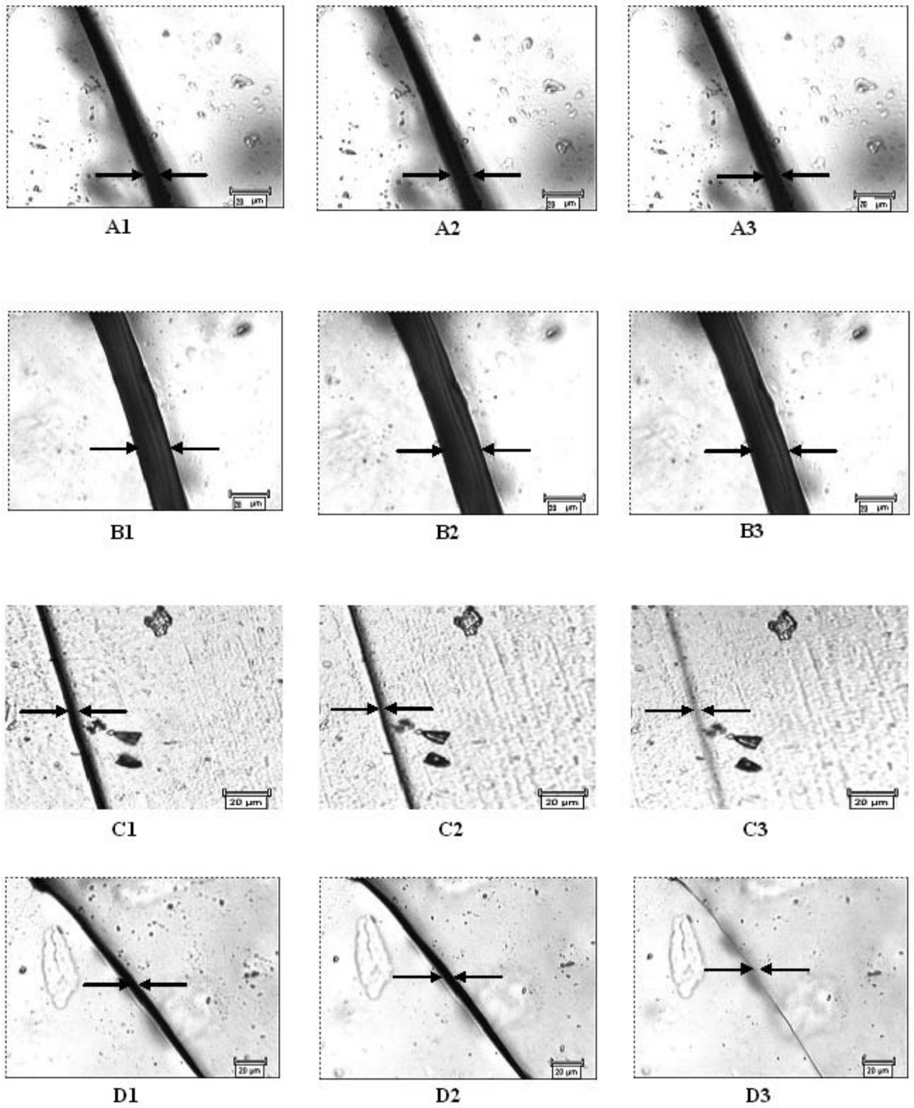

Fig. 3. Optical images of mechanically damaged films: PUR (A1, A2, and A3 are images after exposure for 0, 15, and 30 min to UV radiation; HDI/PEG/CHI = 1:1.5:0); CHI-PUR (B1, B2, and B3 are images after exposure for 0, 15, and 30 min to UV radiation; HDI/PEG/CHI = 1:1.4:0.57 × 10^{-4}); OXE-CHI-PUR (C1, C2, and C3 are images after exposure for 0, 15, and 30 min to UV radiation; HDI/PEG/OXE-CHI = 1:1.4:0.57 × 10^{-4}); OXE-CHI-PUR (D1, D2, and D3 are images after exposure for 0, 15, and 30 min to UV radiation; HDI/PEG/OXE-CHI = 1:1.33:1.17 × 10^{-4}).

Table S1 also shows the damage width as a function of UV exposure evaluations conducted on the specimens shown in Fig. 3. The rate of repair for networks containing half the OXE-CHI precursor concentration is also reduced.

Although a cut is a local event at micrometer or smaller scales, the actual cleavage is a molecular-level event. To determine the mechanism of repair and to follow molecular events in the damaged area, we used localized micro-attenuated total reflectance (ATR) Fourier transform IR (FTIR) spectroscopy (*22*) and internal reflection IR imaging (IRIRI) (*23*). As shown in figs. S6 and S7, the loss of urea and ether linkages of CHI (circled in Fig. 1) containing OXE rings results from the UV light exposure of damaged surface areas responsible for repairing. In these experiments, the repair process uses UV light to recombine free radicals to form crosslinks. In the 280 to 400 nm range, a fluorescent UV lamp generates approximately 0.3 W/m^2 per nm power density, whereas the Sun gives off about 0.25 W/m^2 per nm (*24*). Thus, the time frames for repair of the Sun exposure are very similar, although the energy density changes as a function of the wavelength of radiation for both sources vary somewhat. As a result of stronger Sun radiation during the summer months in the southern United States, the repair process will be about 3 to 4 times as fast compared with the equivalent exposure in the northern United States, but for the winter months this difference will be negligible (*25*). Because crosslinking reactions are not moisture sensitive, dry or humid climate conditions will not affect the repair process. The above networks exhibit the ability to self-repair upon exposure to UV light, but if exactly the same previously repaired spot is damaged again, the ability for further repair may be limited by the thermosetting characteristics of these networks.

We developed a new generation of thermosetting polymers that are of considerable technical and commercial importance. The use of the UV portion of the electromagnetic radiation for repairing mechanical damages in coatings offers an ambient temperature approach to self-healing—critical in a number of applications and technologies that do not require the placement of other, often elaborate, network components—that is controlled by the chemistries and morphologies of polymer networks.

References and Notes

1. J. Leon, E. Rojo, J. J. Sanchez-Serrano, *J. Exp. Bot.* **52**, 1 (2001).
2. R. F. Diegelmann, M. C. Evans, *Front. Biosci.* **9**, 283 (2004).
3. R. Paris, L. Lamattina, C. A. Casalongue, *Plant Physiol. Biochem.* **45**, 80 (2007).
4. G. Henry, W. Li, W. Garner, D. T. Woodley, *Lancet* **361**, 574 (2003).
5. K. G. Mann, K. Brummel-Ziedins, T. Orefo, S. Butenas, *Blood Cells Mol. Dis.* **36**, 108 (2006).
6. P. Sonntag *et al.*, *Nat. Mater.* **3**, 311 (2004).
7. K. Nagaya, S. Ikai, M. Chiba, X. Chao, *JSME Int. J. Ser. C* **49**, 379 (2006).
8. S. R. White *et al.*, *Nature* **409**, 794 (2001).
9. E. N. Brown, M. R. Kessler, N. R. Sottos, S. R. White, *J. Microencapsul.* **20**, 719 (2003).
10. E. N. Brown, S. R. White, N. R. Sottos, *J. Mater. Sci.* **39**, 1703 (2004).
11. M. R. Kessler, N. R. Sottos, S. R. White, *Composites Part A* **34**, 743 (2003).
12. J. W. C. Pang, I. P. Bond, *Compos. Sci. Technol.* **65**, 1791 (2005).
13. J. W. C. Pang, I. P. Bond, *Composites Part A* **36**, 183 (2005).
14. S. R. Trask, H. R. Williams, I. P. Bond, *Bioinspir. Biomim.* **2**, P1 (2007).
15. X. Chen *et al.*, *Science* **295**, 1698 (2002).
16. R. Gheneim, C. Perez-Berumen, A. Gandini, *Macromolecules* **35**, 7246 (2002).
17. S. K. Toohey, N. R. Sottos, J. A. Lewis, J. S. Moore, S. R. White, *Nat. Mater.* **6**, 581 (2007).
18. P. Cordier, F. Tournilhac, C. Soulie-Ziakovic, L. Leiber, *Nat. Lett.* **451**, 977 (2008).
19. D. B. Otts, M. W. Urban, *Polymer (Guildf.)* **46**, 2699 (2005).
20. Materials and methods and additional data are available as supporting material on *Science* Online.
21. Y. Wan, K. A. M. Creber, B. Peppley, V. T. Bui, *J. Polym. Sci. Part B Polym. Phys* **42**, 1379 (2004).
22. M. W. Urban, *Attenuated Total Reflectance Spectroscopy of Polymers; Theory and Applications* (American Chemical Society and Oxford University Press, Washington, DC, 1996)
23. D. Otts, P. Zhang, M. W. Urban, *Langmuir* **18**, 6473 (2002).
24. Average Optimum Direct Global Radiation, Miami, FL, USA; Atlas Material Testing Technology; http://www.atlas-mts.com.
25. National Oceanographic and Atmospheric Administration, 2008; http://www.cpc.ncep.noaa.gov/products/stratosphere/uv_index/gif_files/spectrum.gif (www.noaa.gov).
26. These studies were primarily supported by the National Science Foundation MRSEC under DMR 0213883 and the Materials Research Instrumentation (MRI) Program under DMR 0215873. We thank the Mississippi Division of Marine Resources for partial support.

Supporting Online Material

www.sciencemag.org/cgi/content/full/323/5920/1458/DC1
Materials and Methods
SOM Text
Figs. S1 to S10
Table S1
References

20 October 2008; accepted 29 January 2009
10.1126/science.1167391

Nonporous Organic Solids Capable of Dynamically Resolving Mixtures of Diiodoperfluoroalkanes

Pierangelo Metrangolo,[1]* Yvan Carcenac,[1] Manu Lahtinen,[2] Tullio Pilati,[3] Kari Rissanen,[4] Ashwani Vij,[5] Giuseppe Resnati[1,3]

Halogen bonding has increasingly facilitated the assembly of diverse host-guest solids. Here, we show that a well-known class of organic salts, bis(trimethylammonium) alkane diiodides, can reversibly encapsulate α,ω-diiodoperfluoroalkanes (DIPFAs) through intermolecular interactions between the host's I^- anions and the guest's terminal iodine substituents. The process is highly selective for the fluorocarbon that forms an $I^-\cdots I(CF_2)_mI\cdots I^-$ superanion that is matched in length to the chosen dication. DIPFAs that are 2 to 12 carbons in length (common industrial intermediates) can thereby be isolated from mixtures by means of crystallization from solution upon addition of the dissolved size-matched ionic salt. The solid-state salts can also selectively capture the DIPFAs from the vapor phase, yielding the same product formed from solution despite a lack of porosity of the starting lattice structure. Heating liberates the DIPFAs and regenerates the original salt lattice, highlighting the practical potential for the system in separation applications.

α,ω-Diiodoperfluoroalkanes (α,ω-DIPFAs) are key intermediates (*1*) for the synthesis of various fluorochemicals and fluoropolymers, such as fluorinated elastomers (*2*–*4*). However, the production of DIPFAs has been hampered by the lack of a method to obtain the compounds in high yield and purity. The tetrafluoroethylene telomerization reaction with iodine produces a mixture of DIPFAs, usually separated into its components by fractional distillation (*5*). The heavier DIPFAs cannot easily be separated with this method, thereby limiting the availability of α,ω-DIPFAs that are longer than eight carbon atoms.

Here, we report the application of supramolecular and crystal-engineering principles to the resolution of DIPFA mixtures through selective and reversible capture by ionic organic solids. We initially observed selective crystallization of a given DIPFA **2** from solutions of size-matched bis(trimethylammonium) alkane diiodides **1** (Scheme 1). Furthermore, we found that even microcrystalline powders of the iodide salts could selectively incorporate matched DIPFAs from the gas phase despite the absence of porosity in the static crystal structures. Thus, **1a** to **1f** represent a class of dynamically porous materials (*6*).

We have already demonstrated that DIPFAs behave as robust telechelic halogen-bonding (*7*, *8*) donors, given that fluorine inductively boosts the electron density acceptor ability of the terminal iodine substituents (*9*). For this reason, α,ω-DIPFAs form particularly strong halogen bonds when interacting with naked iodide ions (*10*) and result in trimeric supramolecular anions of the type $I^-\cdots I(CF_2)_mI\cdots I^-$ (*11*). Our goal was to incorporate this superion into a crystal framework that would achieve peak stability for a given-sized DIPFA (*12*). We reasoned that matching the size of this halogen-bonded superanion with a terminally functionalized dication of similar dimensions should increase the strength of electrostatic binding in an ionic lattice, thus driving a selective molecular recognition of the target DIPFA. We therefore selected the iodide salts of the bis(trimethylammonium) alkane derivatives **1a-f** (*13*), which are well-known structure-directing agents in zeolite synthesis (*14*) and guests in supramolecular chemistry (*15*).

Single-crystal x-ray analysis of **1b**·$2H_2O$ (Fig. 1A) (*16*) shows that water is hydrogen-bonded to iodide ions ($H\cdots I^-$ has distances of 2.766 to 2.804 Å) and also weakly interacts with the methyl and methylene H atoms of the cation.

---

[1] Laboratory of Nanostructured Fluorinated Materials, Department of Chemistry, Materials, and Chemical Engineering Giulio Natta, Politecnico di Milano, via L. Mancinelli 7, 20131 Milan, Italy. [2] Department of Chemistry, University of Jyväskylä, Post Office Box 35, Jyväskylä FI–40014, Finland. [3] Istituto di Scienze e Tecnologie Molecolari–Consiglio Nazionale delle Ricerche, University of Milan, 20133 Milan, Italy. [4] Nanoscience Center, Department of Chemistry, University of Jyväskylä, Post Office Box 35, Jyväskylä FI–40014, Finland. [5] Air Force Research Laboratory/RZSP, 10 East Saturn Boulevard, Edwards Air Force Base, CA 93524, USA.

*To whom correspondence should be addressed. E-mail: pierangelo.metrangolo@polimi.it.

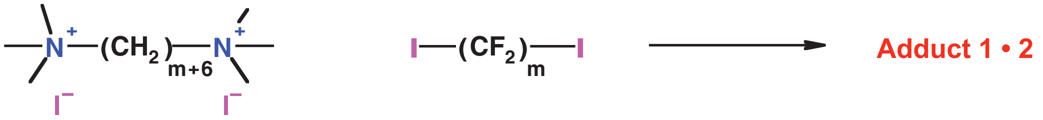

1 **2**

1, 2	a	b	c	d	e	f
m	2	4	6	8	10	12

Adduct	Distance A $^+N(CH_2)_{m+6}N^+$ (Å)	Distance B $I^-\cdots I(CF_2)_mI\cdots I^-$ (Å)		Δ (B - A) (Å)	Distance $I^-\cdots I$ (Å)	Angle $I^-\cdots I\text{-}C$ (°)
1a • 2a	11.290(14)	12.056(5)	MATCH	0.766	3.478(2)	167.8(4)
1b • 2b	13.628(12)	14.483(4)		0.855	3.4517(11)	166.0(4)
1c • 2c	16.395(11)	17.083(5)		0.688	3.4627(11)	167.5(2)
1b • 2d	13.62(4)	18.797(4)	MISMATCH	5.177	3.357(3), 3.410(2)	173.3(7), 176.1(6)
1a • 2b	10.527(8)	14.104(3)		3.577	3.3514(9)	174.7(4)

Scheme 1.

These interactions alongside the anion-cation interactions dominate the crystal structure. The bis(trimethylammonium) decane molecule adopts the usual all-trans conformation, and the hydrocarbon chains are parallel and interdigitated.

The N^+–N^+ intramolecular distance in crystalline **1b** of 13.965 Å is well-matched to the I^-–I^- distance in the $I^-\cdots I(CF_2)_4I\cdots I^-$ superanion, as found in our previous study (*17*). For this reason, we attempted to crystallize **1b** together with 1,4-diiodooctafluorobutane **2b**, starting from their equimolar CH_3OH and $CHCl_3$ solutions, respectively. Upon mixing of the two solutions, the 1:1 supramolecular complex **1b·2b** crystallized in a nearly quantitative yield and purity. Single-crystal x-ray analysis of the complex **1b·2b** confirmed our initial hypothesis: The distance between the intramolecular N atoms of **1b** in the complex is within 1 Å of the iodide ions' spacing in the superanion $I^-\cdots I(CF_2)_4I\cdots I^-$ ($\Delta = 0.855$ Å) (Scheme 1). Four alkyl dications define a rectangular parallelepiped-shaped cavity that encapsulates DIPFA **2b**, trapped by strong halogen bonds to the two I^- ions at either end (Fig. 1, B and C). As a probable consequence of the optimized binding that results from the structural complementarity of the interacting charged moieties and the matching sizes of the two starting compounds **1b** and **2b**, complex **1b·2b** shows a very low solubility in organic solvents as compared with that of pure starting materials. The $I^-\cdots I$-C distance of 3.452 Å, which is noticeably shorter than the sum of the van der Waals radius of the iodine atom and the Pauling radius for the I^- ion (4.14 Å) (*18*), indicates strong halogen bonding (*7*).

To test the generality of the size-matching hypothesis, we challenged salt **1a** with DIPFA **2a** and **1c** with **2c** (Scheme 1), maintaining the scaling relationship of **1b** and **2b**. Indeed, the complexes **1a·2a** (fig. S1) and **1c·2c** (Fig. 1D) both exhibit crystal lattices analogous to that of the **1b·2b** complex. In fact, two of the unit cell dimensions in each case are nearly the same (~6 and ~8 Å), indicating similar packing in those two directions, and the third dimension is related to the relative differences in the length of the molecules.

The importance of size matching was further confirmed by the isolation and structural characterization of two mismatched complexes, **1a·2b** and **1b·2d** (Scheme 1). In complex **1a·2b**, the discrete superanion $I^-\cdots I(CF_2)_4I\cdots I^-$ still forms ($I^-\cdots I$-C has a distance of 3.351 Å and angle of 174.70°), but the crystal packing is completely different from that in the matched structures. There is no cavity in which to trap the DIPFA; instead, the structure consists of cation and superanion layers (fig. S3). An even greater change occurs in the complex **1b·2d**, which crystallizes in a 1:2 stoichiometry and distributes the DIPFAs **2d** with alternating I^- ions in an infinite one-dimensional (1D) halogen-bonded polyanionic chain geometry ($I^-\cdots I$-C has distances of 3.357 and 3.410 Å and angles of 173.30 and 176.10°) (fig. S4).

All matched complexes (**1a·2a**, **1b·2b**, and **1c·2c**) show melting points higher than the mismatched ones in their respective homolog series, which is consistent with a higher stability of the crystal lattices with well-organized cavities around the DIPFAs. We therefore surmised that the enhanced stability should translate to a selective molecular recognition of a given DIPFA from a solution mixture by the size-matched salt **1** (*11*, *19*).

With this in mind, we performed competitive crystallization experiments by dissolving one equivalent of all four commercially available α,ω-DIPFAs **2a-d** into the same $CHCl_3$ solution. When this solution was added to a CH_3OH solution containing one equivalent of a single salt (from among **1a-d**), only the size-matched DIPFA was crystallized from the combined solution. Complexes at all four chain lengths (**a-d**) could be isolated in quantitative yield and purity. Although we were not able to obtain single-crystal x-ray data for the complex **1d·2d**, powder x-ray diffraction (PXRD) analysis confirmed the similarities in packing between **1d·2d** and the other matched complexes **1a-c·2a-c** (figs. S7 to S10). The above-described competitive crystallization experiment confirms the further generality of the size-matching rule for compounds $\mathbf{1_{m+6}}$ and $\mathbf{2_m}$. Once the matched DIPFA had been completely separated from the solution by filtering out the corresponding $\mathbf{1_{m+6}{\cdot}2_m}$ solid adduct, the addition to the solution of another equivalent of the same chain-length salt **1** consistently afforded a white solid comprising a mixture of all the other possible **1·2** mismatched complexes that were present in varying mass fractions.

Intrigued by the isolation of the **1d·2d** complex, we extended the selective crystallization method to a mixture of higher DIPFA telomers that were found in a distillation residue obtained from industry with the following mass fraction composition: 1,8-diiodoperfluorooctane **2d** (24.2%), 1,10-diiodoperfluorodecane **2e** (41.9%), 1,12-diiodoperfluorododecane **2f** (23.0%), 1,14-diiodoperfluorotetradecane (8.3%), and 1,16-diiodoperfluorohexadecane (2.6%). The α,ω-DIPFA mixture was dissolved in CCl_4 and combined with a CH_3OH solution of bis(trimethylammonium) hexadecane diiodide **1e** (one equivalent of **1e** for one equivalent of **2e** in the mixture). A white solid precipitated almost immediately. Gas chromatography (GC)

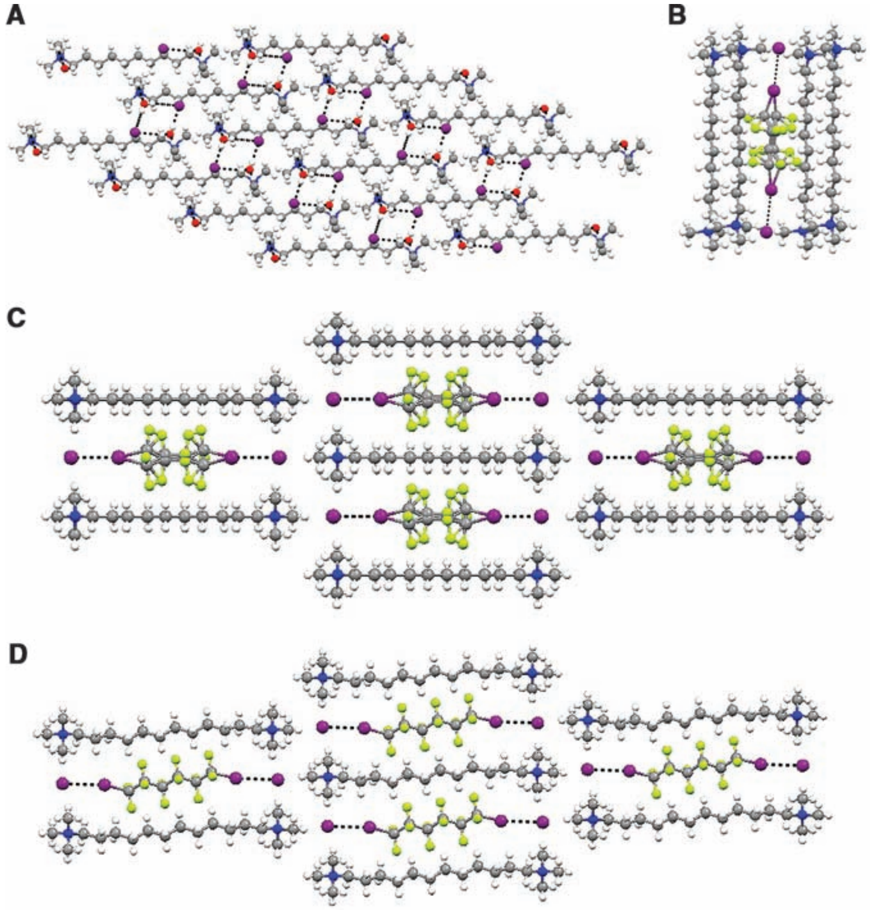

Fig. 1. (**A**) The packing of bis(trimethylammonium) decane diiodide dihydrate **1b**·$2H_2O$ viewed along the *a* axis. (**B**) The complex bis(trimethylammonium) decane diiodide/diiodoperfluorobutane **1b·2b**. Shown is a view of the molecular cavity defined by four alkyl dications, with encapsulated guest **2b** halogen-bonded to I^- ions at the top and bottom. (**C**) The crystal packing of the complex **1b·2b** viewed along the *c* axis. Both of the disordered orientations of **2b** are shown in (B) and (C). (**D**) The crystal packing of the complex **1c·2c** viewed along the *a* axis. The software package Mercury 1.4.2 (available for free download from www.ccdc.cam.ac.uk) was used to construct these images from the crystallographic information files. Gray, carbon; white, hydrogen; green, fluorine; blue, nitrogen; red, oxygen; magenta, iodine. Halogen bonds are depicted as dotted lines.

analysis indicated that **2e** was the only α,ω-DIPFA present in this solid. Nuclear magnetic resonance (NMR) experiments and melting point analysis on the solid confirmed the 1:1 ratio of the perfluorocarbon (PFC) and hydrocarbon (HC) components and thus the formation of the complex **1e·2e**. The same experiment was repeated by adding to a solution of the DIPFA mixture one equivalent of bis(trimethylammonium) octadecane diiodide **1f** in CH_3OH, which led to the rapid precipitation of the almost pure (>90%) 1,12-diiodoperfluorododecane complex **1f·2f** [based on GC, NMR, infrared (IR), and melting-point analysis] despite the low relative amount of **2f** in the starting mixture (23%).

Scattered examples in the open literature report the isolation of analytical samples of **2e** and **2f** by GC (*20*). Even in the vast patent literature on the preparation of α,ω-DIPFAs, we found no evidence of preparative and quantitative separation methods other than time- and energy-consuming fractional distillation, for which there was scarce indication of effectiveness in the purification of the higher telomers (*21*). Having thus characterized a selective crystallization technique with potentially great utility, we explored the reversibility of the binding of the DIPFAs in our matching complexes by means of various techniques. Our expectations were bolstered by the reversibility of halogen bonding and high DIPFA vapor pressure relative to salts **1**. Gas-phase IR spectra at ambient pressure in a sealed heated cell showed that the complex **1a·2a** starts to release **2a** at 433 K (the boiling point of pure **2a** is 385 K) with the maximum release occurring at 463 K, well before the melting temperature of the complex (474 K). Similar behavior was observed by use of thermogravimetric analysis (TGA) for the other **1b-d·2b-d** matched complexes (Table 1, figs. S19 to S30, and tables S8 to S10). In addition, PXRD, IR, melting-point, and NMR analyses confirmed that complete removal of **2a-d** yields the pure salts **1a-d** in the same crystal phases as the starting materials (figs. S15 to S18).

This robust liberation of the guest prompted us to study the reverse process, namely, the uptake of DIPFA vapors by the solid bis(trimethylammonium) alkane derivatives **1a-f**. Practical application of the selective molecular recognition would benefit from a nonsolvent environment. We placed finely ground ionic solids **1a**, **1b**, or **1c** in sealed nested jars so that they were isolated from surrounding liquid samples of the matched DIPFAs **2a**, **2b**, or **2c** but accessible to the corresponding vapor. The 1:1 matching complexes **1a·2a** and **1b·2b** were obtained after 6 hours and 7 days, respectively, at ambient pressure and temperature, and both complexes exhibited the same lattice structure observed from the solution crystallization (figs. S7 and S8). Because of the lower vapor pressure of **1c**, the 1:1 matching complex **1c·2c** required 3 days at 313 K to form fully; once again, the same crystal phase as from the solution was observed (Fig. 2, left). These gas-solid reactions thus transform a nonporous ionic solid into a well-ordered encapsulation complex.

The selectivity of these gas-solid reactions was further probed by the following guest-exchange reaction. The finely ground mismatched complex **1a·2b** was exposed to vapor of the matched DIPFA **2a** in a sealed vessel at ambient pressure and temperature for 7 days. PXRD data indicated that the mismatched DIPFA **2b** was completely replaced in this gas-solid reaction by the matched **2a**, yielding exclusively the 1:1 matching complex **1a·2a** in the same crystal form as had been obtained by means of solution crystallization (Fig. 2, D and E). The same experiment carried out on the matching complex **1a·2a** by means of exposure to vapor of the mismatched DIPFA **2b** did not result in any reaction (Fig. 2, F and G).

Nanoporous solids that are able to absorb and release small molecules in a controllable and selective fashion are rare but known in the literature (*22–26*). An alternative to nanoporosity is the controlled uptake and release of small molecules by means of reversible heterogeneous gas-solid reactions (*27–29*). In the present case of nonporous solid compounds, bis(trimethylammonium) alkane diiodides **1a-f** show a size-matching–based dynamic response upon exposure to gaseous α,ω-DIPFAs

Table 1. Observed and calculated weight losses for DIPFA removal from matching complexes **1a-d·2a-d**. Δwt_{obs}, observed weight loss for leaving compound; Δwt_{calc}, theoretical weight loss for leaving DIPFA; T_{end}, observed end temperature of DIPFA removal; T_m, melting point of the starting complex; β, heating rate.

Complex	Formula weight (g/mol)	Δwt_{obs} (%)	Δwt_{calc} (%)	T_{end} (K)	T_m (K)	β (K/min)
1a·2a	838.05	37.7	42.22 (**2a**)	464	474	10
1a·2a*		41.7	42.22 (**2a**)	463	474	10/isotherm
1b·2b	966.12	47.0	46.97 (**2b**)	493	503	10
1b·2b*		44.6	46.97 (**2b**)	463	503	10/isotherm
1c·2c	1094.20	50.5	50.62 (**2c**)	468	500	2
1c·2c*		49.8	50.62 (**2c**)	463	500	10/isotherm
1d·2d	1222.28	53.1	53.47 (**2d**)	486	504	2
1d·2d†		52.4	53.47 (**2d**)	486	504	10/isotherm

*Thermogravimetric run included an isothermal step at 463 K for 60 min. †Thermogravimetric run included an isothermal step at 448 K for 60 min.

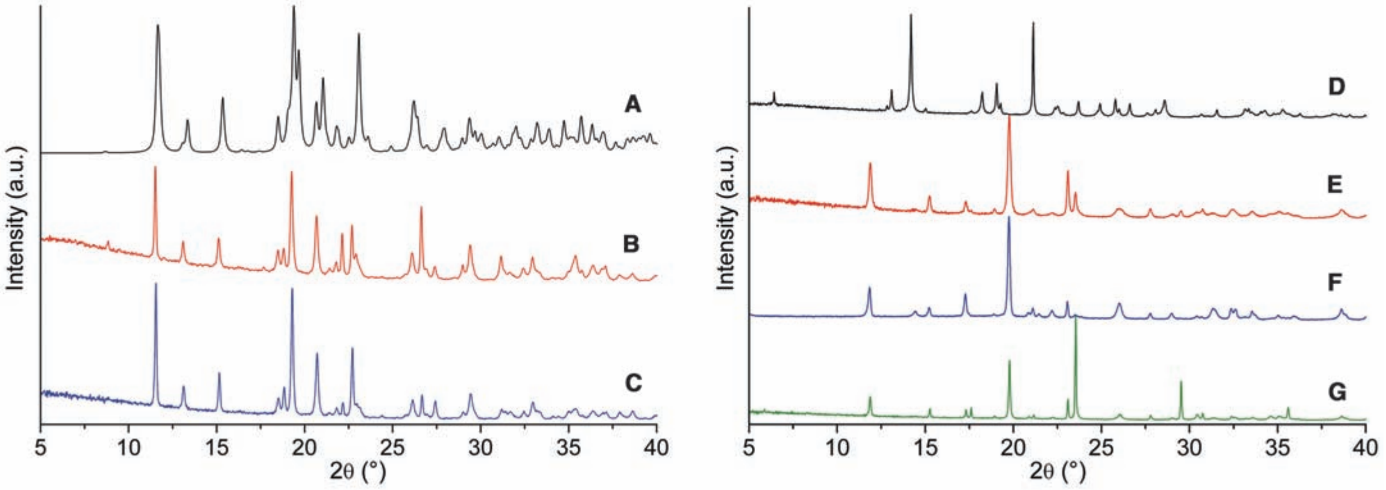

Fig. 2. (Left) PXRD patterns of the complex **1c·2c** (**A**) simulated from single-crystal x-ray data, (**B**) acquired after solution crystallization, and (**C**) acquired after gas-solid reaction. (Right) PXRD patterns of the mismatched complex **1a·2b** obtained from solution crystallization (**D**) before and (**E**) after exposure to vapor of 1,2-diiodoperfluoroethane **2a**. Below these are PXRD patterns of the matched complex **1a·2a** obtained from solution crystallization (**F**) before and (**G**) after exposure to vapor of 1,4-diiodoperfluorobutane **2b**.

2a-f, yielding the homologous series of supramolecular complexes $\mathbf{1}_{m+6}\cdot\mathbf{2}_m$. In such complexes, the complementarity of size leads to a structure type that overrides the strong driving force of PFC-HC segregation. This process is expected to require surmounting a considerable energy barrier, especially in the case of the very long DIPFA **2c**. Although the size-matching leads to one product, the PFC-HC segregation does not distinguish between various sizes of PFC and HC segments, as was proven by the observation of a variety of complexes produced from a size-mismatched PFC-HC mixture. Despite a lack of porosity of the starting materials **1a-f**, the DIPFAs **2a-f** are readily transported through the solid until a thermodynamically stable porous structure is achieved. A comparison with the x-ray structure of the pure salt **1b** (Fig. 1A) suggests that once the size-matching DIPFA forms halogen bonds with the I^- ions, the $I^-\cdots I(CF_2)_mI\cdots I^-$ superanion acts as a template of the porous structure observed by promoting the positional and/or orientational rearrangement of the hydrocarbon dications (analogously to the sliding filament model, such as what occurs between thick and thin filaments in myofibrils). Our results show the relevance of a supramolecular-templated assembly of dynamically porous materials.

Gas-solid reactions often entail profound transformations of the chemical and physical nature of the solid materials and rarely are of practical use. In the present case, the full reversibility of the process, whereby DIPFAs can first be selectively complexed and then quantitatively evacuated, yields purified fluorinated telomers and a reusable ionic scaffold. Beyond the practical potential for separating mixtures of α,ω-DIPFAs, we envision the application of this purification method to another vast class of compounds of industrial interest, the α,ω-diiodoperfluoropolyethers (DIPFPEs), which are useful intermediates for the synthesis of fluorocontaining resins, elastomers, and surfactants.

References and Notes

1. N. O. Brace, *J. Fluor. Chem.* **108**, 147 (2001).
2. B. Ameduri, B. Boutevin, *Well-Architectured Fluropolymers: Synthesis, Properties and Applications* (Elsevier, Amsterdam, 2004).
3. K. Baum, T. G. Archibald, A. A. Malik, *J. Org. Chem.* **59**, 6804 (1994).
4. A. L. Logothetis, in *Organofluorine Chemistry*, R. E. Banks, B. E. Smart, J. C. Tatlow, Eds. (Plenum, New York, 1994), pp. 373–396.
5. H.-P. Cao, Q.-Y. Chen, *J. Fluor. Chem.* **128**, 1187 (2007).
6. S. J. Dalgarno, P. K. Thallapally, L. J. Barbour, J. L. Atwood, *Chem. Soc. Rev.* **36**, 236 (2007).
7. P. Metrangolo, G. Resnati, *Chem. Eur. J.* **7**, 2511 (2001).
8. K. Rissanen, *CrystEngComm* **10**, 1107 (2008).
9. P. Metrangolo, G. Resnati, *Science* **321**, 918 (2008).
10. P. Metrangolo, H. Neukirch, T. Pilati, G. Resnati, *Acc. Chem. Res.* **38**, 386 (2005).
11. P. Metrangolo, F. Meyer, T. Pilati, G. Resnati, G. Terraneo, *Angew. Chem. Int. Ed.* **47**, 6114 (2008).
12. M. I. Nelen, A. V. Eliseev, *J. Chem. Soc. Perkin Trans. 2* 1359 (1997).
13. H.-G. Löhr *et al.*, *J. Org. Chem.* **49**, 1621 (1984).
14. P. Sun, Q. Jin, L. Wang, B. Li, D. Ding, *J. Porous Mater.* **10**, 145 (2003).
15. E. Menozzi, J. Rebek, *Chem. Commun. (Camb.)* **44**, 5530 (2005).
16. Materials and methods are available as supporting material on *Science* Online.
17. R. Liantonio, P. Metrangolo, T. Pilati, G. Resnati, *Cryst. Growth Des.* **3**, 355 (2003).
18. A. Bondi, *J. Phys. Chem.* **68**, 441 (1964).
19. M. W. Hosseini, J. M. Lehn, *J. Am. Chem. Soc.* **104**, 3525 (1982).
20. S. Boneva, St. Kotov, *Chromatographia* **25**, 735 (1988).
21. H. Dindi, J. J. Hagedorn, M.-H. Hung, U.S. Patent 6825389 (2004).
22. J. L. Atwood, L. J. Barbour, A. Jerga, B. L. Schottel, *Science* **298**, 1000 (2002).
23. P. K. Thallapally *et al.*, *Nat. Mater.* **7**, 146 (2008).
24. B. D. Chandler *et al.*, *Nat. Mater.* **7**, 229 (2008).
25. J. L. Atwood, L. J. Barbour, A. Jerga, *Science* **296**, 2367 (2002).
26. S. Kitagawa, K. Uemura, *Chem. Soc. Rev.* **34**, 109 (2005).
27. D. Braga *et al.*, *Angew. Chem. Int. Ed.* **45**, 142 (2006).
28. J. J. Vittal, *Coord. Chem. Rev.* **251**, 1781 (2007).
29. S. Libri *et al.*, *Angew. Chem. Int. Ed.* **47**, 1693 (2008).
30. P.M., T.P., and G.R. thank Fondazione Cariplo (Project "Self-Assembled Nanostructured Materials: A Strategy for the Control of Electrooptic Properties") for generous support. K.R. thanks the Academy of Finland (project 212588) for generous support. A.V. thanks the U.S. Air Force Research Laboratory/Air Force Office of Scientific Research for a generous Window on Europe grant, A. Garscadden for his endorsement, and R. Channell, R. Corley, and M. Huggins for their support. The authors declare no conflict of interest. A part of the present work is the object of the patent application PCT/EP2008/058588 (2008), priority date 7 November 2007, by Y.C., P.M., and G.R. to Politecnico di Milano. The authors' contributions were as follows: A.V., Y.C., M.L., T.P., and P.M. performed experiments; P.M., G.R., K.R., M.L., T.P., and Y.C. performed data analysis; and P.M., G.R., K.R., M.L., and T.P. wrote the paper. Crystallographic data for compounds **1a•2a**, **1a•2b**, **1b•2b**, **1b•2d**, **1b**, and **1c•2c** can be obtained free of charge from the Cambridge Crystallographic Data Centre via www.ccdc.cam.ac.uk/data_request/cif under reference numbers CCDC 709470 to 709475, respectively.

Supporting Online Material

www.sciencemag.org/cgi/content/full/323/5920/1461/DC1
Materials and Methods
Figs. S1 to S30
Tables S1 to S10
Schemes S1 to S2
References

18 November 2008; accepted 22 January 2009
10.1126/science.1168679

Time-Resolved Molecular Frame Dynamics of Fixed-in-Space CS_2 Molecules

Christer Z. Bisgaard,[1] Owen J. Clarkin,[1,2] Guorong Wu,[1] Anthony M. D. Lee,[1,2]* Oliver Geßner,[3] Carl C. Hayden,[4] Albert Stolow[1,2]†

Random orientation of molecules within a sample leads to blurred observations of chemical reactions studied from the laboratory perspective. Methods developed for the dynamic imaging of molecular structures and processes struggle with this, as measurements are optimally made in the molecular frame. We used laser alignment to transiently fix carbon disulfide molecules in space long enough to elucidate, in the molecular reference frame, details of ultrafast electronic-vibrational dynamics during a photochemical reaction. These three-dimensional photoelectron imaging results, combined with ongoing efforts in molecular alignment and orientation, presage a wide range of insights obtainable from time-resolved studies in the molecular frame.

Most molecules are non-spherical and so exhibit a dependence on their relative orientation in interactions with other molecules or with light. Measurements, therefore, should ideally be made in the molecular reference frame (MF). Unfortunately, in the gas and liquid phases, molecules are generally randomly oriented in the laboratory frame (LF) to which most standard techniques are referenced, leading to blurred observations of molecular properties and processes. An analogy is the difference between single-crystal versus powder x-ray diffraction, the former revealing the greatest details of molecular structure. Other examples include the determination of vector correlations in photodissociation dynamics (*1*) and measurements of (time-independent) photoelectron angular distributions (PADs) of fixed-in-space molecules, which has been a goal of researchers since the 1970s (*2*) and was achieved for selected cases (*3*, *4*). Promising ultrafast techniques for imaging structural and electronic changes during molecular processes, such as time-resolved x-ray (*5*) and electron (*6*, *7*) diffraction, tomographic orbital imaging (*8*), time-resolved photoelectron spectroscopy (TRPES) (*9*, *10*), laser-induced electron diffraction (*11*), and high harmonic generation (*12*), would all benefit from avoidance of this

---

[1] Steacie Institute for Molecular Sciences, National Research Council Canada, 100 Sussex Drive, Ottawa, Ontario K1A 0R6, Canada. [2] Department of Chemistry, Queen's University, Kingston, Ontario K7L 3N6, Canada. [3] Chemical Sciences Division, Lawrence Berkeley National Laboratory, One Cyclotron Road, M/S 2-300, Berkeley, CA 94720, USA. [4] Combustion Research Facility, Sandia National Laboratory, Livermore, CA 94551, USA.

*Present address: Department of Cancer Imaging, BC Cancer Research Centre, Vancouver, British Columbia V5Z 1L3, Canada.

†To whom correspondence should be addressed. E-mail: albert.stolow@nrc.ca

orientational averaging of MF observables. Here we present ultrafast time-resolved imaging measurements of a complex molecular process (a nonadiabatic photochemical reaction) from the MF, employing a laser technique that transiently fixes the molecules' alignment in space for sufficiently long to permit field-free dynamic measurements.

Strong nonresonant laser fields can induce molecular axes alignment within the LF (*13*) but may themselves modify excited-state dynamics (*14*). The goal of probing molecules that are aligned but field-free can be accomplished by applying a short laser pulse (*15*) that leaves the molecules transiently aligned (fixed-in-space) for, typically, a few picoseconds. This very brief molecular alignment can only be fully exploited by ultrafast measurement techniques—in our case, by TRPES, a method sensitive to both electronic and vibrational rearrangements (*16*–*19*). We chose to investigate the nonadiabatic photodissociation reaction $CS_2 + h\upsilon \rightarrow CS_2^* \rightarrow CS(X) + S(^1D)/S(^3P)$. CS_2 is notable as a triatomic system because it exhibits three general features of photodissociation dynamics: (i) vibrational mode coupling, (ii) internal conversion, and (iii) intersystem crossing. Consequently, CS_2 has complex photodissociation dynamics and, despite numerous studies, many details remain unresolved (*20*). Our study of coupled electronic and vibrational rearrangements occurring during this reaction combined impulsive alignment (*15*) with time-resolved photoelectron three-dimensional (3D) imaging (*10*) and quantum beat spectroscopy (*21*) to reveal details of the scattering resonances discernable only within the MF.

The ultraviolet (UV, 200 nm) photodynamics of the initially linear CS_2 molecule involves complex nonadiabatic and spin-orbit mixing, leading to multiple product states. The excitation from a nonbonding S atom orbital to an antibonding π^* molecular orbital lengthens the C–S bonds and leads to a bent equilibrium geometry. Thus, the absorption spectrum contains progressions assigned to combined excitations of the symmetric stretch and bend vibrations. In addition, nonadiabatic interactions with a nearby excited state lead to the mixing of electronic character at bent geometries. The excited-state bending frequency is nearly degenerate with that of the considerably weakened symmetric stretch, leading to combination bands of symmetric stretch and bend with peaks spaced by ~400 cm^{-1}, each further split (~30 cm^{-1}) because of this near degeneracy (*22*). The barrier to linearity in this electronically excited state is at ~49600 cm^{-1} (201.6 nm), the excitation energy used in our experiments. Therefore, Franck-Condon (FC) factors favor excitation into a quasi-linear geometry. Because photoabsorption leads to dissociation, these spectral peaks may be understood as photodissociation scattering resonances having lifetimes exceeding several vibrational periods. The two open product channels, $CS + S(^3P_J)$ and $CS + S(^1D_2)$, have a wavelength-dependent branching ratio (*23*) and broad translational energy distributions (*24*). From the peak widths in the absorption and S atom action spectra, with estimated resonance lifetimes of <1 ps (*23*). Femtosecond time-resolved ion yield (*25*, *26*) and photoelectron (*20*) measurements confirmed this subpicosecond behavior. Coexisting with the sharp resonances in the 6-eV region is a broad underlying continuum (*23*) attributable to very short-lived scattering resonances (direct dissociation) involving the antisymmetric stretch vibration (*27*).

A depiction of our time-resolved photoelectron probing of CS_2 photodissociation dynamics is presented in Fig. 1. After transient alignment of the CS_2, a femtosecond UV pump pulse prepared a coherent superposition of scattering resonances in a linear geometry, leading to quasi-bound vibrational motions followed by dissociation to both singlet and triplet products (Fig. 1). This superposition was probed as a function of time by a delayed probe pulse (125-fs pump-probe cross-correlation) that ionized the molecule. The emitted photoelectron was analyzed as a function of energy, 3D recoil angle, and pump-probe delay. The duration of the alignment (~4 ps full width at half maximum) was longer than the time scale of the photoreaction (< 1 ps), rendering the molecules effectively fixed in space during the measurement.

The resolved series of resonances allowed us to combine our time-resolved photoelectron 3D imaging method (*28*) with another powerful technique for probing excited-state dynamics: quantum beat spectroscopy (*21*). By tuning the central wavelength (bandwidth ~ 250 cm^{-1}) of our femtosecond pump laser to 201.2 nm, we coherently prepared a superposition of two scattering resonances, differing only in the degree of symmetric stretch versus bending excitation. Quantum interference in photoionization of coherently prepared scattering resonances was previously reported in ion yield measurements for IBr (*29*) and CS_2 (*26*) photodissociation. In the present case, the quantum beat interference between two long-lived scattering resonances in our MF photoelectron data permits access to intimate details of the electronic-vibrational couplings associated with the decay of these resonances.

A time-resolved photoelectron spectrum acquired for unaligned CS_2 is given in Fig. 2A, showing photoelectron kinetic energies as a function of delay. At short delays, the 0.7-eV peak, broadened because of an unresolved 55-meV spin-orbit splitting, arises from ionization into the vibrationless (0,0,0) cation ground state. The low-energy features correspond to ionization into highly excited vibrational states. The time-resolved spectrum is composed of a fast initial decay, as well as a slow decay across the whole spectrum, and a slow, periodic modulation of the high-energy electrons. We employed 2D global methods to simultaneously fit all photoelectron energies at all time delays to within experimental errors. Our kinetic model involved two independent exponential decays, with the longer one modulated by a harmonic oscillation (*28*). The global fit yielded time constants of $\tau_1 = 70 \pm 20$ fs and $\tau_2 = 830 \pm 40$ fs, with a modulation period of $T = 1010 \pm 20$ fs. The decay-associated photoelectron spectra of these three kinetic components are presented in Fig. 2B. As expected, the long-lived τ_2 component samples highly distorted geometries that ionize to vibrationally excited ions (low photoelectron energies). In Fig. 2C, we show the time evolution of the LF photoelectron signal at 0.7 eV and the global fit (red line), corresponding to ionization into the cation (0,0,0) ground state. The quantum beat signal can be clearly seen. The extracted time constant τ_2 is in very good agreement with the lifetime estimated from analysis of rotational band contours in the action spectrum (*23*). The

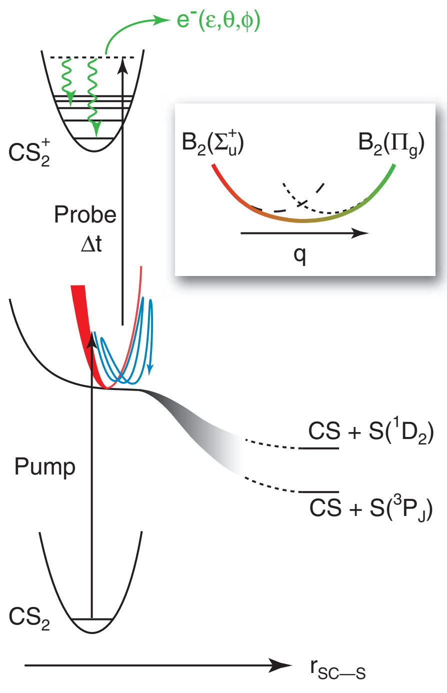

Fig. 1. Schematic representation of our femtosecond time-resolved photoelectron 3D imaging measurements of the predissociation dynamics of CS_2. Dissociation proceeds via asymmetric stretching to singlet and triplet products. Because of the geometry change in the excited state, the initial nuclear motion proceeds along the bending and symmetric stretch coordinates (blue trajectory). Upon bending and stretching, the excited Σ_u^+ state adiabatically develops Π_g electronic character (**inset**). The quasi-bound dynamics are probed by measuring the energy and 3D emission direction of the photoelectrons emitted upon ionization into the bound ground state of the cation. q, a generalized vibrational coordinate; Δt, the pump-probe time delay; ε, kinetic energy; θ, the polar angle; ϕ, the azimuthal angle of the emitted electron.

1010-fs period matches the 34-cm^{-1} splitting observed at 201 nm in the absorption spectrum. We can, therefore, assign the periodic modulation to the quantum beat interference between the two quasi-bound scattering resonances. Our measurements confirm both the previously reported quantum beat (*26*) and the bi-exponential decay (*20*) measurements. The time constant τ_1 confirms the presence of broad, short-lived resonances (*23*). The laser alignment of CS_2 leaves these global time constants unchanged (i.e., the fitted MF and LF time constants are the same), suggesting that ground-state vibrations are not excited by the alignment laser.

This kinetic model of CS_2 excited-state decay reveals insuffcient details of the underlying electronic-vibrational dynamics of the resonance decay. To advance, we applied the transient alignment method to make MF measurements. In Fig. 3, we show the two-photon ion yield as a function of the delay between the alignment pulse and the 201-nm pump pulse, in the vicinity of the rotational half-revival (greatest alignment). To quantify the alignment, we carried out simulations taking into account thermal averaging, spatial focal volume averaging over laser intensities, and the relative magnitudes of the parallel versus perpendicular ionization transition dipoles (*28*). The red curve in Fig. 3 shows the best fit to a degree of alignment of $\langle \cos^2\theta \rangle = 0.55 \pm 0.07$. Within the pump-probe window (<1.5 ps) across which MF time-resolved measurements were carried out, the molecules were effectively fixed-in-space.

To acquire time-resolved MF PADs of CS_2 photodissociation, we set the delay between the alignment and pump pulses to 73.5 ps, slightly before the maximal alignment. The 201-nm fs pump pulse, polarized parallel to the alignment axis, interacted with this aligned sample. Because of the parallel transition dipole, excitation further sharpened the excited-state alignment to an estimated value of $\langle \cos^2\theta \rangle = 0.74$. Energy-resolved PADs resulting from photoionization due to the 268-nm fs probe laser, also polarized parallel to the alignment axis, were recorded as a function of pump-probe delay within the time window shown in Fig. 3. The MF PADs for ionization into the (0,0,0) state of the cation (Fig. 2C) are shown at five time delays on the right side of Fig. 4. The analogous PADs for the unaligned sample are given on the left. A dramatic change in the MF PADs is observed in the photoelectron intensity parallel to the MF axis. At early times there is a local minimum along the MF direction, whereas at $t = 500$ fs there is a maximum in this direction. At $t = 900$ fs, the MF PAD has mostly reverted back to its form at $t = 100$ fs. As confirmed by the time scale, this occurs because of the quantum beat interference in the MF PAD between the two scattering resonances.

The selection of the MF PADs in Fig. 4 from the (0,0,0) cation ground state has important implications for the analysis of their structure and time evolution. First, FC factors restrict photoionization to quasi-linear geometries, simplifying a symmetry analysis. Second, photoionization of either scattering resonance produced the same cation vibrational state. Within the Born-Oppenheimer and FC approximations, electronic and nuclear dynamics are fully separated, and both resonances should produce the same PADs (i.e., the free electron departs from the same ion core), differing only in amplitude because of their distinct FC factors. If the PAD shape also varies during the quantum beat, as in Fig. 4, then the PADs from the two scattering resonances must differ in form. This means that there must be a vibrational coordinate dependence to the ionization transition dipole, a failure of the FC approximation.

This coordinate dependence can originate from the variation of electronic structure with vibrational coordinates in the final continuum state, the neutral excited state, or both. Our final state is the (0,0,0) state of the strongly bound cation: The vibrational wave function is restricted to a small range of internuclear distances where we do not expect mixing with other cation electronic states. We also argue that there are no resonances in the ionization continuum within our range of energies [see the supporting online material (SOM) text]. Therefore, neither the cation nor the free-electron wave function probably has strong vibrational coordinate dependence. It is rather the nuclear coordinate dependence of the electronic character of the excited neutral state that causes the PADs to evolve during the quantum beat and signifies the differential electronic character sampled by the different vibrational excursions of the two scattering resonances.

The above explanation is strongly supported by theory. In our case, one scattering resonance has more symmetric stretch character and less bend amplitude, whereas the other has the opposite. Energetically located just above the linear initial state $(^1\Sigma_u^+)$ is an optically dark state $(^1\Pi_g)$. In linear geometries, these two states do not interact. Upon bending, however, the degenerate upper state splits into two components, one of which interacts strongly with the initial state when bending and stretching. Therefore, as shown in the inset of Fig. 1, we expect mixing of Π_g character into the wave function as the molecule bends and stretches (q in Fig. 1). We thus attribute the time evolution of the MF PADs in Fig. 4 to the difference in bending and stretching amplitude between the two scattering resonances, sampling different degrees of Π_g character upon vibration. Our calculations reveal a strong mixing between these states at very small bending angles (fig. S2 and SOM text).

A complete determination of the photoionization dynamics requires knowledge of the amplitudes and phases for all partial waves. Although approximate methods for determining photoionization amplitudes exist, calculating the phase shifts of all partial waves for excited states of a polyatomic molecule undergoing nonadiabatic dynamics is currently computationally intractable. Furthermore, attempts to extract amplitudes and phases directly from the data will not yield a unique fit to the PADs. Therefore, precluding a

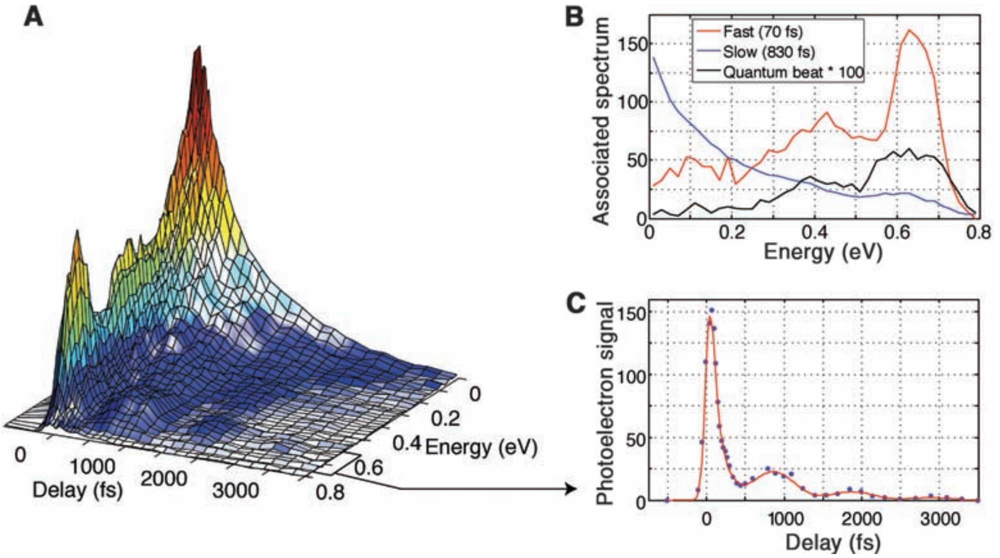

Fig. 2. (**A**) Time-resolved photoelectron spectrum of CS_2 after excitation to the $^1\Sigma_u^+$ state pumped at 201.2 nm. The decay-associated spectra resulting from a 2D global analysis of the data are shown in (**B**), with the photoelectron signal fit at all energies and all delays simultaneously. In (**C**), we show the evolution of the photoelectron band corresponding to ionization into the vibrational ground state of the cation, along with the result of the global fit. The quantum beat can be clearly seen.

detailed analysis of the photoionization dynamics, we consider a symmetry analysis based on the quasi-linear behavior sampled by our (0,0,0) final state (*28*). The quantum beat phenomenon leads to signals that oscillate between the sum and the difference of the two ionization transitions. Therefore, the PADs at *t* = 100 fs and 900 fs reflect the average electronic character of the two scattering resonances, whereas the PAD at *t* = 500 fs reflects the difference in electronic characters between the two. The symmetry-expected MF PAD from the initial state (*t* = 100 fs) has minima in directions both parallel and perpendicular to the molecular axis. As seen from Fig. 4, this expectation is in good qualitative agreement (consistent with imperfect axis alignment) with the MF PAD observed at *t* = 100 fs. By *t* = 500 fs (corresponding to the minimum of the quantum beat in Fig. 2C), the angular distribution appears qualitatively different, now peaking parallel to the MF axis. The PAD observed at *t* = 500 fs is consistent with ionization from a state of Π_g symmetry, the expected difference between the two resonance wave functions. By *t* = 900 fs, approaching the first maximum of the quantum beat, the MF PADs again appears very similar to that at *t* = 100 fs.

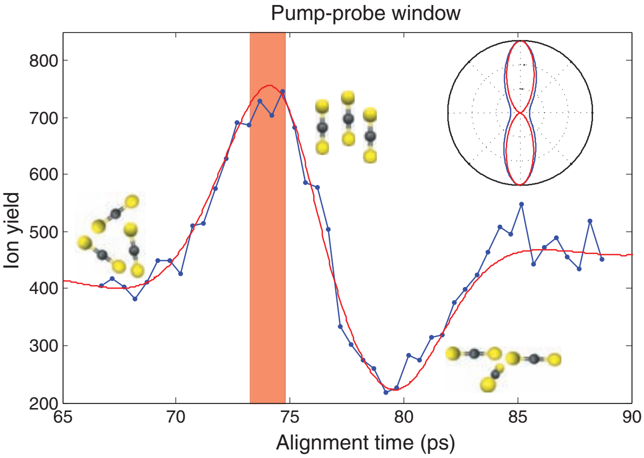

Fig. 3. Jet-cooled CS_2 molecules are transiently aligned by a short (100-fs), nonresonant (805-nm) laser pulse, creating a rotational wave packet. The alignment dynamics around the half-revival are monitored via the two-photon ionization yield (blue dots). To estimate the degree of alignment, we simulated the ion yield as a function of delay using direct integration of the time-dependent Schrödinger equation to propagate the rotational wave packet. The calculated axis angular distribution is shown in the inset for the ground-state (blue) and excited-state (red) molecules. Within the window used for the pump-probe experiment (red band), the molecules are fixed in space.

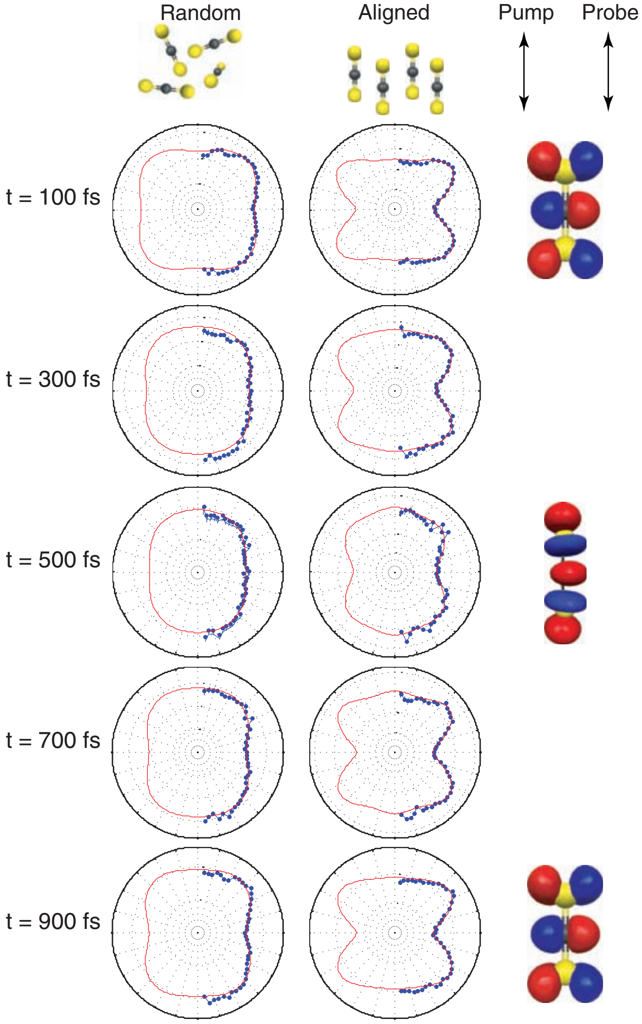

Fig. 4. Time-resolved PADs for unaligned (left) and aligned (right) CS_2 molecules. The LF laser polarization vectors are shown at top right. Also shown are the orbitals with the highest contribution to the state evolving adiabatically from the $^1B_2(^1\Sigma_u^+)$ state in the FC region. Top and bottom right panels show the π* orbital that dominates in the FC region, whereas the middle right panel shows the σ* orbital that contributes at geometries that are both stretched and bent. The MF PADs (aligned) reveal details of the dynamics not seen in the randomly aligned sample.

Simplifying still further, if we employ single-active electron pictures, the MF PADs are directly determined by the initial orbital and the MF direction of the ionization transition dipole (*19*, *28*). The changes in the PADs then directly reflect changes in orbital character. In the FC region, the initial state is predominantly of *n* → π* character (the corresponding orbital is plotted at the top right of Fig. 4). As the molecule bends and stretches, state mixing introduces some *n* → σ* character (middle right of Fig. 4). The qualitative changes in the MF PADs agree well with the changes in orbital character of the excited state, as the quantum beat phenomenon amplifies the differences between the two resonances. The MF PADs do show an energy dependence (fig. S1): Different ion vibrational states exhibit different PADs. However, their temporal evolution is very similar to that of the (0,0,0) state, with comparable changes at all energies. That the PADs are final state–dependent is consistent with the different ion states having different Condon points and, therefore, reflecting different aspects of the excited-state evolution.

The fact that the MF PADs exhibit an oscillatory behavior that is in phase at all energies highlights an important aspect of this observable (*16*): The time evolution of the PADs (Fig. 4) for fixed-in-space molecules is predominantly determined by changes in the electronic symmetry of the excited state. In contrast, the time evolution of the photoelectron spectrum (Fig. 2) is primarily sensitive to the vibrational dynamics and population decay: When several vibrational states of the cation are accessible, details of the dynamics may become obscured by averaging over these states. This is why the quantum beat is not observed in the photoelectron yield at low electron energies but stands out clearly in the MF PADs. In a simple model, the PADs are determined by the shape of the orbital being ionized and the ionic potential from which the electron is ejected. For small amplitude vibrational motion, which is ensured by our choice of final state, the changes in the PADs are then mostly determined by the re-organization of the electrons due to the coupling between electronic states. The time-evolution of the photoelectron spectrum and the MF PADs, therefore, add complementary information about the dynamics, highlighting the power of combining field-free alignment techniques with ultrafast spectroscopy.

References and Notes

1. T. P. Rakitzis, A. J. van den Brom, M. H. M. Janssen, *Science* **303**, 1852 (2004).
2. D. Dill, *J. Chem. Phys.* **65**, 1130 (1976).
3. J. H. D. Eland, *J. Chem. Phys.* **70**, 2926 (1979).
4. K. G. Low, P. D. Hampton, I. Powis, *Chem. Phys.* **100**, 401 (1985).
5. A. M. Lindenberg *et al.*, *Science* **308**, 392 (2005).
6. H. Ihee *et al.*, *Science* **291**, 458 (2001).
7. B. J. Siwick, J. R. Dwyer, R. E. Jordan, R. J. D. Miller, *Science* **302**, 1382 (2003).
8. J. Itatani *et al.*, *Nature* **432**, 867 (2004).
9. V. Blanchet, M. Z. Zgierski, T. Seideman, A. Stolow, *Nature* **401**, 52 (1999).
10. O. Geßner *et al.*, *Science* **311**, 219 (2006); published online 14 December 2005 (10.1126/science.1120779).
11. M. Meckel *et al.*, *Science* **320**, 1478 (2008).
12. W. Li *et al.*, *Science* **322**, 1207 (2008); published online 29 October 2008 (10.1126/science.1163077).
13. H. Stapelfeldt, T. Seidemann, *Rev. Mod. Phys.* **75**, 543 (2003).
14. B. J. Sussman, D. Townsend, M. Y. Ivanov, A. Stolow, *Science* **314**, 278 (2006).
15. F. Rosca-Pruna, M. J. J. Vrakking, *Phys. Rev. Lett.* **87**, 153902 (2001).
16. T. Seideman, *Annu. Rev. Phys. Chem.* **53**, 41 (2002).
17. K. L. Reid, *Annu. Rev. Phys. Chem.* **54**, 397 (2003).
18. T. Suzuki, *Annu. Rev. Phys. Chem.* **57**, 555 (2006).
19. A. Stolow, J. G. Underwood, *Adv. Chem. Phys.* **139**, 497 (2008).
20. D. Townsend *et al.*, *J. Chem. Phys.* **125**, 234302 (2006).
21. E. Hack, J. R. Huber, *Int. Rev. Phys. Chem.* **10**, 287 (1991).
22. R. J. Hemley, D. G. Leopold, J. L. Roebber, V. Vaida, *J. Chem. Phys.* **79**, 5219 (1983).
23. A. Mank, C. Starrs, M. N. Jego, J. W. Hepburn, *J. Chem. Phys.* **104**, 3609 (1996).
24. D. Xu, J. Huang, W. M. Jackson, *J. Chem. Phys.* **120**, 3051 (2004).
25. A. P. Baronavski, J. C. Owrutsky, *Chem. Phys. Lett.* **221**, 419 (1994).
26. P. Farmanara, V. Stert, W. Radloff, *J. Chem. Phys.* **111**, 5338 (1999).
27. R. R. Sadeghi, S. R. Gwaltney, J. L. Krause, R. T. Skodje, P. M. Weber, *J. Chem. Phys.* **107**, 6570 (1997).
28. Materials and methods are available as supporting material on *Science* Online.
29. M. J. J. Vrakking, D. M. Villeneuve, A. Stolow, *J. Chem. Phys.* **105**, 5647 (1996).
30. This work was supported by the Natural Sciences and Engineering Research Council of Canada (A.M.D.L. and A.S.). We gratefully acknowledge J. G. Underwood, S. Patchkovskii, C.-Y. Ng, M. Brouard, and D. M. Wardlaw for stimulating discussions.

Supporting Online Material
www.sciencemag.org/cgi/content/full/323/5920/1464/DC1
Materials and Methods
Figs. S1 and S2
References

1 December 2008; accepted 29 January 2009
10.1126/science.1169183

Clear Sky Visibility Has Decreased over Land Globally from 1973 to 2007

Kaicun Wang,[1]* Robert E. Dickinson,[2] Shunlin Liang[1]

Visibility in the clear sky is reduced by the presence of aerosols, whose types and concentrations have a large impact on the amount of solar radiation that reaches Earth's surface. Here we establish a global climatology of inverse visibilities over land from 1973 to 2007 and interpret it in terms of changes in aerosol optical depth and the consequent impacts on incident solar radiation. The aerosol contribution to "global dimming," first reported in terms of strong decreases in measured incident solar radiation up to the mid-1980s, has monotonically increased over the period analyzed. Since that time, visibility has increased over Europe, consistent with reported European "brightening," but has decreased substantially over south and east Asia, South America, Australia, and Africa, resulting in net global dimming over land.

Uncertainty about how much the concentration of atmospheric aerosols has increased over the past century and its impact on the global radiation balance have been major obstacles to establishing how observed changes of climate are related to changes in greenhouse gas concentrations. Some long-period observational constraints on aerosols are provided by measurement of solar radiation incident at the surface (*1*) and by estimation of emissions by fossil fuel combustion (*2*). The former can be equally or more greatly affected by changes of cloudiness (*3*), and the latter can be used to estimate changes of limited aerosol types (*2*). Much better estimates of global aerosol impacts can be made over the past decade from both surface and satellite measurements of aerosol optical depth (AOD) (*4*, *5*). For a given vertical profile of aerosols, the meteorological visibility inverse (ViI) is directly proportional to AOD. Thus, we can use these recent measurements of AOD to evaluate the accuracy of ViI in terms of its mean and spatial variability. This evaluation establishes the ViI climatology as a data set that characterizes the spatial and temporal variability of over-land aerosols for the past several decades.

We calculated ViI in km^{-1} from the National Climatic Data Center (NCDC) Global Summary of Day (GSOD) database collected from about 3250 meteorological stations from 1973 to 2007. It is multiplied by a scaling factor of 1.0 km, as inferred from rules described in (*6*). This index is used as an estimate of AOD for a particular aerosol profile, and has other uncertainties described in (*6*). However, its evaluation against other more recent and more direct data sets shows that it estimates AOD with an accuracy comparable to that of the other measures (*6*) and thus can be used to discuss the effects of aerosols on the incidence of solar radiation.

The geographic long-term variation of this AOD measure is determined by aggregating the meteorological station data into continental regions where such data are available, removing time means, and calculating the area-weighted monthly anomaly values for regions where data are available for more than 80% of the stations [see (*6*) for explanation of the gap; see fig. S7 for domains). Aerosols increased on average over all continental regions between 1979 and 2006, with the exception of Europe (Fig. 1). In particular, they increased from 1979 over Australia and south Asia (including India and China), decreased over South America and Africa from 1979 to about 1985, and then increased and were relatively unchanged over north Asia (Siberia).

The large increases of Asian AODs likely were consequences of large increases in industrial activities and are consistent with long-term observations of incident solar radiation and cloud cover in India (*7*) and China (*8*). The European decreases are consistent with numerous past studies based on long-term measurements of aerosols, solar radiation, and clouds (*9*–*11*), which are consistent with changes in emissions of aerosol precursors, $\mathrm{SO_2}$ (*12*, *13*), black carbon (*14*), and organic carbon (*14*, *15*).

The variability of measured changes between stations from 1973 to 2007 is summarized in terms of linear trends for the period 1973 to 2007. Figure 2 shows the spatial distribution of the 58% of the stations that have magnitudes of their trends greater than 0.0015 year^{-1}—that is, 50% larger than the global area-weight average linear trend of 0.001 year^{-1}. This change in AOD is not the same everywhere; AODs substantially declined in Europe after peaking in the 1980s. These changes vary widely from location to location (Fig. 2). Overall, the largest increases of AOD have been in Asia, and these increases have accelerated over the past decade, producing the rapid global increase over this period.

Aerosols reduce solar radiation at Earth's surface by upward reflection and absorption. The energy lost in this manner either escapes to space or heats the air. Aerosols can further affect surface radiation by modifying cloud cover and other cloud properties. The long-term trend in over-land ViI AOD that we report is consistent with the long-term variation in incident solar radiation in China, India, and Europe (*7*–*11*). Wild *et al.* (*1*) documented that solar radiation

---

[1] Department of Geography, University of Maryland, College Park, MD 20742, USA. [2] Department of Geological Sciences, University of Texas, Austin, TX 78712, USA.

*To whom correspondence should be addressed. E-mail: kcwang@umd.edu

Fig. 1. Regional and global averaged monthly AOD anomaly (red dots) over land and their smoothed 5-year averages (blue dots).

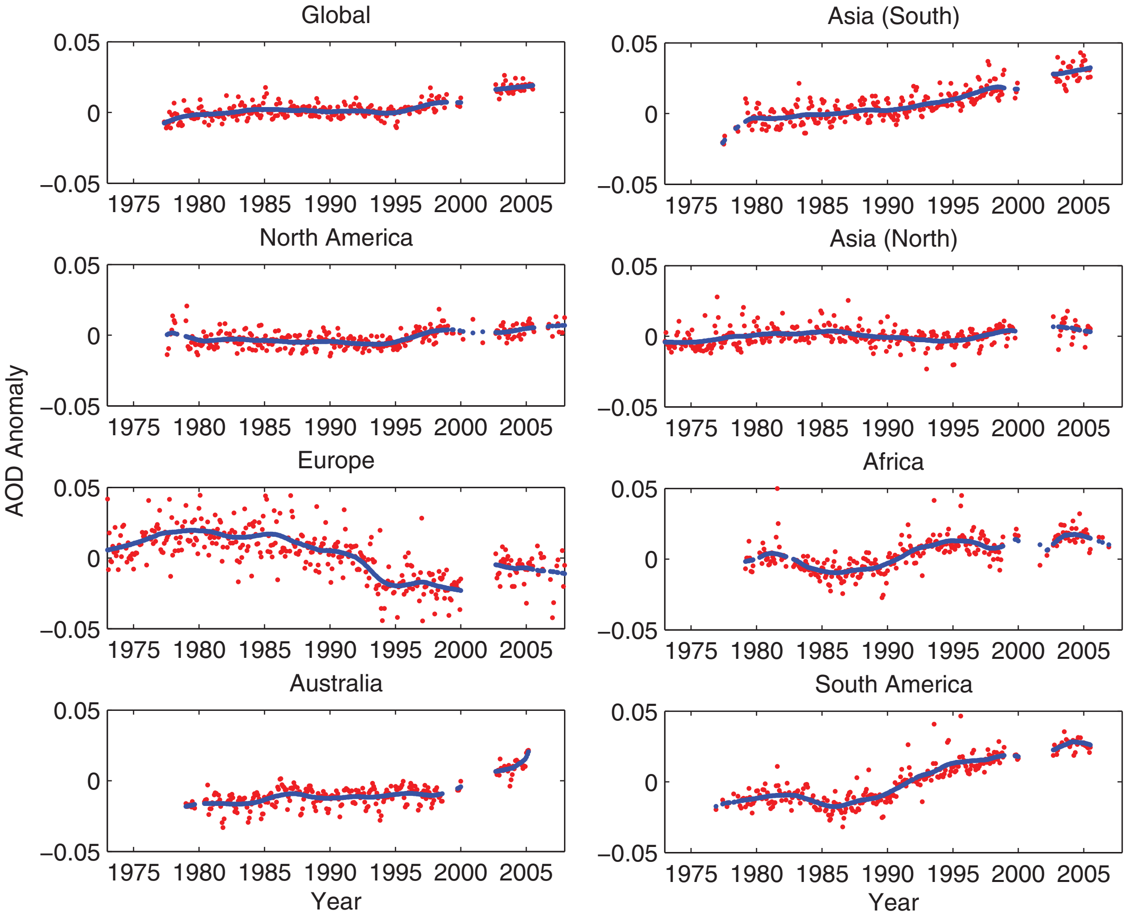

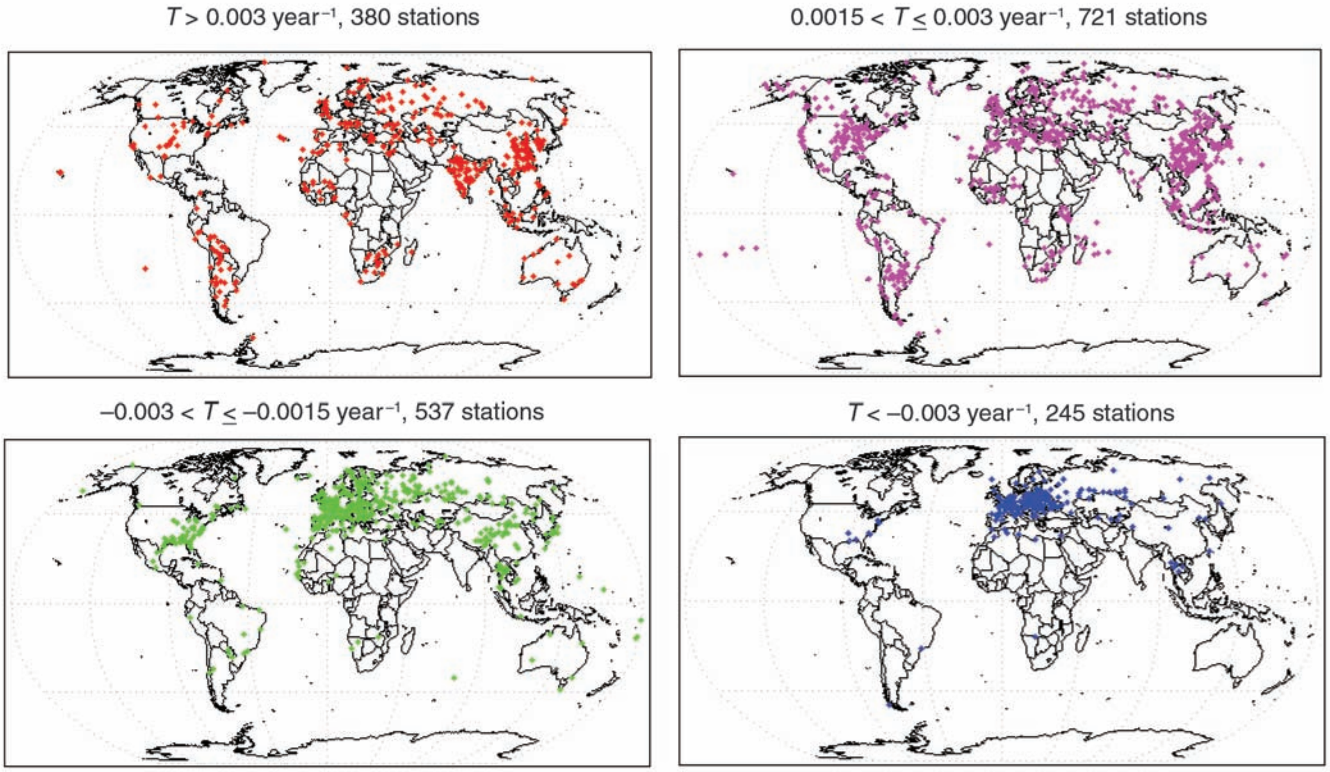

Fig. 2. Locations of the ~58% of the 3250 stations where the magnitude of VIl AOD changed (linear trend, T) by more than 0.0015 year^{-1} from 1973 to 2007.

increased in Europe after 1990, in agreement with the AOD changes seen in Figs. 1 and 2. However, many more stations have measured visibility and many have longer histories. The use of emissions to infer aerosols introduces considerable uncertainty in the estimation of aerosol impacts on radiation (*16*).

The ViI AOD over land is a complementary constraint to satellite-derived AOD (*4*, *5*) that is most readily obtained over oceans. The latter includes volcanic and high-level dust contributions that are necessarily excluded by the ViI approach. The AOD estimated from the Advanced Very High Resolution Radiometer (AVHRR) instrument (*17*–*19*) for the period 1991 to 2005, averaged globally over the oceans, indicates a change comparable in magnitude but opposite in sign to that indicated by Fig. 1. Changes seen in regional analyses of these data (*18*, *19*), however, appear to be entirely consistent with those found here, showing decreases in Europe and increases in industrializing Asia. In particular, the strongest decreases (greater than 0.003 year^{-1}) indicated in Fig. 2 are over a belt north of the Mediterranean extending into Asia, matching the analyses over the Mediterranean, Black, and Caspian seas (*19*), and the strongest increases (greater than 0.003 year^{-1}) are in near-coast industrializing Asia, thereby matching these analyses (*19*). Thus, it would appear that estimates of change over these regions for the period since 1991 might be improved by combining the ViI and AVHRR estimates.

Although increases in the concentrations of many types of aerosols may have contributed to the AOD increase, by far the largest documented changes in aerosols and their precursors are those from the increased use of fossil fuels, in particular SO_2. If so, the changes reported here appear to be inconsistent with the conclusions of the Intergovernmental Panel on Climate Change (IPCC) [(*20*), chapter 2, p. 160], which cited studies concluding that global emissions of sulfate aerosol decreased by 10 to 20 Tg year^{-1} from 1980 to 2000. Those estimates may not have adequately accounted for the 20 Tg year^{-1} increase of sulfate emission over Asia during that period (*21*). Increases in biomass burning of tropical forest and agriculture (*22*, *23*) may also have contributed to increases in AOD. The decrease of AOD in Europe is a consequence of near-constant fossil fuel use coupled with a large decrease in sulfur content as required by air quality regulations.

Current descriptions of AOD as provided by satellite data (*6*) have been used as a major constraint on the aerosol radiative forcing used as part of the IPCC modeling of climate change (*4*, *5*). However, the objective of simulating the 20th-century climate as a means of validating the models has been limited by an absence of observational information on the time history of AOD, a shortcoming that is remedied by the data set described here.

References and Notes

1. M. Wild *et al.*, *Science* **308**, 847 (2005).
2. D. I. Stern, *Glob. Environ. Change* **16**, 207 (2006).
3. J. R. Norris, M. Wild, *J. Geophys. Res.* **112**, D08214 (2007).
4. N. Bellouin, O. Boucher, J. Haywood, M. S. Reddy, *Nature* **438**, 1138 (2005).
5. H. Yu *et al.*, *Atmos. Chem. Phys.* **6**, 613 (2006).
6. See supporting material on *Science* Online.
7. T. W. Biggs, C. A. Scott, B. Rajagopalan, H. N. Turral, *Int. J. Climatol.* **27**, 1505 (2007).
8. Y. Qian, D. P. Kaiser, L. R. Leung, M. Xu, *Geophys. Res. Lett.* **33**, L01812 (2006).
9. H. C. Power, *Theor. Appl. Climatol.* **76**, 47 (2003).
10. J. R. Norris, M. Wild, *J. Geophys. Res.* **112**, D08214 (2007).
11. C. Ruckstuhl *et al.*, *Geophys. Res. Lett.* **35**, L12708 (2008).
12. V. Vestreng, M. Adams, J. Goodwin, *Inventory Review 2004: Emission Data Reported to CLRTAP and the NEC Directive. EMEP/EEA Joint Review Report* (Norwegian Meteorological Institute, Oslo, 2004).
13. D. G. Streets *et al.*, *J. Geophys. Res.* **108**, 8809 (2003).
14. A. Ito, J. E. Penner, *Global Biogeochem. Cycles* **19**, GB2028 (2005).
15. T. Novakov *et al.*, *Geophys. Res. Lett.* **30**, 1324 (2003).
16. J. M. Haywood, O. Boucher, *Rev. Geophys.* **38**, 513 (2000).
17. M. I. Mishchenko *et al.*, *Science* **315**, 1543 (2007).
18. M. I. Mishchenko, I. V. Geogdzhayev, *Opt. Express* **15**, 7423 (2007).
19. T. X.-P. Zhao *et al.*, *J. Geophys. Res.* **113**, D07201 (2008).
20. Intergovernmental Panel on Climate Change, *Climate Change 2007: The Physical Science Basis. Contribution of Working Group I to the Fourth Assessment Report of the Intergovernmental Panel on Climate Change*, S. Solomon *et al.*, Eds. (Cambridge Univ. Press, Cambridge, 2007).
21. T. Ohara *et al.*, *Atmos. Chem. Phys.* **7**, 4419 (2007).
22. C. Venkataraman, G. Habib, A. Eiguren-Fernandez, A. H. Miguel, S. K. Friedlander, *Science* **307**, 1454 (2005).
23. A. L. Westerling, H. G. Hidalgo, D. R. Cayan, T. W. Swetnam, *Science* **313**, 940 (2006); published online 5 July 2006 (10.1126/science.1128834).
24. We thank A. Riter for her editing and proofreading of the manuscript. GSOD data are available at ftp://ftp.ncdc.noaa.gov/pub/data/gsod.

Supporting Online Material
www.sciencemag.org/cgi/content/full/323/5920/1468/DC1
Materials and Methods
Figs. S1 to S7
Table S1
References

22 October 2008; accepted 23 January 2009
10.1126/science.1167549

Recent Changes in Phytoplankton Communities Associated with Rapid Regional Climate Change Along the Western Antarctic Peninsula

Martin Montes-Hugo,[1] Scott C. Doney,[2] Hugh W. Ducklow,[3] William Fraser,[4] Douglas Martinson,[5] Sharon E. Stammerjohn,[6] Oscar Schofield[1]

The climate of the western shelf of the Antarctic Peninsula (WAP) is undergoing a transition from a cold-dry polar-type climate to a warm-humid sub-Antarctic–type climate. Using three decades of satellite and field data, we document that ocean biological productivity, inferred from chlorophyll a concentration (Chl a), has significantly changed along the WAP shelf. Summertime surface Chl a (summer integrated Chl a ~63% of annually integrated Chl a) declined by 12% along the WAP over the past 30 years, with the largest decreases equatorward of 63°S and with substantial increases in Chl a occurring farther south. The latitudinal variation in Chl a trends reflects shifting patterns of ice cover, cloud formation, and windiness affecting water-column mixing. Regional changes in phytoplankton coincide with observed changes in krill (*Euphausia superba*) and penguin populations.

Over the past several decades, the marine ecosystem along the western continental shelf of the Antarctic Peninsula (WAP) (62° to 69°S, 59° to 78°W, ~1000 by 200 km) has undergone rapid physical climate change (*1*). Compared with conditions in 1979 at the beginning of satellite data coverage, seasonal sea ice during 2004 arrived 54 ± 9 (1 SE) days later in autumn and departed 31 ± 10 days earlier in spring (*2*). Winter air temperatures, measured between 62.2°S, 57.0°W and 65.3°S, 64.3°W, warmed at up to 4.8 times the global average rate during the past half-century (*3*–*5*). This warming is the most rapid of the past 500 years and stands in contrast to a marked cooling between 2700 and 100 years before the present (*5*–*7*). As the once-perennial sea ice and glaciers retreat (*6*, *8*), maritime conditions are expanding southward to displace the continental, polar system of the southern WAP (*9*).

As a result, populations of sea ice–dependent species of lower and higher trophic levels are being demographically displaced poleward and are being replaced by ice-avoiding species (e.g.,

---

[1] Coastal Ocean Observation Lab, Institute of Marine and Coastal Sciences, School of Environmental and Biological Sciences, Rutgers University, New Brunswick, NJ 08901, USA. [2] Department of Marine Chemistry and Geochemistry, Woods Hole Oceanographic Institution, Woods Hole, MA 02543, USA. [3] The Ecosystems Center, Marine Biological Laboratory, Woods Hole, MA 02543, USA. [4] Polar Oceans Research Group, Post Office Box 368, Sheridan, MT 59749, USA. [5] Lamont-Doherty Earth Institute, Palisades, NY 10964, USA. [6] Ocean Sciences, University of California, Santa Cruz, CA 95064, USA.

*To whom correspondence should be addressed. E-mail: montes@marine.rutgers.edu

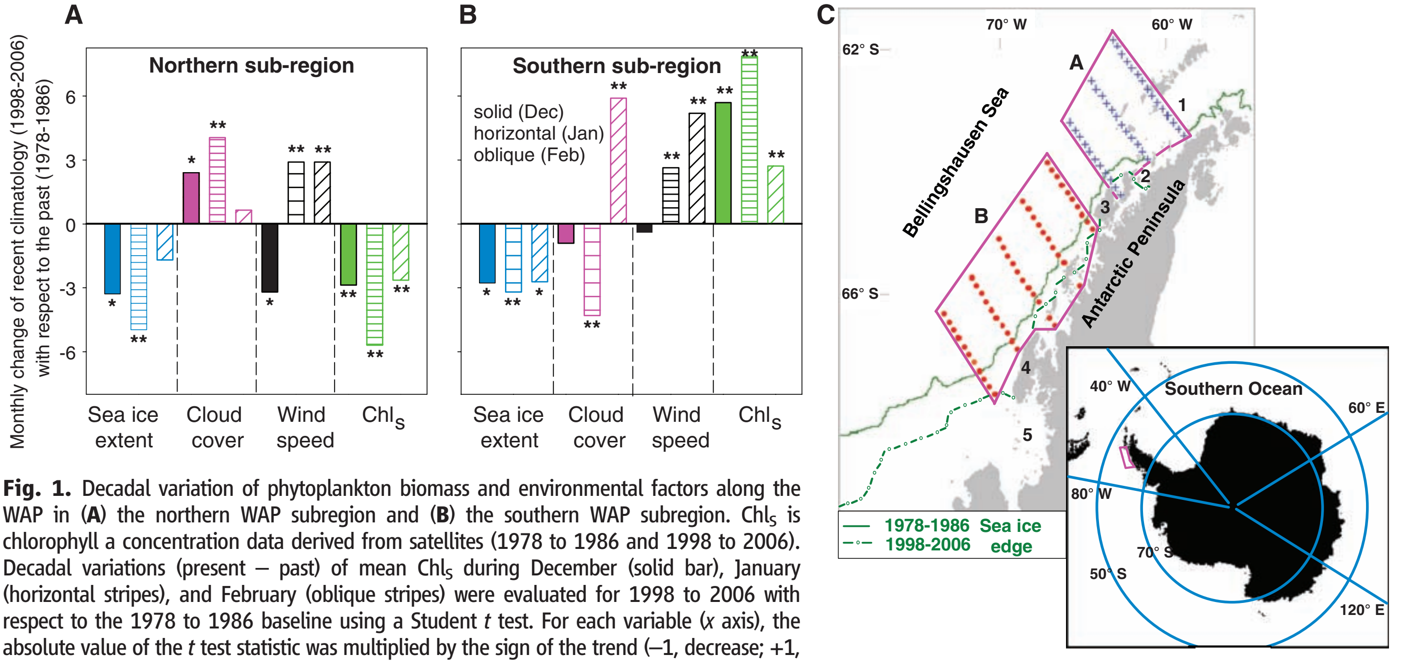

Fig. 1. Decadal variation of phytoplankton biomass and environmental factors along the WAP in (**A**) the northern WAP subregion and (**B**) the southern WAP subregion. Chl$_S$ is chlorophyll a concentration data derived from satellites (1978 to 1986 and 1998 to 2006). Decadal variations (present – past) of mean Chl$_S$ during December (solid bar), January (horizontal stripes), and February (oblique stripes) were evaluated for 1998 to 2006 with respect to the 1978 to 1986 baseline using a Student *t* test. For each variable (*x* axis), the absolute value of the *t* test statistic was multiplied by the sign of the trend (–1, decrease; +1, increase) of the present monthly mean with respect to the mean of the historical period (*y* axis). For January and February, Student *t* of Chl$_S$ was divided by 5. Significant differences between the periods at 95% (*) and 99% (**) confidence levels are indicated. (**C**) Spatial domains A (northern subregion) and B (southern subregion) overlap the original transects of the Palmer-LTER regional grid, where ship-based stations are denoted by blue crosses and red circles, respectively. 1, Bransfield Strait; 2, Gerlache Strait; 3, Anvers Island; 4, Adelaide Island; 5, Marguerite Bay. Average January sea ice extent during 1978 to 1986 (solid green line) and 1998 to 2006 (broken dotted green line) is indicated.

krill are being replaced by salps, and Adélie penguins by Chinstrap penguins) (*1*, *10*, *11*). Do these biogeographic modifications originate from changes at the base of the food web?

In the short term (monthly-interannual scale) and during spring and summer, variations in latitudinal gradients in phytoplankton biomass as a function of time have been associated with sea ice timing and extent (*12*, *13*). However, this mechanism has not been investigated over a longer time scale of decades. Further, the relative importance of subregional differences in climate variables other than sea ice (e.g., cloudiness and currents) in determining WAP alongshore phytoplankton dynamics is not known. In contrast to previous work, we suggest that alongshore phytoplankton distribution in this region has been adjusting to the ongoing, long-term sea ice decline and spatial modifications of other physical climate factors. Short-term evidence from seasonal cruises (*13*–*15*) suggests an inverse relationship between phytoplankton biomass in surface waters (0- to 50-m depth) and the depth of the upper mixed layer (UML). As the UML becomes less stratified, mean light levels for phytoplankton photosynthesis decrease, and phytoplankton growth is not large enough compared with Chl a loss (e.g., grazing and sinking) to support Chl a accumulation in surface waters (*14*). Because deepening of UML is mainly determined by greater surface wind stress (*14*), particularly during ice-free conditions, the expectation is for a general decrease (increase) of phytoplankton biomass at <64°S (>64°S) due to deeper (shallower) UML given a shorter (longer) sea ice season and greater (smaller) influence of wind in determining UML depth and, therefore, mean light levels.

Table 1. Field validation satellite-based chlorophyll a concentration changes between the summers of 1978 to 1986 (past period) and 1998 to 2006 (present period), calculated for the northern and southern WAP subregions. Chl_s^{past} is the monthly average of satellite-derived Chl a (mg m^{-3}) from 1978 to 1986; $dChl_s^{(present-past)}$ is the arithmetic average of pixel-by-pixel differences in satellite-derived Chl a between the 1978 to 1986 period and the 1998 to 2006 period; dChl$_s$% and dChl$_{in\ situ}$% are relative changes in monthly averaged Chl a [100 (Chl a$_{1998\text{-}2006}$ – Chl a$_{1978\text{-}1986}$)/Chl a$_{1978\text{-}1986}$] based on satellite-derived and shipboard Chl a measurements, respectively. Significant increase (+) or decrease (–) of Chl a indicated with a confidence limit of 95% (*) and 99% (**); two SE shown in parentheses.

Subregion		Chl_s^{past}	$dChl_s^{(present-past)}$	dChl$_s$%	dChl$_{in\ situ}$%
Northern	December	1.39 (0.11)	–1.36 (0.26)**	–97.8**	
	January	5.59 (0.20)	–5.43 (0.26)**	–97.1**	–25.2*
	February	2.96 (0.18)	–2.12 (0.49)**	–71.6**	–74.0**
Southern	December	0.89 (0.03)	+1.25 (0.08)**	+140.4**	
	January	0.89 (0.02)	+0.49 (0.03)**	+55.1**	+228.6**
	February	0.94 (0.03)	+0.02 (0.14)	+2.1	–13.6

Based on Chl a concentration derived from satellites [Coastal Zone Color Scanner (CZCS) and Sea-Viewing Wide Field-of-View Sensor (SeaWiFS)] (Chl$_S$) and in situ shipboard measurements (Chl$_{in\ situ}$) (*16*), we report a two-decadal (1978–1986 to 1998–2006) increase (decrease) of biomass in summer (December to February) phytoplankton populations in the continental shelf waters situated south (north) with respect to the central part of the WAP region (Palmer Archipelago, 64.6°S, 63.6°W). These spatial trends were mainly associated with geographic differences in receding sea ice cover and solar illumination of the sea surface.

Since the 1970s, there has been a 7.5% areal decline in summer sea ice throughout the WAP, with the declines varying regionally (Fig. 1, blue bars, and fig. S5, A and E). Cloudiness (Fig. 1, pink bars, and fig. S5, B and F) and wind patterns (Fig. 1, black bars, and fig. S5, C and G) have also changed during the past decade. In the 1970s, overcast skies tended to be positively associated with windy conditions, but in the past 10 years this covariation has weakened considerably (fig. S5, B, C, F, and G). Surface winds have become more intense (up to 60% increase) during mid to late summer (January and February) (Fig. 1 and fig. S5, C to G). Overall, these climate variations were associated with a 12% decline in Chl$_S$ over the entire study region (Table 1) that resembles Chl$_S$ declines reported in northern high latitudes (>40°N) between 1979–1986 and 1997–2000 (*17*).

In the northern subregion of the WAP (61.8° to 64.5°S, 59.0° to 65.8°W), the skies have become cloudier, winds persistently stronger (monthly mean up to 8 m s^{-1}), and summer sea ice extent less, conditions favoring deeper wind-mixing during the months most critical for phytoplankton growth (December and January) (Fig. 1 and fig. S5, A to D). Hence, phytoplankton cells inhabiting these waters have been exposed to a deeper mixed layer and overall less light for photosynthesis (*14*) that may explain the dramatic Chl_S decrease (seasonal average, 89%) detected in recent years (Fig. 1, Fig. 2A, and fig. S5D). Additionally, recent declines of Chl a over the northern WAP subregion might also be partially related to a greater advection of relatively poor–Chl a waters coming from the Weddell Sea into the Bellingshausen Sea through the Bransfield and Gerlache Straits (*18*). A Chl a decrease was less evident during February (Table 1), which suggests that increased mixing early in the growth season caused a lag in phytoplankton bloom initiation but did not influence Chl a levels as strongly later in the growth season. Two possible trigger mechanisms for such a delay are stronger winds [up to 5.4% increase, January (table S5)] and an insufficient volume of fresh water from melting sea ice [up to 79% less sea ice, December (table S5)] that otherwise would create a favorable, strongly stratified, shallow UML (*13*–*15*).

In the southern subregion of the WAP (63.8° to 67.8°S, 64.4° to 73.0°W), remotely sensed Chl a has undergone a remarkable increase (66% on average) from 1978–1986 to 1998–2006 (Fig. 1, fig. S5H, Fig. 2A, and Table 1) that can be attributed mainly to high Chl_S values (monthly mean up to 6.58 mg m^{-3}) during 2005 and 2006. These years were characterized by a substantial decrease in sea ice extent (~17.4×10^3 km^2, ~80% with respect to the 1978 to 1986 average, December), cloud cover (~11.1%, January), and wind intensity (up to 19%, December and January) (Fig. 1, fig. S5, E to G, and table S5). Unlike the northern WAP, the decrease in summer sea ice extent in the southern WAP has occurred in areas that were previously sea ice covered most of the year. Therefore, the increase in ice-free summer days translates into more favorable conditions in the UML (e.g., increased light) for phytoplankton growth. Together these environmental changes are expected to enhance photosynthesis and favor Chl a accumulation due to lower light limitation.

Regions with high Chl a levels in the WAP are characterized by a larger fraction of phytoplankton with fucoxanthin, a pigment marker for diatoms, and a larger fraction of relatively large cells (>20 μm) (contribution of cells >20 μm to total Chl a ≥ 0.5) (Fig. 2B). Therefore, the observed trends of decreasing Chl a in the northern subregion and increasing Chl a in the southern subregion are likely accompanied by shifts in community composition with a greater (lesser) fraction of diatoms and large cells in the southern (northern) region. This restructuring of the phytoplankton community has major implications for biogeochemical cycles of the WAP region. Large (>5 μm) phytoplankton contribute 80% of the particulate organic carbon export at high latitudes, with diatoms making up the majority of large phytoplankton export in the Southern Ocean (*19*).

Historical shipboard measurements of Chl a within the study area confirmed the general north-south transitions seen in the satellite data with higher (lower) phytoplankton biomass in the southern (northern) WAP subregion in the past decade compared with 1978 to 1986 (Table 1 and tables S3 and S4). In fact, available field measurements during January and February evidenced a greater occurrence of phytoplankton blooms (Chl a > 5 mg m^{-3}) in the northern (southern) WAP subregion from 1978 to 1986 (1987 to 2006) (SOM Text, S6D) (*16*).

In the northern WAP, the maximum chlorophyll values measured by satellite (up to 40 mg m^{-3}, January) or in situ (up to 38 mg m^{-3}, February) were larger in the past (1978 to 1986) compared with the present (1997 to 2006). Conversely, in the southern WAP this pattern was reversed, and spaceborne and shipborne observations consistently showed higher pigment values in the last decade (satellite, up to 33 mg m^{-3}; ship, up to 25 mg m^{-3}, January) (tables S4 and S5). Monthly Chl a differences between northern and southern WAP locations were also statistically coherent

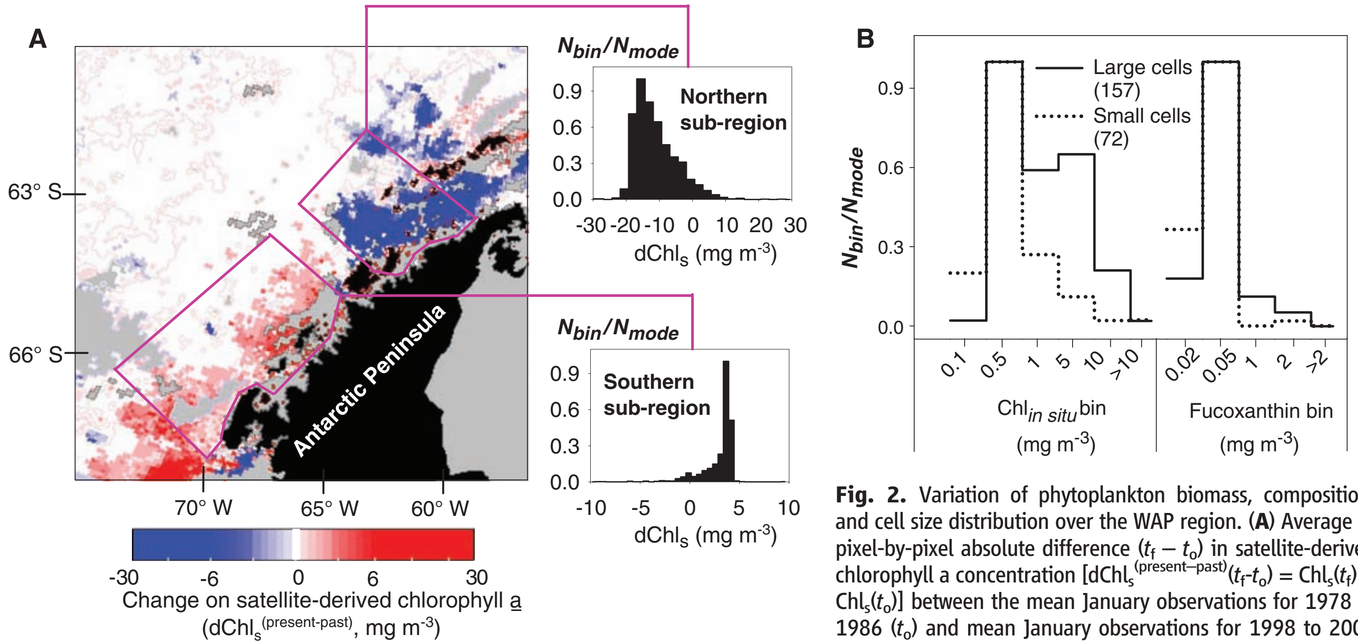

Fig. 2. Variation of phytoplankton biomass, composition, and cell size distribution over the WAP region. (**A**) Average of pixel-by-pixel absolute difference ($t_f - t_o$) in satellite-derived chlorophyll a concentration [$\text{dChl}_s^{\text{(present–past)}}(t_f\text{-}t_o) = \text{Chl}_s(t_f) - \text{Chl}_s(t_o)$] between the mean January observations for 1978 to 1986 (t_o) and mean January observations for 1998 to 2006 (t_f). Positive (negative) dChl_s corresponds to an increase (decrease) of Chl_s with respect to the 1970s. Negative (by a factor of ~2, northern subregion, upper histogram) and positive (by a factor of ~1.5, southern subregion, lower histogram) trends in Chl_s are evident in the satellite data. $N_{\text{bin}}/N_{\text{mode}}$ is the relative frequency of observations per bin, normalized by the mode. Gray pixels indicate areas without data or without valid geophysical retrieval due to cloud and sea ice contamination; black pixels indicate land. (**B**) Histograms of contribution of diatoms (fucoxanthin marker) and phytoplankton communities dominated by large (≥20 μm) versus small (<20 μm) cell diameter to total in situ chlorophyll a concentration ($\text{Chl}_{\text{in situ}}$). Phytoplankton cell size spectra were computed from satellite imagery (1998 to 2006) (*16*), and phytoplankton pigments were measured over the northern and southern WAP subregions and during 1993 to 2006 Palmer-LTER cruises. Number of samples used to construct each histogram shown in parentheses.

with satellite-derived and field Chl a trends, and in both cases latitudinal phytoplankton biomass gradients were greater during January compared with February (Fig. 1 and tables S4 and S5).

Our study provides evidence for the occurrence of substantial and statistically significant latitudinal shifts at the base of the Antarctic Peninsula marine food web that may be contributing to observations of an apparent reorganization of northern WAP biota during the past decade [e.g., *Euphausia superba* (Antarctic krill), *Pleuragramma antarcticum* (Antarctic silverfish), and *Pygoscelis Adeliae* (Adélie penguin)] that rely on ice-edge diatom blooms (20, *21*). The southward relocation of phytoplankton patches with abundant and large cells (>20 μm) due to local alterations in environmental variables is expected to exacerbate the reduction of krill abundance in the northern WAP. This represents a setback for the survival of fish (silverfish) and birds (Adélie penguins) that depend on krill but favors other species, including *Electrona antarctica* (Lanternfish), *Pygoscelis papua* (Gentoo penguin), and *Pygoscelis antarcticus* (Chinstrap penguin) (*21*, *22*).

The observed latitudinal response of phytoplankton communities along the WAP with respect to historical sea ice variability can be compared with that estimated from geological proxies for similar paleo-oscillations in sea ice extent and rate of change identified during the Holocene (*5*, *23*, *24*). Paleo-records show that analogous climate variations have occurred in the past 200 to 300 years, and over longer 2500-year cycles, with rapid (decadal) transitions between warm and cool phases in the WAP (*5*, *25*, *26*). In this study (~30 years), the Chl a trend evidenced in the southern subregion of the WAP presented similar characteristics to those trends detected during typical interneoglacial periods (~200 to 300 years) (i.e., high phytoplankton biomass, and presumably productivity, due to less area covered by permanent sea ice) (*26*). Since the 1970s, Chl a trends over the whole WAP were also attributed to other factors not necessarily ice-related (e.g., spatial differences in cloud cover) (*27*) or coupled with the length of the ice-free season (e.g., wind-driven changes in mixed layer depth) (*14*, *15*, *28*) that were equally important in determining phytoplankton blooms.

This work suggests that a combination of atmosphere-, ice-, and ocean-mediated processes have been shaping the along-shelf distribution of phytoplankton biomass over the WAP region since the 1970s. The shift toward higher Chl a to the south was first detected using ocean color imagery and subsequently confirmed with in situ historical measurements. The spatial asymmetry of decadal changes in Chl a reported here may explain the ongoing latitudinal compositional changes in fish, zooplankton, and marine bird species over the WAP, a testimonial to which may be the recent success of krill recruitment and the bonanza of krill feeders in nearby Marguerite Bay (68.3°S, 68.3°W) (*29*).

References and Notes

1. H. W. Ducklow *et al.*, *Philos. Trans. R. Soc. London Ser. B* **362**, 67 (2007).
2. S. E. Stammerjohn *et al.*, *Deep Sea Res. Part II Top. Stud. Oceanogr.* **55**, 2041 (2008).
3. D. G. Vaughan *et al.*, *Clim. Change* **60**, 243 (2003).
4. L. G. Thompson *et al.*, *Ann. Glaciol.* **20**, 420 (1994).
5. A. Leventer *et al.*, *Geol. Soc. Am. Bull.* **108**, 1626 (1996).
6. J. Turner *et al.*, *Int. J. Climatol.* **25**, 279 (2005).
7. H. D. Pritchard, D. G. Vaughan, *J. Geophys. Res.* **112**, F03S29 (2007).
8. A. J. Cook *et al.*, *Science* **308**, 541 (2005).
9. R. C. Smith, S. E. Stammerjohn, *Ann. Glaciol.* **33**, 493 (2001).
10. R. C. Smith *et al.*, *Bioscience* **49**, 393 (1999).
11. V. Loeb *et al.*, *Nature* **387**, 897 (1997).
12. R. Smith *et al.*, *Deep Sea Res. Part II Top. Stud. Oceanogr.* **55**, 1949 (2008).
13. I. A. Garibotti *et al.*, *Mar. Ecol. Prog. Ser.* **261**, 21 (2003).
14. G. Mitchell, O. Holm-Hansen, *Deep-Sea Res.* **38**, 981 (1991).
15. M. Vernet *et al.*, *Deep Sea Res. Part II Top. Stud. Oceanogr.* **55**, 2068 (2008).
16. Materials and methods are available as supporting material on *Science* Online.
17. W. W. Gregg, M. E. Conkright, *Geophys. Res. Lett.* **29**, 1730 (2002).
18. M. A. Bárcena *et al.*, *Deep Sea Res. Part II Top. Stud. Oceanogr.* **49**, 935 (2002).
19. X. Jin *et al.*, *Global Biogeochem. Cycles* **20**, GB2015 (2006).
20. M. A. Moline *et al.*, *Ann. N. Y. Acad. Sci.* **1134**, 267 (2008).
21. G. A. Knox, *Biology of the Southern Ocean* (CRC Press, Boca Raton, FL, ed. 2, 2006).
22. W. Fraser, E. E. Hoffmann, *Mar. Ecol. Prog. Ser.* **265**, 1 (2003).
23. M. J. Bentley *et al.*, *Geology* **33**, 173 (2005).
24. C. J. Pudsey, J. Evans, *Geology* **29**, 787 (2001).
25. E. W. Domack, C. E. McClennen, in R. Ross, E. Hofmann, L. Quetin, Eds., *Foundations for Ecosystem Research West of the Antarctic Peninsula* (Antarctic Research Series, Vol. 70) (American Geophysical Union, Washington, DC, 1996).
26. J. Fabrés *et al.*, *Holocene* **10**, 703 (2000).
27. P. R. Burkholder, E. F. Mandelli, *Limnol. Oceanogr.* **57**, 437 (1965).
28. R. B. Dunbar *et al.*, *J. Geophys. Res.* **103**, 30741 (1998).
29. M. Marrari *et al.*, *Deep-Sea Res.* **55**, 377 (2008).

30. This research is part of the Palmer Antarctica Long-Term Ecological Research (LTER) project (http://pal.lternet.edu). It was supported by NSF Office of Polar Programs grants 0217282 to H.W.D. and the Virginia Institute of Marine Science and 0823101 to H.W.D. at the Marine Biological Laboratory.

Supporting Online Material

www.sciencemag.org/cgi/content/full/323/5920/1470/DC1
Materials and Methods
SOM Text
Figs. S1 to S5
Tables S1 to S9
References

11 August 2008; accepted 12 January 2009
10.1126/science.1164533

A Recessive Mutation in the APP Gene with Dominant-Negative Effect on Amyloidogenesis

Giuseppe Di Fede,[1] Marcella Catania,[1] Michela Morbin,[1] Giacomina Rossi,[1] Silvia Suardi,[1] Giulia Mazzoleni,[1] Marco Merlin,[1] Anna Rita Giovagnoli,[1] Sara Prioni,[1] Alessandra Erbetta,[2] Chiara Falcone,[3] Marco Gobbi,[4] Laura Colombo,[4] Antonio Bastone,[4] Marten Beeg,[4] Claudia Manzoni,[4] Bruna Francescucci,[5] Alberto Spagnoli,[5] Laura Cantù,[6] Elena Del Favero,[6] Efrat Levy,[7] Mario Salmona,[4] Fabrizio Tagliavini[1]*

β-Amyloid precursor protein (APP) mutations cause familial Alzheimer's disease with nearly complete penetrance. We found an APP mutation [alanine-673→valine-673 (A673V)] that causes disease only in the homozygous state, whereas heterozygous carriers were unaffected, consistent with a recessive Mendelian trait of inheritance. The A673V mutation affected APP processing, resulting in enhanced β-amyloid (Aβ) production and formation of amyloid fibrils in vitro. Co-incubation of mutated and wild-type peptides conferred instability on Aβ aggregates and inhibited amyloidogenesis and neurotoxicity. The highly amyloidogenic effect of the A673V mutation in the homozygous state and its anti-amyloidogenic effect in the heterozygous state account for the autosomal recessive pattern of inheritance and have implications for genetic screening and the potential treatment of Alzheimer's disease.

A central pathological feature of Alzheimer's disease (AD) is the accumulation of β-Aβ in the form of oligomers and amyloid fibrils in the brain (*1*). Aβ is generated by sequential cleavage of the APP by β- and γ-secretases and exists as short and long isoforms, Aβ1-40 and Aβ1-42 (*2*). Aβ1-42 is especially prone to misfolding and builds up aggregates that are thought to be the primary neurotoxic species involved in AD pathogenesis (*2*, *3*). AD is usually sporadic, but a small fraction of cases is familial (*4*). The familial forms show an autosomal dominant pattern of inheritance with virtually complete penetrance and are linked to mutations in the APP, presenilin 1, and presenilin 2 genes (*5*). The APP mutations close to the sites of β- or γ-secretase

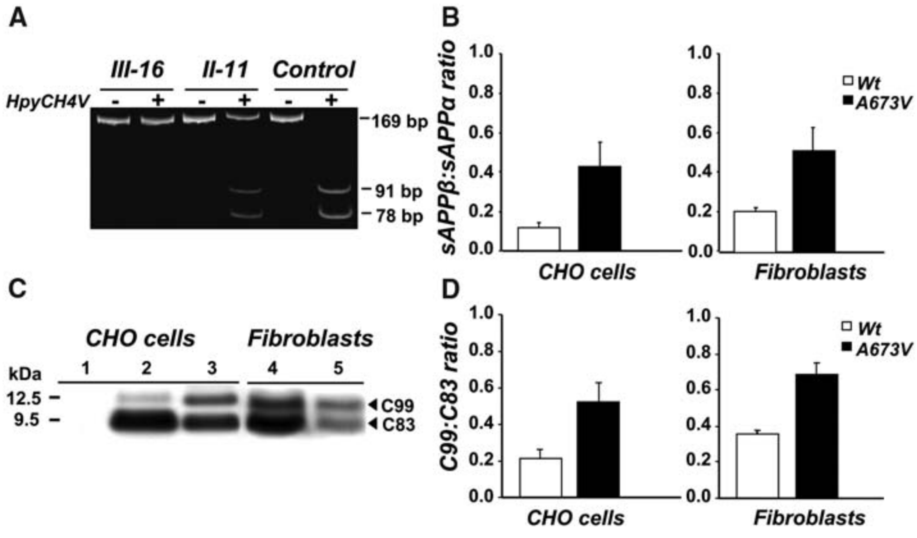

Fig. 1. Analysis of APP gene and APP processing. (**A**) APP gene analysis by restriction fragment length polymorphism of 169–base pair (bp) polymerase chain reaction (PCR) products amplified from homozygous (III-16), heterozygous (II-11), and control subjects. In the absence of the A673V mutation, the enzyme HpyCH4V generates two fragments of 91 and 78 bp. The mutation abolishes the restriction site, and the PCR product remains uncut. (**B**) sAPPβ:sAPPα ratio in conditioned media from CHO cells transfected with wild-type or A673V-mutated APP and fibroblasts of the proband and four controls. Error bars represent means ± SD. (**C**) APP carboxy-terminal fragments C99 and C83 (arrowheads) in CHO cells transfected with wild-type (lane 2) or A673V-mutated (lane 3) APP and fibroblasts from a control (lane 4) and the proband (lane 5), as shown by immunoblot analysis. Lane 1 corresponds to from nontransfected CHO cells. (**D**) Densitometric analysis of immunoblots, showing a significant increase in the C99:C83 ratio ($P = 0.0001$) in cells carrying the A673V mutation. Error bars represent means ± SD.

cleavage flanking the Aβ sequence overproduce total Aβ or only Aβ1-42, respectively, whereas those that alter amino acids within Aβ result in greater propensity to aggregation in vitro (*6*, *7*).

We have identified an APP mutation [$\mathrm{Ala}^{673}\rightarrow\mathrm{Val}^{673}$ (A673V)] that causes disease only in the homozygous state. The mutation consists of a C-to-T transition that results in an alanine-to-valine substitution at position 673 (APP770 numbering) corresponding to position 2 of Aβ (Fig. 1A and fig. S1) (*8*). The genetic defect was found in a patient with early-onset dementia and in his younger sister, who now shows multiple-domain mild cognitive impairment (MCI) (*9*). Six relatives aged between 21 and 88 years, from both parental lineages, who carry the A673V mutation in the heterozygous state were not affected, as deduced by formal neuropsychological assessment [supporting online material (SOM) text, fig. S2, and table S1], consistent with a recessive Mendelian trait of inheritance. The A673V mutation was not found in 200 healthy individuals and 100 sporadic AD patients. Both mutated and wild-type APP mRNA were expressed in heterozygous carriers (*8*).

In the patient, the disease presented with behavioral changes and cognitive deficits at the age of 36 years and evolved toward severe

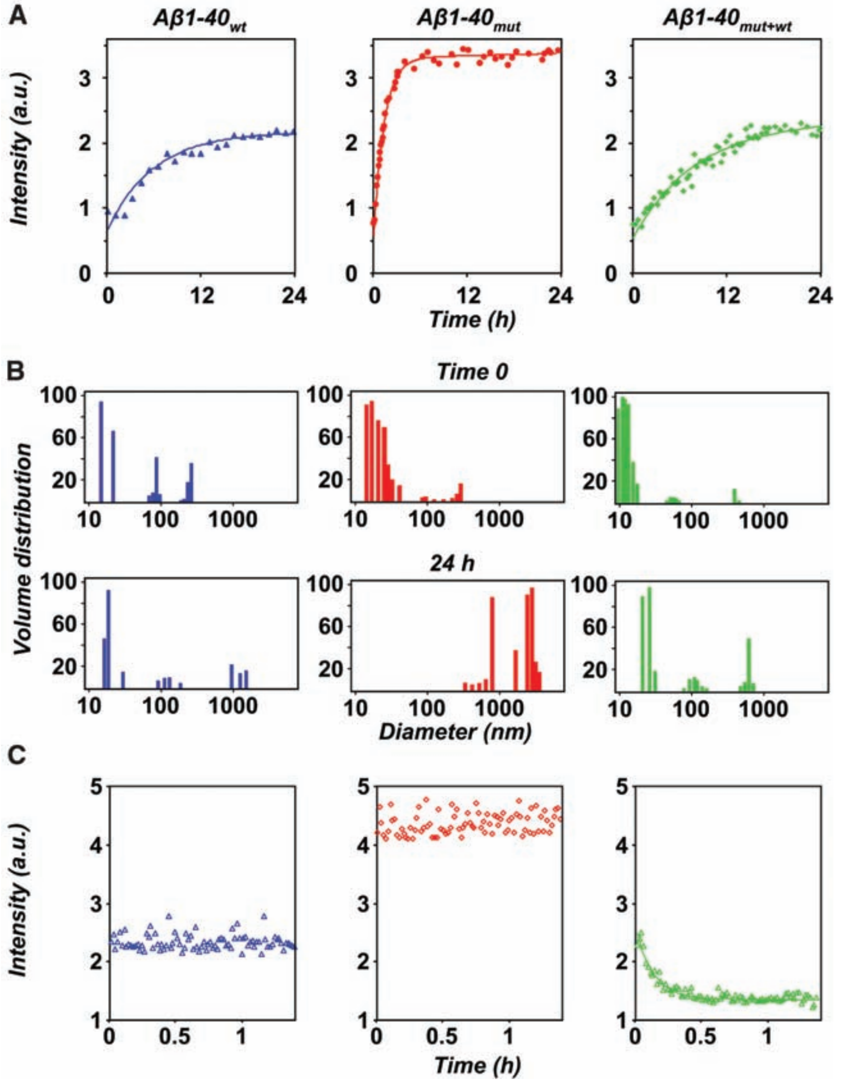

Fig. 2. Short-time kinetics of Aβ assembly and disassembly, determined by laser light scattering. (**A**) Course of the light intensity scattered by solutions of Aβ1-40_{wt} (blue), Aβ1-40_{mut} (red), and their equimolar mixture (green). The corresponding exponential fits are indicated by full lines. (**B**) Particle size distribution of Aβ1-40_{wt} (blue), Aβ1-40_{mut} (red), and the peptide mixture (green) immediately after sample preparation (time 0) and after 24 hours. (**C**) Short-time dissolution kinetics of 48-hour-aged peptide aggregates after fivefold dilution with buffer. a.u., arbitrary units.

---

[1] Division of Neurology and Neuropathology, "Carlo Besta" National Neurological Institute, 20133 Milan, Italy. [2] Division of Neuroradiology, "Carlo Besta" National Neurological Institute, 20133 Milan, Italy. [3] Division of Neuroepidemiology, "Carlo Besta" National Neurological Institute, 20133 Milan, Italy. [4] Department of Molecular Biochemistry and Pharmacology, Istituto di Ricerche Farmacologiche "Mario Negri," 20156 Milan, Italy. [5] Division of Cognitive Disorders, Centro Sant'Ambrogio Fatebenefratelli, Cernusco sul Naviglio, 20063 Milan, Italy. [6] Department of Medical Chemistry, Biochemistry, and Biotechnology, University of Milan, Segrate, 20090 Milan, Italy. [7] Departments of Pharmacology and Psychiatry, New York University School of Medicine, and Nathan S. Kline Institute, Orangeburg, NY 10962, USA.

*To whom correspondence should be addressed. E-mail: ftagliavini@istituto-besta.it

dementia with spastic tetraparesis, leading to complete loss of autonomy in about 8 years (SOM text). Serial magnetic resonance imaging showed progressive cortico-subcortical atrophy (fig. S3). Cerebrospinal fluid analysis evidenced decreased Aβ1-42 and increased total and 181T-phosphorylated tau compared with that of nondemented controls and similarly to AD subjects (table S2 and fig. S4) (*8*). In the plasma of the patient and his A673V homozygous sister, Aβ1-40 and Aβ1-42 were higher than those in nondemented controls, whereas the six A673V heterozygous carriers had intermediate amounts (table S2 and fig. S4).

In conditioned media of fibroblasts prepared from skin biopsies (*8*), Aβ1-40 and Aβ1-42 were 2.1- and 1.7-fold higher in the patient than in four age-matched controls with no change in Aβ1-42:Aβ1-40 ratio (table S2 and fig. S4), suggesting that the A673V variant alters APP processing, which promotes an increase in Aβ formation. To confirm this, we transiently transfected Chinese hamster ovary (CHO) and COS-7 cells with either mutant or wild-type APP cDNA and measured Aβ in conditioned media by enzyme-linked immunosorbent assay (ELISA) (*8*). Cells expressing A673V APP had significantly higher amounts of both Aβ1-40 and Aβ1-42 than did cells transfected with wild-type APP, with no change in Aβ1-42:Aβ1-40 ratio (table S2). CHO and COS-7 cells with the A673V mutation also had increased secretion of amino-terminally truncated Aβ species, including Aβ11-40, Aβ11-42, and AβN3pE-42 (table S2). These differences were paralleled by differences in the production of soluble forms of APP (sAPPβ and sAPPα) and of APP carboxy-terminal fragments (C99 and C83) that derived from the amyloidogenic β-secretase or nonamyloidogenic α-secretase processing (*8*). Fibroblasts of the patient showed increased secretion of sAPPβ and 2.5-fold increase in sAPPβ:sAPPα ratio (mean of three determinations: 0.5) compared with those of four age-matched controls [0.2 ± 0.01 (SD)] as deduced by ELISA. Similarly, the sAPPβ:sAPPα ratio was significantly higher in media from CHO cells expressing the A673V mutation (0.4 ± 0.1) than in media from control cells (0.1 ± 0.03, $P = 0.03$) (Fig. 1B). Immunoblot analysis of cell lysates with an antibody to the carboxy-terminal region of APP (*8*) showed a 1.9 ± 0.2 increase in C99:C83 ratio in patient's fibroblasts (mean of three determinations: 0.67) compared with that in control fibroblasts (0.35 ± 0.02) and 2.5 ± 0.2 increase in mutated CHO cells (0.52 ± 0.10) compared with that of control cells (0.21 ± 0.05, $P = 0.0001$) (Fig. 1, C and D).

We then investigated the effects of the A673V mutation on the aggregation and amyloidogenic properties of Aβ by using synthetic peptides homologous to residues 1 to 40 with and without the A-to-V substitution at position 2 (Aβ1-40$_{\text{mut}}$ and Aβ1-40$_{\text{wt}}$) (*8*). Laser light scattering measurements over short periods (first 24 hours after sample preparation) showed that the aggregation kinetics was faster for Aβ1-40$_{\text{mut}}$ than for Aβ1-40$_{\text{wt}}$ and that the time constants of the exponential increase were 1.3 hours and 5.8 hours, respectively (Fig. 2A). Furthermore, although the initial size distribution of particles generated by the two peptides was similar, after 24 hours Aβ1-40$_{\text{mut}}$ assemblies were much larger than Aβ1-40$_{\text{wt}}$ aggregates (Fig. 2B). Polarized-light and electron microscopy (EM) showed that Aβ1-40$_{\text{mut}}$ aggregates with the tinctorial properties of amyloid (i.e., birefringence after Congo red staining) ultrastructurally formed by straight, unbranched, 8-nm-diameter fibrils were already apparent after 4 hours. Amyloid progressively increased up to 5 days, when the samples contained only fibrils organized in dense meshwork (Fig. 3, B, E, H, and K). Aβ1-40$_{\text{wt}}$ followed a qualitatively similar assembly path but with much slower kinetics. The 8-nm-diameter amyloid fibrils were first observed after 72 hours, mingled with oligomers and protofibrils (Fig. 3, A and G), and the size and density of congophilic aggregates reached a plateau only after 20 days (Fig. 3, D and J). Similar differences were observed between wild-type and mutated peptides homologous to residues 1 to 42 of Aβ (Fig. 3, M and N), although the aggregation kinetics was faster compared with that of Aβ1-40.

The finding that the A673V mutation strongly boosts Aβ production and fibrillogenesis raises the question of why heterozygous carriers do not develop disease, so we analyzed the effects of the interaction between Aβ1-40$_{\text{mut}}$ and Aβ1-40$_{\text{wt}}$. Laser light scattering showed that the time constant of aggregate formation of equimolar mixtures of wild-type and mutated peptides was higher (8.3 hours) than the time to aggregate for either Aβ1-40$_{\text{mut}}$ (1.3 hours) or Aβ1-40$_{\text{wt}}$ alone (5.8 hours) (Fig. 2A) and that the size distribution of particles was lowest both at time 0 and after

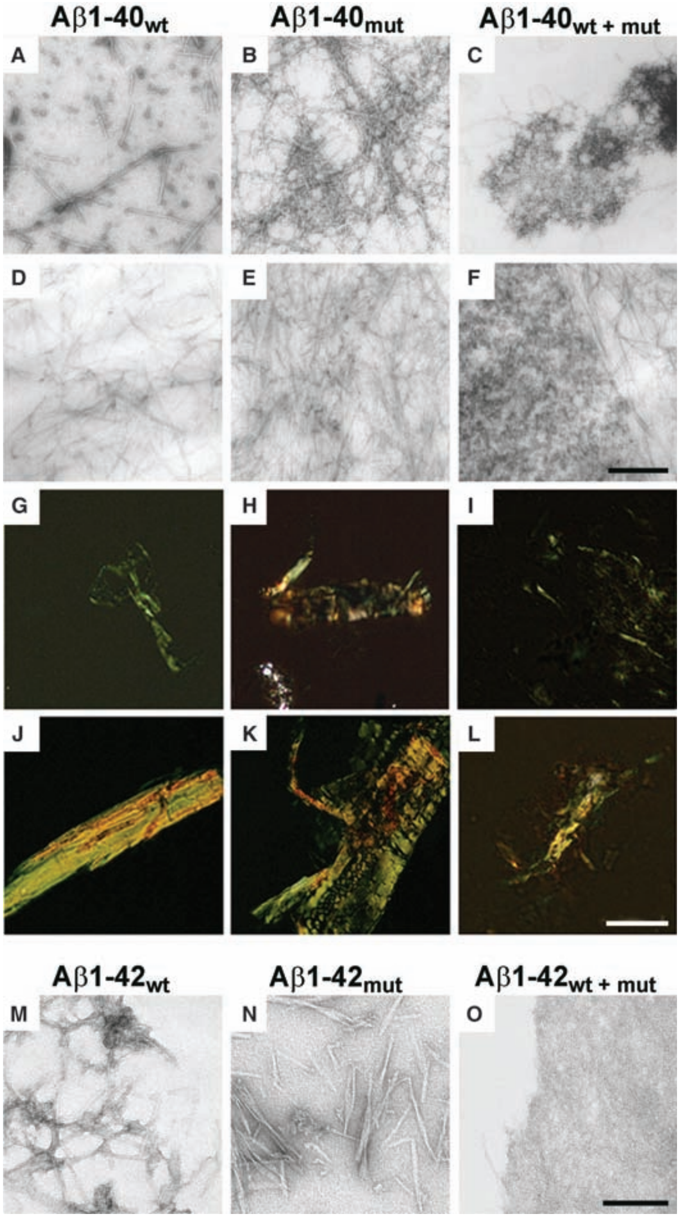

Fig. 3. Aggregation properties of mutated and wild-type Aβ peptides. (**A** to **F**) Electron micrographs of aggregates generated by Aβ1-40$_{\text{wt}}$, Aβ1-40$_{\text{mut}}$, and equimolar mixtures after 72 hours [(A) to (C), negative staining] and 20 days incubation [(D) to (F), positive staining]. (**G** to **L**) Polarized light microscopy of Aβ aggregates stained with Congo red after 72 hours [(G) to (I)] and 20 days [(J) to (L)]. (**M** to **O**) Electron micrographs of negatively stained aggregates generated by Aβ1-42$_{\text{wt}}$ (M), Aβ1-42$_{\text{mut}}$ (N), and equimolar mixtures (O) after 5 days incubation. The peptide mixture contains mainly amorphous material (O), whereas wild-type and mutated Aβ1-42 are assembled in fibrillary structures. Scale bars indicate 250 nm [(A) to (F)], 50 μm [(G) to (L)], and 125 nm [(M) to (O)].

24 hours (Fig. 2B). Furthermore, the aggregates formed by peptide mixtures were far more unstable than those generated by either Aβ1-40$_{\text{wt}}$ or Aβ1-40$_{\text{mut}}$ after dilution with buffer, with a characteristic dissolution time of 8 min. At the same time, no dissolution kinetics was observed for samples of Aβ1-40$_{\text{wt}}$ and Aβ1-40$_{\text{mut}}$ alone (Fig. 2C). This was confirmed by urea denaturation studies of peptide aggregates (*8*). Size exclusion chromatography showed that the elution profiles of Aβ1-40$_{\text{wt}}$ and Aβ1-40$_{\text{mut}}$ were marked by a single peak corresponding to the dimer, whereas the mixture gave a smaller peak area corresponding to the dimer and a second small peak corresponding to the monomer (Fig. 4A). Polarized light and EM showed that the peptide mixture built up much fewer congophilic aggregates than not only Aβ1-40$_{\text{mut}}$ but also Aβ1-40$_{\text{wt}}$ (Fig. 3, C, F, I, and L). Similar results were observed with Aβ1-42 peptides (Fig. 3, M to O). Amyloid formation was also inhibited when Aβ1-40$_{\text{wt}}$ was incubated with a hexapeptide homologous to residues 1 to 6 containing the A-to-V substitution in position 2 (Aβ1-6$_{\text{mut}}$) at 1:4 molar ratio (fig. S5).

We analyzed the binding of Aβ peptides with and without the A673V mutation to Aβ1-40$_{\text{wt}}$ by using surface plasmon resonance (*8*). In addition to Aβ1-40$_{\text{wt}}$ and Aβ1-40$_{\text{mut}}$, we used the hexapeptides Aβ1-6$_{\text{wt}}$ and Aβ1-6$_{\text{mut}}$ to evaluate the independent contribution of the amino-terminal sequence containing the mutation. No difference in binding to immobilized Aβ1-40$_{\text{wt}}$ fibrils was observed between Aβ1-40$_{\text{wt}}$ and Aβ1-40$_{\text{mut}}$, consistent with the finding that Aβ aggregation is primarily driven by hydrophobic stretches in the central and carboxy-terminal parts of the peptide (Fig. 4B) (*10*). However, the amino-terminal fragment Aβ1-6$_{\text{mut}}$ showed greater ability to bind to wild-type Aβ1-40 than did Aβ1-6$_{\text{wt}}$ (Fig. 4C), indicating that the A-to-V substitution at position 2 favors the interaction between mutant and wild-type Aβ.

Lastly, we treated human neuroblastoma SH-SY5Y cells with Aβ1-42$_{\text{wt}}$, Aβ1-42$_{\text{mut}}$, or mixtures thereof at 5 μM for 24 hours and assessed cell viability by 3-(4,5-dimethylthiazol-2-yl)-2,5-diphenyl tetrasodium bromide (*8*): Aβ1-42$_{\text{mut}}$ was more toxic than Aβ1-42$_{\text{wt}}$, and the mixture was significantly less toxic than either peptide alone (Fig. 4D).

We have identified a mutation in the APP gene showing a recessive Mendelian trait of inheritance. Recently, a homozygous APP mutation (A693Δ) was detected in three AD patients from two Japanese pedigrees (*11*). Because one out of four heterozygous individuals had MCI, in the absence of experimental studies mimicking the situation in heterozygotes, it is hard to establish whether A693Δ is a recessive mutation or a dominant APP variant with incomplete penetrance.

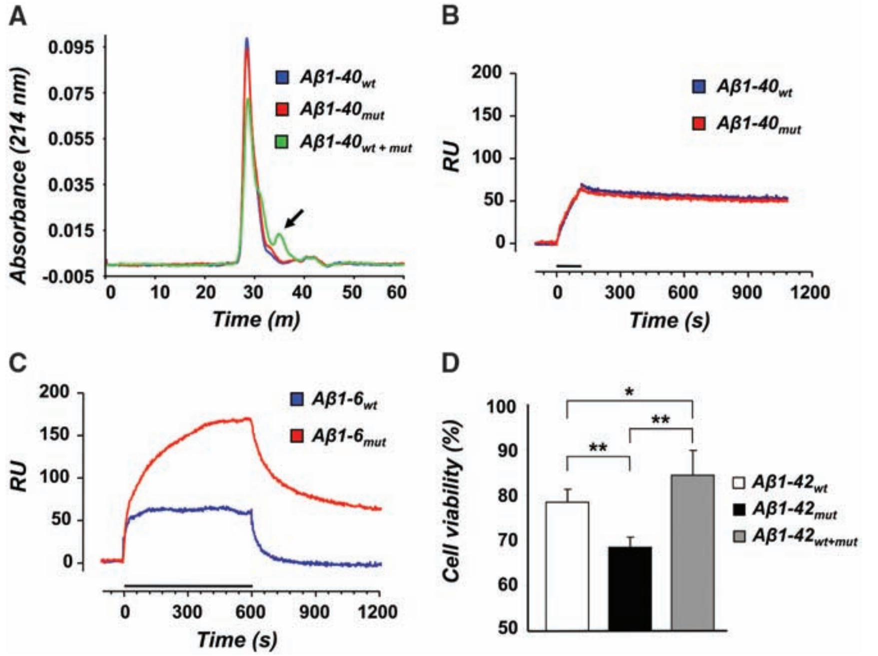

Fig. 4. Physicochemical and biological properties of mutated and wild-type Aβ peptides. (**A**) Size exclusion chromatograms of Aβ1-40$_{\text{wt}}$, Aβ1-40$_{\text{mut}}$, and equimolar peptide mixture aggregates after treatment with 1 M urea for 24 hours. Monomeric species (arrow) are only seen in the peptide mixture. (**B** and **C**) Binding of wild-type and mutated Aβ1-40 (B) or Aβ1-6 (C) to amyloid fibrils of Aβ1-40$_{\text{wt}}$ determined by surface plasmon resonance. Solutions of Aβ1-40 (1 μM) or Aβ1-6 (500 μM) were injected onto Aβ1-40$_{\text{wt}}$ fibrils immobilized on the sensor chip for the time indicated by the bars. (**D**) Viability of human neuroblastoma cells after 24 hours exposure to 5 μM Aβ1-42$_{\text{wt}}$, Aβ1-42$_{\text{mut}}$, and the equimolar mixture. Error bars represent SD of the mean of eight replicates. $^{*}P = 0.026$, $^{**}P < 0.001$.

The A673V APP mutation has two pathogenic effects: it (i) shifts APP processing toward the amyloidogenic pathway and (ii) enhances the aggregation and fibrillogenic properties of Aβ. However, the interaction between mutant and wild-type Aβ, favored by the A-to-V substitution at position 2, interferes with nucleation or nucleation-dependent polymerization, or both, hindering amyloidogenesis and neurotoxicity and thus protecting the heterozygous carriers.

Until recently, the importance of the amino-terminal sequence of Aβ in misfolding and disease was underestimated because this region is highly disordered in the fibrillar form of the peptide (*12*). However, the amino-terminal domain of Aβ is selectively perturbed in amyloidogenesis, and, most importantly, changes in its primary sequence trigger peptide assembly and fibril formation (*13*, *14*). The importance of this domain is further supported by the finding that antibodies against it are optimal for plaque clearance in animal models (*15*). A previous study reported a distinct heterozygous APP mutation at codon 673 [$\text{Ala}^{673}\rightarrow\text{Tyr}^{673}$ (A673T)] in a participant without clinical signs of dementia (*16*). Histological analysis did not detect amyloid deposits in the brain. However, when the A673T mutation was introduced in a synthetic Aβ1-40 peptide, it increased the propensity to aggregate, with a much shorter lag phase than that of the wild-type peptide (*17*). These observations, together with our results, suggest that mutations at position 2 of Aβ confer amyloidogenic properties that lead to AD only in the homozygous state. The finding that the interaction between A673V-mutated and wild-type Aβ hinders amyloidogenesis, and especially the anti-amyloidogenic properties of the mutated six-residue peptide, may offer grounds for the development of therapeutic strategies based on modified Aβ peptides or peptido-mimetic compounds (*18*, *19*) for both sporadic and familial AD.

The present data highlight the importance of screening demented and nondemented human populations for mutations of the Aβ encoding region of APP. Genetic variants that could be regarded as normal polymorphisms may turn out to be pathogenic in homozygous individuals. The identification of such mutations would help to prevent the occurrence of the disease in their carriers.

References and Notes

1. J. Hardy, D. J. Selkoe, *Science* **297**, 353 (2002).
2. D. J. Selkoe, *Physiol. Rev.* **81**, 741 (2001).
3. D. M. Walsh *et al.*, *Nature* **416**, 535 (2002).
4. L. Bertram, R. E. Tanzi, *J. Clin. Investig.* **115**, 1449 (2005).
5. A. Rocchi, S. Pellegrini, G. Siciliano, L. Murri, *Brain Res. Bull.* **61**, 1 (2003).
6. P. H. St George-Hyslop, *Biol. Psychiatry* **47**, 183 (2000).
7. E. Levy *et al.*, *Science* **248**, 1124 (1990).
8. Materials and methods are available as supporting material on *Science* Online.

9. R. C. Petersen *et al.*, *Arch. Neurol.* **58**, 1985 (2001).
10. M. Cecchini, R. Curcio, M. Pappalardo, R. Melki, A. Caflisch, *J. Mol. Biol.* **357**, 1306 (2006).
11. T. Tomiyama *et al.*, *Ann. Neurol.* **63**, 377 (2008).
12. A. D. Williams *et al.*, *J. Mol. Biol.* **335**, 833 (2004).
13. K. H. Lim, *ChemBioChem* **7**, 1662 (2006).
14. Y. Hori *et al.*, *J. Biol. Chem.* **282**, 4916 (2007).
15. F. Bard *et al.*, *Proc. Natl. Acad. Sci. U.S.A.* **100**, 2023 (2003).
16. M. L. Peacock, J. T. Warren, A. D. Roses, J. K. Fink, *Neurology* **43**, 1254 (1993).
17. J. Meinhardt *et al.*, *Protein Sci.* **16**, 1214 (2007).
18. C. Soto *et al.*, *Nat. Med.* **4**, 822 (1998).
19. C. Adessi *et al.*, *J. Biol. Chem.* **278**, 13905 (2003).
20. This work was supported by grants from the Italian Ministry of Health (533F/Q/1 to F.T. and M.S., and 71.6/2006 and RFPS 2007/02 to F.T.), CARIPLO Foundation (Guard) to F.T. and M.S., ERA-Net Neuron (nEUROsyn) to F.T., Negri-Weizmann Foundation to M.S., the National Institute of Neurological Disorders and Stroke (NS42029) to E.L., and the American Heart Association (0040102N) to E.L. A patent application related to this work has been filed by Fondazione IRCCS Istituto Nazionale Neurologico "Carlo Besta."

Supporting Online Material
www.sciencemag.org/cgi/content/full/323/5920/1473/DC1
Materials and Methods
SOM Text
Figs. S1 to S5
Tables S1 and S2

25 November 2008; accepted 12 January 2009
10.1126/science.1168979

Structure of the Anaphase-Promoting Complex/Cyclosome Interacting with a Mitotic Checkpoint Complex

Franz Herzog,[1]* Ivana Primorac,[1] Prakash Dube,[2] Peter Lenart,[3] Björn Sander,[2] Karl Mechtler,[1] Holger Stark,[2]† Jan-Michael Peters[1]†

Once all chromosomes are connected to the mitotic spindle (bioriented), anaphase is initiated by the protein ubiquitylation activity of the anaphase-promoting complex/cyclosome (APC/C) and its coactivator Cdc20 (APC/C$^{\text{Cdc20}}$). Before chromosome biorientation, anaphase is delayed by a mitotic checkpoint complex (MCC) that inhibits APC/C$^{\text{Cdc20}}$. We used single-particle electron microscopy to obtain three-dimensional models of human APC/C in various functional states: bound to MCC, to Cdc20, or to neither (apo-APC/C). These experiments revealed that MCC associates with the Cdc20 binding site on APC/C, locks the otherwise flexible APC/C in a "closed" state, and prevents binding and ubiquitylation of a wide range of different APC/C substrates. These observations clarify the structural basis for the inhibition of APC/C by spindle checkpoint proteins.

Chromosome segregation is delayed by the spindle checkpoint until all chromosomes are connected to both poles (bioriented) of the mitotic or meiotic spindle. Defects in this checkpoint can lead to aneuploidy, which is associated with tumorigenesis, congenital trisomies, and aging (*1*). The spindle checkpoint is activated in prometaphase by the presence of kinetochores that are not properly attached to microtubules or not under tension by spindle-pulling forces (*2*, *3*). The checkpoint inhibits Cdc20, which activates the ubiquitin-protein ligase APC/C in mitosis and helps to recruit substrates to APC/C. APC/C initiates chromosome segregation by ubiquitylating cyclin B, an activating subunit of cyclin-dependent kinase 1 (Cdk1), and securin, an inhibitor of the protease separase. After ubiquitin-mediated degradation of these proteins, separase becomes active and dissolves the cohesion between sister chromatids (*4*).

Inhibition of Cdc20 by the spindle checkpoint depends on mitotic arrest–deficient 2 (Mad2) (*5*). This protein associates with Cdc20 at unattached kinetochores (*6*–*9*). In animal cells, Cdc20 is also inhibited by association with budding uninhibited by benzimidazoles–related 1 (BubR1) and its binding partner budding uninhibited by benzimidazoles 3 (Bub3). Mad2 and BubR1-Bub3 can bind to Cdc20 either separately (*10*, *11*) or simultaneously, forming a MCC (*12*), and these proteins can associate with APC/C (*13*–*16*). Similar complexes exist in yeast, in which a BubR1-related Mad3 protein might inhibit Cdc20 as a pseudosubstrate (*17*, *18*).

Structural information will be essential to understand how checkpoint proteins inhibit APC/C$^{\text{Cdc20}}$, but it is known only how Mad2 interacts with a short Cdc20 peptide (*19*, *20*). We therefore analyzed with single-particle electron microscopy (EM) the structure of APC/C that is bound to checkpoint proteins. We first established conditions under which checkpoint-inhibited APC/C could be purified and characterized these complexes biochemically. We isolated APC/C from human HeLa cells that had been arrested in prometaphase by the microtubule-stabilizing agent Taxol, which keeps the checkpoint active. For comparison, we purified APC/C from Taxol-arrested cells in which the checkpoint had been inactivated by hesperadin, an inhibitor of Aurora B kinase (*15*, *21*). Quantitative fluorescence microscopy of chromosome morphology, cyclin B levels, and kinetochore association of Mad2, BubR1, and Bub1 confirmed that cells had been arrested in prometaphase with either an active or inhibited spindle checkpoint (fig. S1). Mass spectrometry (table S1) and SDS–polyacrylamide gel electrophoresis (SDS-PAGE) followed by silver staining (Fig. 1A) or semiquantitative immunoblotting (Fig. 1B) revealed that four times more BubR1, Bub3, and Mad2 were associated with APC/C in cells in which the checkpoint was active than in hesperadin-treated cells. The amount of Cdc20 bound to APC/C was twofold greater when the checkpoint was active, perhaps because checkpoint proteins stabilize APC/C–Cdc20 interactions. Immunoprecipitation of BubR1 confirmed that more BubR1, Bub3, Mad2, and Cdc20 were bound to APC/C when the checkpoint was active (Fig. 1A and table S1). In a reconstituted system, ubiquitylation of cyclin B and securin was reduced to 17% when APC/C was isolated from cells with an active checkpoint as compared with reactions mediated by APC/C from cells with an inactive checkpoint. This difference was even greater when samples were normalized to the amounts of APC/C–associated Cdc20, which is rate-limiting for APC/C activity (Fig. 1, C and D). Surprisingly, APC/C from cells with an active checkpoint was similarly less active toward cyclin A and never-in-mitosis A (NIMA)–related kinase 2A (Nek2A), which are normally degraded in prometaphase when the checkpoint is active (Fig. 1E and fig. S2). The checkpoint appears not to inhibit APC/C$^{\text{Cdc20}}$ in a substrate-specific manner, as was proposed to explain Nek2A degradation in prometaphase (*22*), but by recruiting substrates before checkpoint activation, as shown for cyclin A (*23*).

Similar results were obtained when APC/C was isolated from cells with active or inactive checkpoints that were obtained with a different protocol in which cells had not been treated with hesperadin (fig. S3), indicating that hesperadin caused changes in APC/C's subunit composition and activity by checkpoint inhibition and not by an unrelated mechanism. Our results therefore indicated that checkpoint activation leads to association of BubR1, Bub3, and Mad2 with APC/C and to the general inhibition of APC/C's ubiquitylation activity. However, our SDS-PAGE–silver staining analysis of APC/C from cells in which the checkpoint is active suggested that BubR1, Bub3, and Mad2 were present in substoichiometric amounts relative to APC/C (Fig. 1A). We therefore separated APC/C purified from cells with an active checkpoint into different subpopulations (Fig. 1F). We first captured a subpopulation of APC/C with BubR1, Cdc20, or Mad2 antibodies and then isolated the remaining

---

[1] Research Institute of Molecular Pathology, Dr. Bohr-Gasse 7, 1030 Vienna, Austria. [2] Max-Planck-Institute for Biophysical Chemistry, Am Fassberg 11, 37077 Goettingen, Germany. [3] European Molecular Biology Laboratory, Meyerhofstraße 1, 69117 Heidelberg, Germany.

*Present address: Institute of Molecular Systems Biology, Eidgenössische Technische Hochschule Zurich, 8093 Zurich, Switzerland.

†To whom correspondence should be addressed. E-mail: hstark1@gwdg.de (H.S.); peters@imp.univie.ac.at (J.-M.P.)

particles with antibodies to the APC/C subunit Apc4 (Fig. 1, G and H, and fig. S4). These experiments revealed that cells with an active checkpoint contained two forms of APC/C. One contained BubR1, Bub3, Cdc20, and Mad2, whereas the other one lacked all of these proteins. We refer to these forms as APC/C^{MCC} and apo-APC/C, respectively. In cyclin B–ubiquitylation assays, the specific activities of APC/C^{MCC} and apo-APC/C were similarly low (Fig. 1I). Purified Cdc20 and the related coactivator Cdc20 homolog 1 (Cdh1) activated apo-APC/C in a dose-dependent manner, suggesting that this form of APC/C is inactive because it is lacking a coactivator. In contrast, APC/C^{MCC} could be stimulated by coactivators only to a small degree, indicating that this form of APC/C represents a truly inhibited state (Fig. 1I).

To understand how checkpoint proteins inhibit APC/C, we determined the structures of APC/C^{MCC}, apo-APC/C, and APC/C^{Cdc20}. We isolated APC/C^{MCC} by means of sequential immunoprecipitation with antibodies to Cdc27 and BubR1. We isolated apo-APC/C with antibodies to Apc4 from the supernatant of the BubR1 immunoprecipitation. After a peptide elution, both samples were further purified by use of glycerol density-gradient centrifugation (*24*) and analyzed by use of both negative staining at low temperatures and unstained cryo-EM in a vitrified buffer (Fig. 2, figs. S5 and S6, and table S2). We used a technique based on three-dimensional (3D) alignment of random conical tilt (RCT) reconstructions and subsequent 3D multivariate statistical analysis for initial structure determination and simultaneous unsupervised analysis of the heterogeneity in the data set. For apo-APC/C, we identified three conformers that differ mainly in the relative orientation of their two major domains: the platform and

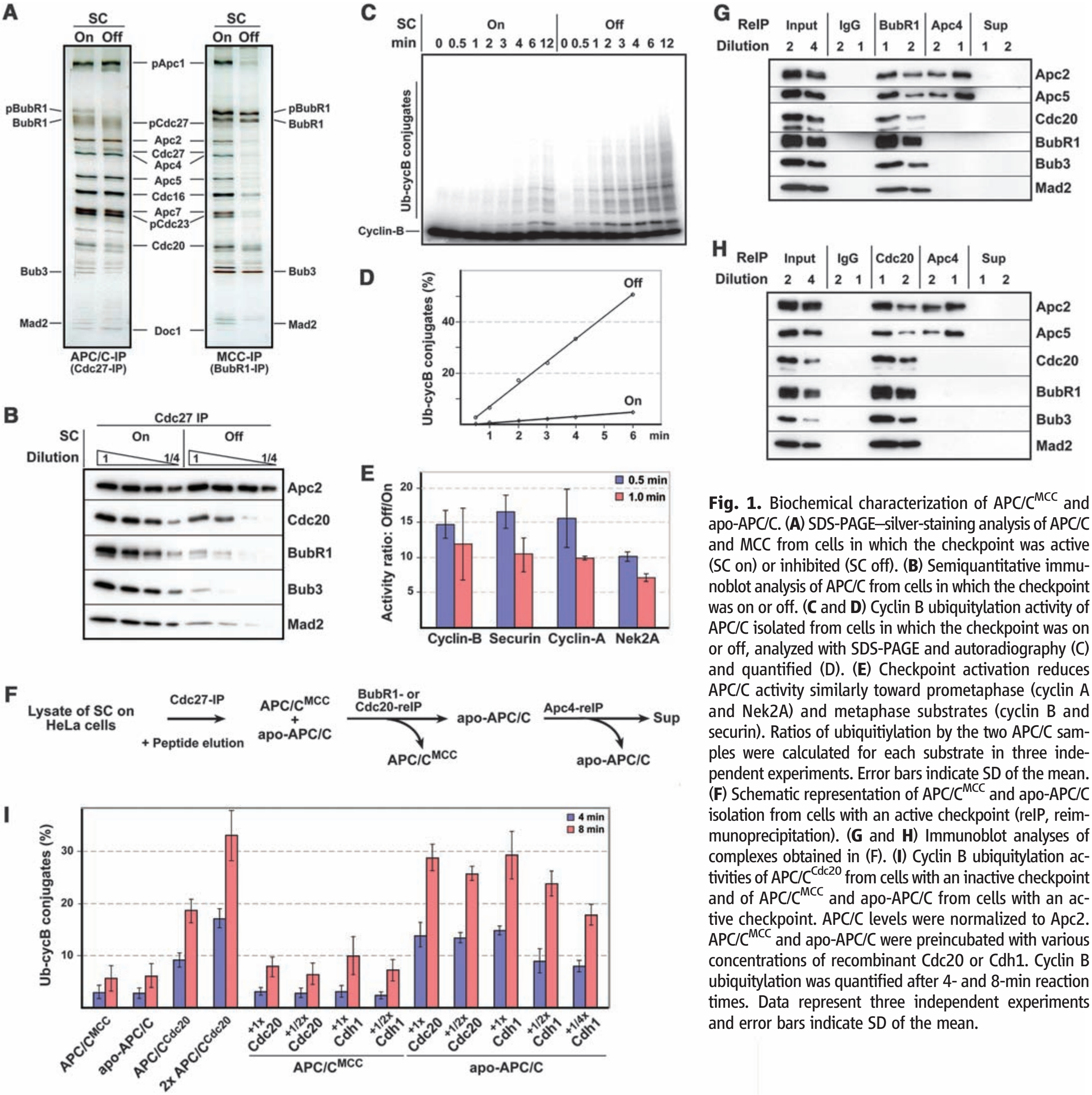

Fig. 1. Biochemical characterization of APC/C^{MCC} and apo-APC/C. (**A**) SDS-PAGE–silver-staining analysis of APC/C and MCC from cells in which the checkpoint was active (SC on) or inhibited (SC off). (**B**) Semiquantitative immunoblot analysis of APC/C from cells in which the checkpoint was on or off. (**C** and **D**) Cyclin B ubiquitylation activity of APC/C isolated from cells in which the checkpoint was on or off, analyzed with SDS-PAGE and autoradiography (C) and quantified (D). (**E**) Checkpoint activation reduces APC/C activity similarly toward prometaphase (cyclin A and Nek2A) and metaphase substrates (cyclin B and securin). Ratios of ubiquitiylation by the two APC/C samples were calculated for each substrate in three independent experiments. Error bars indicate SD of the mean. (**F**) Schematic representation of APC/C^{MCC} and apo-APC/C isolation from cells with an active checkpoint (reIP, reimmunoprecipitation). (**G** and **H**) Immunoblot analyses of complexes obtained in (F). (**I**) Cyclin B ubiquitylation activities of APC/C^{Cdc20} from cells with an inactive checkpoint and of APC/C^{MCC} and apo-APC/C from cells with an active checkpoint. APC/C levels were normalized to Apc2. APC/C^{MCC} and apo-APC/C were preincubated with various concentrations of recombinant Cdc20 or Cdh1. Cyclin B ubiquitylation was quantified after 4- and 8-min reaction times. Data represent three independent experiments and error bars indicate SD of the mean.

the arc lamp domains (Fig. 2A and 3D-PDF S1) (*25*). The initial RCT 3D structures were used to determine the handedness (fig. S7) and as templates for further refinement of the existing subpopulations of apo-APC/C (Fig. 2A). We suspect that these conformers represent the structural variability of apo-APC/C in solution and represent a continuum of flexible states (for an animation of the corresponding movements, see movie S1).

In the APC/C^{MCC} sample, a large additional density was found inserted into the "front" side of the platform domain (Fig. 2C, red, and 3D-PDF S2). The 3D volume of this density element corresponds to a mass of 180 to 200 kD, slightly less than MCC's theoretical mass of 236 kD (if every subunit is present once). We confirmed that this mass represents MCC by identifying the location of BubR1 by means of antibody labeling (fig. S8). To obtain a 3D model of APC/C^{Cdc20}, we bound recombinant Cdc20 to purified apo-APC/C and determined the structures as above. In 30% of APC/C molecules, we found an additional globular 50-kD mass on the front side of APC/C in a location that overlaps with the site to which MCC is bound in APC/C^{MCC} (Fig. 2B and fig. S9). The Cdc20 density does not fully overlap with the MCC density and is ~20 Å away from a perfect fit. The precise position of Cdc20 may thus change upon MCC binding to APC/C (Fig. 2D). APC/C^{Cdc20} showed similar conformational flexibility as apo-APC/C.

Comparison of the apo-APC/C and APC/C^{MCC} structures revealed a number of differences in addition to the presence of an extra mass in APC/C^{MCC}. To interpret these changes, we mapped the 3D location of APC/C core subunits with antibody labeling (fig. S8). Antibodies to Apc1, Apc4, and Apc5 bound to distinct sites in the platform domain with Apc5 at the bottom, Apc4 at the front, and Apc1 at the right-hand side (Fig. 3, A and B). The volumes of the labeled domains are consistent with the predicted masses of Apc1, Apc4, and Apc5 (Fig. 3B). The modeling of these subunits into the APC/C 3D structure suggests that Apc5 is close to the interface of the platform and arc lamp domains, and the mass accommodated by Apc1 spans from the front to the inner mass (Fig. 3B). Part of the subunit that we identified as Apc4 has a ring-shaped structure (Fig. 3B, right), which is consistent with bioinformatic analyses that Apc4 contains an N-terminal propeller-shaped WD40 domain (*4*). Cdc27 antibodies bound to the headlike protrusion that is located at the top end of the arc lamp domain (Fig. 3A). We confirmed that Apc2 is located at the inner mass on the front side of APC/C (*25*), residing in close vicinity to Apc1 and Cdc27 (Fig. 3, A and B). Antibodies to Cdc16 and Apc7 were bound at multiple locations on the arc lamp domain (fig. S8), presumably because these subunits are present in more than one copy per APC/C molecule (*25*). The arc lamp domain is bent and has an unusual repetitive regularity (Fig. 3B), features that are characteristic of tetratricopeptide repeat (TPR) domains present in Cdc16 and Apc7 and also in Cdc27 and Cdc23. These observations indicate that a major part of the arc lamp domain consists of TPR subunits. With the exception of Apc2 and Apc4 topology, our 3D model of subunit topology is consistent with the 2D positions of subunits determined in fission yeast APC/C (*26*).

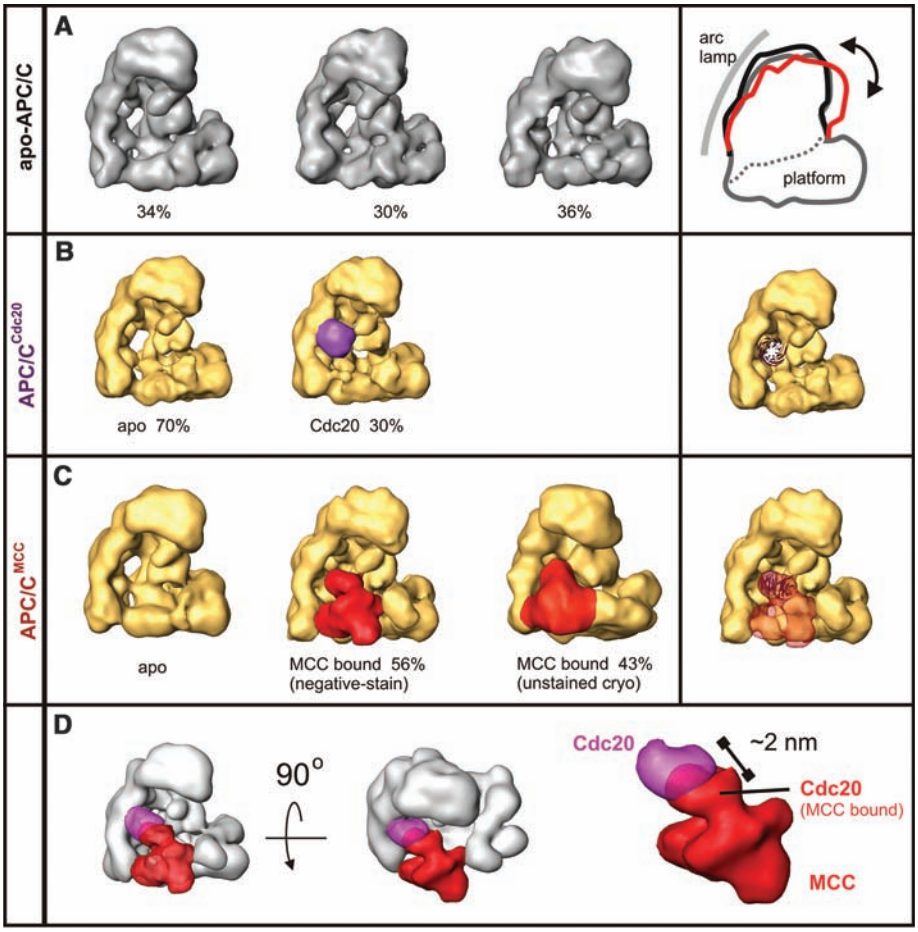

Fig. 2. Localization of Cdc20 and MCC bound to APC/C, analyzed by negative-staining EM. (**A**) Distinct conformers of apo-APC/C isolated from cells with an active checkpoint. (**B**) Localization of recombinant Cdc20 (purple) bound to apo-APC/C. A model of Cdc20's WD40 propeller is projected onto APC/C. (**C**) 3D structure of APC/C^{MCC}. MCC is labeled in red. (**D**) Superposition of the MCC (red) and Cdc20 (purple) densities shown from orthogonal directions.

This subunit map indicates that MCC binds in the vicinity of Apc2, Apc4, and Apc5, which are located toward the right-hand side of MCC (Fig. 3, B, D, and E, and 3D-PDFs S1 and S2). On the left-hand side, MCC contacts the arc lamp domain, which suggests that MCC also interacts with TPR subunits. Little if any conformational flexibility was observed among populations of APC/C^{MCC}. Instead, APC/C^{MCC} adopts a closed conformation (Fig. 3D). In addition, Apc4 is bent upward by 35° in APC/C^{MCC} as compared with its position in apo-APC/C, and the position of a more centrally located subunit, possibly Apc2, is also changed (Fig. 3E). This rearrangement might be required for MCC binding and, together with a higher curvature of the arc lamp, results in a more compact appearance of APC/C^{MCC} as compared with that of apo-APC/C.

To understand the functional consequences of these structural changes, we compared the interactions of different forms of APC/C with the ubiquitin-conjugating enzyme UbcH10 and substrate proteins. Binding of UbcH10 to APC/C was reduced to 50% when the checkpoint was active (fig. S10). It is unlikely that this small change can explain the almost complete inhibition of APC/C by checkpoint proteins. In contrast, we saw a substantial reduction in substrate binding to checkpoint-inhibited APC/C. When APC/C was isolated from cells with an active checkpoint, much less binding of an N-terminal fragment of fission yeast cyclin B or of full-length human securin was detected as compared with the binding that was observed with APC/C from cells in which the checkpoint was inhibited (Fig. 4, A to C). As reported (*27*), binding of cyclin B to APC/C required the presence of a destruction box (D box) in the substrate (Fig. 4, A and B). Similar results were obtained when a D box–containing fragment of budding yeast Hsl1 was used as a substrate (fig. S11). Even a 35-fold increase in substrate concentration resulted in less Hsl1 binding to APC/C from cells with an active checkpoint, as compared with Hsl1 binding to APC/C from cells in which the checkpoint was inactive.

Our data indicate that activation of the spindle checkpoint leads to association of BubR1, Bub3, and Mad2 with APC/C$^{\mathrm{Cdc20}}$, in which the checkpoint proteins occupy a site that partially overlaps with the Cdc20 binding site. The association of checkpoint proteins with APC/C coincides with inhibition of APC/C toward a broad range of prometaphase and metaphase substrates, indicating that checkpoint activation inhibits APC/C generally and not in a substrate-specific manner. This inhibition is at least in part caused by the prevention of substrate binding, which agrees well with the proposed role of Cdc20 as a substrate adaptor (*28*, *29*) and of yeast Mad3 as a pseudosubstrate inhibitor (*17*). Partial overlap of positions of Cdc20 binding to APC/C$^{\mathrm{Cdc20}}$ and APC/C$^{\mathrm{MCC}}$ raises the possibility that APC/C inhibition may be mediated by MCC-induced repositioning of Cdc20. MCC binding also induces conformational changes in APC/C itself and appears to lock it in a closed conformational state.

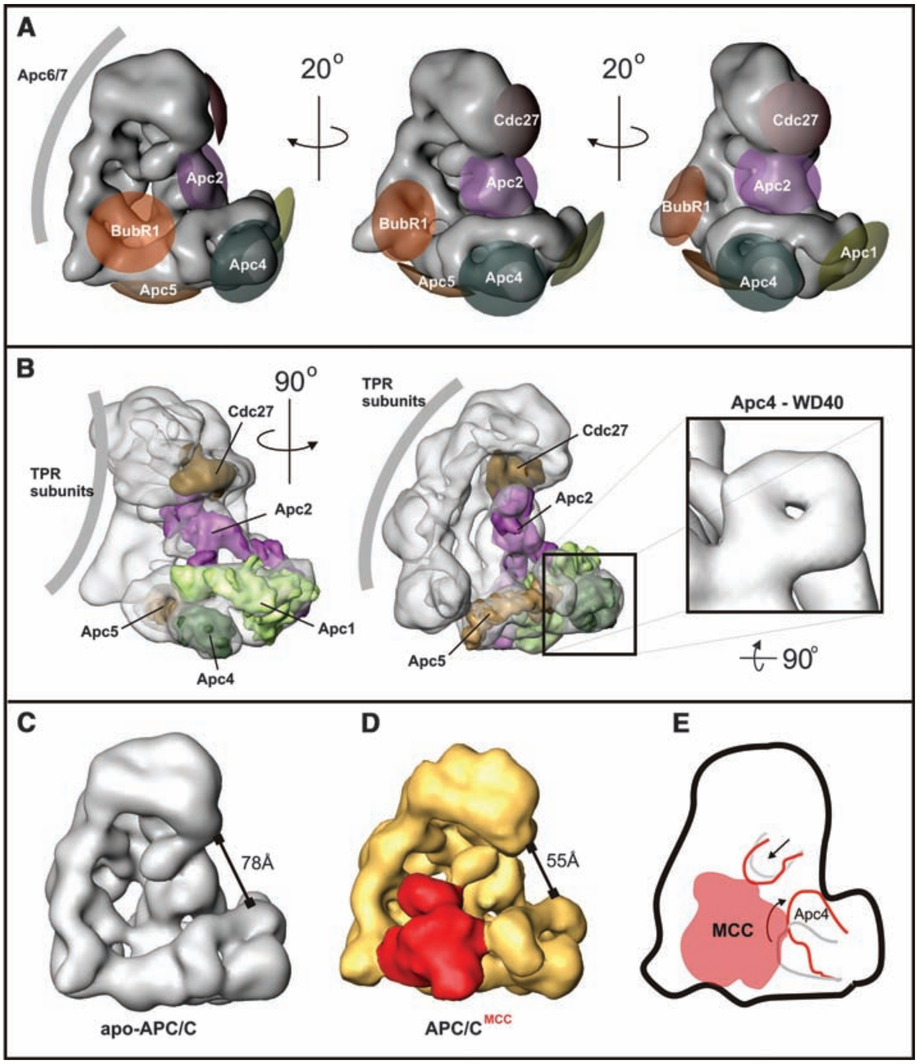

Fig. 3. APC/C subunit topology and structural changes upon MCC binding. (**A**) APC/C subunits were localized with antibody labeling. Antibody epitopes are marked on the surface of the APC/C 3D model, and the labeling accuracy is indicated by the size of the differently colored areas. (**B**) Models of Apc1, Apc2, Apc4, Apc5, and Cdc27 were docked into the 3D density of the APC/C reconstruction. (**C**) The apo-APC/C structure in its most open conformation. (**D**) The APC/C$^{\mathrm{MCC}}$ structure with a closed conformation. (**E**) Conformational changes induced by MCC binding to APC/C.

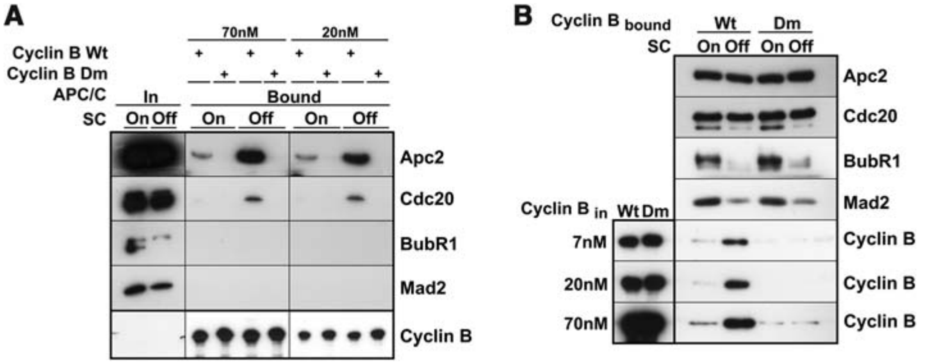

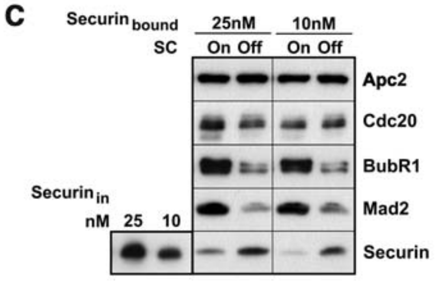

Fig. 4. MCC inhibits the binding of substrates to APC/C. (**A**) A tandem fragment of wild-type (wt) or D-box mutant (dm) fission yeast cyclin B was immobilized on glutathione beads at the indicated concentrations, and binding of APC/C from cells with checkpoints on or off was analyzed with SDS-PAGE immunoblotting. (**B**) APC/C from cells with checkpoints on or off was bound to beads coupled with antibody to Cdc27, and binding of soluble wild-type or D-box mutant cyclin B was analyzed in the same manner as in (A). (**C**) The binding of full-length human securin to APC/C was analyzed in the same manner as in (B).

References and Notes

1. D. J. Baker, J. Chen, J. M. van Deursen, *Curr. Opin. Cell Biol.* **17**, 583 (2005).
2. C. L. Rieder, R. W. Cole, A. Khodjakov, G. Sluder, *J. Cell Biol.* **130**, 941 (1995).
3. B. M. Stern, A. W. Murray, *Curr. Biol.* **11**, 1462 (2001).
4. J. M. Peters, *Mol. Cell* **9**, 931 (2002).
5. R. Li, A. W. Murray, *Cell* **66**, 519 (1991).
6. G. Fang, H. Yu, M. W. Kirschner, *Genes Dev.* **12**, 1871 (1998).
7. L. H. Hwang *et al.*, *Science* **279**, 1041 (1998).
8. S. H. Kim, D. P. Lin, S. Matsumoto, A. Kitazono, T. Matsumoto, *Science* **279**, 1045 (1998).
9. A. DeAntoni, V. Sala, A. Musacchio, *Philos. Trans. R. Soc. London Ser. B* **360**, 637 (2005).
10. Z. Tang, R. Bharadwaj, B. Li, H. Yu, *Dev. Cell* **1**, 227 (2001).
11. G. Fang, *Mol. Biol. Cell* **13**, 755 (2002).
12. V. Sudakin, G. K. Chan, T. J. Yen, *J. Cell Biol.* **154**, 925 (2001).
13. M. Kallio, J. Weinstein, J. R. Daum, D. J. Burke, G. J. Gorbsky, *J. Cell Biol.* **141**, 1393 (1998).
14. K. Wassmann, R. Benezra, *Proc. Natl. Acad. Sci. U.S.A.* **95**, 11193 (1998).
15. C. J. Morrow *et al.*, *J. Cell Sci.* **118**, 3639 (2005).
16. I. Braunstein, S. Miniowitz, Y. Moshe, A. Hershko, *Proc. Natl. Acad. Sci. U.S.A.* **104**, 4870 (2007).
17. J. L. Burton, M. J. Solomon, *Genes Dev.* **21**, 655 (2007).
18. M. Sczaniecka *et al.*, *J. Biol. Chem.* **283**, 23039 (2008).
19. X. Luo, Z. Tang, J. Rizo, H. Yu, *Mol. Cell* **9**, 59 (2002).
20. L. Sironi *et al.*, *EMBO J.* **21**, 2496 (2002).
21. S. Hauf *et al.*, *J. Cell Biol.* **161**, 281 (2003).
22. M. J. Hayes *et al.*, *Nat. Cell Biol.* **8**, 607 (2006).
23. R. Wolthuis *et al.*, *Mol. Cell* **30**, 290 (2008).
24. Materials and methods are available as supporting material on *Science* Online.
25. P. Dube *et al.*, *Mol. Cell* **20**, 867 (2005).
26. M. D. Ohi *et al.*, *Mol. Cell* **28**, 871 (2007).
27. H. Yamano, J. Gannon, H. Mahbubani, T. Hunt, *Mol. Cell* **13**, 137 (2004).
28. J. L. Burton, V. Tsakraklides, M. J. Solomon, *Mol. Cell* **18**, 533 (2005).
29. C. Kraft, H. C. Vodermaier, S. Maurer-Stroh, F. Eisenhaber, J. M. Peters, *Mol. Cell* **18**, 543 (2005).
30. We are grateful to M. Madalinski, M. Gmachl, and G. Kohlmaier for reagents; J. Deckert and R. Lührmann for support; and S. Westermann for comments on the manuscript. Research in the laboratory of H.S. was supported by grants from the Federal Ministry of Education and Research, Germany, and the Sixth Framework Programme of the European Union via the Integrated Project 3DRepertoire. Research in the laboratories of J.-M.P. and K.M. were supported by Boehringer Ingelheim, the Vienna Spots of Excellence Programme, and the Austrian Science Fund. The structural coordinates have been deposited in the Electron Microscopy Data Bank Database at the European Molecular Biology Laboratory–European Bioinformatics Institute. The structures of APC/C$^{\text{MCC}}$ and apo-APC/C can be accessed under the codes EMD-1591 and EMD-1592, respectively.

Supporting Online Material
www.sciencemag.org/cgi/content/full/323/5920/1477/DC1
Materials and Methods
Figs. S1 to S11
Tables S1 and S2
References
3D PDFs S1 and S2
Movie S1

15 July 2008; accepted 29 January 2009
10.1126/science.1163300

A Functional Genomics Approach Reveals CHE as a Component of the *Arabidopsis* Circadian Clock

Jose L. Pruneda-Paz, Ghislain Breton, Alessia Para, Steve A. Kay*

Transcriptional feedback loops constitute the molecular circuitry of the plant circadian clock. In *Arabidopsis*, a core loop is established between CCA1 and TOC1. Although CCA1 directly represses *TOC1*, the TOC1 protein has no DNA binding domains, which suggests that it cannot directly regulate *CCA1*. We established a functional genomic strategy that led to the identification of CHE, a TCP transcription factor that binds specifically to the *CCA1* promoter. CHE is a clock component partially redundant with LHY in the repression of *CCA1*. The expression of *CHE* is regulated by CCA1, thus adding a CCA1/CHE feedback loop to the *Arabidopsis* circadian network. Because CHE and TOC1 interact, and CHE binds to the *CCA1* promoter, a molecular linkage between TOC1 and *CCA1* gene regulation is established.

The circadian system provides an adaptive advantage by allowing the anticipation of daily changes in the environment (*1*, *2*). For example, in plants, the resonance between the internal timekeeper and environmental cues enhances their fitness and survival (*3*, *4*).

Circadian networks are composed of multiple positive and negative factors organized in interlocked autoregulatory loops (*1*, *2*). In *Arabidopsis thaliana*, the molecular wiring of these regulatory circuits is mainly based on transcriptional feedback loops (*5*, *6*). The core clock stems from the reciprocal regulation between the evening-phased pseudoresponse regulator TIMING OF CAB EXPRESSION 1 (TOC1) and the two morning-expressed MYB transcription factors CIRCADIAN CLOCK ASSOCIATED 1 (CCA1) and LATE ELONGATED HYPOCOTYL (LHY) (*7*). CCA1 and LHY are DNA binding proteins that repress *TOC1* expression through direct binding to its promoter region (*7*, *8*). In contrast, no functional domains have been recognized in the TOC1 protein (*9*), and direct regulators of *CCA1* or *LHY* expression have never been identified (*5*, *6*, *10*).

Functional redundancies among gene families provide barriers to identifying clock-related transcription factors by classic forward genetic screens. Thus, to uncover direct regulators of *CCA1/LHY*, we implemented an alternative genomics approach in which the yeast one-hybrid system was used to screen a collection of transcription factors for their binding to the *CCA1/LHY* regulatory regions (fig. S1). The high-throughput design of this strategy allowed us to test several tiled fragments for each promoter, thus minimizing the negative effect that the distance from the cis elements to the TATA box has over transcriptional activation in yeast (*11*). We termed this approach "promoter hiking." Because most clock components identified to date exhibit a circadian pattern of mRNA expression, we created a comprehensive library of circadian-regulated transcription factors (table S1) (*12*). We identified a transcription factor that belongs to the class I TCP (TB1, CYC, PCFs) family (*13*) (*Arabidopsis* Genome Initiative locus identifier At5g08330), hereafter referred to as CCA1 HIKING EXPEDITION (CHE). CHE specifically binds to the *CCA1* promoter fragment encompassing nucleotides (nt) –363 to –192 (Fig. 1A) but not to any of the *LHY* promoter fragments tested (Fig. 1B and fig. S2). Consistent with this result, a motif present in the promoter fragment bound matches the consensus class I TCP-binding site (TBS) (GGNCCCAC) (*14*). The binding of CHE to the TBS in the *CCA1* promoter (GGTCCCAC) was confirmed by electrophoretic mobility shift assays (EMSAs) (Fig. 1C) and was further corroborated by the yeast one-hybrid system with a synthetic TBS trimer (fig. S2).

To address whether CHE regulates *CCA1* in vivo, we performed assays in *Arabidopsis* protoplasts in which the *CCA1* promoter activity was monitored with a CCA1::LUC+ reporter construct. The overexpression of CHE when a 35*S*::CHE effector construct was used caused a reduction of the luciferase activity, suggesting that CHE functions as a repressor of *CCA1* (fig. S3). This possibility is consistent with the observation that *CHE* mRNA levels oscillate 9 hours out of phase with the *CCA1* transcript (Fig. 1D). Moreover, we demonstrated that CHE protein accumulates in the nuclei (Fig. 1, E and F) and that both CHE and CCA1 exhibit a similarly broad tissue expression pattern (Fig. 1, G and H). If CHE act as a repressor through binding to the TBS, mutations in this motif should result in increased *CCA1* promoter activity. This hypothesis was confirmed by using promoter::LUC+ fusions (Fig. 1I and fig. S4), indicating that the TBS mediates a repressor function. Altogether, these results support the notion that CHE directly represses *CCA1* promoter activity in a TBS-

---

Section of Cell and Developmental Biology, Division of Biological Sciences, University of California San Diego, La Jolla, CA 92093, USA.

*To whom correspondence should be addressed. E-mail: skay@ucsd.edu

specific manner. To investigate this interaction in vivo, transgenic seedlings overexpressing green fluorescent protein (GFP)–tagged CHE (fig. S5, A and B) were used to perform chromatin immunoprecipitations (ChIPs). This assay revealed a CHE-specific enrichment of *CCA1* promoter fragments containing the TBS (Fig. 1J and fig. S5C), indicating that CHE binds to the *CCA1* promoter in vivo.

The proper regulation of *CCA1* is required to maintain normal clock function (*15*, *16*), thus we hypothesized that any factor modulating *CCA1* expression may be part of the *Arabidopsis* circadian network. To analyze whether CHE has a role in the *Arabidopsis* oscillator, we overexpressed CHE in transgenic plants carrying a CCA1::LUC+ reporter construct (fig. S6A). Consistent with its role as a repressor, elevated levels of *CHE* result in an overall reduction of the *CCA1* promoter activity (Fig. 2A). The luciferase levels oscillate with a period close to 24 hours (fig. S6B), but the peak of expression exhibits a phase advance (Fig. 2, A and B), suggesting that the constitutive expression of *CHE* leads to an earlier repression of *CCA1* at the beginning of the subjective day.

To further characterize the role of CHE in the *Arabidopsis* clock, we isolated two independent transferred DNA (T-DNA) insertion lines with reduced *CHE* expression levels, named *che-1* and *che-2* (fig. S7, A and B). These mutant seedlings were crossed to the CCA1::LUC+ reporter background, and the resulting lines were used to evaluate the clock function under constant light conditions. Consistent with the function of CHE as a transcriptional repressor, both T-DNA insertion lines displayed an overall increase in *CCA1* promoter activity (Fig. 2C). However, no significant change in the period length or phase of the luciferase expression was observed (Fig. 2C and fig. S7C), suggesting the presence of redundant repressor activities that may counteract the effect of reduced *CHE* expression on the clock function. The *Arabidopsis* genome encodes 12 other TCP transcription factor genes that contain a DNA binding domain similar to CHE (fig. S8, A and B), suggesting that they could also bind to the TBS. To test whether this motif is targeted by repressor activities other than the one caused by CHE (potentially another TCP), we transformed *che* mutant seedlings with CCA1::LUC+ constructs and compared the promoter activities in the presence or absence of a functional TBS. In this condition, similar luciferase levels were obtained with the native or mutant promoter constructs (Fig. 2D and fig. S9, A to C), indicating that *CCA1* promoter activity is affected in a similar fashion by mutations in the TBS or by the reduction of *CHE* expression levels. This result suggests that CHE is the main repressor acting through the TBS. Therefore, the repressor activity redundant with CHE, if any, should occur through binding to other *CCA1* promoter motifs. LHY inhibits *CCA1* expression (*17*), probably through direct binding to a CCA1-binding site (*18*) (AGATTTTT) located 479 nt upstream of the TBS. Hence, we reasoned that the repressor effects of LHY and CHE could be redundant. Consistent with this hypothesis, the pace of the clock in *che/lhy* double mutant lines exhibited a significantly shorter period length as compared to that in the *lhy* single mutant (Fig. 2E), suggesting that LHY is at least partially redundant with CHE or that it regulates the expression of a CHE redundant factor. We conclude that CHE functions within the *Arabidopsis* circadian system as a repressor of *CCA1*.

Reciprocal feedback loops are a common feature in clock regulatory networks (*2*). Analysis of the *CHE* promoter sequence revealed a CCA1-binding site located between nt –956 and –949 (AAAAATCT), suggesting that CCA1 and LHY could reciprocally modulate *CHE* expression. In fact, although the expression of *CHE* oscillated in wild-type seedlings, it was constant-

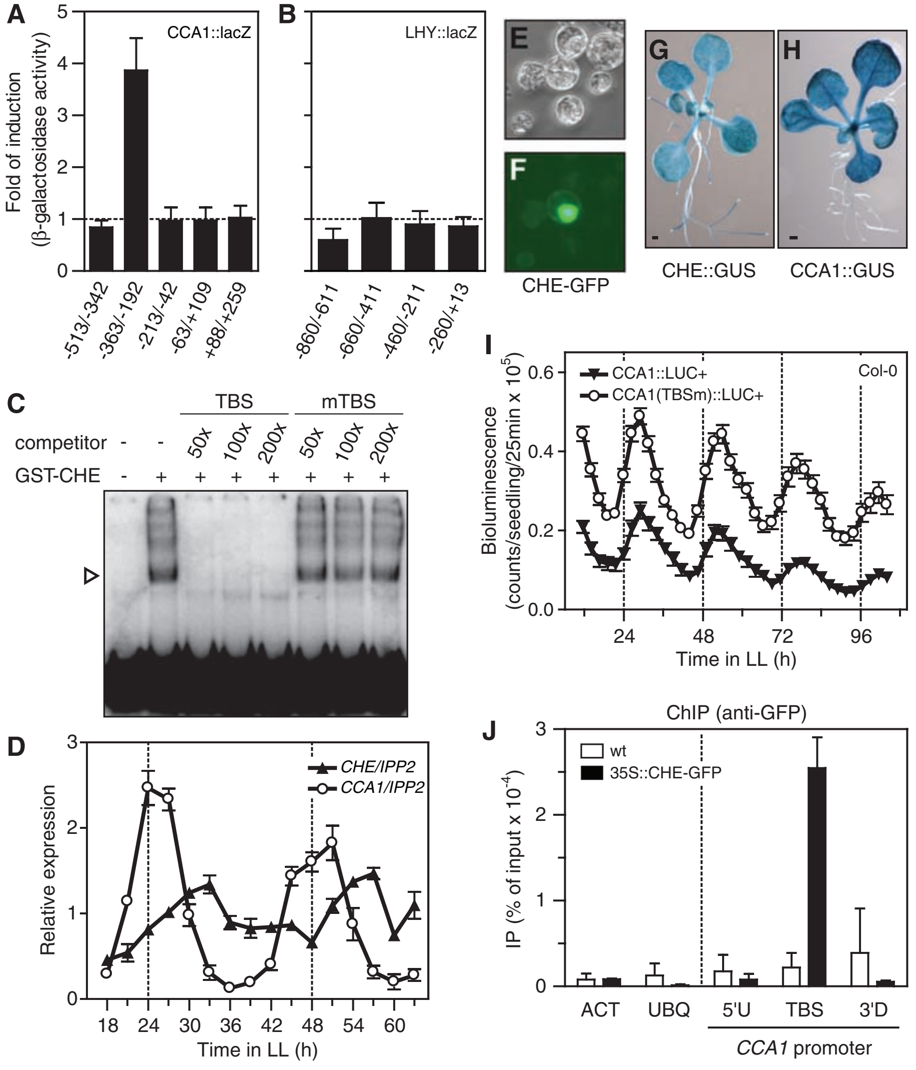

Fig. 1. CHE is a *CCA1* promoter–binding protein. (**A** and **B**) Interaction of CHE with different regions of *CCA1* (A) and *LHY* (B) promoters in yeast. Bars represent the fold of induction in β-galactosidase activity for each of the DNA fragments indicated ($n = 6$). (**C**) Binding of CHE to the TBS in the *CCA1* promoter determined by EMSA. The DNA/CHE complex (indicated by the arrowhead) was competed with unlabeled wild-type (TBS) or mutant (TBSm) probes. (**D**) *CHE* and *CCA1* expression in Col-0 wild-type seedlings growing under constant light (LL; h, hours). mRNA levels were normalized to *IPP2* expression ($n = 3$ independent experiments). (**E** and **F**) Subcellular localization of CHE in *Arabidopsis* protoplasts [(E), visible light; (F), GFP channel]. (**G** and **H**). CHE and CCA1 expression patterns determined by histochemical staining for GUS activity in CHE::GUS (G) and CCA1::GUS (H) transgenic seedlings. Scale bars, 0.5 mm. (**I**) Effect of mutations within the TBS on *CCA1* promoter activity. Promoter::luciferase constructs [CCA1::LUC+ and CCA1(TBSm)::LUC+] were transformed into Col-0 seedlings. Luciferase activity was determined in first-generation transgenic seedlings (T1) ($n = 27$). (**J**) Binding of CHE to the *CCA1* promoter in vivo. ChIP assays (IP) were performed with 35*S*::CHE-GFP or wild-type CCA1::LUC+ (wt) seedlings. Immunoprecipitated DNA was quantified by real-time polymerase chain reaction (PCR) with primers specific for the TBS in the *CCA1* promoter (TBS), and for control regions (5′U, 3′D, ACT, and UBQ) (*12*). Results were normalized to the input DNA ($n = 4$ independent experiments). Values represent means ± SEM in (A), (B), (D), (I), and (J).

ly elevated at peak levels in a *cca1/lhy* double mutant background (Fig. 3A). Moreover, EMSAs indicate that CCA1 and LHY specifically bind to the CCA1-binding site in the CHE promoter (Fig. 3B and fig. S10). These results support the notion that CCA1 and LHY repress *CHE* expression through direct binding to the CCA1-binding site of the *CHE* promoter. The binding of CCA1 to the *CHE* promoter was further confirmed in vivo by ChIP assays with transgenic seedlings expressing GFP-tagged CCA1 (Fig. 3C and fig. S11). The mutual regulation observed between CCA1 and CHE establishes a transcriptional feedback module within the *Arabidopsis* core clock network.

The molecular basis of the regulation of *CCA1/LHY* expression by TOC1 remains unclear. The mechanism appears to be more complex than originally thought, due to the facts that there is a lack of DNA binding domains in TOC1 protein (*9*) and that either reduced or elevated TOC1 levels lead to low *CCA1/LHY* mRNA expression (*7*, *19*). It has been proposed that TOC1 could regulate the expression or protein turnover of a direct regulator of *CCA1/LHY*, or that TOC1 could regulate transcription by interacting with a transcription factor specific for *CCA1/LHY* promoters. Therefore, the discovery of CHE as a direct regulator of *CCA1* provides the opportunity to investigate whether CHE is part of the mechanism by which TOC1 regulates the expression of *CCA1*. There is a spatiotemporal coincidence in the expression of CHE and TOC1. Both proteins are nuclear-localized [Fig. 1F and (*9*)], and their expression is broadly distributed in *Arabidopsis* seedlings [Fig. 1G and (*20*)], reaching maximum levels at similar times of the day [zeitgeber time (ZT) 9 and ZT13, respectively] [Fig. 1D and (*9*)]. Consistently, when using the yeast two-hybrid system, we observed a direct protein-protein interaction between TOC1 and the N-terminal domain of CHE (Fig. 4A). To confirm this interaction in vivo, we performed coimmunoprecipitations using CHE- and TOC1-tagged proteins transiently coexpressed in *Nicotiana benthamiana* leaves. In these experiments, TOC1 was detected only in the samples where CHE had been immunoprecipitated (Fig. 4B), indicating that CHE and TOC1 directly interact in planta and therefore that CHE may recruit TOC1 to the *CCA1* promoter.

To test whether TOC1 binds in vivo to the *CCA1* promoter region encompassing the TBS, seedlings expressing a yellow fluorescent protein (YFP)–tagged TOC1 under the regulation of its endogenous promoter were used to perform ChIP experiments. Analysis of the DNA recovered after immunoprecipitation revealed a specific enrichment in *CCA1* promoter fragments containing the TBS (Fig. 4C and fig. S12), indicating that TOC1 is linked to the *CCA1* promoter in vivo. A direct interaction of TOC1 with the *CCA1* promoter was investigated by EMSAs and the yeast one-hybrid system, but no binding was detected with these approaches, suggesting that TOC1 is unable to bind directly to the *CCA1* promoter. Thus, TOC1 could be recruited to the *CCA1* promoter through the interaction with CHE or with other *CCA1* promoter–binding proteins bound to cis elements close to the TBS. Alternatively, a specific posttranslational modification or cofactor could be required for TOC1 to bind directly to the DNA.

The pace of the clock is particularly sensitive to changes in TOC1 activity or concentration, but the period varies only in correlation with TOC1 dosage when TOC1 expression is above endogenous levels (*21*). Therefore, we reasoned that a sensitized background where TOC1 levels are moderately elevated would be the best scenario in which to explore whether there is a functional interaction between TOC1 and CHE. The overexpression of *CHE* in this context resulted in a significant shortening of the period as compared to that in the parental line (Fig. 4D and fig. S13). These results indicate that the interaction between CHE and TOC1 exerts a biologically meaningful and opposite effect over the control of the period length in vivo. Thus, CHE may not merely recruit TOC1 to the *CCA1* promoter but seems antagonistic to TOC1 function as well. For example, high levels of CHE could sequester TOC1 and interfere with its interaction with other transcription factors bound to the *CCA1* promoter.

We have applied a yeast one-hybrid genomic strategy toward the discovery and molecular characterization of CHE, which is a component of the *Arabidopsis* clock that negatively regulates *CCA1* expression. *CHE* and *CCA1* exhibit a reciprocal regulation, which uncovers a feedback loop at the core of the *Arabidopsis* circadian network. Our data indicate that CHE directly interacts with TOC1 and that both proteins are associated with the same region of

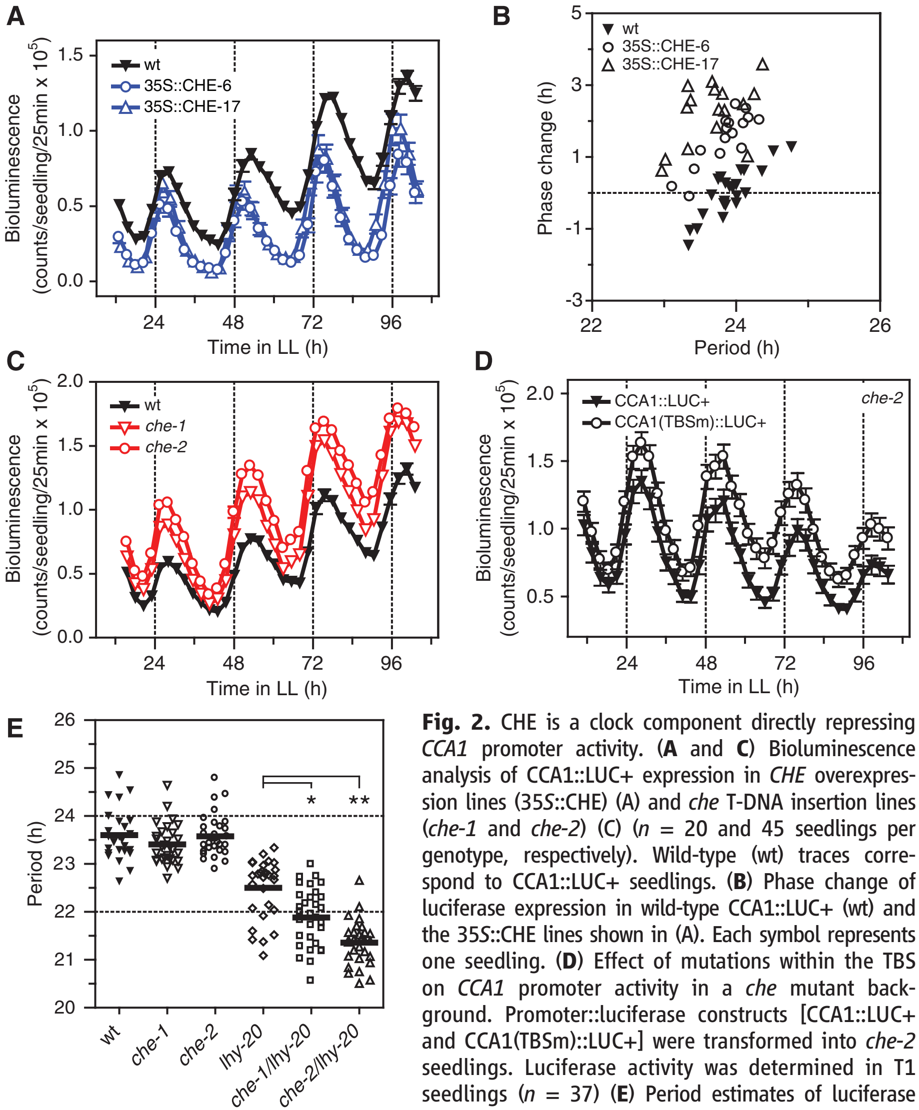

Fig. 2. CHE is a clock component directly repressing *CCA1* promoter activity. (**A** and **C**) Bioluminescence analysis of CCA1::LUC+ expression in *CHE* overexpression lines (35*S*::CHE) (A) and *che* T-DNA insertion lines (*che-1* and *che-2*) (C) (n = 20 and 45 seedlings per genotype, respectively). Wild-type (wt) traces correspond to CCA1::LUC+ seedlings. (**B**) Phase change of luciferase expression in wild-type CCA1::LUC+ (wt) and the 35*S*::CHE lines shown in (A). Each symbol represents one seedling. (**D**) Effect of mutations within the TBS on *CCA1* promoter activity in a *che* mutant background. Promoter::luciferase constructs [CCA1::LUC+ and CCA1(TBSm)::LUC+] were transformed into *che-2* seedlings. Luciferase activity was determined in T1 seedlings (n = 37) (**E**) Period estimates of luciferase expression in wild-type CCA1::LUC+ (wt), *che*, and *lhy* T-DNA insertion lines (*che-1*, *che-2*, and *lhy-20*), and *che/lhy* double mutants (*che-1/lhy-20* and *che-2/lhy-20*). Each symbol represents one seedling, and the line is the average period value (*$P <$ 0.0005, **$P <$ 0.0001). Values represent means ± SEM in (A), (C), and (D).

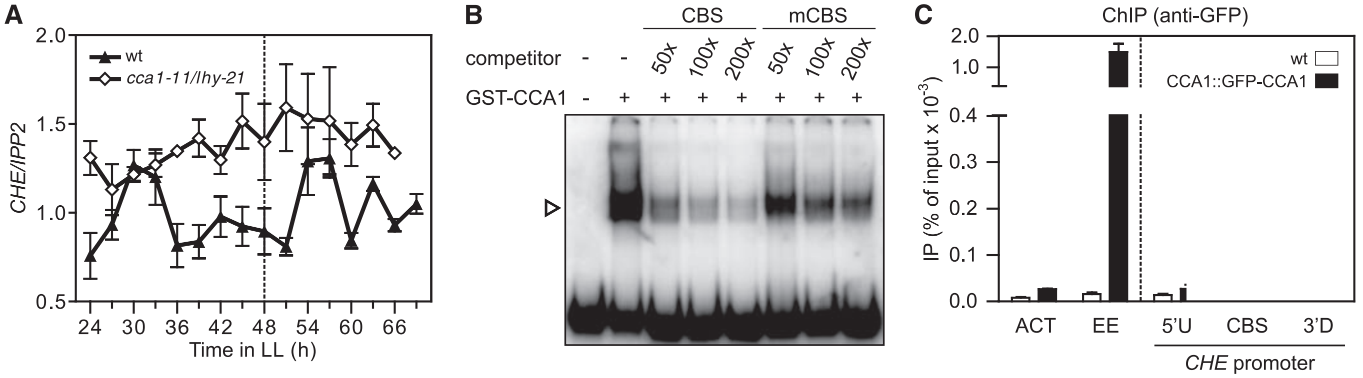

Fig. 3. *CHE* expression is regulated by CCA1 and LHY. (**A**) Expression of *CHE* in wild-type Ws (wt) and *cca1-11/lhy-21* double mutant seedlings growing in constant light (LL). mRNA levels were normalized to the expression of *IPP2* (*CHE/IPP2*). (**B**) Binding of CCA1 to the CCA1-binding site in the *CHE* promoter determined by EMSA. The DNA/CCA1 complex (indicated by the arrowhead) was competed with unlabeled wild-type (CBS) or mutant (mCBS) probes. (**C**) Binding of CCA1 to the *CHE* promoter in vivo. ChIP assays were performed with CCA1::GFP-CCA1 or wild-type Ws (wt) seedlings. Immunoprecipitated DNA was quantified by real-time PCR with primers specific for the CCA1-binding site in the *CHE* promoter (CBS) and for control regions (ACT, EE, 5′U, and 3′D) (*12*). Results were normalized to the input DNA. Values represent means ± SEM (*n* = 3 independent experiments) in (A) and (C).

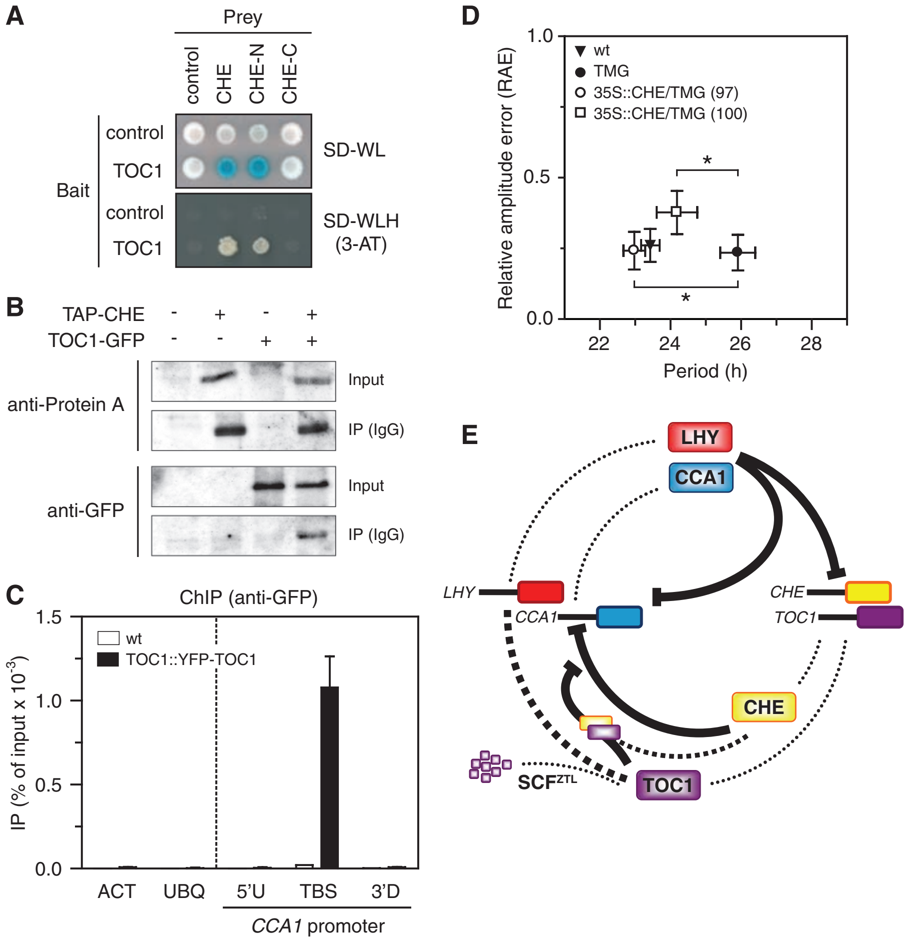

Fig. 4. CHE interacts with TOC1. (**A**) Interaction between CHE and TOC1 proteins in yeast. SD-WL medium was used for the selection of bait and prey proteins, and a β-galactosidase overlay assay was performed to visualize the interaction. SD-WLH (3-AT) medium was used for the auxotrophic selection of bait and prey protein interactions. (**B**) Coimmunoprecipitation assay between TOC1 (GFP-TOC1) and CHE (TAP-CHE) expressed in tobacco leaves. The results are representative of four independent experiments. (**C**) Binding of TOC1 to the *CCA1* promoter in vivo. ChIP assays were performed with TOC1::YFP-TOC1 or wild-type CAB2::LUC (wt) seedlings. DNA was quantified by real-time PCR with primers specific for the TBS in the *CCA1* promoter and for control regions (5′U, 3′D, ACT, and UBQ) (*12*). Results were normalized to the input DNA. Values represent means ± SEM (*n* = 4 independent experiments). (**D**) Genetic interaction between CHE and TOC1. CHE was overexpressed in the TOC1::YFP-TOC1 (TMG) background (35*S*::CHE/TMG). Period and relative amplitude error estimates of CAB2::LUC (wt) expression were determined in T3 seedlings (*$P < 0.0001$). Values represent means ± SD (*n* = 20 seedlings per genotype). (**E**) Model for the proposed role of CHE in the *Arabidopsis* clock. At dawn, high levels of CCA1 and LHY repress *CHE* and their own expression. CHE levels rise as the day progresses to maintain *CCA1* at a minimum. By the end of the day, TOC1 antagonizes CHE, resetting the cycle. SCF^{ZTL}, ZEITLUPE-mediated proteasomal degradation.

the *CCA1* promoter, establishing a molecular link between TOC1 protein levels and *CCA1* expression (Fig. 4E). The promoter hiking strategy, as presented here, is limited by the use of a circadian-regulated transcription factor library. Although for our purposes this was an effective enrichment, the collection screened represents only about 10% of all the transcription factors encountered in *Arabidopsis*, suggesting that additional regulators of *CCA1* are yet to be discovered.

References and Notes

1. D. Bell-Pedersen *et al.*, *Nat. Rev. Genet.* **6**, 544 (2005).
2. H. Wijnen, M. W. Young, *Annu. Rev. Genet.* **40**, 409 (2006).
3. A. N. Dodd *et al.*, *Science* **309**, 630 (2005).
4. R. M. Green, S. Tingay, Z. Y. Wang, E. M. Tobin, *Plant Physiol.* **129**, 576 (2002).
5. M. J. Gardner, K. E. Hubbard, C. T. Hotta, A. N. Dodd, A. A. Webb, *Biochem. J.* **397**, 15 (2006).
6. C. R. McClung, *Plant Cell* **18**, 792 (2006).
7. D. Alabadi *et al.*, *Science* **293**, 880 (2001).
8. M. Perales, P. Mas, *Plant Cell* **19**, 2111 (2007).
9. C. Strayer *et al.*, *Science* **289**, 768 (2000).
10. A. Baudry, S. Kay, *Adv. Bot. Res.* **48**, 69 (2008).
11. K. C. Dobi, F. Winston, *Mol. Cell. Biol.* **27**, 5575 (2007).
12. Materials and methods are available as supporting material on *Science* Online.

13. P. Cubas, N. Lauter, J. Doebley, E. Coen, *Plant J.* **18**, 215 (1999).
14. S. Kosugi, Y. Ohashi, *Plant J.* **30**, 337 (2002).
15. R. M. Green, E. M. Tobin, *Proc. Natl. Acad. Sci. U.S.A.* **96**, 4176 (1999).
16. Z. Y. Wang, E. M. Tobin, *Cell* **93**, 1207 (1998).
17. R. Schaffer *et al.*, *Cell* **93**, 1219 (1998).
18. Z. Y. Wang *et al.*, *Plant Cell* **9**, 491 (1997).
19. S. Makino, A. Matsushika, M. Kojima, T. Yamashino, T. Mizuno, *Plant Cell Physiol.* **43**, 58 (2002).
20. A. Para *et al.*, *Plant Cell* **19**, 3462 (2007).
21. P. Mas, D. Alabadi, M. J. Yanovsky, T. Oyama, S. A. Kay, *Plant Cell* **15**, 223 (2003).
22. We thank T. Imaizumi, E. Hamilton, E. Farre, B. Chow, D. A. Nusinow, and M. Sawa for critical reading of the manuscript; K. Yamada for providing the YM187 yeast strain; Y. Zhao for microscopy assistance; and A. Schopke, R. Sawaya, and S. Asbaghi for technical assistance. This work was supported by NIH grants GM56006 and GM67837 to S.A.K. and partially by postdoctoral fellowships from Fundacion Antorchas to J.L.P.-P., the National Sciences and Engineering Research Council of Canada to G.B., and Wenner-Gren Stiftelserna to A.P.

Supporting Online Material
www.sciencemag.org/cgi/content/full/323/5920/1481/DC1
Materials and Methods
Figs. S1 to S13
Table S1
References

14 October 2008; accepted 7 January 2009
10.1126/science.1167206

Paternal Control of Embryonic Patterning in *Arabidopsis thaliana*

Martin Bayer,[1]* Tal Nawy,[1]† Carmela Giglione,[2] Mary Galli,[1]‡ Thierry Meinnel,[2] Wolfgang Lukowitz[1,3]§

The *YODA* (*YDA*) mitogen-activated protein kinase pathway promotes elongation of the *Arabidopsis* zygote and development of its basal daughter cell into the extra-embryonic suspensor. Here, we show that the interleukin-1 receptor–associated kinase (IRAK)/Pelle-like kinase gene *SHORT SUSPENSOR* (*SSP*) regulates this pathway through a previously unknown parent-of-origin effect. *SSP* transcripts are produced in mature pollen but do not appear to be translated. Instead, they are delivered via the sperm cells to the zygote and the endosperm, where SSP protein transiently accumulates. Ectopic expression of SSP protein in the leaf epidermis is sufficient to activate *YDA*-dependent signaling. We propose that SSP protein produced from paternal transcripts upon fertilization triggers zygotic *YDA* activity, providing an essential temporal cue for the regulation of the asymmetric first division.

Multicellular organisms rely on robust spatial and temporal coordinates to guide embryonic development. Little is known about the cues used by plants to derive such a framework. Growth of plant zygotes is typically polar, and their division asymmetric (*1*). In *Arabidopsis*, the zygote elongates about threefold (Fig. 1A) before dividing into a small apical cell, the founder of the spherical proembryo, and a large basal cell, the founder of a filamentous, largely extra-embryonic support structure called the suspensor (Fig. 1E). This fundamental fate decision is regulated by *YODA* (*YDA*)-dependent signaling. Loss of the mitogen-activated protein kinase kinase (MAPKK) kinase *YDA* (*2*) or the MAP kinases *MPK3* and *MPK6* (*3*) suppress elongation of the zygote (Fig. 1B) and suspensor formation. Hyperactive variants of *YDA* promote extensive elongation of the zygote and exaggerated suspensor growth (*2*). Here, we report that the interleukin-1 receptor–associated kinase (IRAK)/Pelle-like kinase gene *SHORT SUSPENSOR* (*SSP*) links activation of the *YDA* MAP kinase cascade to fertilization through a unique parent-of-origin effect and propose a mechanistic basis for our finding.

Mutations in the *SSP* gene have no discernible impact on adults but closely mimic the effect of *yda* mutations on embryogenesis (*2*). Mutant zygotes fail to elongate and generate basal cells of diminished size (Fig. 1C) (23 ± 5 µm, compared with 61 ± 7 µm for wild type). Reduced growth and aberrant divisions in the basal cell lineage subsequently result in a spectrum of defects, ranging from the absence of a recognizable suspensor (Fig. 1F) to cone-shaped suspensors with multiple cell layers (Fig. 1G) and rudimentary or short suspensors (Fig. 1, H and I). These phenotypes imply that *SSP* promotes extra-embryonic or suspensor fates. In support of this view, expression of a molecular marker for the suspensor (*4*) is not detected in *ssp* mutants (Fig. 1K).

Genetic analysis suggests that *SSP* acts upstream of the *YDA* MAP kinase cascade in a common pathway. Double mutant *ssp-1 yda-1* embryos are anatomically indistinguishable from *yda-1* single mutants (table S1), arguing against an independent function of the two genes. Hyperactive variants of the *YDA* MAPKK kinase reverse the suspensor phenotype caused by *ssp* mutations (table S1), suggesting that *SSP* participates in activating the *YDA* MAP kinase cascade.

Map-based cloning (*5*) revealed that *SSP* corresponds to At2g17090, a member of the RLCK II family of IRAK/Pelle-like kinases [also known as receptor-like kinases (*6*)]. Four mutations, including a premature stop (*ssp-1*) and an RNA null (*ssp-2*), generate essentially indistinguishable mutant phenotypes, which are complemented by the introduction of a 9.8–kilobase pair genomic DNA fragment spanning the locus (316 normal embryos in 580 total) (*7*). Three motifs can be identified in the predicted SSP protein (Fig. 2A): an N-terminal consensus for myristoylation and palmitoylation, a central protein kinase domain of the Pelle/IRAK superfamily, and a C-terminal tetratricopeptide repeat (TPR). Insertion of a yellow fluorescent protein (YFP) moiety on either side of the kinase domain does not impair SSP function (Fig. 2A).

N-myristoylation at Gly^2 and subsequent S-palmitoylation at neighboring cysteines are predicted to mediate stable plasma membrane association (*8*). Consistent with this prediction, cells overexpressing YFP-tagged SSP variants show robust fluorescence at their surface (Fig. 2B). A point mutation abolishing both N-myristoylation and S-palmitoylation [G2→A2 (G2A) (*9*)] renders the mutant protein cytoplasmic (Fig. 2C) and unable to complement *ssp* mutants ($n = 479$ embryos). Eliminating only palmitoylation [C3→S3 and C4→S4 (C3,4S) (*9*)] has a similar effect ($n = 450$ embryos). Peptides representing the N terminus of wild-type SSP or the C3,4S mutant are efficiently modified by *Arabidopsis* N-myristoyl transferase NMT1 in vitro (*10*), whereas a peptide representing the G2A mutant is not (Fig. 2D). We conclude that diacylation-mediated membrane association is essential for *SSP* function.

In contrast, protein kinase catalytic activity may be dispensable. Alternative splicing of intron 2 generates a short *SSP* transcript harboring an 18–amino acid in-frame deletion in the kinase domain (Fig. 2A). This cDNA does not complement the phenotype of *ssp* mutants when expressed from the endogenous promoter ($n = 311$ embryos), whereas the long cDNA species does (218 normal embryos in 449 total), suggesting that gross structural changes in the kinase domain are not tolerated. However, key residues of the active site, most conspicuously the aspartate of the canonical DFG (*9*) motif involved in Mg^{++} binding and phospho-transfer, are not found in SSP. Moreover, a transition-state mutant predicted to reduce catalytic activity to negligible rates while leaving substrate binding unaffected (*11*) fully complements the phenotype of *ssp* mutants (Fig. 2A) [K78R (*9*); 211 normal embryos in 442 total]. Although we cannot rule out that SSP uses a noncanonical reaction mechanism

---

[1] Cold Spring Harbor Laboratory, Cold Spring Harbor, NY 11724, USA. [2] Institut des Sciences du Végétal, Centre National de la Recherche Scientifique, 91198 Gif-sur-Yvette, cedex, France. [3] Department of Plant Biology, University of Georgia, Athens, GA 30602, USA.

*Present address: Institute of Plant Biology, University of Zürich, 8008 Zürich, Switzerland.

†Present address: Biology Department, New York University, NY 10003, USA.

‡Present address: The Salk Institute, San Diego, CA 92186, USA.

§To whom correspondence should be addressed. E-mail: lukowitz@uga.edu

(*12*), the primary role of the kinase domain may lie in protein binding. Mammalian IRAK proteins often lack kinase activity but rather contribute to the assembly of receptor complexes (*13*). Similarly, a number of plant IRAK/Pelle kinases does not require catalytic activity for function (*14*).

The importance of protein-protein interactions is further implied by similarity of the SSP C terminus to TPR domains (Fig. 2A) (cluster KOG0548) mediating the association of heat shock protein 70 (HSP70) co-chaperone complexes (*15*). Deletion of the entire TPR motif or only the third, cryptic repeat unit completely inactivates the protein (Fig. 2A) [for mutant Y300Z, *n* = 408 embryos; for W431Z, *n* = 433 embryos (*9*)]. These results argue that SSP acts as an adaptor at the plasma membrane, possibly recruiting a pathway activator.

In the course of our analysis, it became clear that *ssp* mutations result in atypical segregation of normal and mutant phenotypes. Self-fertilized *ssp* plants hemizygous for a functional transgene generate normal and mutant embryos in a ratio of 1:1. The same 1:1 distribution is also seen in the progeny of self-fertilized *ssp-1*/+ or *ssp-2*/+ plants (94 normal embryos in 194 total and 204 in 394, respectively). Our mapping data indicate that transmission of the *ssp-1* allele through the haploid generation is not substantially distorted (*5*), pointing to a parent-of-origin effect as a likely cause for this phenomenon. Reciprocal crosses indeed demonstrate that the phenotype of the embryo is strictly dependent on the genotype of the pollen. When homozygous *ssp* plants were crossed with wild-type pollen, all embryos developed normally (*ssp-1 n* = 104 and *ssp-2 n* = 185). Conversely, all embryos resulting from a cross of wild-type plants with pollen from homozygous *ssp* plants developed abnormally (*ssp-1 n* = 121 and *ssp-2 n* = 185). We conclude that *SSP* exerts a male gametophytic, or paternal, effect on embryonic patterning (*16*).

Parent-of-origin effects in plants and mammals often arise from imprinting (*17*), in large part mediated by differential DNA methylation (*18*). However, *SSP* function is not sensitive to global changes in DNA methylation (*5*), arguing against epigenetic control. Alternatively, a paternal effect may arise from pollen-specific expression. A reverse transcription polymerase chain reaction (RT-PCR) indicates that *SSP* mRNA accumulates to readily detectable amounts only in mature pollen (fig. S1A). *Arabidopsis* pollen consists of a large vegetative cell that completely encloses two small sperm cells. In situ hybridization of germinated pollen reveals robust signals associated with the sperm (Fig. 3A). In support of this result, microarray profiling of isolated sperm identified *SSP* as 1 of 74 genes preferentially expressed in this cell type (*19*).

Surprisingly, the accumulation of SSP protein, determined by using functional YFP-tagged variants, does not coincide with RNA production. No YFP fluorescence is apparent in germinated pollen (fig. S1, C and D). SSP protein became detectable only upon fertilization, when weak fluorescence of the zygote was observed (Fig. 3D). This signal was transient and no longer seen by the time of the first division. Reciprocal crosses confirmed the absence of a specific signal in zygotes produced by nontransgenic pollen. A fluorescent reporter, consisting of the *SSP* upstream region fused at the translational start site to a nuclear-localized triple YFP, corroborates these results. Again, no YFP fluorescence is apparent in pollen, although *YFP* transcripts are present (fig. S1B). When this construct was crossed via the pollen, a transient fluorescent signal appeared in the nuclei of the zygote and the micropylar endosperm (Fig. 3E).

Our findings suggest a simple mechanistic basis for the paternal effect: *SSP* transcripts are produced but not translated in the sperm cells; rather, they are delivered to the seed, where they become translated and cause transient accumulation of SSP protein in both products of double fertilization, the zygote and central cell. In support of this view, in situ hybridization reveals weak signals in the zygote and the micropylar endosperm (fig. S2). The presence and origin of *SSP* transcripts after fertilization was independently confirmed in RNA samples prepared from about 2000 immature seed dissected 24 hours after pollination of *Ws* plants with *Col* pollen (*5*). RT-PCR from this material detected only RNA transcribed from the paternal *Col* allele (Fig. 3C).

We next sought to clarify whether SSP has a role in the endosperm by examining *fie* seed generated by *fie*; *cdc2a* pollen (*5*). In this genetic combination, a relatively normal seed is formed even though a single sperm fertilizes only

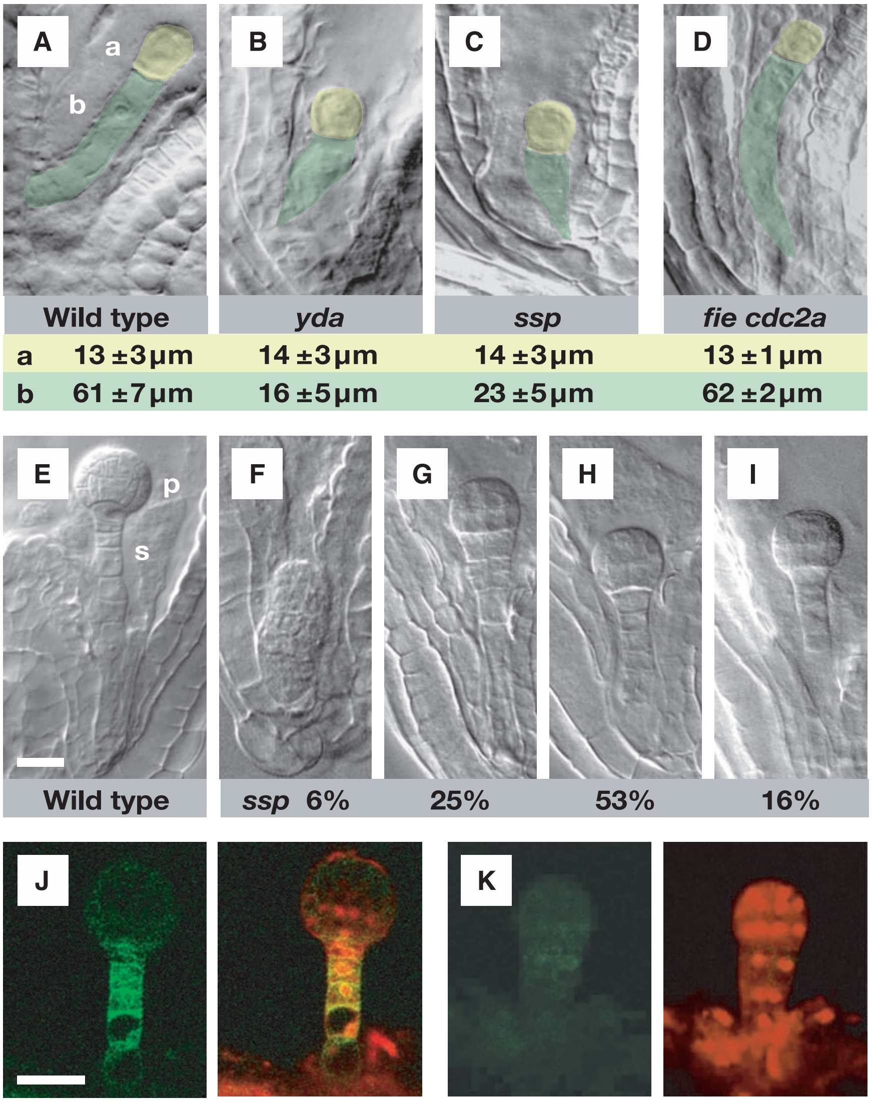

Fig. 1. Phenotype of *ssp* embryos. (**A** to **D**) Size of the apical (a) and basal (b) cell in wild-type (A), *yda* (B), *ssp* (C), and *fie cdc2a* background (*5*) (D); average length and standard deviation (*n* > 20) noted below. (**E** to **I**) Wild-type (E) and *ssp-1* (F to I) globular embryos; frequency of phenotypic classes listed below (*n* > 400); p indicates proembryo; s, suspensor. (**J** and **K**) Confocal microscopy of suspensor-specific marker *SUC3* in wild type (J) and *ssp* (K); green indicates reporter fluorescence; red, propidium iodide counterstain; scale bars, 20 µm.

the egg, leaving the endosperm without paternal contribution (*20*). Despite this, zygote elongation and suspensor development are similar to those in wild type (Fig. 1D), suggesting that *SSP* mRNA is not required in the endosperm.

The tight control of *SSP* expression implies that *YDA*-dependent signaling may be sensitive to the presence of SSP protein. Indeed, seedlings expressing *SSP* from a strong, broadly active promoter (*5*) exhibit a variety of dominant defects that eventually become lethal. Perhaps most strikingly, almost all primary transgenics completely lack stomata on their embryonic leaves (Fig. 4A), faithfully mimicking the phenotype caused by hyperactive *YDA* variants (*21*). This effect is dependent on the presence of a functional *SSP* variant in the construct as well as an intact endogenous *YDA* MAP kinase cascade (Fig. 4, B and C), revealing that SSP protein is sufficient to activate *YDA*-dependent signaling in the leaf epidermis. We propose that, by analogy, SSP protein translated from paternal mRNA triggers activation of the *YDA* MAP kinase cascade in the zygote. According to this model, *SSP* generates a temporal cue linking the onset of *YDA*-dependent signaling to fertilization. Turnover of the sperm-provided mRNA may also limit the duration of this signaling event. It remains to be determined through which mechanism such a temporal signature contributes to regulating the asymmetric first division and thus embryo polarity.

Maternally provided factors are of key importance for animal development because the

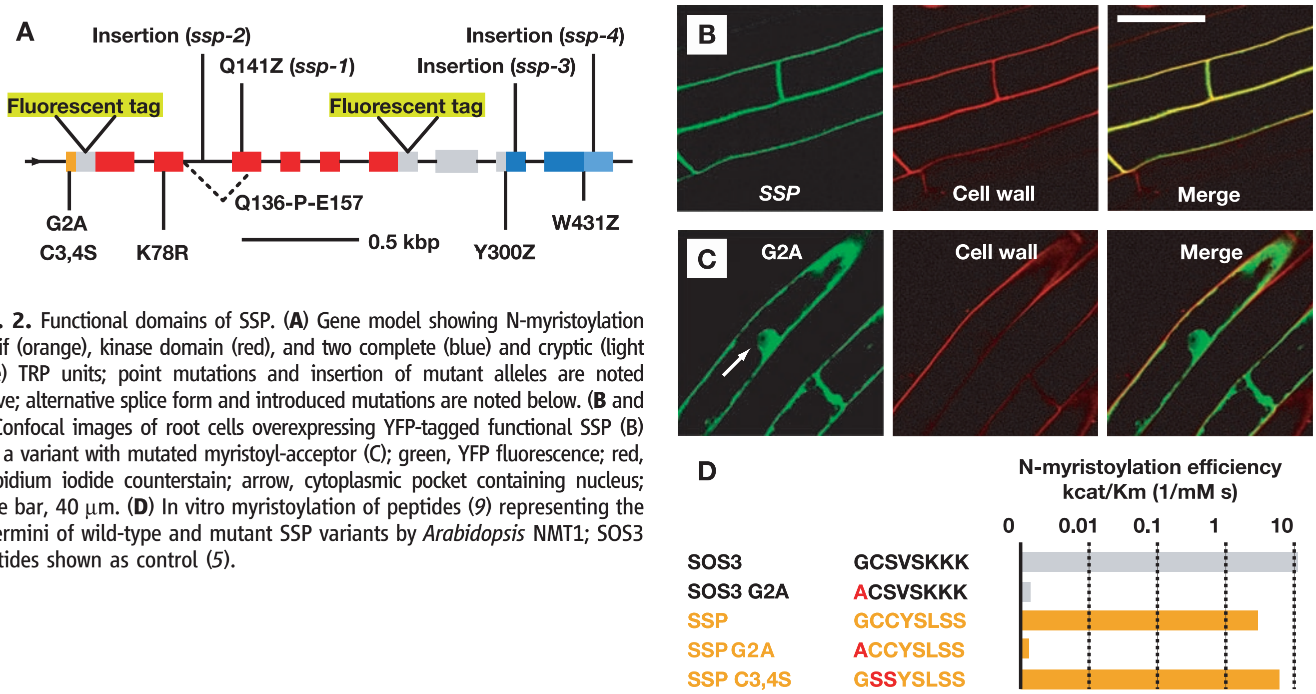

Fig. 2. Functional domains of SSP. (**A**) Gene model showing N-myristoylation motif (orange), kinase domain (red), and two complete (blue) and cryptic (light blue) TRP units; point mutations and insertion of mutant alleles are noted above; alternative splice form and introduced mutations are noted below. (**B** and **C**) Confocal images of root cells overexpressing YFP-tagged functional SSP (B) and a variant with mutated myristoyl-acceptor (C); green, YFP fluorescence; red, propidium iodide counterstain; arrow, cytoplasmic pocket containing nucleus; scale bar, 40 μm. (**D**) In vitro myristoylation of peptides (*9*) representing the N-termini of wild-type and mutant SSP variants by *Arabidopsis* NMT1; SOS3 peptides shown as control (*5*).

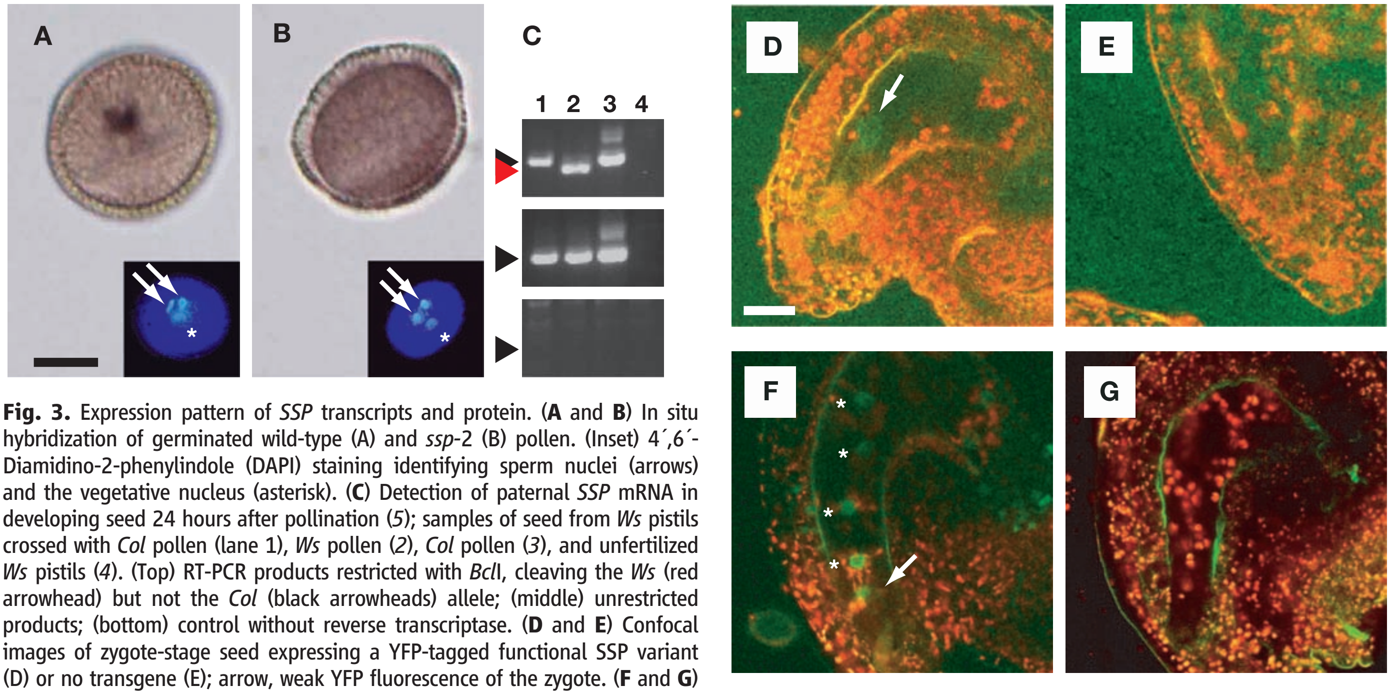

Fig. 3. Expression pattern of *SSP* transcripts and protein. (**A** and **B**) In situ hybridization of germinated wild-type (A) and *ssp*-2 (B) pollen. (Inset) 4´,6´-Diamidino-2-phenylindole (DAPI) staining identifying sperm nuclei (arrows) and the vegetative nucleus (asterisk). (**C**) Detection of paternal *SSP* mRNA in developing seed 24 hours after pollination (*5*); samples of seed from *Ws* pistils crossed with *Col* pollen (lane 1), *Ws* pollen (*2*), *Col* pollen (*3*), and unfertilized *Ws* pistils (*4*). (Top) RT-PCR products restricted with *Bcl*I, cleaving the *Ws* (red arrowhead) but not the *Col* (black arrowheads) allele; (middle) unrestricted products; (bottom) control without reverse transcriptase. (**D** and **E**) Confocal images of zygote-stage seed expressing a YFP-tagged functional SSP variant (D) or no transgene (E); arrow, weak YFP fluorescence of the zygote. (**F** and **G**) Confocal images of seed expressing a nuclear SSP reporter crossed via the pollen (F) or no transgene (G), about 24 hours after pollination; asterisks, endosperm nuclei; arrow, nucleus of zygote; green, YFP fluorescence, red, propidium iodide counterstain; scale bars, 20 μm.

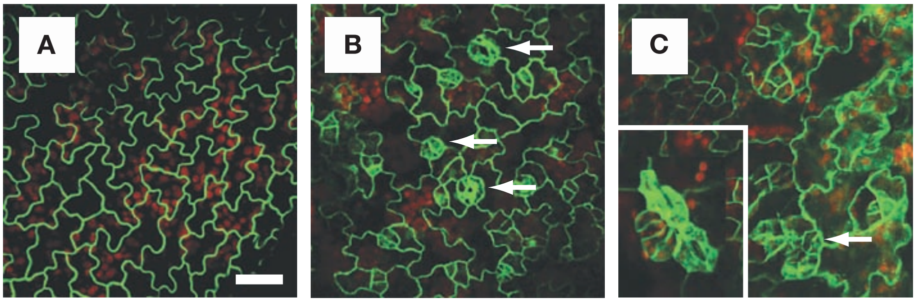

Fig. 4. Ectopic expression of SSP. (**A** to **C**) Confocal images of leaves producing a YFP-tagged functional SSP variant (A), a myristoylation-deficient variant (B), and a functional variant in a *yda* background (C); arrows, stomata; green, YFP fluorescence; red, chlorophyll fluorescence; scale bar, 20 μm. (Inset) Cluster of stomata progenitor cells, as typical for *yda*.

zygotic genome typically does not become active until some time after fertilization [maternal-zygotic transition (*22*)]. Plant embryos apparently develop with more autonomy (*23*), and it is open whether an equivalent to the maternal-zygotic transition of animals exists (*24*). The most prominent parent-of-origin effect in plants targets gene expression in the endosperm and is thought to arise from a parental conflict: Imprinting presumably enforces maternal control over nutrient allocation to the embryo (*25*, *26*). Direct delivery of transcripts to the seed would provide a general mechanism for subverting such epigenetic regulation. Thus, paternal control over growth of the suspensor, the other organ mediating nutrient flux to the embryo, perhaps evolved to antagonize maternal influences in this conflict.

References and Notes

1. C. W. Wardlaw, *Embryogenesis in Plants* (Wiley, New York, 1955).
2. W. Lukowitz, A. Roeder, D. Parmenter, C. Somerville, *Cell* **116**, 109 (2004).
3. H. Wang, N. Ngwenyama, Y. Liu, J. C. Walker, S. Zhang, *Plant Cell* **19**, 63 (2007).
4. S. Meyer *et al.*, *Plant Physiol.* **134**, 684 (2004).
5. For details see materials and methods, available as supporting material on *Science* Online.
6. S.-H. Shiu, A. B. Bleeker, *Proc. Natl. Acad. Sci. U.S.A.* **98**, 10763 (2001).
7. For all molecular complementation experiments, the frequency of normal and *ssp* embryos produced by five or more independent primary transgenic lines was determined; these results were confirmed in the progeny of selected lines.
8. M. D. Resh, *Biochim. Biophys. Acta* **1451**, 1 (1999).
9. Single-letter abbreviations for the amino acid residues are as follows: A, Ala; C, Cys; D, Asp; E, Glu; F, Phe; G, Gly; H, His; I, Ile; K, Lys; L, Leu; M, Met; N, Asn; P, Pro; Q, Gln; R, Arg; S, Ser; T, Thr; V, Val; W, Trp; and Y, Tyr.
10. B. Boisson, T. Meinnel, *Anal. Biochem.* **322**, 116 (2003).
11. J. A. Adams, *Chem. Rev.* **101**, 2271 (2001).
12. K. Mukherjee *et al.*, *Cell* **133**, 328 (2008).
13. S. Janssens, R. Beyaert, *Mol. Cell* **11**, 293 (2003).
14. E. Castells, J. M. Casacuberta, *J. Exp. Bot.* **58**, 3503 (2007).
15. C. Scheufler *et al.*, *Cell* **101**, 199 (2000).
16. Both the diploid sporophyte and the haploid gametophyte may affect embryo development; for simplicity, we refer to "male gametophytic" effects as "paternal."
17. R. Feil, F. Berger, *Trends Genet.* **23**, 192 (2007).
18. J. H. Huh, M. J. Bauer, T.-F. Hsieh, R. Fischer, *Curr. Opin. Genet. Dev.* **17**, 480 (2007).
19. F. Borges *et al.*, *Plant Physiol.* **148**, 1168 (2008).
20. M. K. Nowack *et al.*, *Nature* **447**, 312 (2007).
21. D. C. Bergmann, W. Lukowitz, C. R. Somerville, *Science* **304**, 1494 (2004).
22. A. F. Schier, *Science* **316**, 406 (2007).
23. P. D. Jenik, C. S. Gillmor, W. Lukowitz, *Annu. Rev. Cell Dev. Biol.* **23**, 207 (2007).
24. S. Meyer, S. Scholten, *Curr. Biol.* **17**, 1686 (2007).
25. R. J. Scott, M. Spielman, J. Bailey, H. G. Dickinson, *Development* **125**, 3329 (1998).
26. C. Spillane *et al.*, *Nature* **448**, 349 (2007).
27. This work was supported by the NSF (grant IOB-0446103 to W.L.), the Deutsche Forschungsgemeinschaft (M.B.), the Cold Spring Harbor Laboratory Association (T.N.), and the Association pour le Recherche sur le Cancer (grant 4920 to T.M.). Seed of *ssp-1* have been deposited with the *Arabidopsis* stock center. Materials were kindly made available by P. Das (Caltech), F. Besnard and T. Vernoux (Ecole Normale Supérieure Lyon, pENTR triple Venus), S. McCormick (University of California Berkeley, *GEX2* marker), N. Sauer (Erlangen University, *SUC3* marker), A. Schnittger (Strasbourg University, *cdc2a;fie1*), and K. Slotkin and R. Martienssen (Cold Spring Harbor Laboratory, *met1*, *ddm1*, *cmt3*, *drm2*, and *rdr1*; *rdr2*; *rdr6*). S. Alabaster and J. A. Traverso provided help in the early phases of the project. We thank T. Berleth (University of Toronto), C. S. Gillmor and M. Willman (University of Pennsylvania), S. Jeong and C. Schulz (University of Georgia), R. Schwab (Cold Spring Harbor Laboratory), and D. Weijers (Wageningen University) for comments on the manuscript.

Supporting Online Material

www.sciencemag.org/cgi/content/full/323/5920/1485/DC1
Materials and Methods
Figs. S1 and S2
Tables S1 to S3

28 October 2008; accepted 6 January 2009
10.1126/science.1167784

Preferential Generation of Follicular B Helper T Cells from Foxp3$^+$ T Cells in Gut Peyer's Patches

Masayuki Tsuji,[1]* Noriko Komatsu,[2]* Shimpei Kawamoto,[1,4]* Keiichiro Suzuki,[1] Osami Kanagawa,[3] Tasuku Honjo,[4] Shohei Hori,[2]† Sidonia Fagarasan[1]†

Most of the immunoglobulin A (IgA) in the gut is generated by B cells in the germinal centers of Peyer's patches through a process that requires the presence of CD4$^+$ follicular B helper T (T_{FH}) cells. The nature of these T_{FH} cells in Peyer's patches has been elusive. Here, we demonstrate that suppressive Foxp3$^+$CD4$^+$ T cells can differentiate into T_{FH} cells in mouse Peyer's patches. The conversion of Foxp3$^+$ T cells into T_{FH} cells requires the loss of Foxp3 expression and subsequent interaction with B cells. Thus, environmental cues present in gut Peyer's patches promote the selective differentiation of distinct helper T cell subsets, such as T_{FH} cells.

The production and secretion of immunoglobulin A (IgA) by the host is critical for the maintenance of a vast community of commensal bacteria in the intestinal lumen with minimal penetration of the gut epithelium (*1*, *2*). Most of this IgA synthesis requires germinal center (GC) formation in Peyer's patches (PPs), aggregations of lymphoid follicles in the gut. In GCs, activated B cells express activation-induced cytidine deaminase (AID) and switch from making IgM to IgA (*3*–*5*). GC development in PPs requires bacteria in the gut; germ-free mice have small GCs, probably induced by bacterial components in food (*1*). T cells, by providing cytokines and costimulatory molecules to B cells, are also required for GC induction. Mice that lack T cells are devoid of GCs, and GC formation can be rescued by the adoptive transfer of CD4$^+$ T cells (*1*, *6*, *7*).

We investigated the origin of T_{FH} in PPs by examining the contribution of Foxp3$^+$CD4$^+$ T cells (*8*–*10*) obtained from Foxp3^{EGFP} reporter mice (*11*), which express green fluorescent protein (GFP) under the control of the Foxp3 promoter. Total CD4$^+$ T cells, Foxp3/GFP$^+$ CD4$^+$ T cells (hereafter called Foxp3$^+$ T cells) or Foxp3/GFP$^-$ CD4$^+$ (hereafter called Foxp3$^-$ T cells) that were isolated from the spleen and lymph nodes (LNs) of Foxp3^{EGFP} reporter mice were adoptively

---

[1] Laboratory for Mucosal Immunity, RIKEN, Yokohama 1-7-22, Tsurumi, Yokohama, 230-0045, Japan. [2] Research Unit for Immune Homeostasis, RIKEN, Yokohama 1-7-22, Tsurumi, Yokohama, 230-0045, Japan. [3] Laboratory for Autoimmune Regulation, Research Center for Allergy and Immunology, RIKEN, Yokohama 1-7-22, Tsurumi, Yokohama, 230-0045, Japan. [4] Department of Immunology and Genomic Medicine, Kyoto University, Graduate School of Medicine, Sakyo-ku, Kyoto 606-8501, Japan.

*These authors contributed equally to this work.
†To whom correspondence should be addressed. E-mail: shohei@rcai.riken.jp (S.H.); sidonia-f@rcai.riken.jp (S.F.)

transferred into T cell–deficient, CD3ε$^{-/-}$ mice (*12*). These spleen- and LN-derived Foxp3$^+$ T cells were phenotypically heterogeneous and expressed variable levels of the α chains of interleukin-2 (IL-2) receptor and IL-6 receptor on their surfaces (fig. S1). Transfer of total CD4$^+$ T cells or Foxp3$^+$ or Foxp3$^-$ T cells into CD3ε$^{-/-}$ mice reconstituted the percentage and number of B220$^-$ IgA$^+$ plasma cells in the lamina propria (LP) of the small intestine and of peanut agglutinin–positive (PNA$^+$) Fas$^+$ GC-phenotype B cells in PPs after 4 weeks (Fig. 1, A and B). To our surprise, however, activated B cells formed typical GC clusters (large groups of AID-expressing cells) only when Foxp3$^+$ T cells were transferred, whereas, in mice injected with Foxp3$^-$ T cells, the AID-expressing B cells were scattered throughout the PPs (Fig. 1C). Furthermore, formation of GCs was induced by Foxp3$^+$ T cells in PPs more effectively than by unfractionated CD4$^+$ T cells or by a 1:1 mixture of Foxp3$^+$ and Foxp3$^-$ T cells (Fig. 1C). Thus, Foxp3$^+$ T cells preferentially induced GC formation in PPs and IgA-producing cells in the gut.

How do the Foxp3$^+$ T cells, which are known to suppress T cells, act as B helper T cells? There were many more CD3$^+$ T cells than GFP$^+$ T cells in the PPs of CD3ε$^{-/-}$ mice that received Foxp3$^+$ T cells (Figs. 1C and 2A). Indeed, 80% of Foxp3$^+$ T cells lost GFP expression in PPs, whereas ~50% of CD3$^+$ T cells remained GFP$^+$ in the LP of the small intestine, the large intestine, LNs, and spleen (Fig. 2B). The majority of GFP$^+$ cells transferred to CD3ε$^{-/-}$ host mice, as in nonmanipulated Foxp3^{EGFP} mice, were located in the T cell zone, close to the dendritic cells (DCs), which were stained with CD11c (Fig. 2A). In contrast, most GFP$^-$ CD3$^+$ T cells were located within the B cell follicles, among the AID-expressing cells. Thus, a large fraction of the transferred Foxp3$^+$ T cells lost Foxp3 expression and preferentially localized to B cell follicles in the PPs. These results suggest that the environment of the PPs down-regulates Foxp3 expression or fosters the accumulation of T cells that have lost Foxp3 expression elsewhere, or both.

To assess whether T cells that had down-regulated expression of Foxp3 were among the helper cells able to induce GC formation, we performed serial transfer experiments. Foxp3$^+$ T cells that had down-regulated Foxp3 (designated Foxp3$^{+\rightarrow-}$) were sorted from the spleen and LNs of recipient mice and then transferred into CD3ε$^{-/-}$ recipients. Subsequent GC formation, as indicated by AID-expressing clusters, was comparable to that observed after the initial transfer of Foxp3$^+$ T cells (Fig. 2C, compare with Fig. 1C). Furthermore, the induction of GCs in PPs and the generation of IgA-producing cells in the gut by Foxp3$^{+\rightarrow-}$ T cells were more efficient than either of these resulting from the transfer of unfractionated CD4$^+$ T cells (Fig. 2D and fig. S2). These results indicate that Foxp3 expression is plastic and that cells that have previously expressed Foxp3 are effective precursors for T$_{FH}$ cells that are capable of inducing GC formation in PPs.

T$_{FH}$ cells express surface markers, such as the chemokine receptor CXCR5 and the costimulatory molecules CD40 ligand (CD40L) and inducible T cell costimulator (ICOS) (*13–17*). We examined these markers on CD4$^+$ T cells that either maintained Foxp3 expression or down-regulated Foxp3 expression after transfer of Foxp3$^+$ T cells into CD3ε$^{-/-}$ mice. Over half of the T cells with down-regulated Foxp3 in PPs expressed CXCR5, and these cells were located in the light zone of GCs where the CXCR5 ligand, CXCL13, is abundantly expressed (*16*) (Fig. 3, A and B). In addition, many CXCR5$^+$ Foxp3$^-$ T cells expressed CD40L, ICOS, programmed death-1 (PD-1), and CD28 (Fig. 3A and fig. S3A), all of which are costimulatory molecules necessary for T$_{FH}$ cell generation and function (*17*).

We determined the gene expression profile of T$_{FH}$ cell–like T cells that had down-regulated Foxp3 by dividing the Foxp3$^-$ T cells isolated from PPs of CD3ε$^{-/-}$ mice transferred with Foxp3$^+$ T cells into CXCR5$^+$ and CXCR5$^-$ subsets. We then compared the gene expression profiles in these subsets with those in control Foxp3$^+$ and CXCR5$^+$ T$_{FH}$ cells in PPs, as well as with those in Foxp3$^+$ and Foxp3$^-$ T cells from spleen and LNs of CD3ε$^{-/-}$ mice into which Foxp3$^+$ T cells were transferred. The Foxp3$^+$ T cells, especially those isolated from PPs, expressed abundant transcripts for IL-10, a major anti-inflammatory cytokine in the gut (*18*) (Fig. 3C). In contrast, cyclic nucleotide phosphodiesterase 3B (Pde3b), which is repressed by Foxp3 (*19*), was highly expressed in Foxp3$^-$CXCR5$^+$ T cells derived from Foxp3$^+$ T cells and in control T$_{FH}$ cells (fig. S3B). In addition, the Foxp3$^-$ CXCR5$^+$ cells in the PPs expressed transcripts of two signature genes of T$_{FH}$ cells: the transcription factor Bcl-6 and IL-21 (Fig. 3C), a critical cytokine for both generation of T$_{FH}$ cells and T cell–dependent antibody responses (*17*, *20*, *21*). The transcripts for IL-4, which also contributes to GC formation (*16*), were also highly expressed by Foxp3$^-$ CXCR5$^+$ T cells derived from the Foxp3$^+$ T cells, as well as by control T$_{FH}$ cells (fig. S3B). Although T$_H$17 CD4$^+$ T helper cells (which produce IL-17) have been reported to share attributes of T$_{FH}$ cells (*21*), we detected low mRNA expression for T$_H$17-specific molecules RORγt and IL-17A in Foxp3$^-$ CXCR5$^+$ T cells, as

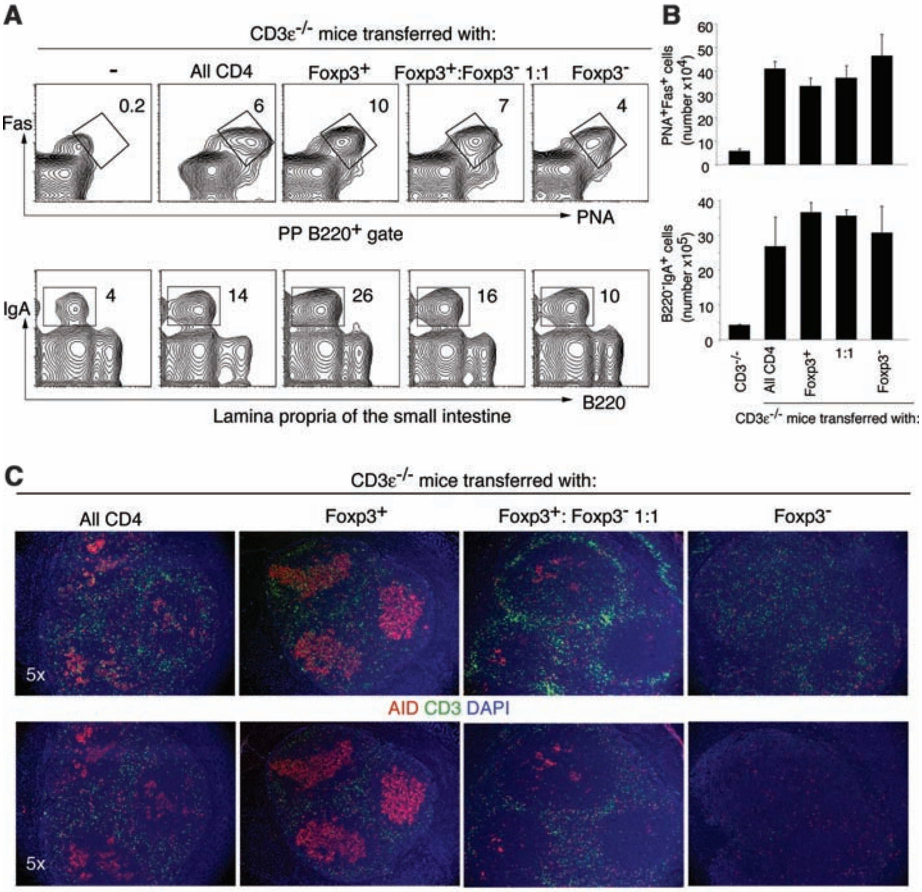

Fig. 1. Induction of GCs in PPs by Foxp3$^+$ T cells. (**A**) Representative flow cytometric profiles of cells stained for the indicated markers. B220 is used as a marker for B cells. Numbers on plots indicate the frequency of cells in the gate. (**B**) Total numbers of GC B cells isolated from the PPs and IgA plasma cells from the LP of the small intestine of CD3ε$^{-/-}$ mice 4 weeks after reconstitution with the indicated T cells. Means ± SEM for three to five mice per group. (**C**) Immunofluorescent microscopy analysis of AID, DAPI (4′,6′-diamidino-2-phenylindole) staining for DNA, and CD3 (upper row) or GFP (lower row) expression in horizontal sections of the PPs from CD3ε$^{-/-}$ mice 4 weeks after reconstitution with the indicated T cell populations.

well as in T_{FH} cells in PPs (*22*, *23*) (fig. S3B). Thus, a fraction of $Foxp3^+$ T cells became T_{FH}-like cells in the PPs after down-regulating Foxp3 expression.

Unexpectedly, $Foxp3^+$ T cells preferentially acquired a T_{FH} cell phenotype even when we transferred a 1:1 mixture of $Foxp3^+$ and $Foxp3^-$ T cells (Fig. 3, D and E, and fig. S3C). Furthermore, in secondary 1:1 transfers of $Foxp3^{+\rightarrow-}$ T cells mixed with control $Foxp3^{-\rightarrow-}$ T cells, CXCR5 was expressed predominantly in T cells derived from $Foxp3^{+\rightarrow-}$ T cells (fig. S4A).

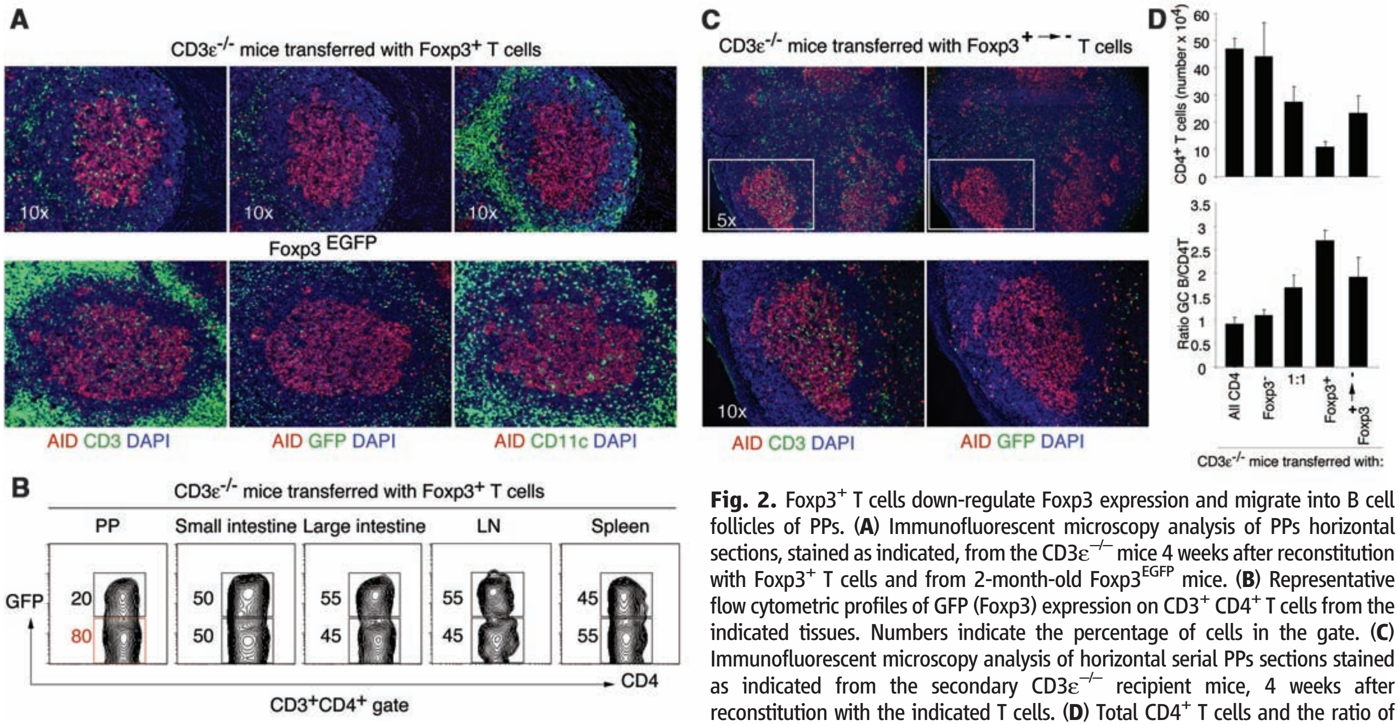

Fig. 2. $Foxp3^+$ T cells down-regulate Foxp3 expression and migrate into B cell follicles of PPs. (**A**) Immunofluorescent microscopy analysis of PPs horizontal sections, stained as indicated, from the $CD3\varepsilon^{-/-}$ mice 4 weeks after reconstitution with $Foxp3^+$ T cells and from 2-month-old $Foxp3^{EGFP}$ mice. (**B**) Representative flow cytometric profiles of GFP (Foxp3) expression on $CD3^+$ $CD4^+$ T cells from the indicated tissues. Numbers indicate the percentage of cells in the gate. (**C**) Immunofluorescent microscopy analysis of horizontal serial PPs sections stained as indicated from the secondary $CD3\varepsilon^{-/-}$ recipient mice, 4 weeks after reconstitution with the indicated T cells. (**D**) Total $CD4^+$ T cells and the ratio of GC B cells to $CD4^+$ T cells in the PPs of $CD3\varepsilon^{-/-}$ mice 4 weeks after reconstitution with the indicated T cells. Means ± SEM for three to five mice per group.

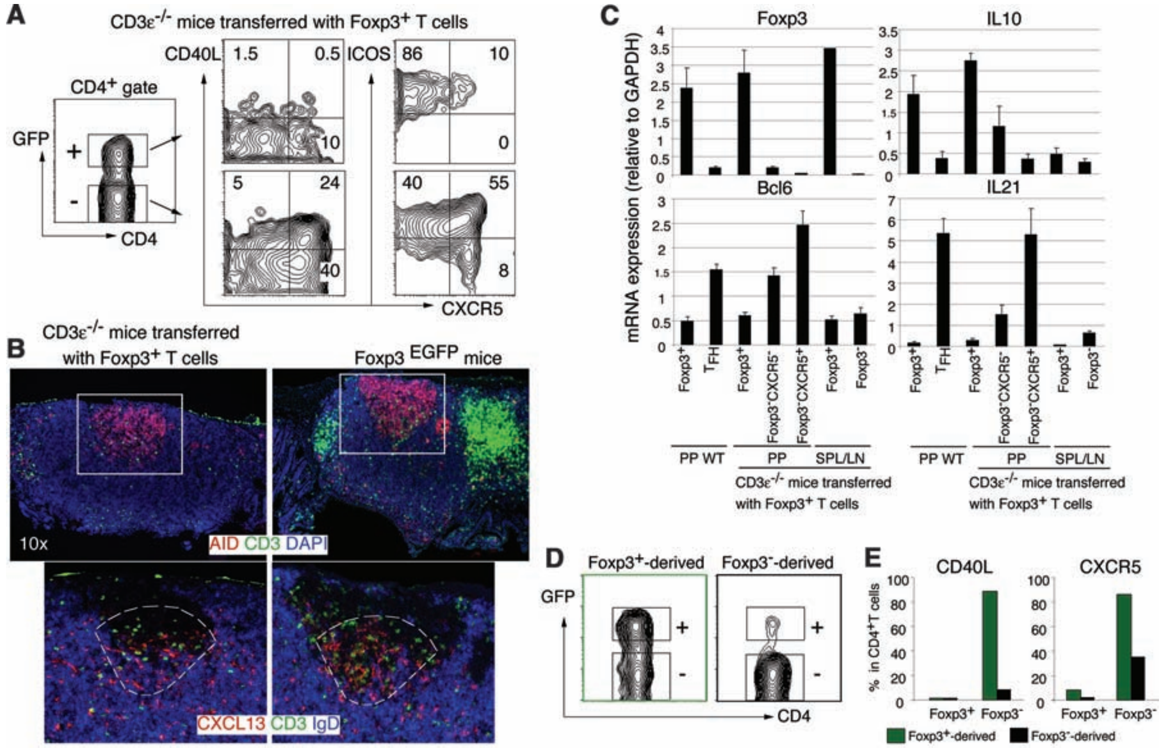

Fig. 3. Differentiation of $Foxp3^-$ T cells derived from $Foxp3^+$ T cells into T_{FH} cells in PPs. (**A**) Flow cytometric analysis of $CD4^+$ T cells from PPs of $CD3\varepsilon^{-/-}$ mice 4 weeks after reconstitution with $Foxp3^+$ T cells. Numbers of graphs indicate the frequency of cells in the gate. (**B**) Immunofluorescent microscopy analysis of consecutive vertical sections from PPs of $CD3\varepsilon^{-/-}$ mice 4 weeks after reconstitution with $Foxp3^+$ T cells and of 2-month-old $Foxp3^{EGFP}$ mice, stained as indicated to reveal the localization of T cells in the CXCL13-rich zone (dashed lines) of the GCs. (**C**) Expression of indicated molecules in sorted T cell populations assessed by real-time reverse transcription polymerase chain reaction. Relative amounts of mRNA normalized to glyceraldehyde-3-phosphate dehydrogenase (GAPDH) are shown. Means ± SEM of three independent experiments. SPL, spleen. (**D**) Flow cytometric analysis of Foxp3 expression (as measured by GFP) on $CD4^+$ T cells from PPs of $CD3\varepsilon^{-/-}$ mice 4 weeks after the reconstitution with a 1:1 mixture of $Foxp3^+$ and $Foxp3^-$ T cells. (**E**) The percentage of $Foxp3^+$- or $Foxp3^-$-derived T cells expressing the indicated surface molecules as determined by flow cytometry. Cells were pooled from three mice. Data represent one of the two experiments with consistent results.

In vitro activation of Foxp3$^+$ T cells but not of Foxp3$^-$ T cells induced CXCR5 expression, especially on Foxp3$^{+\rightarrow-}$ T cells (fig. S4B). Together, these results suggest that Foxp3$^+$ T cells induce enhanced GC formation in PPs because of their ability to differentiate into T$_{\mathrm{FH}}$ cells.

To determine whether B cells are required for the down-regulation of Foxp3 that preceded Foxp3$^+$ T cell differentiation into T$_{\mathrm{FH}}$ cells, we injected Foxp3$^+$ T cells into recombination-activating gene–2$^{-/-}$ (RAG-2$^{-/-}$) recipient mice, which lack both T and B cells. Four weeks after the transfer, 90% of the T cells in PPs were Foxp3$^-$ (Fig. 4A). In the absence of B cells, however, Foxp3$^-$ T cells failed to generate CXCR5$^+$ PD-1$^{\mathrm{high}}$ [elevated programmed death–1 (PD-1) expression] T$_{\mathrm{FH}}$ cells, which suggested that, although Foxp3 down-regulation does not require B cells, B cells are required for acquisition of the T$_{\mathrm{FH}}$ cell phenotype. The cytokines IL-6 and IL-21, abundantly produced by gut DCs and T cells, respectively (fig. S4C), down-regulate Foxp3 expression (*24*). Activation of Foxp3$^+$ T cells in vitro, particularly in the presence of IL-6, decreased Foxp3 expression (Fig. 4B). Addition of IL-6 also enhanced expression of IL-21, a cytokine that induces T$_{\mathrm{FH}}$ cell differentiation, an effect that was partially dependent on autocrine production of IL-21 and transforming growth factor–β (TGFβ) (Fig. 4B and fig. S4D).

The interaction of CD40 on B cells or DCs with CD40L on T cells is critical for the formation of GCs (*25*, *26*). To test whether this interaction is required for the generation of T$_{\mathrm{FH}}$ cells from Foxp3$^+$ T cells in PPs, we injected mice with a CD40L-specific antibody. In antibody-

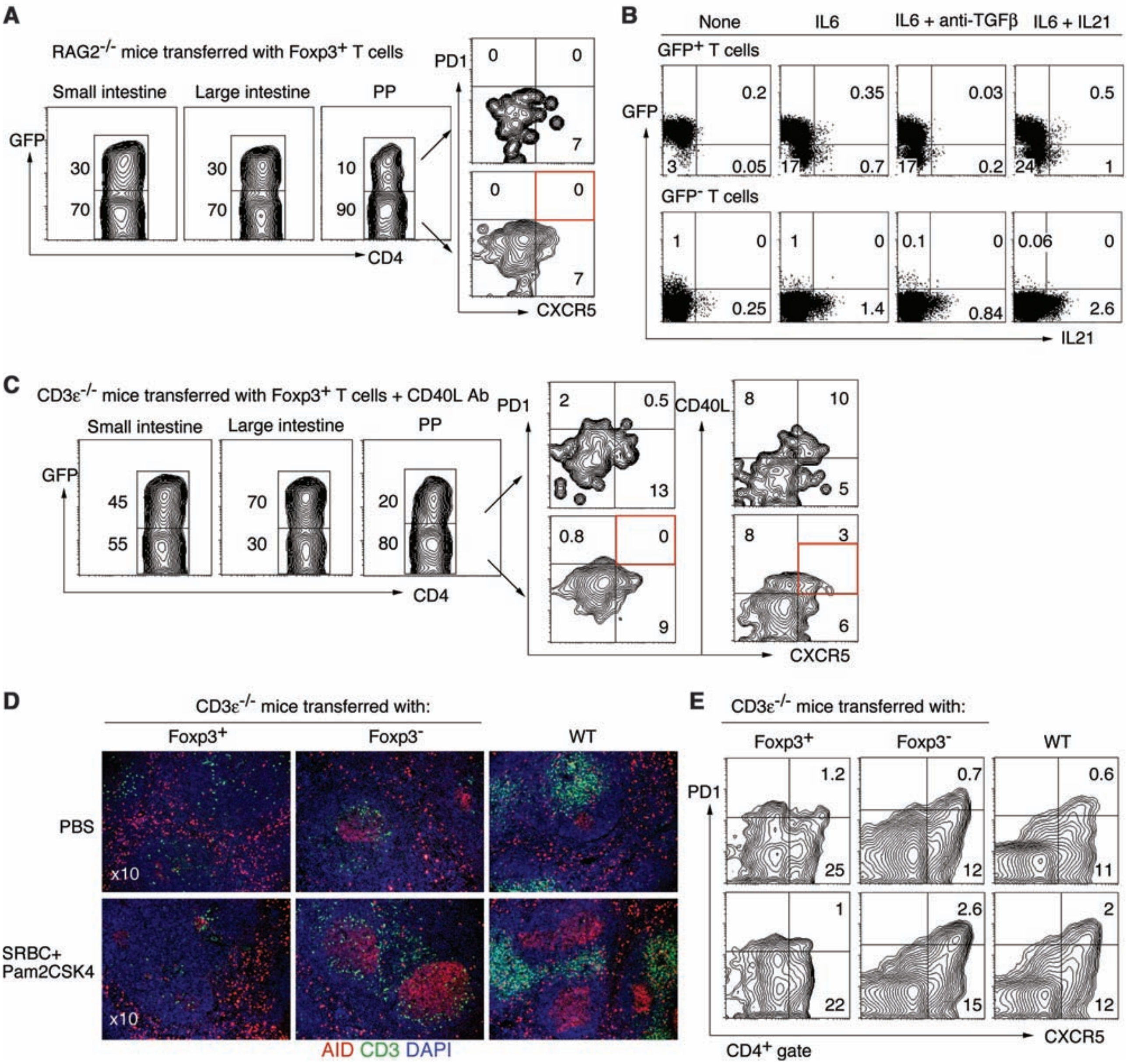

Fig. 4. Differentiation of T$_{\mathrm{FH}}$ cells, but not Foxp3 down-regulation, requires B cells and depends on CD40-CD40L interaction. (**A**) Flow cytometric analysis of the expression of GFP (Foxp3) on CD4$^+$ T cells from PPs of RAG-2$^{-/-}$ mice 4 weeks after reconstitution with Foxp3$^+$ T cells. (**B**) Flow cytometric analysis of the indicated molecules in GFP$^+$ or GFP$^-$ T cells cultured for 5 days with beads coated with antibodies against CD3 and CD28 in the presence of IL-2 and with the indicated cytokines or monoclonal antibodies. Data represent one of the three experiments with consistent results. (**C**) Representative flow cytometric profiles of CD4$^+$ T cells isolated from the indicated tissues of CD3ε$^{-/-}$ mice that received Foxp3$^+$ T cells and CD40L-blocking antibodies (Abs). (**D**) Immunofluorescent microscopy analysis of representative spleen sections from CD3ε$^{-/-}$ mice 4 weeks after reconstitution with the T cell populations indicated. Mice were immunized with SRBCs and Pam2CSK4 (a synthetic lipoprotein) on day 14 and 21 and analyzed 1 week later. Sections from the spleen of wild-type (WT) mice without [phosphate-buffered saline (PBS) only] or with immunization are shown as controls. (**E**) Flow cytometric analysis of CD4$^+$ T cells from spleens of mice analyzed in (D).

treated mice, Foxp3$^+$ T cells still lost Foxp3 expression but did not gain expression of CXCR5, CD40L, and PD-1 (Fig. 4C). Consistent with these observations, blocking CD40-CD40L interactions resulted in a reduction of GC formation in PPs and of B220$^-$ IgA$^+$ plasma cells in the LP (fig. S5, A and B). Thus, the differentiation of Foxp3$^+$ T cells into T$_{FH}$ cells requires B cells and CD40 expression, presumably by either B cells or DCs or both.

Foxp3$^+$ T cells were converted into T$_{FH}$ cells only in PPs; neither T$_{FH}$ cells nor GCs could be detected in spleen or LNs of CD3ε$^{-/-}$ mice adoptively transferred with Foxp3$^+$ T cells (Fig. 4, D and E, and fig. S6). Furthermore, immunization with sheep red blood cells (SRBCs) in the presence of bacterial components failed to induce GCs in spleen of CD3ε$^{-/-}$ mice that received Foxp3$^+$ T cells. In contrast, control mice and CD3ε$^{-/-}$ mice that had received Foxp3$^-$ T cells generated GCs in the spleen after SRBC immunization (Fig. 4, D and E). Thus, the precursors of PP T$_{FH}$ cells are enriched in the Foxp3$^+$ T cell population, whereas other T cells, like Foxp3$^-$ T cells, can differentiate into T$_{FH}$ cells in the spleen on experimental systemic immunization.

Our studies demonstrate that Foxp3$^+$ T cells in PPs can differentiate efficiently into cells with characteristics of T$_{FH}$ cells, which then participate in the induction of GCs and IgA synthesis in the gut. How can we then explain the preferential generation of PP T$_{FH}$ cells from the peripheral Foxp3$^+$ T cell population? Two possible scenarios can be conceived. First, T$_{FH}$ cell differentiation per se may require a Foxp3-dependent molecular program. This is unlikely, however, because adoptively transferred Foxp3$^-$ T cells efficiently generated T$_{FH}$ cells in the spleen on immunization with SRBCs and because *scurfy* T cells, which contain a mutated Foxp3 gene, could generate T$_{FH}$-phenotype cells in PPs, albeit less efficiently than control T cells (fig. S7). A more likely scenario is that PP T$_{FH}$ cell differentiation may be controlled by the same signals that promote Foxp3 expression in gut T cells (*27*–*30*), such as antigen recognition through the T cell receptor (TCR). Consistent with this idea, adoptive transfer of ovalbumin-specific OT-II TCR transgenic RAG-2$^{-/-}$ CD4$^+$ T cells into CD3ε$^{-/-}$ hosts led to generation of Foxp3$^+$ T cells in the gut LP and T$_{FH}$ cells in the PPs if mice were fed ovalbumin (fig. S8). These data suggest that, depending on the environment, TCR stimulation induces either IL-10–producing "suppressor" or IL-21–producing "helper" T cells (fig. S9). Despite the presence of the same antigens that previously induced Foxp3 expression, the IL-6–, IL-21–, and activated B cell–rich environment of PPs results in many Foxp3$^+$ T cells differentiating into T$_{FH}$ cells. These studies have implications for how the suppression of inflammatory reactions and induction of IgA synthesis occur in the gut.

References and Notes

1. A. J. Macpherson, *Curr. Top. Microbiol. Immunol.* **308**, 117 (2006).
2. S. Fagarasan, *Curr. Top. Microbiol. Immunol.* **308**, 137 (2006).
3. I. C. MacLennan, *Annu. Rev. Immunol.* **12**, 117 (1994).
4. M. Muramatsu *et al.*, *J. Biol. Chem.* **274**, 18470 (1999).
5. S. Fagarasan, K. Kinoshita, M. Muramatsu, K. Ikuta, T. Honjo, *Nature* **413**, 639 (2001).
6. L. Wen *et al.*, *J. Exp. Med.* **183**, 2271 (1996).
7. M. Tsuji *et al.*, *Immunity* **29**, 261 (2008).
8. S. Hori, T. Nomura, S. Sakaguchi, *Science* **299**, 1057 (2003).
9. S. Floess *et al.*, *PLoS Biol.* **5**, e38 (2007).
10. N. Komatsu *et al.*, *Proc. Natl. Acad. Sci. U.S.A.* **106**, 1903 (2009).
11. Y. Wang *et al.*, *J. Immunol.* **180**, 1565 (2008).
12. Materials and methods are available as supporting material on *Science* Online.
13. L. S. Walker *et al.*, *J. Exp. Med.* **190**, 1115 (1999).
14. P. Schaerli *et al.*, *J. Exp. Med.* **192**, 1553 (2000).
15. D. Breitfeld *et al.*, *J. Exp. Med.* **192**, 1545 (2000).
16. N. M. Haynes *et al.*, *J. Immunol.* **179**, 5099 (2007).
17. C. G. Vinuesa, S. G. Tangye, B. Moser, C. R. Mackay, *Nat. Rev. Immunol.* **5**, 853 (2005).
18. C. Asseman, S. Mauze, M. W. Leach, R. L. Coffman, F. Powrie, *J. Exp. Med.* **190**, 995 (1999).
19. M. A. Gavin *et al.*, *Nature* **445**, 771 (2007).
20. A. Vogelzang *et al.*, *Immunity* **29**, 127 (2008).
21. R. I. Nurieva *et al.*, *Immunity* **29**, 138 (2008).
22. C. T. Weaver, L. E. Harrington, P. R. Mangan, M. Gavrieli, K. M. Murphy, *Immunity* **24**, 677 (2006).
23. I. I. Ivanov *et al.*, *Cell* **126**, 1121 (2006).
24. X. O. Yang *et al.*, *Immunity* **29**, 44 (2008).
25. T. M. Foy *et al.*, *J. Exp. Med.* **180**, 157 (1994).
26. S. Fillatreau, D. Gray, *J. Exp. Med.* **197**, 195 (2003).
27. D. Mucida *et al.*, *Science* **317**, 256 (2007).
28. J. L. Coombes *et al.*, *J. Exp. Med.* **204**, 1757 (2007).
29. M. J. Benson, K. Pino-Lagos, M. Rosemblatt, R. J. Noelle, *J. Exp. Med.* **204**, 1765 (2007).
30. C. M. Sun *et al.*, *J. Exp. Med.* **204**, 1775 (2007).

31. We thank Y. Doi, A. Yagisawa, T. Miyao, and H. Fujimoto for technical assistance; B. Malissen and K. Itoh for mice; D. Littman and A. Coutinho for inspiring discussions; I. Taniuchi for discussion and for critically reading of the manuscript. This work is supported in part by Grants-in-Aid for Scientific Research in Priority Areas (S.F., S.H.) and for Young Scientists (A) (S.H.), and by the Uehara Memorial Foundation (S.H.). S.H. and S.F. contributed as senior authors.

Supporting Online Material

www.sciencemag.org/cgi/content/full/323/5920/1488/DC1
Materials and Methods
Figs. S1 to S9
References

1 December 2008; accepted 22 January 2009
10.1126/science.1169152

Selective Erasure of a Fear Memory

Jin-Hee Han,[1,2,3] **Steven A. Kushner,**[1,4] **Adelaide P. Yiu,**[1,2] **Hwa-Lin (Liz) Hsiang,**[1,2]
Thorsten Buch,[5] **Ari Waisman,**[6] **Bruno Bontempi,**[7] **Rachael L. Neve,**[8]
Paul W. Frankland,[1,2,3] **Sheena A. Josselyn**[1,2,3]*

Memories are thought to be encoded by sparsely distributed groups of neurons. However, identifying the precise neurons supporting a given memory (the memory trace) has been a long-standing challenge. We have shown previously that lateral amygdala (LA) neurons with increased cyclic adenosine monophosphate response element–binding protein (CREB) are preferentially activated by fear memory expression, which suggests that they are selectively recruited into the memory trace. We used an inducible diphtheria-toxin strategy to specifically ablate these neurons. Selectively deleting neurons overexpressing CREB (but not a similar portion of random LA neurons) after learning blocked expression of that fear memory. The resulting memory loss was robust and persistent, which suggests that the memory was permanently erased. These results establish a causal link between a specific neuronal subpopulation and memory expression, thereby identifying critical neurons within the memory trace.

Ensembles of neurons are thought to serve as the physical representation of memory (the memory trace) (*1*). However, identifying the precise neurons that constitute a memory trace is challenging because these neuronal ensembles are likely sparsely distributed (*2*). Previous studies detected neurons whose activity is correlated with memory encoding, expression, or both (*3*–*7*). However, correlative studies do not address whether these neurons are essential components of the memory trace. A direct test of this requires specifically disrupting only those activated neurons and determining whether subsequent memory expression is blocked. Establishing this causal role has been difficult, because of the limited ability of current techniques to target a specific subset of neurons within a brain region.

To target neurons whose activity is correlated with memory, we took advantage of our recent findings that LA neurons with relatively increased levels of the transcription factor CREB were preferentially activated by auditory fear memory

---

[1]Program in Neurosciences and Mental Health, Hospital for Sick Children, 555 University Avenue, Toronto, ON, M5G 1X8, Canada. [2]Institute of Medical Sciences, University of Toronto, Toronto, ON, M5G 1X8, Canada. [3]Department of Physiology, University of Toronto, Toronto, ON, M5G 1X8, Canada. [4]Department of Psychiatry, Erasmus University Medical Center, 3015 CE Rotterdam, Netherlands. [5]Department of Pathology, University of Zurich, CH-8057 Zurich, Switzerland. [6]I.Medizinische Klinik und Poliklinik, Johannes Gutenberg-Universität Mainz, 55131 Mainz, Germany. [7]Centre de Neurosciences Intégratives et Cognitives, CNRS UMR 5228 and University of Bordeaux 1, 33405 Talence, France. [8]Department of Brain and Cognitive Sciences, Massachusetts Institute of Technology, Cambridge, MA 02139, USA.

*To whom correspondence should be addressed. E-mail: sheena.josselyn@sickkids.ca

training or testing (*8*). To manipulate CREB levels in a subpopulation (roughly 15%) of LA neurons, a region critical for auditory fear memory (*9*–*12*), we used replication-defective herpes simplex viral (HSV) vectors (*13*). Neurons overexpressing CREB (with CREB vector) were three times as likely to be activated as their noninfected neighbors after fear memory training or testing in wild-type (WT) mice and 10 times as likely to be activated in CREB-deficient mice. Conversely, WT neurons with a dominant-negative CREB vector were 1/12 as likely as their neighbors to be activated by fear training or testing. These findings suggest that neurons with relatively higher CREB function are preferentially recruited into the fear memory trace and that posttraining ablation of just these neurons should disrupt expression of the established fear memory.

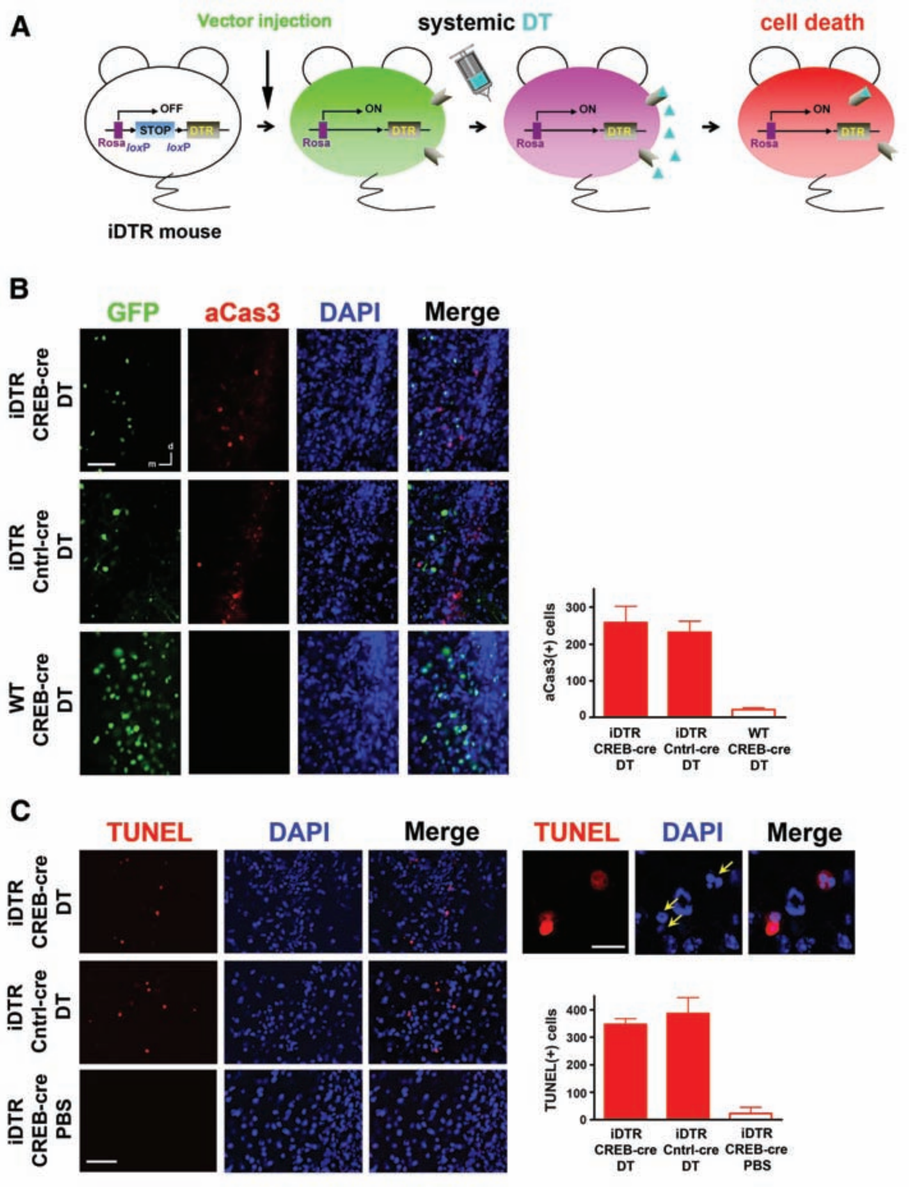

Fig. 1. Selective ablation of LA neurons. (**A**) iDTR mice express DTR under control of a floxed STOP cassette (no DTR expression, indicated by white). CREB-cre or Cntrl-cre microinjected into LA (green). Cre removes STOP cassette, which allows DTR expression (pink). DT (blue triangles) induces apoptosis (red) only in cells that have undergone recombination. (**B**) (Left) Low GFP (with cre vector, green) and high activated caspase-3 (aCas3, red) levels in experimental (iDTR/CREB-cre/DT, iDTR/Cntrl-cre/DT), but not control (WT/CREB-cre/DT), mice. DAPI (4′,6′-diamidino-2-phenylindole)–stained nuclei (blue). Scale bar, 100 μm. (Right) High activated caspase-3 levels in experimental [iDTR/CREB-cre/DT (n = 24), iDTR/Cntrl-cre/DT (n = 17)], but not control [WT/CREB-cre/DT (n = 4)], mice ($F_{2,42} = 6.44$, $P < 0.001$). (**C**) (Left) High TUNEL (red) levels in experimental (iDTR/CREB-cre/DT, iDTR/Cntrl-cre/DT), but not control (iDTR/CREB-cre/PBS), mice. Scale bar, 100 μm. (Right, top) Morphological indicators of apoptosis in experimental mice. Scale bar, 50 μm. (Right, bottom) High TUNEL levels in LA of experimental mice [iDTR/CREB-cre/DT (n = 5), iDTR/Cntrl-cre/DT (n = 6) versus control (n = 5); $F_{2,13} = 22.31$, $P < 0.001$].

To ablate neurons overexpressing CREB in the present study, we used transgenic mice in which cell death may be induced in a temporally and spatially restricted manner. Apoptosis is induced after diphtheria toxin (DT) binds to the DT receptor (DTR) (*14*). Because mice do not express functional DTRs (*15*, *16*), we used transgenic mice that express simian DTR in a Cre-recombinase (cre)–inducible manner (iDTR mice) (*15*). A loxP-flanked STOP cassette that normally silences DTR expression is excised by cre, which allows constitutive expression of DTR. Injection of DT any time thereafter induces apoptosis only in cells expressing DTR.

We restricted DT-induced ablation to neurons overexpressing CREB by inserting cDNA encoding cre recombinase into our CREB vector (CREB-cre). DTR expression only occurs in neurons expressing cre, which allowed us to persistently tag infected neurons for subsequent ablation (Fig. 1A and fig. S1). As a control, we used Cntrl-cre vector to induce apoptosis in a similar portion of LA neurons that are not preferentially activated by fear testing. To examine cell death, we used two markers of apoptosis, caspase-3 activation and terminal deoxynucleotidyl transferase–mediated deoxyuridine triphosphate nick end labeling (TUNEL) (*17*). We microinjected CREB-cre, Cntrl-cre, and CREB alone (without cre) vectors into the LA of iDTR transgenic and WT littermate mice, then administered DT or vehicle. We observed substantial cell death only in LA neurons of iDTR mice microinjected with CREB-cre or Cntrl-cre vectors and administered DT (experimental groups, Fig. 1, B and C, and fig. S2) (*15*). Negligible apoptosis was observed in regions outside the LA (figs. S3 and S4) or in control groups that lacked a key component (iDTR, cre or DT) (Fig. 1, B and C). Note that Cntrl-cre and CREB-cre vectors produced equal levels of cell death (Fig. 1, B and C); however, the efficiency of cell death was not complete (see SOM text). Therefore, this system allows temporally specific ablation of tagged neurons.

To verify that LA neurons overexpressing CREB are selectivity activated by fear memory testing with our modified vector, we microinjected WT mice with CREB-cre or Cntrl-cre vector before auditory fear training. To visualize neurons specifically activated by memory expression, we examined Arc (activity-regulated cytoskeleton-associated protein; Arg3.1) RNA (*18*). Neuronal activity induces a rapid, but transient, burst of Arc RNA that is quickly transported to the cytoplasm, which allows nuclear-localized Arc RNA to serve as a molecular signature of a recently (5 to 15 min previously) active neuron (*18*). Five minutes after testing, we removed brains and examined Arc (activated by fear testing) and green fluorescent protein (GFP) (with vector) RNA. Neurons with CREB-cre vector preferentially expressed Arc after memory testing; neurons with CREB-cre were three times as likely to be activated by fear memory testing as their noninfected neighbors. In contrast, neurons with Cntrl-cre vector and their noninfected neighbors were equally likely to be activated by memory testing (Fig. 2).

We microinjected CREB-cre vector into the LA of iDTR mice before weak auditory fear training. Cntrl-cre vector was used to ablate a similar portion of random LA neurons (i.e., not preferentially activated by fear memory testing). We assessed memory before (test 1) and after (test 2) inducing cell death in tagged neurons by administering DT. The CREB-cre vector enhanced fear memory following weak training (Fig. 3, test 1), consistent with previous results (*8*, *19*–*22*). Selectively deleting neurons with CREB-cre vector completely reversed this enhancement (test 2). Note that CREB-enhanced memory was not blocked if either cre or DT was omitted, consistent with the absence of apoptosis in these control groups. The reversal of CREB-enhanced memory was not due to memory extinction with repeated testing because the control groups froze robustly on test 2. Therefore, increasing CREB in a subpopulation of LA neurons enhances a weak memory and specifically ablating just these neurons reverses this enhancement.

Although increasing CREB in a subpopulation of LA neurons does not further enhance a strong memory, neurons overexpressing CREB are, nevertheless, preferentially activated by fear memory expression (*8*). This suggests that CREB levels dictate which neurons are recruited into a memory trace, even in the absence of behavioral change. To examine the effects of ablating neurons overexpressing CREB on a strong memory, we trained mice that received CREB-cre or Cntrl-cre microinjections using an intense protocol. Strong training produced robust auditory fear memory in both groups before DT administration (Fig. 4A). After DT, only CREB-cre mice showed a loss of auditory fear memory. To investigate whether memory in mice microinjected with CREB-cre is particularly susceptible to the ablation of a small number of neurons, we microinjected both Cntrl-cre and CREB (no cre) vectors, which allowed us to delete only Cntrl-cre neurons after training. Deleting this small portion of neurons (that were not overexpressing CREB) had no effect on memory (fig. S5). Therefore, memory loss was specific; it was not determined by the absolute number of deleted LA neurons but by whether these deleted neurons overexpressed CREB at the time of training.

Administering DT after a fear memory test blocked expression of both CREB-enhanced memory produced by weak training and robust memory produced by strong training in iDTR mice microinjected with CREB-cre (but not Cntrl-cre) vector. Fear memory testing reactivates memory and may trigger a second wave of consolidation (reconsolidation) that, similar to initial consolidation, requires protein synthesis (*23*, *24*). Because DT induces cell death by inhibiting protein synthesis, it is possible that impaired reconsolidation contributes to the memory loss. To assess this, we trained mice but omitted the memory reactivation induced by test 1. Consistent with our previous results, fear memory was blocked in CREB-cre, but not Cntrl-cre, mice (Fig. 4B). Therefore, memory loss was independent of memory reactivation, which ruled out the possibility that blocking reconsolidation accounts for the memory disruption.

If neurons overexpressing CREB during training are critically involved in the subsequent memory trace, then deleting them should permanently block memory expression. To examine the persistence of memory loss, we trained mice, administered DT, and assessed memory 2, 5, and 12 days later. Memory loss in CREB-cre mice was long-lasting, whereas memory remained robust in Cntrl-cre mice (Fig. 4C). Therefore, we found no evidence of memory recovery in mice in which neurons overexpressing CREB were deleted, which suggested that memory was not transiently suppressed. To rule out the possibility that the memory loss was due to a nonspecific impairment in LA function, we showed that CREB-cre mice could relearn (Fig. 4C). Similarly, pretraining deletion of neurons overexpressing CREB did not impair the acquisition, or stability, of a conditioned fear memory (fig. S6). Deleting neurons overexpressing CREB does not affect subsequent learning, presumably because the high portion of remaining (noninfected) neurons are sufficient to encode a new memory. Finally, ablating CREB-overexpressing neurons did not block expression of a memory acquired before surgery (fig. S8). Together, these findings indicate that ablating neurons that were overexpressing CREB at the time of memory encoding blocks memory for that particular learning event, highlighting the specificity of memory loss.

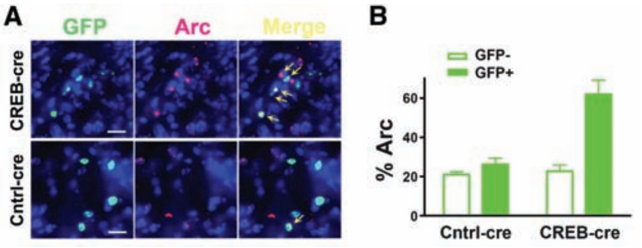

Fig. 2. Neurons overexpressing CREB preferentially activated by fear memory testing. (**A**) Double-labeled nuclei in LA of CREB-cre, but not Cntrl-cre, mice. Nuclei (blue), GFP^+ (with CREB-cre or Cntrl-cre vector, green), Arc^+ (pink), or double-labeled nuclei (GFP^+ and Arc^+; arrows). Scale bar, 20 μm. (**B**) In CREB-cre mice, Arc was preferentially localized in infected (GFP^+), rather than noninfected (GFP^-), neurons. In Cntrl-cre mice, Arc was equally distributed in infected and noninfected neurons (*Vector* × *GFP/Arc colocalization* interaction, $F_{1,5} = 18.74$, $P < 0.05$).

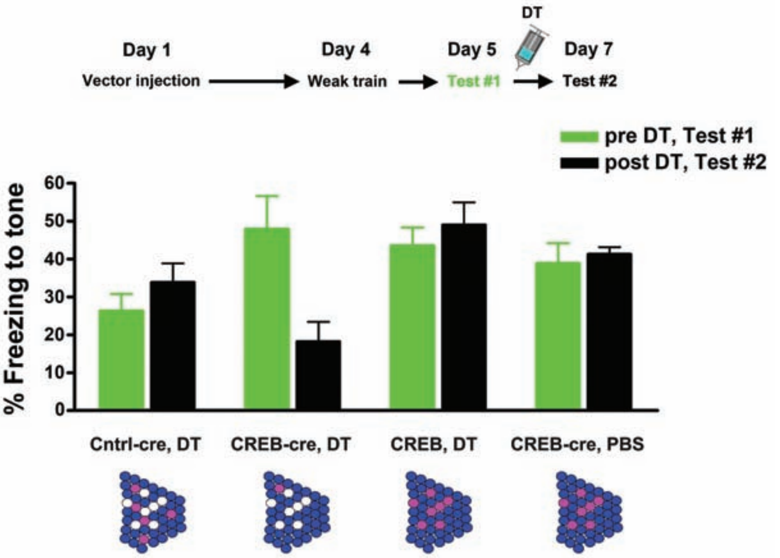

Fig. 3. Overexpressing CREB in LA neurons enhances memory induced by weak training; subsequent ablation of these neurons reverses this enhancement. (**Top**) CREB-cre microinjection enhanced memory after weak training [test 1, CREB-cre/DT ($n = 8$), Cntrl-cre/DT ($n = 9$), $P < 0.001$]. DT administration reversed this memory enhancement (test 2, $P < 0.001$). CREB-enhanced memory was not blocked on test 2 if either cre [CREB/DT ($n = 7$), $P > 0.05$] or DT [CREB-cre/PBS ($n = 6$), $P > 0.05$] was omitted. *Group* × *Test* interaction $F_{3,26} = 13.90$, $P < 0.001$. (**Bottom**) Schematic of LA neurons after DT or PBS. Blue, DAPI-labeled neuronal nuclei; pink, neurons activated by memory; and white, ablated neurons.

Our results show that neurons with increased CREB levels at the time of fear learning are critical to the stability of that memory, because selectively ablating these neurons after training blocks expression of this fear memory. This indicates that these neurons themselves are essential for memory expression in the days after fear conditioning; they are not simply creating a local environment that promotes memory formation (such as releasing trophic factors) (*25*). Deleting neurons whose activity is related to memory expression (overexpressing CREB at the time of training) produced memory loss, whereas ablating a similar number of random neurons (expressing Cntrl vector or overexpressing CREB well before or after training) did not. The observed amnesia was specific, robust, persistent and not due to a disruption in either reconsolidation or overall LA function. Together, these results suggest that ablating neurons overexpressing CREB permanently erases the fear memory (see supporting online material text). Fear learning may generate a broad memory trace that encompasses more LA neurons than affected by our treatment or multiple memory traces throughout the brain (*26*, *27*). However, deleting just neurons overexpressing CREB at the time of training produces amnesia, which suggests that these neurons play an essential role within what is likely a broader fear neuronal network. These results establish a causal link between a defined subpopulation of neurons and expression of a fear memory and, thereby, identify a key component of the memory trace.

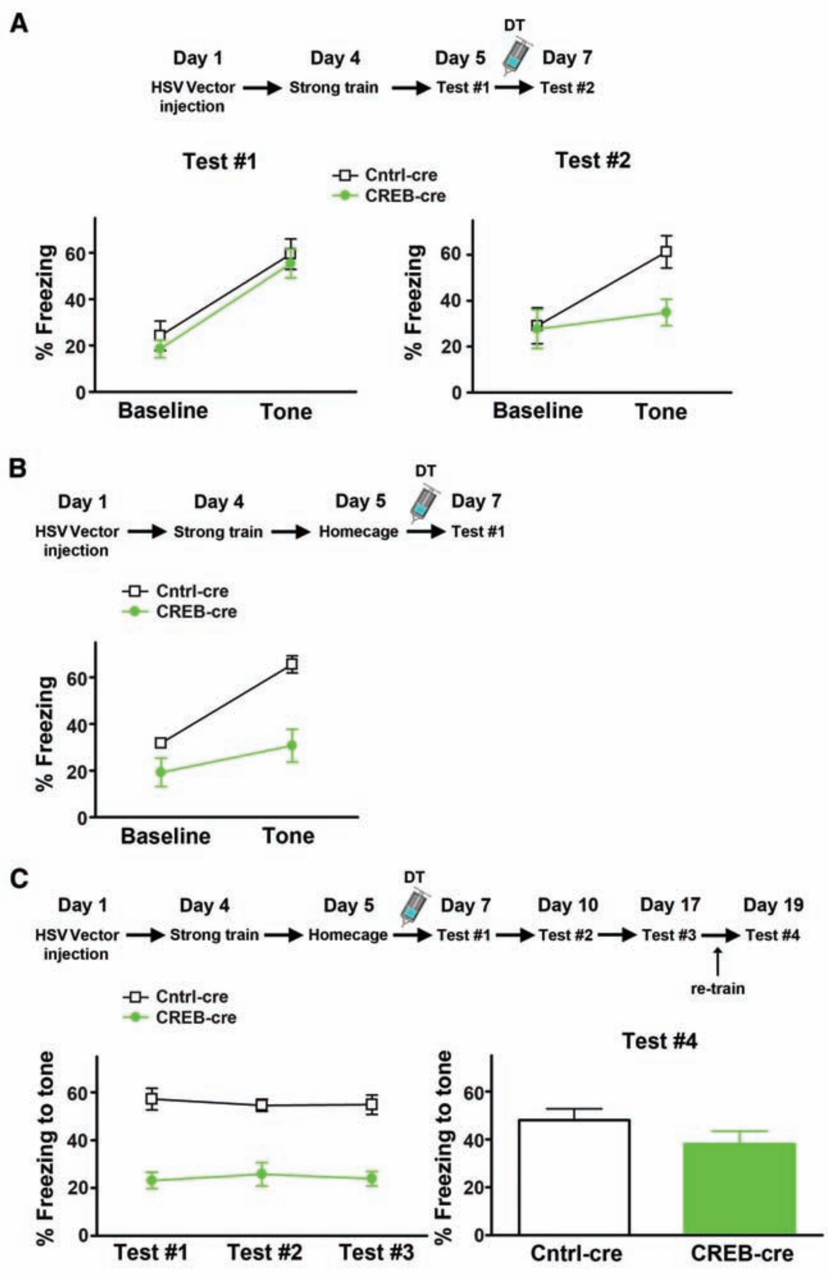

Fig. 4. Specifically ablating LA neurons overexpressing CREB, but not a similar portion of random neurons, blocks expression of strong memory. (**A**) Strong training produced equally robust and specific auditory fear memory (low baseline and high tone freezing) in CREB-cre ($n = 6$) and Cntrl-cre ($n = 6$) mice on test 1. Although Cntrl-cre mice showed robust memory after DT administration (test 2), CREB-cre mice showed impaired memory (low baseline and low tone freezing) (*Vector* × *Test* × *Time* significant three-way interaction, $F_{1,10} = 5.55$, $P < 0.05$). (**B**) Memory loss was not due to disruption of reconsolidation. Cntrl-cre ($n = 5$) mice showed robust auditory fear memory (low baseline but high tone freezing), whereas CREB-cre ($n = 6$) mice showed a loss of auditory fear memory (low baseline and tone freezing) (*Vector* × *Time* interaction, $F_{1,10} = 6.20$, $P < 0.05$). (**C**) Memory loss was persistent in CREB-cre mice, but they could relearn. Over repeated tests (tests 1 to 3), CREB-cre mice ($n = 10$) showed stable, low tone freezing, whereas Cntrl-cre mice ($n = 7$) showed robust tone freezing [*Vector* × *Test* analysis of variance (ANOVA), significant effect of *Vector* $F_{1,15} = 67.81$, $P < 0.05$ only]. (Right) After retraining CREB-cre mice showed an increase in tone freezing ($F_{1,15} = 1.7$, $P > 0.05$).

References and Notes

1. H. L. Roediger, Y. Dudai, S. M. Fitzpatrick, *Science of Memory: Concepts* (Oxford Univ. Press, New York, 2007).
2. J. Perez-Orive *et al.*, *Science* **297**, 359 (2002).
3. G. J. Quirk, C. Repa, J. E. LeDoux, *Neuron* **15**, 1029 (1995).
4. T. W. Berger, P. C. Rinaldi, D. J. Weisz, R. F. Thompson, *J. Neurophysiol.* **50**, 1197 (1983).
5. L. G. Reijmers, B. L. Perkins, N. Matsuo, M. Mayford, *Science* **317**, 1230 (2007).
6. J. F. Guzowski *et al.*, *Curr. Opin. Neurobiol.* **15**, 599 (2005).
7. J. Hall, K. L. Thomas, B. J. Everitt, *J. Neurosci.* **21**, 2186 (2001).
8. J. H. Han *et al.*, *Science* **316**, 457 (2007).
9. J. E. LeDoux, *Annu. Rev. Neurosci.* **23**, 155 (2000).
10. M. S. Fanselow, G. D. Gale, *Ann. N.Y. Acad. Sci.* **985**, 125 (2003).
11. M. Davis, *Annu. Rev. Neurosci.* **15**, 353 (1992).
12. S. Maren, G. J. Quirk, *Nat. Rev. Neurosci.* **5**, 844 (2004).
13. Materials and methods are available as supporting material on *Science* Online.
14. R. B. Dorland, J. L. Middlebrook, S. H. Leppla, *J. Biol. Chem.* **254**, 11337 (1979).
15. T. Buch *et al.*, *Nat. Methods* **2**, 419 (2005).
16. J. G. Naglich, L. Eidels, *Proc. Natl. Acad. Sci. U.S.A.* **87**, 7250 (1990).
17. A. Saraste, K. Pulkki, *Cardiovasc. Res.* **45**, 528 (2000).
18. J. F. Guzowski, B. L. McNaughton, C. A. Barnes, P. F. Worley, *Nat. Neurosci.* **2**, 1120 (1999).
19. A. M. Jasnow, C. Shi, J. E. Israel, M. Davis, K. L. Huhman, *Behav. Neurosci.* **119**, 1125 (2005).
20. S. A. Josselyn *et al.*, *J. Neurosci.* **21**, 2404 (2001).
21. T. L. Wallace, K. E. Stellitano, R. L. Neve, R. S. Duman, *Biol. Psychiatry* **56**, 151 (2004).
22. J. H. Han *et al.*, *Learn. Mem.* **15**, 443 (2008).
23. K. Nader, G. E. Schafe, J. E. Le Doux, *Nature* **406**, 722 (2000).
24. Y. Dudai, M. Eisenberg, *Neuron* **44**, 93 (2004).
25. E. S. Levine, I. B. Black, *Ann. N.Y. Acad. Sci.* **835**, 12 (1997).
26. D. Pare, G. J. Quirk, J. E. Ledoux, *J. Neurophysiol.* **92**, 1 (2004).
27. J. L. McClelland, B. L. McNaughton, R. C. O'Reilly, *Psychol. Rev.* **102**, 419 (1995).

28. We thank T. Pekar, J. Park, and J. Guo for technical assistance. Supported by Canadian Institutes of Health Research (MOP74650, MOP77561) and EJLB Foundation grants to S.A.J. and P.W.F., National Alliance for Research on Schizophrenia and Depression fellowship to J.H.H., travel fellowship (France-Canada Research Foundation), Agence Nationale de la Recherche (France) grant (06-NEURO-027-03) to B.B., and Restracomp Fellowships from the Hospital for Sick Children to A.P.Y. and J.H.H.

Supporting Online Material
www.sciencemag.org/cgi/content/full/323/5920/1492/DC1
Materials and Methods
SOM Text
Figs. S1 to S9
References
Movie S1

4 August 2008; accepted 15 January 2009
10.1126/science.1164139

Human Substantia Nigra Neurons Encode Unexpected Financial Rewards

Kareem A. Zaghloul,[1]* Justin A. Blanco,[2] Christoph T. Weidemann,[3] Kathryn McGill,[1] Jurg L. Jaggi,[1] Gordon H. Baltuch,[1] Michael J. Kahana[3]*

The brain's sensitivity to unexpected outcomes plays a fundamental role in an organism's ability to adapt and learn new behaviors. Emerging research suggests that midbrain dopaminergic neurons encode these unexpected outcomes. We used microelectrode recordings during deep brain stimulation surgery to study neuronal activity in the human substantia nigra (SN) while patients with Parkinson's disease engaged in a probabilistic learning task motivated by virtual financial rewards. Based on a model of the participants' expected reward, we divided trial outcomes into expected and unexpected gains and losses. SN neurons exhibited significantly higher firing rates after unexpected gains than unexpected losses. No such differences were observed after expected gains and losses. This result provides critical support for the hypothesized role of the SN in human reinforcement learning.

Theories of conditioning and reinforcement learning postulate that unexpected rewards play an important role in allowing an organism to adapt and learn new behaviors (*1*, *2*). Research on nonhuman primates suggests that midbrain dopaminergic neurons projecting from the ventral tegmental area and the pars compacta region of the SN encode unexpected reward signals that drive learning (*3*–*6*). These dopaminergic neurons are phasically activated in response to unexpected rewards and depressed after the unexpected omission of reward (*7*–*9*), and they are major inputs to a larger basal ganglia circuit that has been implicated in reinforcement learning across species (*10*–*15*).

The response of these neurons to rewards has not been directly measured in humans. We recorded neuronal activity in human SN while patients undergoing deep brain stimulation (DBS) surgery for Parkinson's disease performed a probability learning task. Patients with Parkinson's disease show impaired learning from positive and negative feedback in cognitive tasks (*16*–*18*), probably because of the degenerative nature of their disease and the decreased number of dopaminergic neurons capable of mounting phasic changes in activity in response to reward signals (*17*–*19*). We sought to capture remaining viable dopaminergic SN cells in our patients and determine whether they exhibit responses modulated by reward expectation.

We used microelectrode recordings to measure intraoperative activity of SN in 10 Parkinson's patients (6 men, 4 women, mean age of 61 years) undergoing DBS surgery of the subthalamic nucleus (STN) while they engaged in a probability learning task. We rewarded participants in the task with virtual financial gains to motivate learning. We identified SN by anatomic location and its unique firing pattern (Fig. 1A) (*20*). The learning task involved choosing between a red and a blue deck of cards presented on a computer screen (Fig. 1B). We informed partici-

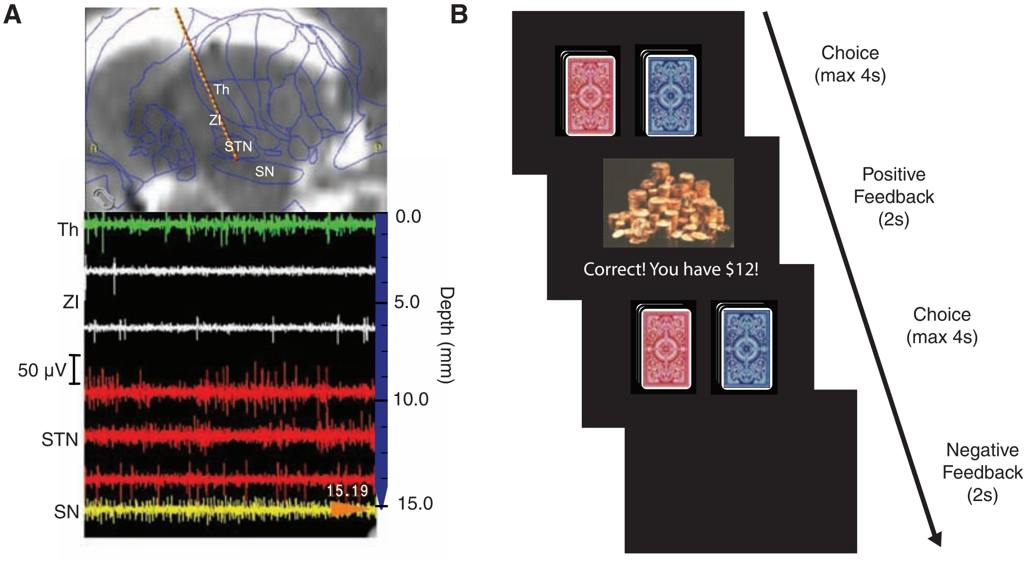

Fig. 1. (**A**) Intraoperative plan for DBS surgery with targeting of the STN. Microelectrodes are advanced along a tract through the anterior thalamic nuclei (Th), zona incerta (ZI), STN, and into the SN to record neural activity. Each anatomical region is identified by surgical navigation maps overlayed with a standard brain atlas (top) and by its unique firing pattern and microelectrode position (bottom). Depth measurements on the right of the screen begin 15 mm above the pre-operatively identified target, the inferior border of STN. In this example, the microelectrode tip lays 0.19 mm below the target. A, anterior; P, posterior. (**B**) Probability learning task. Participants are presented with two decks of cards on a computer screen. They are instructed to repeatedly draw cards from either deck to determine which deck yields the higher reward probability. Participants are given up to four seconds for each draw. After each draw, positive or negative feedback is presented for two seconds. Decks are then immediately presented on the screen for the next choice.

---

[1] Department of Neurosurgery, University of Pennsylvania, Philadelphia, PA 19104, USA. [2] Department of Bioengineering, University of Pennsylvania, Philadelphia, PA 19104, USA. [3] Department of Psychology, University of Pennsylvania, Philadelphia, PA 19104, USA.

*To whom correspondence should be addressed. E-mail: zaghlouk@uphs.upenn.edu (K.A.Z.); kahana@psych.upenn.edu (M.J.K.)

pants that one of the two decks carried a higher probability of yielding a financial reward than the other. Participants were instructed to repeatedly draw cards from either deck to determine which yields a higher return (high reward rate 65%, low reward rate 35%) (*20*). If the draw of a card yielded a reward, a stack of gold coins was displayed along with an audible ring of a cash register and a counter showing accumulated virtual earnings. If the draw did not yield a reward or if no choice was made, the screen turned blank and participants heard a buzz. Participants completed 91.5 ± 13.3 (mean ± SD) trials during the 5-min experiment.

We examined learning rates for the experiment (Fig. 2A) (*20*). Once a participant learns which deck has the higher payoff probability, he or she should preferentially choose that deck. On average, the rate with which participants chose the higher-probability deck improved from 52.5 ± 4.9% (mean ± SEM) to 70.0 ± 4.4% over the course of the experiment.

We sought to determine when observed feedback differed from expected feedback. In previous quantitative models of retention, memory performance falls off approximately as a power function of the retention interval, decaying rapidly in the short term and slowly in the long term (*21*, *22*). Such a functional relation weighs recent experiences more heavily in determining the expected probability of a reward. Here, we use a power function to define the expected reward from a given deck as a function of reward history. Choosing a particular deck, d, on the nth trial will yield an expected reward, $E_d[n]$, defined as

$$E_d[n] = 0.5 + 0.5\sum_{i=1}^{n-1} R_d[n-1]\alpha i^{\tau} \quad n = 2, \ldots N \tag{1}$$

for that deck. $R_d[n]$ is defined as the feedback of the nth trial (total number of trials = N) for deck d and has a value of 1 for positive feedback, –1 for negative feedback, and 0 for trials when deck d was not selected. Expectation is thus computed as a weighted sum of previous outcomes, where the weights fall off with the power function determined by τ. We set α such that the weights of the power function approximate one over infinite trials for a given τ. This ensures an unbiased estimate of the effect of prior outcomes on expectation and limits expectation to the range between zero and one. We fit Eq. 1 to the sequence of choices and rewards observed in each experimental session to determine the best-fitting τ for every participant [τ = 1.68 ± 0.32 (mean ± SEM)] (*20*). Based on the best fitting τ values in this model, participants selected the deck with the higher expected reward on 74.9 ± 3.1% of the trials. We used this model of expected reward to classify the feedback associated with each trial into one of four categories: (i) unexpected gains, (ii) unexpected losses, (iii) expected gains, and (iv) expected losses (*23*). The expected reward associated with one deck for a single experiment from a single participant is shown in Fig. 2B as a function of trial number n.

We extracted and sorted single-unit activity captured from SN microelectrode recordings to find 67 uniquely identified spike clusters (3.94 ± 0.6 clusters per recording) (Fig. 2C). To restrict our analysis to dopaminergic cells, we applied to each cluster stringent criteria pertaining to firing rate, spike morphology, and response to feedback, derived from previous studies (Fig. 2D) (*20*, *24*, *25*). Ultimately, we retained 15 putatively dopaminergic spike clusters, hereafter referred to as cells, for analysis [0.88 ± 0.21 (mean ± SEM) cells and 21.4 ± 6.5% of total spikes per recording; 10 microelectrode recordings contributed to this subset]. Average recorded waveforms from one cell and an example of an individual waveform are shown in Fig. 2E.

Representative spike activity recorded from a single SN cell in a single participant is shown in Fig. 3. We quantified the differences in spike activity during 225-msec non-overlapping intervals (*20*), focusing our analyses on the interval between 150 and 375 msec after the onset of feedback. Preliminary analyses demonstrated that this interval was particularly responsive (*20*), and this interval is consistent with response latencies shown in animal studies (*6*, *7*). Raw spike count increased in response to positive feedback and decreased in response to negative feedback during this interval [$F_{1,110}$ = 4.6, mean squared error (MSE) = 1.1, P = 0.04] (Fig. 3A). Fig. 3B shows spike activity during trials associated with unexpected gains and losses, recorded from the same SN cell. The difference in activity between responses to unexpected gains and losses during this interval was statistically significant [$F_{1,57}$ = 6.9, MSE = 1.8, P = 0.01] and notably clearer than the difference between positive and negative feedback.

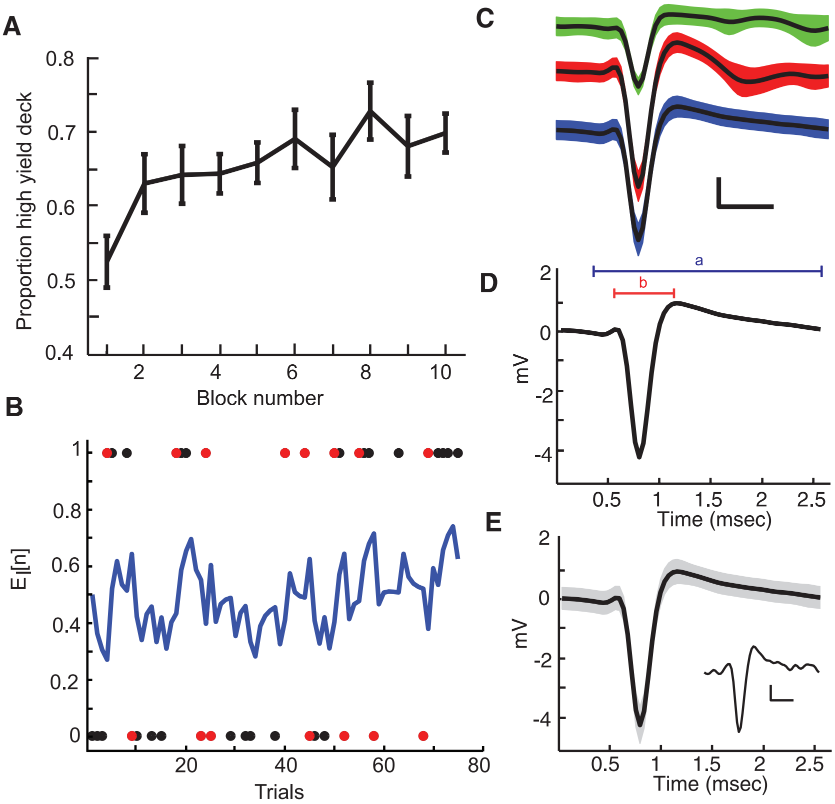

Fig. 2. (**A**) Learning rates are quantified by dividing the total number of trials (draws from the decks) into 10 equally sized blocks and determining how often participants correctly chose the (objectively) better deck during that block. Trace represents mean learning rate across all participants. Error bars represent SEM. (**B**) Expected reward associated with one deck in a single experiment. For each trial, we show the expected reward computed for the left deck, $E_l[n]$ (blue line) (Eq. 1). The outcome of each trial when this deck was selected is shown as a circle. Circles having value 1 represent positive outcomes, whereas circles having value 0 represent negative outcomes. Black circles denote expected outcomes, and red circles denote unexpected outcomes. We base our analysis on unexpected outcomes. (**C**) Mean waveforms of three unique spike clusters from one participant are shown in black, with SD colored for each cluster. Scale bar, 10 mV and 0.5 msec. (**D**) For each identified cluster, we calculated the average time from the beginning of the spike waveform to its return to baseline (a) and the average time between the two positive peaks of the waveform (b). We restricted our analysis to those clusters that had average baseline widths greater than 2 msec and peak-to-peak widths greater than 0.8 msec. (**E**) Mean (n = 4703) waveform of spikes from a single cell from one participant is shown in black with SD in gray. (Inset) Example waveform. Inset scale bar, 1 mV and 1 msec.

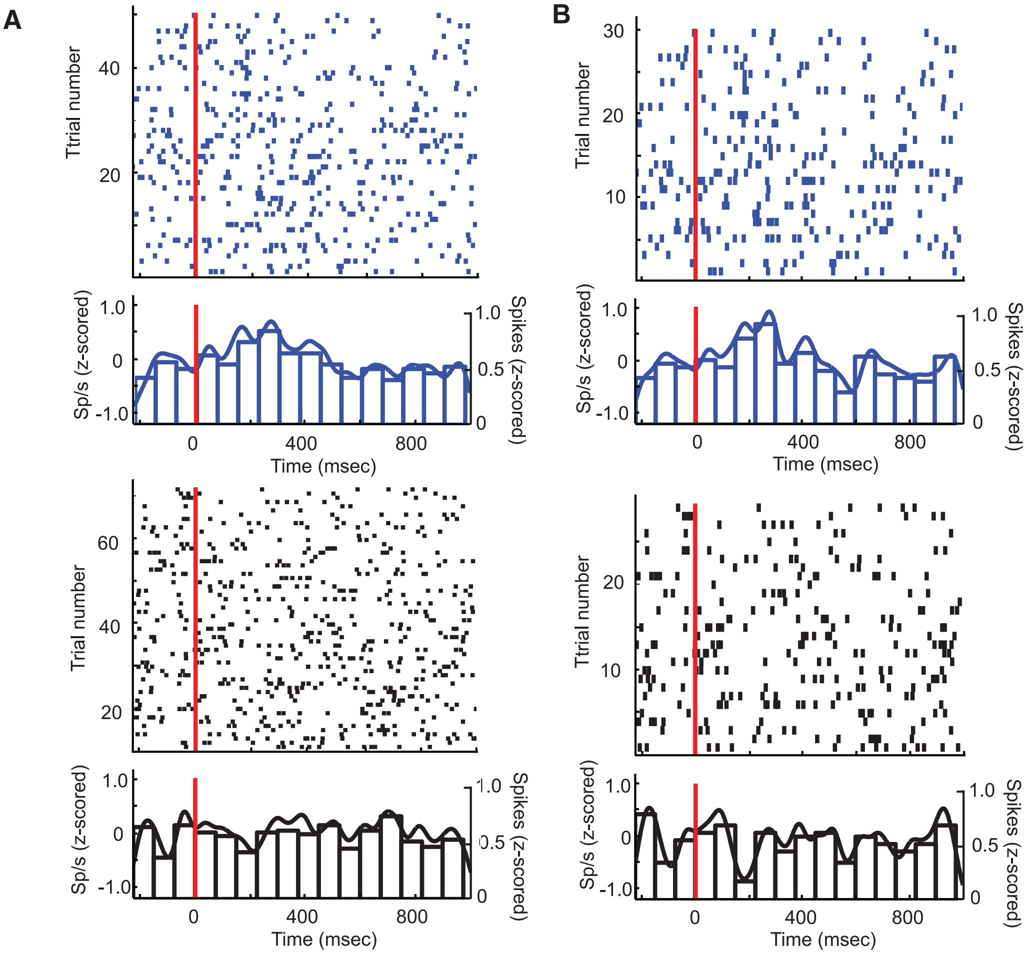

Fig. 3. (**A**) Spike raster for a single experiment from one participant. Individual spike activity recorded from SN for trials during positive (blue) and negative (black) feedback is shown for each trial as a function of time. Below each spike raster is the average *z*-scored continuous-time firing rate (continuous trace) and histogram (bars, 75-msec intervals). The red vertical line indicates feedback onset. (**B**) Individual spike activity, recorded from the same cell as shown in Fig. 3A, for trials in response to unexpected gains (blue) and losses (black) is shown for each trial as a function of time.

To determine how SN neurons encode behavioral feedback across participants, we pooled results for all cells meeting our inclusion criteria. We compared continuous-time firing rates and spike histograms for each SN cell to its baseline spiking activity to generate average *z*-scored continuous-time firing rates and histograms for each cell (Fig. 3) (*20*). We compared neural responses to unexpected and expected positive and negative feedback using a three-way analysis of variance for the interval between 150 and 375 msec after feedback onset (*20*). We found a significant difference between responses to positive and negative feedback in *z*-scored firing rate [$F_{1,14} = 9.3$, MSE = 29, $P = 0.0082$] and spike counts [$F_{1,14} = 16$, MSE = 16, $P < 0.005$]. In addition, we found that this main effect of feedback was modulated by a significant interaction with expectation [$F_{1,14} = 11.3$, MSE = 26, $P < 0.005$] for continuous-time firing rate and [$F_{1,14} = 15.0$, MSE = 17, $P < 0.005$] for spike count. The other post-feedback intervals (*20*) exhibited no significant differences between responses to positive and negative feedback. In addition, we found no significant change in activity in response to deck presentation itself [supporting online material (SOM) text].

To further investigate the strong modulatory effect of expectation, we examined the pooled activity across participants in response to unexpected gains and losses only. During the same post-feedback interval (gray shaded region, Fig. 4A) (*20*), spike rates in response to unexpected gains were significantly greater than spike rates in response to unexpected losses [$F_{1,14} = 16.5$, MSE = 49, $P < 0.001$] (Fig. 4A). Similarly, *z*-scored spike counts were also significantly greater in response to unexpected gains than to unexpected losses [$F_{1,14} = 18.2$, MSE = 24, $P < 0.001$] (Fig. 4B). This difference in spike activity was driven by a statistically significant response to unexpected gains greater than baseline activity (SOM text).

We confirmed that this difference in aggregated spike activity was consistently observed in individual cells by examining the relative differences in spike activity in response to unexpected gains and losses for each cell. During this interval, significantly more cells [14 out of 15 cells; $\chi^2(1) = 11.27$, $P < 0.001$] exhibited higher normalized spike rates in response to unexpected gains than to unexpected losses [mean difference of 0.67 ± 0.14 (mean ± SEM) *z*-scored spikes per second].

To confirm that human SN activity is primarily responsible for differentiating only between unexpected gains and losses, we examined differences in spiking activity between expected gains and losses. In the same 225-msec post-feedback interval, the difference in spike rates and normalized spike counts between expected gains and losses did not approach significance [$F_{1,14} < 1$, n.s.] (Fig. 4C). Similarly, the remaining intervals exhibited no significant differences in spike rate or normalized spike count in response to expected gains and losses.

The computation of how outcomes differ from expectation, often referred to as prediction error (*2*), is a central component of models of reinforcement learning and thought to be encoded by the activity of dopaminergic neurons (*5*–*7*, *15*, *26*). We examined the correlation between spike activity and changes in expected reward as determined by Eq. 1 under the assumption that this change can be used as a surrogate for prediction error. We defined prediction error here as the trial-to-trial adjustment each participant makes to the expected reward for each deck as determined by our model of expectation. Mean spike rates in the same post-feedback interval during trials associated with large positive prediction errors were larger than spike rates associated with small positive prediction errors, but this difference was only marginally significant [$F_{1,14} = 3.2$, MSE = 8, $P = 0.09$] (*20*). As trial-to-trial differences in expected reward in-

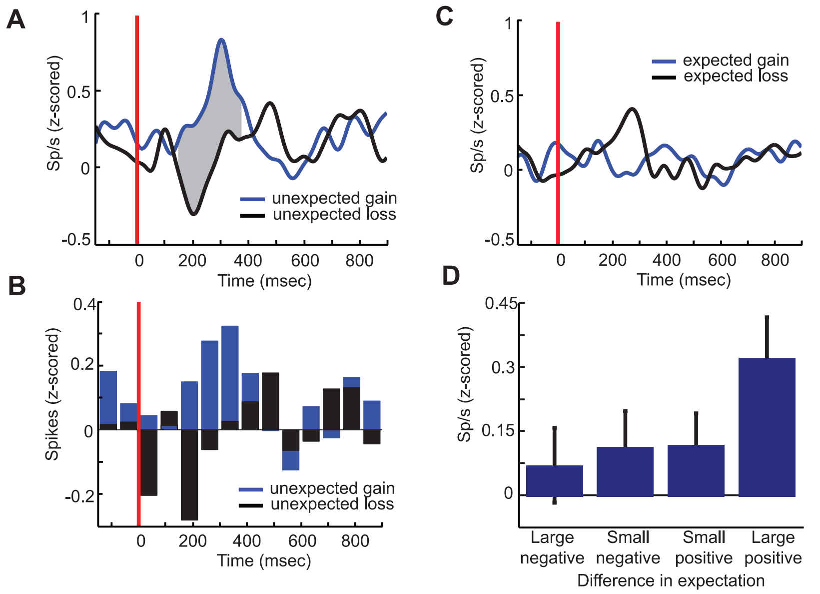

Fig. 4. (**A**) Average *z*-scored spike rate for unexpected gains (blue trace) compared with unexpected losses (black trace). The red line indicates feedback onset. The gray shaded region indicates the 225-msec interval between 150 and 375 msec after feedback onset. Traces represent average activity from 15 SN cells recorded from 10 participants. (**B**) Average *z*-scored spike histograms for unexpected gains (blue bars) compared to unexpected losses (black bars). The red vertical line indicates feedback onset. Histograms represent average *z*-scored spike counts from the same 15 SN cells. (**C**) Average *z*-scored spike rate for expected gains (blue trace) did not differ significantly from expected losses (black trace) for any interval. The red line indicates feedback onset. (**D**) For every participant, the median positive and negative trial-to-trial change in expected reward, as determined by Eq. 1, is used to classify prediction error into large and small positive and negative differences. Mean *z*-scored spike rate, captured between 150 and 375 msec after feedback onset for all cells, is shown for each level of prediction error. Error bars represent SEM.

creased, there was a general increase in spike activity, but this trend was also only marginally significant (Fig. 4D) (*20*).

Our results show that differences in human SN responses to positive and negative feedback are mainly driven by unexpected outcomes, with no significant differences in neural activity for outcomes that are anticipated according to our model. By responding to unexpected financial rewards, these putatively dopaminergic cells encode information that probably helps participants maximize reward in the probabilistic learning task.

Our results address the important question of whether extrapolating findings about the reward properties of dopaminergic SN neurons from nonhuman primates to humans is reasonable (*27*). Whereas the role of midbrain dopaminergic neurons in reward learning has been studied extensively in animals (*4*–*8*, *15*, *26*), the evidence presented here represents direct measurement of SN neurons in humans who were engaged in a probabilistic learning task. Our findings should serve as a point of validation for animal models of reward learning.

The reward for choosing the correct deck in our study was a perceptual stimulus designed to evoke a cognitive representation of financial reward. Primate studies, which often rely on highly salient first-order reward stimuli such as food and water, have demonstrated that dopaminergic neurons are also capable of responding to second-order associations (*28*), which are items that can be used to directly satisfy first-order needs. Because no monetary compensation was directly provided, our abstract rewards (i.e., images of second-order rewards) may be considered third-order. That the modest third-order rewards used here elicited a significant dopaminergic response, when they were unexpected, suggests that SN activity may play a more widespread role in reinforcement learning than was previously thought.

Our findings suggest that neurons in the human SN play a central role in reward-based learning, modulating learning based on the discrepancy between the expected and the realized outcome (*1*, *2*). These findings are consistent with the hypothesized role of the basal ganglia, including the SN, in addiction and other disorders involving reward-seeking behavior (*29*). More importantly, these findings are consistent with models of reinforcement learning involving the basal ganglia, and they suggest a neural mechanism underlying reward learning in humans.

References and Notes

1. R. A. Rescorla, A. R. Wagner, *Classical Conditioning II: Current Research and Theory* (Appleton Century Crofts, New York, 1972), pp. 64–99.
2. R. Sutton, A. Barto, *Learning and Computational Neuroscience: Foundations of Adaptive Networks* (MIT Press, Cambridge, MA, 1990), pp. 497–437.
3. P. R. Montague, P. Dayan, T. J. Sejnowski, *J. Neurosci.* **16**, 1936 (1996).
4. J. Mirenowicz, W. Schultz, *Nature* **379**, 449 (1996).
5. W. Schultz, P. Dayan, P. R. Montague, *Science* **275**, 1593 (1997).
6. W. Schultz, *Neuron* **36**, 241 (2002).
7. J. R. Hollerman, W. Schultz, *Nat. Neurosci.* **1**, 304 (1998).
8. M. A. Ungless, P. J. Magill, J. P. Bolam, *Science* **303**, 2040 (2004).
9. H. M. Bayer, P. W. Glimcher, *Neuron* **47**, 129 (2005).
10. S. M. McClure, D. I. Laibson, G. Loewenstein, J. D. Cohen, *Science* **306**, 503 (2004).
11. S. C. Tanaka *et al.*, *Nat. Neurosci.* **7**, 887 (2004).
12. A. M. Graybiel, *Curr. Opin. Neurobiol.* **15**, 638 (2005).
13. M. J. Frank, *J. Cogn. Neurosci.* **17**, 51 (2005).
14. N. Daw, K. Doya, *Curr. Opin. Neurobiol.* **16**, 199 (2006).
15. G. Morris, A. Nevet, D. Arkadir, E. Vaadia, H. Bergman, *Nat. Neurosci.* **9**, 1057 (2006).
16. B. J. Knowlton, J. A. Mangels, L. R. Squire, *Science* **273**, 1399 (1996).
17. R. Cools, R. Barker, B. J. Sahakian, T. W. Robbins, *Cereb. Cortex* **11**, 1136 (2001).
18. M. J. Frank, L. Seeberger, R. C. O'Reilly, *Science* **306**, 1940 (2004); published online 4 November 2004 (10.1126/science.1102941).
19. R. Cools, R. Barker, B. J. Sahakian, T. W. Robbins, *Neuropsychologia* **41**, 1431 (2003).
20. Materials and methods are available as supporting material on *Science* Online.
21. J. Wixted, E. Ebbesen, *Psychol. Sci.* **2**, 409 (1991).
22. D. Rubin, A. Wenzel, *Psychol. Rev.* **103**, 734 (1996).
23. For every trial, $E_l[n]$ represents the current expected reward for the left deck. If $E_l[n]$ exceeds 0.5 for a particular trial n, and if choosing the left deck on that trial yields positive feedback, we label this event an expected win. Conversely, if $E_l[n]$ is below 0.5 for a trial that yields positive feedback after choosing the left deck, we label this event an unexpected win. Similarly, we define expected and unexpected losses as those cases when negative feedback occurs when $E_l[n]$ is below or above 0.5, respectively. For trials when the right deck is chosen, we use $E_r[n]$ in identical fashion to classify responses into one of these four categories.
24. W. Schultz, A. Ruffieux, P. Aebischer, *Exp. Brain Res.* **51**, 377 (1983).
25. W. Schultz, *J. Neurophysiol.* **56**, 1439 (1986).
26. H. Nakahara, H. Itoh, R. Kawagoe, Y. Takikawa, O. Hikosaka, *Neuron* **41**, 269 (2004).
27. C. D. Hardman *et al.*, *J. Comp. Neurol.* **445**, 238 (2002).
28. W. Schultz, P. Apicella, T. Ljunberg, *J. Neurosci.* **13**, 900 (1993).
29. S. E. Hyman, R. C. Malenka, E. J. Nestler, *Annu. Rev. Neurosci.* **29**, 565 (2006).
30. This work is partially supported by NIH grant MH61975, Conte Center grant MH062196, and the Dana Foundation. We thank the staff of the Pennsylvania Neurological Institute for their assistance. We also thank J. Wachter and A. Krieger for statistical advice, A. Geller for cognitive task programming, and M. Kilpatrick and P. Connolly for assistance with DBS surgery.

Supporting Online Material

www.sciencemag.org/cgi/content/full/323/5920/1496/DC1
Materials and Methods
SOM Text
References

17 October 2008; accepted 16 January 2009
10.1126/science.1167342

RSY-1 Is a Local Inhibitor of Presynaptic Assembly in *C. elegans*

Maulik R. Patel[1] and Kang Shen[1,2,3]*

As fundamental units of neuronal communication, chemical synapses are composed of presynaptic and postsynaptic specializations that form at specific locations with defined shape and size. Synaptic assembly must be tightly regulated to prevent overgrowth of the synapse size and number, but the molecular mechanisms that inhibit synapse assembly are poorly understood. We identified regulator of synaptogenesis–1 (RSY-1) as an evolutionarily conserved molecule that locally antagonized presynaptic assembly. The loss of RSY-1 in *Caenorhabditis elegans* led to formation of extra synapses and recruitment of excessive synaptic material to presynaptic sites. RSY-1 directly interacted with and negatively regulated SYD-2/liprin-alpha, a master assembly molecule that recruits numerous synaptic components to presynaptic sites. RSY-1 also bound and regulated SYD-1, a synaptic protein required for proper functioning of SYD-2. Thus, local inhibitory mechanisms govern synapse formation.

Synapse formation is a highly dynamic and regulated process. Although many positive factors that promote synaptogenesis have been identified (*1*–*3*), less is known about negative regulators of synapse formation and their mode of action (*4*–*10*). We investigated synapse development and its regulation in the hermaphrodite-specific neuron HSNL, one of a pair of motor neurons that controls egg-laying behavior in *Caenorhabditis elegans* (*11*). Presynaptic specializations in the HSNL neuron assemble within a spatially discrete location along the axon that is stereotyped between animals (Fig. 1, A and B) (*12*). These presynaptic sites were visualized by transgenically expressing fluorophore-tagged synaptic proteins such as synaptic vesicle component synaptobrevin (SNB-1) or active-zone components ERC/CAST/Bruchpilot (ELKS-1) and GIT-1 (Fig. 1B and fig. S1) (*12*, *13*). SYD-1 and SYD-2 are essential for synapse development in the HSNL neuron; numerous synaptic components failed to localize to presynaptic sites in *syd-1* and *syd-2* mutants (Fig. 1, C and E, and fig. S1) (*13*, *14*). However, increasing SYD-2 function in *syd-1* null mutants, either by overexpressing SYD-2 or by introducing a gain-of-function (gf) mutation in *syd-2*, rescues the synaptic defects observed in *syd-1* mutants (*13*, *14*). Thus, under normal circumstances, SYD-1 is required for SYD-2 function. The existence of such positive regulators suggests that negative regulators of SYD-2 might counteract and balance the pro-synaptic function of SYD-1.

To isolate putative negative regulators of synaptogenesis, we performed a visual genetic screen for mutants that suppress the synaptic defects in the HSNL of *syd-1* mutants (*15*). We recovered two alleles of *r*egulator of *sy*naptogenesis–1 (*rsy-1*). In *syd-1*;*rsy-1* double mutants, the accumulation of SNB-1::yellow fluorescent protein (YFP) in the synaptic region of the HSNL was significantly higher than in *syd-1* single mutants (Fig. 1, C to E). The accumulation of SNB-1::YFP in these double mutants probably represents a restoration of functional synapses. First, active-zone components ELKS-1 and GIT-1 also localized at higher levels to presynaptic sites *in rsy-1*;*syd-1* double mutants than in *syd-1* single mutants (fig. S1). Second, defects in the egg-laying behavior in *syd-1* mutants, which are a cell-autonomous consequence of the presynaptic assembly defects in the HSNL neuron, were rescued in *rsy-1*;*syd-1* double mutants (Fig. 1F). Thus RSY-1 appears to counteract and balance the pro-synaptic function of SYD-1.

We mapped *rsy-1* to the genetic locus Y53H1A.1, which encodes two isoforms. Isoform A encodes a 589–amino acid protein with a proline-rich region, a coiled-coil domain, and a serine/arginine–rich (SR) domain (fig. S2). The SR domain of RSY-1 contains multiple putative nuclear localization sequences (NLSs). Isoform B encodes a smaller 517–amino acid protein that lacks the SR domain, which is replaced by 22 amino acids with a single putative NLS that is unique to the B isoform (fig. S2). RSY-1 is well conserved in vertebrates with both a long and a short isoform in *Mus musculus* (fig. S2). The vertebrate homolog of RSY-1 interacts with pinin (*16*), a dual resident of the nucleus and the desmosome junction with proposed functions including cell adhesion, transcription, and splicing (*17*–*20*). Beyond its interaction with pinin, no function has yet been assigned to RSY-1.

Both alleles of *rsy-1* that we isolated contained mutations that generate early stop codons, suggesting that they are likely to be null alleles (fig. S2). To determine where *rsy-1* is expressed, we made transgenic animals with a synthetic operon in which expression of both RSY-1 and cytoplasmic green fluorescent protein (GFP) is under control of the *rsy-1* promoter (fig. S3). RSY-1 was reproducibly expressed in the HSNL (Fig. 2A), as well as in other neurons and tissues (fig. S4). To determine whether RSY-1 functions cell-autonomously in the HSNL, we transgenically expressed isoform A of RSY-1 under the control of the *unc-86* promoter, which only expresses in the HSNs in the vulva region (*21*). Expression of the *Punc-86::rsy-1* transgene in *rsy-1*;*syd-1* double mutants restored synaptic defects in the HSNL of *syd-1* single mutants (Fig. 2B and fig. S5), consistent with a cell-autonomous role for RSY-1 in inhibiting presynaptic assembly.

Next, we sought to determine the subcellular localization of RSY-1. GFP-tagged RSY-1 (iso-

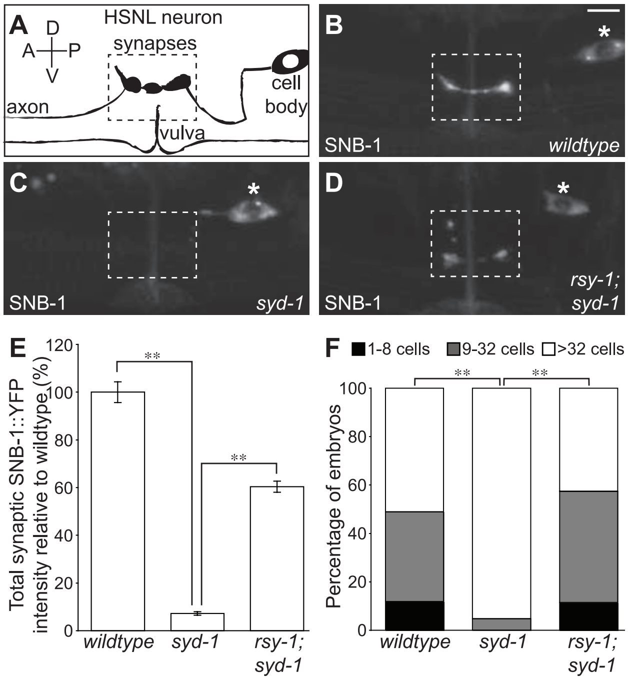

Fig. 1. RSY-1 antagonizes the pro-synaptic function of SYD-1. (**A**) Schematic of the HSNL neuron. Synapses are shown in the dotted rectangle. Anterior, A; posterior, P; dorsal, D; ventral, V. (**B**) SNB-1::YFP is expressed in the HSNL in *wildtype(N2)*, (**C**) *syd-1(ju82)*, and (**D**) *rsy-1(wy94);syd-1(ju82)* mutants. All images are of adults. The dotted rectangle indicates the synaptic region, and the asterisk marks the HSNL cell body. Scale bar, 5 μm. (**E**) Total SNB-1::YFP intensity at the synaptic region normalized to wild type. $^{**}P < 0.01$; Student's *t* test; $n > 20$ per group. Error bars indicate SEM. (**F**) Proportion of eggs at a particular stage when laid. Scored double blind. $^{**}P < 0.01$; Fisher's exact test; $n > 20$ per group.

---

[1] Neurosciences Program, Stanford University, 385 Serra Mall, Herrin Labs, Room 144, Stanford University, Stanford, CA 94305, USA. [2] Howard Hughes Medical Institute, Stanford University, Stanford, CA 94305, USA. [3] Departments of Biology and Pathology, 385 Serra Mall, Herrin Labs, Room 144, Stanford University, Stanford, CA 94305, USA.

*To whom correspondence should be addressed. E-mail: kangshen@stanford.edu

form A) expressed in the HSNL localized to presynaptic sites as well as to the nucleus (Fig. 2C and fig. S6). Because both isoforms of RSY-1 contain putative NLSs at the C terminus, we used a truncated version of RSY-1 (RSY-1ΔSR) that lacks all putative NLSs to determine whether the synaptic function of RSY-1 requires its localization to the nucleus. When expressed in the HSNL of *rsy-1*;*syd-1* double mutants, RSY-1ΔSR completely restored the reduction of SNB-1::YFP accumulation at presynaptic sites to levels observed in *syd-1* mutants (Fig. 2B). Furthermore, GFP-tagged RSY-1ΔSR was mostly excluded from the HSNL nucleus but robustly localized to the presynaptic sites, where it colocalized with RAB-3, a synaptic vesicle marker (Fig. 2D and fig. S6). Thus, localization of RSY-1 at the presynaptic sites (but not in the nucleus) is probably important for its function in inhibiting synaptogenesis.

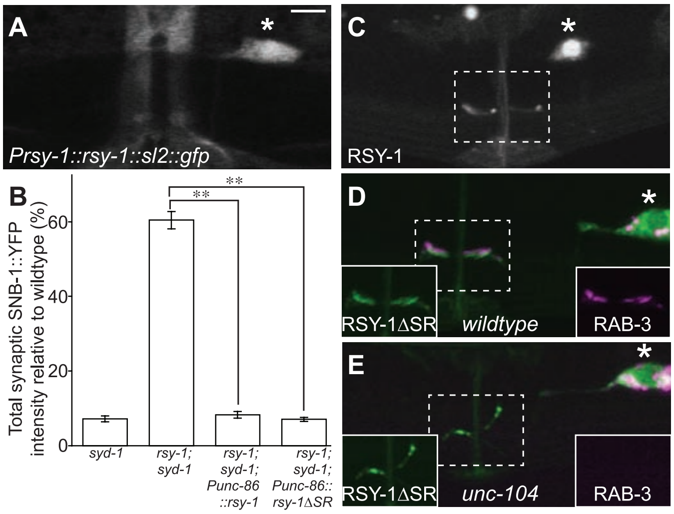

Fig. 2. Molecular characterization of *rsy-1*. (**A**) *rsy-1::sl2::gfp* expressed under the *rsy-1* promoter, which consists of 580 base pairs upstream of the *rsy-1* start site. (**B**) Total SNB-1::YFP intensity at the synaptic region normalized to wild type. *Punc-86::rsy-1* and *Punc-86::rsy-1ΔSR* denote transgenic expression of *rsy-1* or *rsy-1ΔSR* cDNA (isoform A), respectively. **$P < 0.01$; Student's t test; $n > 20$. Error bars indicate SEM. (**C**) GFP::RSY-1 (isoform A) expressed in the HSNL under the *unc-86* promoter. (**D**) GFP::RSY-1ΔSR (RSY-1 without amino acids 503 to 589 of isoform A) (in green) and mCherry::RAB-3 (in magenta) coexpressed in the HSNL in wild-type (*N2*) and (**E**) in *unc-104(e1265)* mutants. Insets in the lower left-hand corner in (D) and (E) show GFP::RSY-1ΔSR (green) alone, and insets in the lower right-hand corner show mcherry::RAB-3 (magenta) alone. All images are of adults. The dotted rectangle indicates the synaptic region, and the asterisk marks the HSNL cell body. Scale bar, 5 μm.

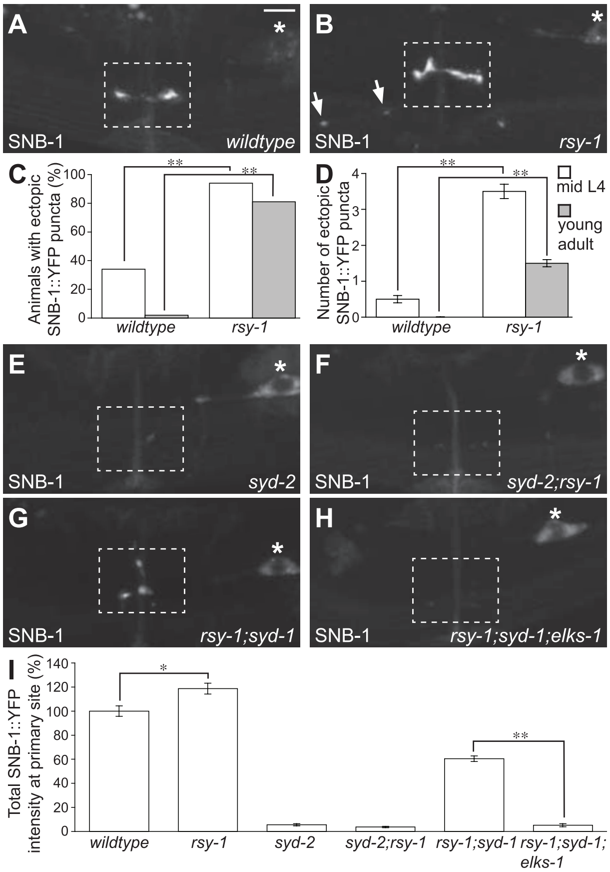

Fig. 3. RSY-1 is a negative regulator of SYD-2–dependent synapse assembly. (**A**) SNB-1::YFP expressed in the HSNL *wildtype(N2)* and (**B**) *rsy-1(wy94)* mutants. Arrows denote ectopic SNB-1::YFP puncta. (**C**) Percentage of animals with ectopic SNB-1::YFP puncta in *wildtype(N2)* and *rsy-1(wy94)* mutants at mid-L4 and young adult stages. **$P < 0.01$; Fisher's exact test; $n = 100$ per group. (**D**) Average number of ectopic SNB-1::YFP puncta in *wildtype(N2)* and *rsy-1(wy94)* mutants at mid-L4 and young adult stages. **$P < 0.01$; Student's t test; $n = 100$ per group. Error bars indicate SEM. (**E**) SNB-1::YFP accumulation at synapses in *syd-2(ju37)*, (**F**) *syd-2(ju37);rsy-1(wy94)*, (**G**) *rsy-1(wy94);syd-1(ju82)*, and (**H**) *rsy-1(wy94);syd-1(ju82);elks-1(tm1233)* mutants. All images are of adults. The dotted rectangle indicates the synaptic region, and the asterisk marks the HSNL cell body. Scale bar, 5 μm. (**I**) Total SNB-1::YFP intensity at the primary synaptic region in the HSNL relative to wild type. *$P < 0.05$; **$P < 0.01$; Student's t test; $n > 20$ per group. Error bars indicate SEM.

To further characterize presynaptic localization of RSY-1, we examined RSY-1ΔSR localization in *unc-104* mutants. UNC-104 is an ortholog of the vertebrate Kif1A, a kinesin motor essential for trafficking of synaptic vesicles (*22*). RSY-1ΔSR localization to presynaptic sites was not affected in *unc-104* mutants (Fig. 2E), suggesting that RSY-1 is not associated with synaptic vesicles. Furthermore, RSY-1ΔSR tightly colocalized with active-zone component SYD-2 (fig. S7). RSY-1ΔSR also colocalized with synaptic protein GIT-1 and was juxtaposed to another active-zone protein, ELKS-1 (fig. S8). Thus, RSY-1 occupies a particular subdomain of the active zone and locally regulates synapse assembly.

To determine when RSY-1 acts during the synaptic maturation process, we examined the localization of RSY-1ΔSR at nascent synapses of HNSL in the early and mid-L4 stages of development (*12*). RSY-1 accumulated at the developing presynaptic sites in early and mid-L4 stages concomitantly with RAB-3 (fig. S9), suggesting that RSY-1 could regulate synaptogenesis from the very early stages of synapse development. Future localization study of endogenous RSY-1 protein will probably provide additional information.

If RSY-1 is a negative regulator of synapse formation, then *rsy-1* single mutants should have elevated synaptogenic activity. SNB-1::YFP levels at presynaptic sites in the HSNL were increased in *rsy-1* mutants (Fig. 3, A, B, and I), suggesting that excessive synaptic material is recruited to the presynaptic sites. During development, synapses form at secondary sites outside of the normal synaptic region of the HSNL, which are then gradually eliminated as animals reach adulthood (*8*). Elimination of these synapses is partially dependent on proteasomal degradation (*8*). We observed a partial failure in the elimination of SNB-1::YFP localized to these secondary sites in *rsy-1* mutants (Fig. 3, A to D). These SNB-1::YFP accumulations probably represent presynaptic specializations because RAB-3 colocalized with the active-zone components ELKS-1 and GIT-1 at these sites (fig. S10). The persistence of synapses at secondary sites in *rsy-1* mutants suggests that local inhibition of presynaptic assembly by RSY-1 also contributes to the elimination of synapses. Thus, RSY-1 plays a role in controlling the size and number of presynaptic sites.

RSY-1 can inhibit synaptogenesis by either negatively regulating SYD-2 function or antagonizing an unknown SYD-2–independent parallel assembly pathway. Similar to *syd-1* suppression, if *rsy-1* mutation is able to suppress synaptic defects in *syd-2* mutants, then the data would be indicative of a model in which RSY-1 functions in parallel with SYD-2. However, we found that *syd-2* is epistatic to *rsy-1*; synaptic defects in *syd-2* mutants, as assayed by localization of synaptic proteins and the egg-laying behavior, were not rescued in *syd-2*;*rsy-1* double mutants (Fig. 3, E, F, and I, and fig. S5). Thus, RSY-1 probably acts upstream of or in parallel with SYD-2. Both models suggest that RSY-1 is a negative regulator of SYD-2–dependent synapse assembly.

According to the linear model in which *syd-2* acts downstream of *rsy-1*, the function of SYD-2 should increase in *rsy-1* mutants. If this is the case, then the phenotype in *rsy-1* mutants and *syd-2(gf)* animals should be similar. Indeed, more synaptic material was recruited to presynaptic sites in the HSNL in *syd-2(gf)* animals (*14*), similar to our observation in *rsy-1* loss-of-function mutants (Fig. 3I). The linear model also predicts that the rescued synapse assembly in *rsy-1*;*syd-1* mutants, like in *syd-2(gf)*;*syd-1* mutants, is due to an increase in SYD-2 function. If this is the case, then synapses in both double mutants should be similarly susceptible to various genetic manipulations. ELKS-1 is a presynaptic active-zone component shown to be important for the development of presynaptic terminals at the neuromuscular junction in *Drosophila* (*23*, *24*). In *C. elegans*, although the loss of ELKS-1 function by itself does not result in any detectable defects in synapse assembly (*13*, *14*, *25*), synapse formation in the HSNL of *syd-2(gf)*;*syd-1* mutants is crucially dependent on ELKS-1 (*14*). Thus, ELKS-1 functions redundantly with SYD-1 to promote synapse assembly. Synapse formation in *rsy-1*;*syd-1* double mutants was also dependent on *elks-1* (Fig. 3, G to I, and fig. S5). Thus, the synapse assembly program deployed in *rsy-1*;*syd-1* mutants is similar to the one in *syd-2(gf)*;*syd-1* mutants. In summary, the loss of RSY-1 function has similar consequences as the gain of SYD-2 function. Although these results do not rule out the possibility that RSY-1 functions in parallel with SYD-2, given that RSY-1 interacts with SYD-2 as described below, they are consistent with a genetic model in which RSY-1 is a negative regulator of SYD-2.

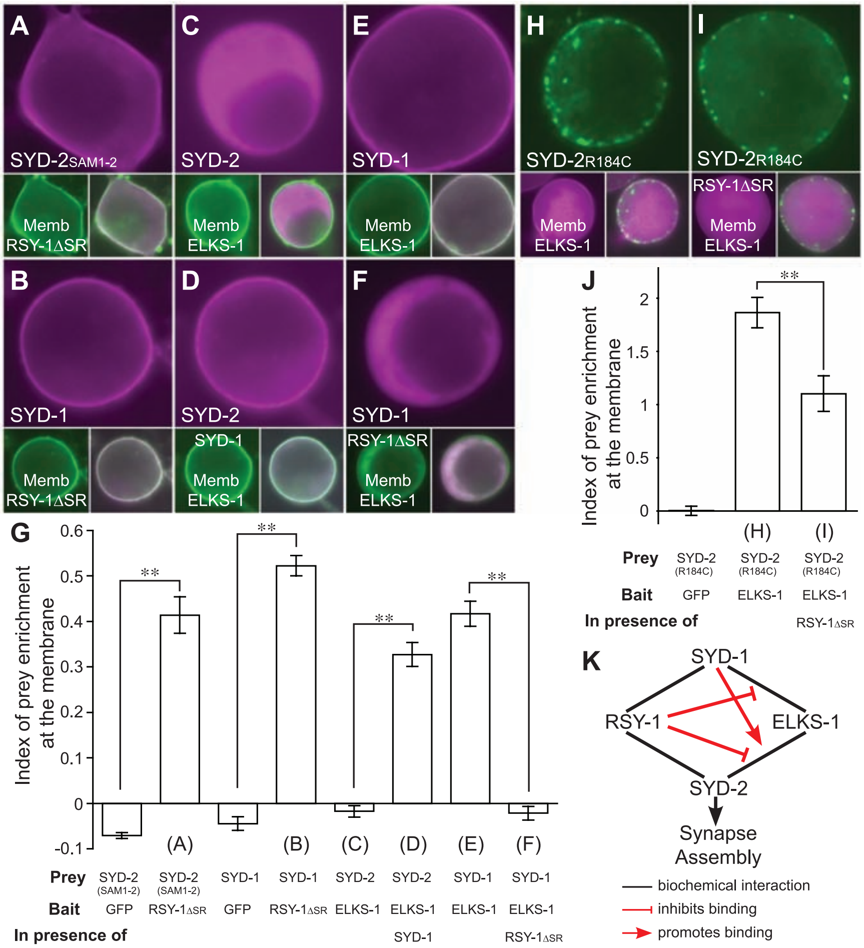

Fig. 4. Molecular mechanisms of RSY-1 function. (**A**) mCherry::SYD-2SAM1-2 (amino acids 853 to 1085 of SYD-2) (magenta, main panel) coexpressed in Hek293T cells with membrane-targeted GFP::RSY-1ΔSR (green, lower left panel; lower right panel shows a merged image). (**B**) mCherry::SYD-1 coexpressed with membrane-targeted GFP::RSY-1ΔSR. (**C**) mCherry::SYD-2 coexpressed with membrane-targeted GFP::ELKS-1 in the absence of and (**D**) in the presence of cytoplasmic GFP::SYD-1. (**E**) mCherry::SYD-1 coexpressed with membrane-targeted GFP::ELKS-1 in the absence of and (**F**) in the presence of cytoplasmic GFP::RSY-1ΔSR. (**G**) Quantification of prey translocation to the plasma membrane. (**H**) eYFP::SYD-2R184C (arginine amino acid at position 184 switched to cysteine) (green, main panel) coexpressed with membrane-targeted mCerulean::ELKS-1 (magenta, lower left panel; lower right panel shows a merged image) in the absence of and (**I**) in the presence of cytoplasmic mCherry::RSY-1ΔSR. (**J**) Quantification of prey translocation to the plasma membrane. In (G) and (J), the index of prey enrichment at the membrane was calculated by the following expression: (prey fluorescence intensity at the cell membrane/cytoplasm) – 1. An index of 0 indicates equal fluorescence intensity at the membrane and in the cytoplasm. $^{**}P < 0.01$; Student's *t* test; $n = 15$ per group. Error bars indicate SEM. Letters corresponding to figure panels are shown below the appropriate bar. The prey, membrane-targeted bait, and third cytoplasmic protein present are indicated below each bar. (**K**) Summary of biochemical interactions and their consequences. Promotion of SYD-2/ELKS-1 interaction by SYD-1 supports the genetic data that *syd-1* is normally required for *syd-2* function. Inhibition of SYD-2/ELKS-1 and SYD-1/ELKS-1 interaction by RSY-1 supports the genetic role of *rsy-1* in antagonizing *syd-2* directly and indirectly via syd-1.

RSY-1 could interfere with the pro-synaptic function of SYD-2 directly or inhibit the function of SYD-2 indirectly by blocking SYD-1. To test these possibilities, we used a single-cell in situ protein-protein interaction assay (*26*, *27*), in which translocation of the prey to the plasma membrane is tested in the presence of a membrane-tethered bait, to determine whether RSY-1 physically interacts with SYD-2 and SYD-1. RSY-1ΔSR bound to both SYD-2 [via the first two SAM domains] and SYD-1 (note the enrichment of SYD-2SAM1-2 and SYD-1 on the plasma membrane in the presence of membrane-targeted RSY-1ΔSR) (Fig. 4, A, B, and G). Furthermore, coimmunoprecipitation from worm lysates confirmed that RSY-1ΔSR interacted with both SYD-2 and SYD-1 in vivo (fig. S11).

To study the molecular consequence of interaction of RSY-1 with SYD-2 and SYD-1, we first established a readout of SYD-2 function. Vertebrate homologs of ELKS-1 and SYD-2 directly bind in vitro (*28*), whereas in *C. elegans*, SYD-2 and ELKS-1 coimmunoprecipitate from worm lysate (*14*). Furthermore, *syd-2* loss-of-function analysis suggests that SYD-2 is necessary for localizing ELKS-1 to presynaptic sites, whereas experiments with the *syd-2(gf)* allele suggest that SYD-2 is sufficient for recruiting ELKS-1 (*13*, *14*). Given these data and the genetic evidence that ELKS-1 is an important component of the presynaptic assembly program, we used the ELKS-1/SYD-2 interaction as one of the readouts of SYD-2 function.

Although there was little detectible interaction between ELKS-1 and SYD-2 in our assay, the interaction was greatly enhanced in the presence of SYD-1 (Fig. 4, C, D, and G), suggesting that SYD-1 facilitates binding between ELKS-1 and SYD-2. Consistent with this result, SYD-1 directly interacted with ELKS-1 (Fig. 4, E and G), and this interaction was weakened in the presence of RSY-1ΔSR (Fig. 4, F and G). Thus, one way in which RSY-1 regulates SYD-2 function is indirectly by weakening the interaction of SYD-1 with ELKS-1 and thus potentially blocking the ability of SYD-1 to facilitate SYD-2 function (Fig. 4K).

Given that the ELKS-1/SYD-2 binding is very weak in the absence of SYD-1 in our assay, we could not test whether interaction of RSY-1 with SYD-2 inhibited ELKS-1/SYD-2 binding. However, the ELKS-1/SYD-2 interaction does increase when SYD-2 contains a gain-of-function mutation, Arg^{184} → Cys^{184} (R184C) (*14*), which was verified in our cell-based assay (Fig. 4, H and J). We then tested the effect of RSY-1 on this interaction and found that the interaction between ELKS-1 and SYD-2R184C was weakened in the presence of RSY-1ΔSR (Fig. 4, I and J), suggesting that, besides acting via SYD-1, RSY-1 can also directly antagonize the ability of SYD-2 to recruit ELKS-1 (Fig. 4K).

It is increasingly clear that positive and negative regulators control synapse development at multiple levels. For example, the transcription factor MEF2 globally regulates the number of excitatory synapses (*7*). Three ubiquitin ligase complexes also regulate presynaptic development (*5*, *8*, *29*). Here, RSY-1 was shown to act as a negative regulator of synaptogenesis by counteracting SYD-1 function to inhibit SYD-2–dependent presynaptic assembly in the HSNL neuron. RSY-1 controls the amount of synaptic material recruited to presynaptic sites. RSY-1 also plays a role in establishing a balance between synapse formation and synapse elimination. RSY-1 achieves these functions by interacting with integral components of the synapse assembly machinery and by regulating a dense network of protein-protein interactions between various active-zone molecules (Fig. 4K).

References and Notes

1. M. Zhen, Y. Jin, *Nature* **401**, 371 (1999).
2. M. Zhen, Y. Jin, *Curr. Opin. Neurobiol.* **14**, 280 (2004).
3. C. L. Waites, A. M. Craig, C. C. Garner, *Annu. Rev. Neurosci.* **28**, 251 (2005).
4. Q. Chang, R. J. Balice-Gordon, *Neuron* **26**, 287 (2000).
5. P. van Roessel, D. A. Elliott, I. M. Robinson, A. Prokop, A. H. Brand, *Cell* **119**, 707 (2004).
6. K. Nakata *et al.*, *Cell* **120**, 407 (2005).
7. S. W. Flavell *et al.*, *Science* **311**, 1008 (2006).
8. M. Ding, D. Chao, G. Wang, K. Shen, *Science* **317**, 947 (2007); published online 11 July 2007 (10.1126/science.1145727).
9. M. P. Klassen, K. Shen, *Cell* **130**, 704 (2007).
10. V. Y. Poon, M. P. Klassen, K. Shen, *Nature* **455**, 669 (2008).
11. C. Desai, H. R. Horvitz, *Genetics* **121**, 703 (1989).
12. K. Shen, C. I. Bargmann, *Cell* **112**, 619 (2003).
13. M. R. Patel *et al.*, *Nat. Neurosci.* **9**, 1488 (2006).
14. Y. Dai *et al.*, *Nat. Neurosci.* **9**, 1479 (2006).
15. Materials and methods are available as supporting material on *Science* Online.
16. G. Zimowska *et al.*, *Invest. Ophthalmol. Vis. Sci.* **44**, 4715 (2003).
17. P. Ouyang, *Biochem. Biophys. Res. Commun.* **263**, 192 (1999).
18. J. H. Joo *et al.*, *Mol. Vis.* **11**, 133 (2005).
19. R. Alpatov *et al.*, *Mol. Cell. Biol.* **24**, 10223 (2004).
20. P. Wang, P. J. Lou, S. Leu, P. Ouyang, *Biochem. Biophys. Res. Commun.* **294**, 448 (2002).
21. R. Baumeister, Y. Liu, G. Ruvkun, *Genes Dev.* **10**, 1395 (1996).
22. D. H. Hall, E. M. Hedgecock, *Cell* **65**, 837 (1991).
23. D. A. Wagh *et al.*, *Neuron* **49**, 833 (2006).
24. R. J. Kittel *et al.*, *Science* **312**, 1051 (2006); published online 13 April 2006 (10.1126/science.1126308).
25. S. L. Deken *et al.*, *J. Neurosci.* **25**, 5975 (2005).
26. D. Blanchard, H. Hutter, J. Fleenor, A. Fire, *Mol. Cell. Proteomics* **5**, 2175 (2006).
27. M. D. Muzumdar, B. Tasic, K. Miyamichi, L. Li, L. Luo, *Genesis* **45**, 593 (2007).
28. J. Ko, M. Na, S. Kim, J. R. Lee, E. Kim, *J. Biol. Chem.* **278**, 42377 (2003).
29. T. A. Fulga, D. Van Vactor, *Neuron* **57**, 339 (2008).
30. We would like to thank the *Caenorhabditis* Genetics Center and the Japanese NBPR for strains; Y. Kohara (National Institute of Genetics, Japan) for Y53H1A.1 cDNAs; J. Audhya (University of California, San Diego) for *C. elegans* optimized mCherry cDNA; L. Luo (Stanford University) for vertebrate mCherry cDNA; T. Meyer (Stanford University) for eYFP-C3 plasmid; M. Park (Stanford University) for mCerulean-C1 plasmid; C. Gao for technical assistance; and members of the Shen lab, C. Bargmann, T. Clandinin, and L. Luo for critical comments on the manuscript. We would also like to thank B. Grill (Stanford University) for providing protocol and guidance for coimmunoprecipitation experiments. This work was funded by grants awarded to K.S. [from NIH (1R01NS048392), the Human Frontier Science Foundation, the Howard Hughes Medical Institute, and the W. M. Keck Foundation] and by a National Research Service Award predoctoral fellowship awarded to M.R.P. by NIH.

Supporting Online Material
www.sciencemag.org/cgi/content/full/323/5920/1500/DC1
Materials and Methods
Figs. S1 to S11
References

26 November 2008; accepted 7 January 2009
10.1126/science.1169025

The Role of Fingerprints in the Coding of Tactile Information Probed with a Biomimetic Sensor

J. Scheibert,* S. Leurent, A. Prevost,† G. Debrégeas‡

In humans, the tactile perception of fine textures (spatial scale <200 micrometers) is mediated by skin vibrations generated as the finger scans the surface. To establish the relationship between texture characteristics and subcutaneous vibrations, a biomimetic tactile sensor has been designed whose dimensions match those of the fingertip. When the sensor surface is patterned with parallel ridges mimicking the fingerprints, the spectrum of vibrations elicited by randomly textured substrates is dominated by one frequency set by the ratio of the scanning speed to the interridge distance. For human touch, this frequency falls within the optimal range of sensitivity of Pacinian afferents, which mediate the coding of fine textures. Thus, fingerprints may perform spectral selection and amplification of tactile information that facilitate its processing by specific mechanoreceptors.

The hand is an important means for human interaction with the physical environment (*1*). Many of the tasks that the hand can undertake—such as precision grasping and manipulation of objects, detection of individual defects on smooth surfaces, and discrimination of textures—depend on the exquisite tactile sensitivity of the fingertips. Tactile information is conveyed by populations of mechanosensitive afferent fibers innervating the distal fingerpads (*2*, *3*). In recent years, a breakthrough in our understanding of the coding of roughness perception has been made with the experimental confirmation of Katz's historical proposition of the existence of two independent coding channels that are specific for the perception of coarse and fine textures (*4*–*6*). The perception of coarse textures (with features of lateral dimensions larger than about 200 μm) relies on spatial variations of the finger/substrate contact stress field and is mediated by the slowly adapting mechanoreceptors (*7*). The perception of finer textures (<200 μm) requires the finger to be scanned across the surface because it is based on the cutaneous vibrations thus elicited. These vibrations are intensively encoded, principally by Pacinian fibers (*8*), which are characterized by a band-pass behavior with a best frequency (i.e., the stimulus frequency where maximum sensitivity occurs) on the order of 250 Hz (*9*). The most elaborated description of the latter coding scheme was given by Bensmaïa and Hollins, who directly measured the skin vibrations of fingers scanning finely tex-

---

Laboratoire de Physique Statistique de l'Ecole Normale Supérieure, CNRS UMR 8550, Associé aux Universités Paris 6 et Paris 7, 24 rue Lhomond, 75231 Paris Cedex 05, France.

*Present address: Physics of Geological Processes, University of Oslo, Post Office Box 1048 Blindern, N-0316 Oslo, Norway.
†Present address: Laboratoire de Physique Théorique, 24 rue Lhomond, 75231 Paris Cedex 05, France.
‡To whom correspondence should be addressed. E-mail: georges.debregeas@lps.ens.fr.

tured substrates. They were able to correlate the perceived roughness of the surface with the power of the texture-induced vibrations weighted by the Pacinian spectral sensitivity (*10*, *11*).

Among the four types of mechanoreceptors that convey tactile information, Pacinian corpuscles (PCs) have the most extended receptive field and therefore the lowest spatial resolution. This may seem paradoxical given their involvement in the tactile perception of fine features (*12*, *13*). In standard psychophysical tests, the substrates used as stimuli are made of regularly spaced dots or bars (*1*). The resulting skin vibrations are confined to a single frequency whose value can be actively tuned by the subject through the scanning velocity so that it falls within the PC optimal range of sensitivity. Such regular stimuli substrates thus favor tactile identification or classification tasks. In contrast, for natural surfaces where features are randomly distributed and exhibit a wide spectrum of size, the elicited skin vibrations are expected to be spread over a large range of frequencies, among which only a limited fraction contributes to the PC activity.

To address this question on how low-resolution receptors encode fine textural information, the present study investigates the mechanical filtering properties of the skin. It aims at characterizing how textural information at any spatial scale (less than the finger/substrate contact diameter) is converted into subcutaneous vibrations in the vicinity of the mechanoreceptors during a dynamic tactile exploration. Because there is currently no way to measure experimentally the subcutaneous stress using a human subject, our approach is based on the use of a biomimetic tactile sensor whose functioning principle and main geometrical characteristics are matched to those of the human fingertip. This allows us to test, in particular, the role of epidermal ridges (fingerprints) in this transduction process. Two distinct functional roles have been so far attributed to these characteristic structures of the digital skin. Fingerprints are believed to reinforce friction and adhesion of the fingerpads, thus improving the ability to securely grasp objects or supports (*1*, *14*). They may also be implicated in tactile perception, each of them acting as a magnifying lever, thus increasing the subsurface strain with respect to the surface deformation (*15*, *16*). Here, we show that fingerprints may have a strong impact on the spectral filtering properties of the skin in dynamic tactile exploration.

The tactile sensor aims at mimicking the operation of the PC in dynamic tactile exploration (*17*, *18*). As far as possible, the various geometrical and mechanical characteristics of the sensor are scaled to its biological counterpart (see fig. S1 for a comparison of key parameters). The sensing element consists of a microelectro mechanical system (MEMS) device that provides force measurements in a region of millimeter extension. This microforce sensor is attached to a rigid base and covered with an elastic spherical cap mimicking the fingertip skin (Fig. 1A). This cap, made of cross-linked poly(dimethylsiloxane) (PDMS), has a maximum thickness h = 2 mm. Its surface is either "smooth" or "fingerprinted," that is, patterned with a regular square wave grating of period λ = 220 μm and depth 28 μm. The tactile sensor is mounted on a double cantilever system, allowing one to record the normal and tangential loads using capacitive position sensors. In a typical experiment, the sensor is scanned at constant velocity across a rigid, nominally flat substrate under a constant normal load P = 1.71 N, yielding a contact zone of centimeter extension. This value for the load, together with the periodicity of the fingerprint-like structure, is chosen so that the number of ridges within the contact in the artificial system is close to that observed with an actual fingerpad under standard exploratory load (as illustrated in Fig. 1, B and C).

The stimuli consist of white-noise one-dimensional (1D) textured substrates (Fig. 1A,

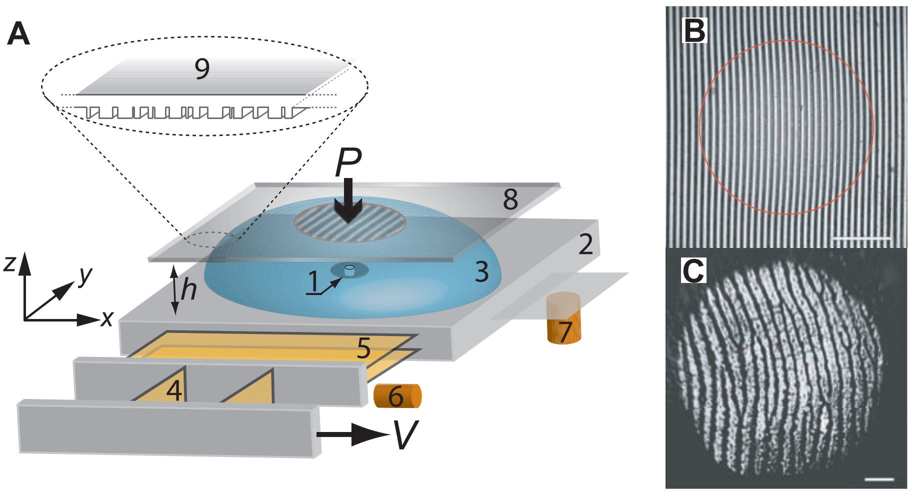

Fig. 1. (**A**) Sketch of the experimental setup. A MEMS microforce sensor (1) is mounted on a rigid base (2). It is covered with a spherical elastomer cap (3) of maximum thickness h = 2 mm and whose surface is smooth or patterned with parallel ridges. The resulting tactile sensor is mounted on a double-cantilever system (4, 5) allowing one to measure the total normal and tangential loads exerted on the sensor using capacitive position sensors (6, 7). In a typical experiment, the tactile sensor is scanned at constant speed v (using a linear motor) and under constant normal load P, across glass slides (8) whose surface is patterned with a 1D random square-wave grating (9). (**B**) Snapshot of the contact between the fingerprinted cap and a smooth glass slide in steady sliding. Wells between the elastomer's ridges appear bright, and the red circle, also shown on (A), defines the border of the contact. Actual contact only occurs on the ridges' summits. Ridges are slightly deformed at the periphery of the contact zone because of interfacial friction. (**C**) For comparison, this snapshot displays the contact between a human fingertip and a smooth glass surface with $P \approx 0.5$ N (a typical value in tactile exploration). Scale bars, 2 mm.

Fig. 2. (**A**) Typical pressure variation $p - \langle p \rangle$ measured with the smooth (blue) and fingerprinted (red) biomimetic fingers as a function of the substrate displacement u. The stimulus substrate used to produce these signals is a patterned glass slide exhibiting 1D random roughness. (**B**) Normalized power spectra of both signals obtained by Fourier transform averaged over four data sets, equivalent to a substrate of total length 180 mm. Shown in dashed lines is the theoretical power spectrum of the random pattern used as stimuli.

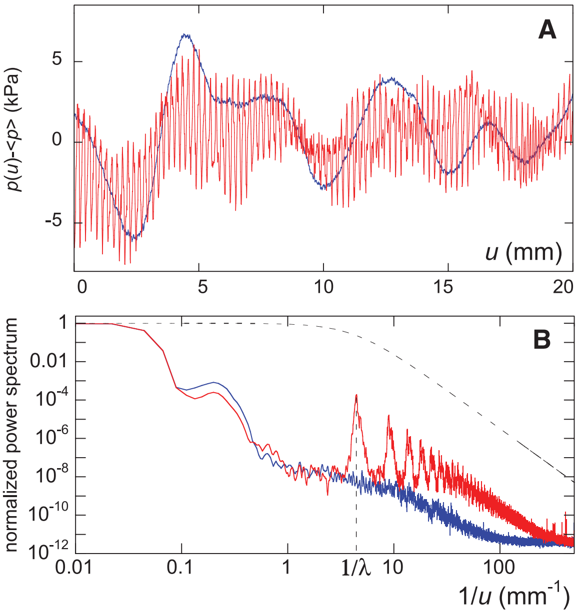

upper inset). They are obtained by patterning glass slides with a 28-μm-deep square wave grating whose edges are positioned at random positions with a mean grating width of 75 μm (*17*). The fingerprint-like ridges (when present) and substrate gratings are parallel to each other and oriented perpendicularly to the sliding direction. For moderate scanning velocities ($v <$ 0.4 mm/s) and a given normal load, the pressure signal $p(t)$ is found to be a sole function of the substrate position at time t, regardless of the scanning velocity v (figs. S2 and S3). All experiments are performed at constant v = 0.2 mm/s, well within this velocity-independent regime of friction. To facilitate the analysis, data are systematically plotted as a function of the sensor/substrate relative displacement $u = vt$, as a strict equivalence exists between time and substrate displacement in steady sliding.

Figure 2A shows the typical pressure variations $p(u) - \langle p \rangle$ (where $\langle p \rangle$ is the average pressure) measured with the microforce device as the sensor is scanned across a textured surface. The smooth sensor exhibits pressure modulations with a characteristic wavelength in the millimeter range. The fingerprinted system reveals similar long-wavelength modulations to which are superimposed rapid oscillations whose period corresponds to a displacement of the substrate over the interridge distance λ = 220 μm. A characterization of both sensors' filtering properties is given in Fig. 2B, which displays the power spectra of both signals together with that of the input stimulus, that is, the substrate topography (dashed line). The smooth sensor acts as a low-pass filter as it rapidly attenuates all pressure modulations induced by texture components of wavelength smaller than ≈1 mm. In contrast, the fingerprinted sensor exhibits band-pass filtering characteristics around the spatial frequency $1/\lambda$ (with further harmonics at integer multiples of $1/\lambda$). The presence of fingerprint-like ridges results in an amplification by a factor of 100 of the pressure modulations induced by a texture of wavelength λ (*19*).

These filtering characteristics can be interpreted to first order using a linear mechanical description of tactile sensing (*20*). Consider a small linear force sensor embedded at depth h in an elastic skin and located at ($x = 0$, $y = 0$). Its response to localized unit forces applied at various positions (x,y) on the skin surface defines its receptive field $F(x,y)$. The sensor signal p induced by any stress field $\sigma^s(x,y)$ applied at the skin surface then reads $p = \iint F(x, y)\sigma^s(x, y)\,dx\,dy$. We denote $\bar{\sigma}(x, y)$ the (time invariant) contact stress field resulting from the continuous rubbing of a smooth substrate under a given load. If the substrate exhibits a fine texture, the stress field σ^s becomes dependent on the substrate position u. As u varies, σ^s is modulated around the reference field $\bar{\sigma}(x, y)$. The use of substrates exhibiting a two-level topography and a large enough contrast prevents any contact above the wells (as optically evidenced in fig. S4). The contact pressure is thus zero over half of the apparent contact region, whereas it is expected to be about twice the time-averaged stress field $\bar{\sigma}(x, y)$ at the location of the substrate summits. As a first approximation, one may thus write the superficial stress field as a function of u in the form

$$\sigma^s(x, y) = \bar{\sigma}(x, y).(1 + T(u - x)) \qquad (1)$$

where $T(x)$ is the normalized two-level function ($T = \pm 1$), representing the topography of the surface. An exact calculation of the contact stress at a given location should take into account the local topography of the substrate and not just the average fraction of summits. The induced corrections should be important at short length-scales but become small when considering stress modulations over distances larger than the mean grating period.

With this expression, the pressure signal is then given by

$$p(u) = \langle p \rangle + \iint (F.\bar{\sigma})(x, y).T(u - x)dxdy \quad (2)$$

The transduction of tactile information is controlled by the product of the receptive field F and the reference stress field $\bar{\sigma}$. The function F characterizes the intrinsic properties of the receptor. It is expected to have a typical lateral extension of order h and to be fairly independent of the skin topography (such as fingerprints), provided that the height of the surface features is less than h (*21*). The reference field $\bar{\sigma}$ depends on the exploratory conditions such as the normal load P, the friction coefficient, or the position of the contact zone with respect to the sensor location. Unlike F, the stress field $\bar{\sigma}$ is highly sensitive to the skin surface topography. In particular, the presence of fingerprints a few tens of micrometers deep leads to a complete extinction of $\bar{\sigma}$ along regularly spaced lines (as illustrated in fig. S6), resulting in the observed spectral amplification of the signal at the frequency $1/\lambda$.

Equation 2 can be rewritten as $p(u) = \langle p \rangle + \int g_1(x)T(u - x)dx$ where $g_1(x) = \int (F.\bar{\sigma})(x, y)dy$ now defines the linear response function of the sensor with respect to 1D two-level stimuli substrates. The use of white-noise stimuli enables us to implement a Wiener-Volterra reverse-correlation method and extract $g_1(x)$directly from the measurements, $g_1(x) = \langle p(u)T(u - x) \rangle$ (*22*, *23*). The result of this computation for both smooth and fingerprinted sensors is plotted on Fig. 3. In qualitative agreement with the linear model, both response functions exhibit an

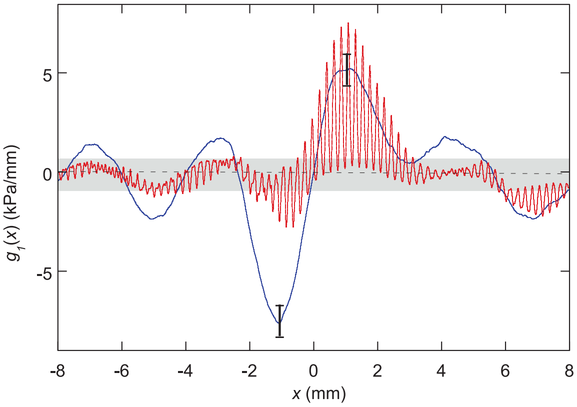

Fig. 3. Linearized stimulus-signal response functions $g_1(x)$ computed by cross-correlating the pressure signals and the stimulus topography $T(x)$, for both smooth (blue) and fingerprinted (red) systems. These data were obtained by averaging over three data sets, each one corresponding to a substrate length of 45 mm. The expected statistical deviation due to the finite length of the substrates was estimated numerically to be ±0.75 kPa/mm. This value is shown with the error bars and the shaded rectangle.

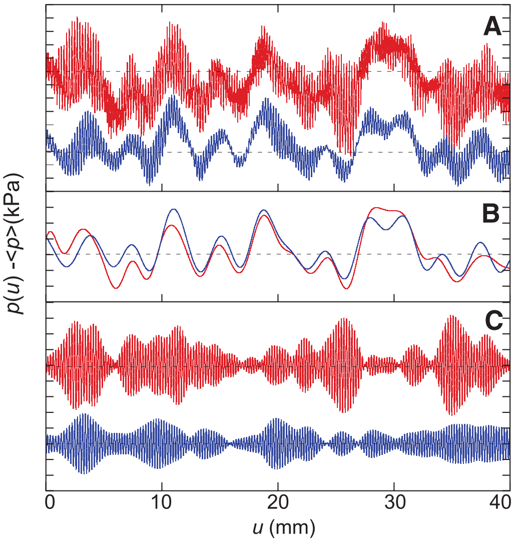

Fig. 4. (**A**) In red, pressure signal $p - \langle p \rangle$ measured with the fingerprinted sensor on a rough substrate. In blue, predicted signal obtained by convoluting the substrate topography function $T(x)$ with the linear response function $g_1(x)$. The latter was obtained independently by reverse correlation using two distinct 45-mm-long substrates. The dotted line indicates the $y = 0$ axis, and each interval along the y axis corresponds to a pressure variation of 1 kPa. For easier comparison, the same signals are plotted after applying (**B**) a low-pass filter with a cutoff frequency of $1/(2\lambda)$ and (**C**) a band-pass filter centered around the peak frequency $1/\lambda$.

envelope of lateral extension of order h, and the response function of the fingerprinted sensor is further modulated with a spatial period λ. These functions can be tested by confronting actual measurements of $p(u) - \langle p \rangle$ with the predicted signal $\int g_1(x)T(u - x)dx$ as shown in Fig. 4A for the fingerprinted system. To facilitate the comparison, Fig. 4, B and C, displays the low- and high-frequency components, respectively. The linear response function allows one to reproduce the low-frequency signal. Although it correctly predicts the maxima and minima of the high-frequency component, it fails to capture its amplitude, which indicates that nonlinear effects might not be negligible for small length-scales. These effects could be taken into account by correlating p with the successive powers of T in order to include additional terms of the Wiener-Volterra series to describe the response function. However, this computation would require using a much larger set of stimuli to provide sufficient statistics.

Although the biomimetic tactile sensor used in this study offers a crude version of the finger physiology (*24*, *25*), the mechanism of spectral selection it helped unravel depends on a very limited set of ingredients and should therefore be relevant to human digital touch. Namely, it requires that the surface of the tactile sensor displays a regularly ridged topography whose spatial period and amplitude are much smaller than the receptive field diameter and the mechanoreceptor's depth. In these conditions, such ridges have little influence on the skin deformations induced by a coarse texture (of spatial scale larger than the interridge distance λ). However, by shaping the interfacial contact stress field, such epidermal ridges give rise to an amplification of the subsurface stress modulations induced by a texture of characteristic wavelength equal to λ. In the time domain, this spatial period corresponds to a frequency $f_0 = v/\lambda$ where v is the finger/substrate relative velocity. In natural exploratory conditions, v is observed to be on the order of 10 to 15 cm/s (*1*). With a typical interridge distance $\lambda \approx 500$ μm, this yields a frequency $f_0 \approx 200$ to 300 Hz on the order of the best frequency of the Pacinian fibers that mediate the coding of fine textures. Fingerprints thus allow for a conditioning of the texture-induced mechanical signal that facilitates its processing by specific mechanoreceptors. It should be noted that this process is strongly dependent on the orientation of the ridges with respect to the scanning direction (fig. S7). In humans, fingerprints are organized in elliptical twirls so that each region of the fingertip (and thus each PC) can be ascribed with an optimal scanning orientation. Further studies are needed to elucidate how this may reflect on the exploratory procedures (such as fingertip trajectory and contacting zone) used by humans during texture evaluation tasks.

Remarkably, the response function of the fingerprinted system displayed in Fig. 3 is analogous to a Gabor filter because it provides both spatial and spectral resolution. Such filters are classically used in image analysis and have been identified in visual systems at the neural level (*26*). They are known to provide orientation discrimination, contrast enhancement, and motion detection. One may therefore expect, beyond the spectral filtering process discussed here, other interesting functional consequences of fingerprints, presumably relevant to the design of realistic haptic interfaces for humanoid robots (*27*, *28*).

References and Notes

1. L. A. Jones, S. J. Lederman, *Human Hand Function* (Oxford Univ. Press, 2006).
2. I. Darian-Smith, in *Handbook of Physiology: The Nervous System: Sensory Processes* (American Physiological Society, Bethesda, MD, 1984), vol. 3, chap. 17.
3. K. O. Johnson, J. R. Phillips, *J. Neurophysiol.* **46**, 1177 (1981).
4. D. Katz, *The World of Touch*, I. E. Krueger, Transl. and Ed. (Hillsdale, NJ, Erlbaum, 1989; original work published 1925).
5. M. Hollins, S. J. Bensmaïa, S. Washburn, *Somatosens. Mot. Res.* **18**, 253 (2001).
6. M. Hollins, S. J. Bensmaia, *Can. J. Exp. Psychol.* **61**, 184 (2007).
7. S. J. Lederman, M. M. Taylor, *Percept. Psychophys.* **12**, 401 (1972).
8. M. A. Srinivasan, J. M. Whitehouse, R. H. Lamotte, *J. Neurophysiol.* **63**, 1323 (1990).
9. J. C. Makous, R. M. Friedman, C. J. Vierck, *J. Neurosci.* **15**, 2808 (1995).
10. S. J. Bensmaia, M. Hollins, *Somatosens. Mot. Res.* **20**, 33 (2003).
11. S. J. Bensmaia, M. Hollins, *Percept. Psychophys.* **67**, 842 (2005).
12. R. S. Johansson, *J. Physiol.* **281**, 101 (1978).
13. M. Hollins, S. R. Risner, *Percept. Psychophys.* **62**, 695 (2000).
14. M. Cartmill, *Am. J. Phys. Anthropol.* **50**, 497 (1979).
15. N. Cauna, *Anat. Rec.* **119**, 449 (1954).
16. R. S. Fearing, J. M. Hollerbach, *Int. J. Robot. Res.* **4**, 40 (1985).
17. Materials and methods are available as supporting material on *Science* Online.
18. J. Scheibert, A. Prevost, J. Frelat, P. Rey, G. Debrégeas, *Europhys. Lett.* **83**, 34003 (2008).
19. A comparable spectral amplification is observed with finely abraded glass substrates (see fig. S5).
20. R. D. Howe, M. R. Cutkosky, *IEEE Trans. Robot. Autom.* **9**, 140 (1993).
21. K. L. Johnson, *Contact Mechanics* (Cambridge Univ. Press, Cambridge, 1985).
22. N. Wiener, *Nonlinear Problems in Random Theory* (MIT Press, Cambridge, MA, 1958).
23. F. Rieke, D. Warland, R. de Ruyter van Steveninck, W. Bialek, *Spikes: Exploring The Neural Code* (MIT Press, Cambridge, MA, 1999).
24. K. Dandekar, B. I. Raju, M. A. Srinivasan, *J. Biomed. Eng.* **125**, 682 (2003).
25. Q. Wang, V. Hayward, *J. Biomech.* **40**, 851 (2007).
26. J. P. Jones, L. A. Palmer, *J. Neurophysiol.* **58**, 1233 (1987).
27. R. Crowder, *Science* **312**, 1478 (2006).
28. V. Maheshwari, R. F. Saraf, *Science* **312**, 1501 (2006).
29. This project was supported primarily by CNRS basic funding and in part by the EU-NEST (New and Emerging Science and Technology) program, MONAT (Measurement of Naturalness) project (contract 21, number 29000). We are grateful to D. Chatenay and L. Bourdieu for fruitful discussions and careful reading of the manuscript.

Supporting Online Material

www.sciencemag.org/cgi/content/full/1166467/DC1
Materials and Methods
Figs. S1 to S7
References

26 September 2008; accepted 16 January 2009

10.1126/science.1166467
Include this information when citing this paper.

Inverted Microscope with LED Light

The Leica DM IL LED is the first inverted, routine microscope to combine superior optics with state-of-the-art LED illumination. The system's low-maintenance light source with no heat build-up, long free working distance, and high stability create suitable conditions for imaging live samples. The microscope's applications include a wide variety of cell and tissue culture examinations in biology and medicine, studies in developmental biology, micromanipulation, and live-cell experiments in transgenics and electrophysiology, but the instrument's transmitted light illumination, condensers, and contrast techniques are designed for cytobiological applications. A fluorescence version is also available for applications such as green fluorescent protein labeling. Both versions can be configured with a wide range of optics and accessories

Leica Microsystems
For information 847-405-7026
www.leica-microsystems.com

Refrigerating/Heating Circulator

The Model 9712 Refrigerating/Heating Circulator features a -40°C to 200°C temperature range, ± 0.01°C temperature stability, and a 13-liter reservoir. Typical applications include the control of jacketed reactor vessels and reaction blocks as well as polymerization, polycondensation, and distillation. The variable-speed pressure/suction cup is capable of delivering pressure flow rates as high as 30 liters per minute. A sophisticated programmable controller is capable of storing up to 10 different 50-step time/temperature programs. It also allows the operator to control the temperature at the point of application, eliminating temperature shifts due to heat loss along tubing lines. Other controller features include data logging capability, multilanguage help menus, and a built-in RS-232 interface.

PolyScience
For information 800-229-7569
www.polyscience.com

Bone Density Software

A new software module enables users to perform bone mineral density analysis of small animals and in vitro specimens using multienergy digital X-ray imaging when using the Kodak In-Vivo Multispectral FX, Kodak In-Vivo FX Pro, and Kodak DXS 4000 Pro systems. The software is designed for applications ranging from the study of diseases of the bone, such as arthritis and osteoporosis, to the efficacy of drugs and other treatment options that may affect bone mineral and other densities. An optional component of Kodak Molecular Imaging Software, the module makes use of a cylindrical modeling method to calculate the bone column density of selected long bones such as the tibia, fibula, metatarsals, and phalanges in small animals.

Carestream Molecular Imaging
For information 877-747-4357
www.carestreamhealth.com

Genotyping Tools

The new polymerase chain reaction (PCR)–based product line Type-it is designed to make genotyping accurate and reliable, with three kits now available. The Type-it Microsatellite PCR Kit is a multiplex PCR-based kit for detection of microsatellite loci in humans, animals, plants, and bacteria using any detection platform. It allows high-yield coamplification of all fragments without the need for time-consuming optimization of PCR parameters. The Type-it Mutation Detect PCR Kit is for detection of mutations such as deletions and translocations or for preamplification of single nucleotide polymorphisms (SNPs) using multiplex PCR technology. Multiple mutation targets are amplified in parallel using one protocol. The Type-it Fast SNP Probe PCR Kit enables accurate SNP genotyping using 5'-nuclease assays. It ensures high call rates, even when targeting difficult SNP loci or when using low template amounts. Time savings of up to 40 percent are possible compared with conventional methods due to the significantly reduced PCR run times.

Qiagen
For information 240-686-7686
www.qiagen.com

Cardiac Myocyte Growth Media

Clonetics Rat Cardiac Myocyte Growth Media is available for culturing rat cardiac myocytes for diverse research applications including hypertension, inflammation, ion channel flux studies, tissue engineering, and toxicology and cytotoxicology in drug development. The Myocyte Growth Media was developed and optimized for use with Clonetics Neonatal Rat Cardiac Myocytes to deliver exceptional survival and synchronized beating of these cells in culture.

Lonza Group
For information 301-898-7025
www.lonza.com

Fermentation Systems

Two types of programmable fermentation systems offer a high level of performance and reproducibility. They are suitable for a wide variety of cell types, including microbes, yeast, and fungi, as well as mammalian, insect, and plant cell lines. Both models are designed for benchtop use. The CSL-FS-S modular is a small-scale fermentation system for one vessel of up to 1.5 liters. The CSL-F1 is available in four different sizes, covering capacities of 3 liters, 5 liters, 7 liters, or 10 liters, or for dual vessels. Double-jacket vessels are available for mammalian cell culture. Each system includes a built-in 15-step programmable software package and integrated control panel that enables real-time recording and communication with a personal computer. The controller can be set to keep the microbes in various growth phases for maximum yield; a pH probe enables automatic control of acid or base input via peristaltic pumps.

Cleaver Scientific
For information +44-(0)-1788-565-300
www.cleaverscienfic.com

Electronically submit your new product description or product literature information! Go to **www.sciencemag.org/products/newproducts.dtl** for more information.